SLAC-R-518
UC-404
(SSRL-M)

SYNCHROTRON RADIATION TOTAL REFLECTION X-RAY FLUORESCENCE SPECTROSCOPY FOR MICROCONTAMINATION ANALYSIS ON SILICON WAFER SURFACES

Norikatsu Takaura

Stanford Linear Accelerator Center
Stanford Synchrotron Radiation Laboratory
Stanford University, Stanford, California 94309

June 1997

Prepared for the Department of Energy under contract number DE-AC03-76SF00515

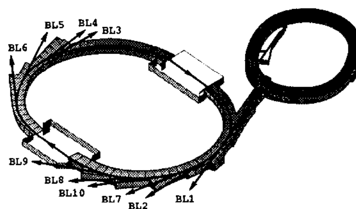

Printed in the United States of America. Available from the National Technical Information Service, U.S. Department of Commerce, 5285 Port Royal Road, Springfield, Virginia 22161

* Ph.D. thesis

SYNCHROTRON RADIATION TOTAL REFLECTION X-RAY FLUORESCENCE SPECTROSCOPY FOR MICROCONTAMINATION ANALYSIS ON SILICON WAFER SURFACES

A DISSERTATION

SUBMITTED TO THE DEPARTMENT OF

MATERIALS SCIENCE AND ENGINEERING

AND THE COMMITTEE ON GRADUATE STUDIES

OF STANFORD UNIVERSITY

IN PARTIAL FULFILLMENT OF THE REQUIREMENTS

FOR THE DEGREE OF

DOCTOR OF PHILOSOPHY

Norikatsu Takaura

June 1997

© Copyright by Norikatsu Takaura 1997

All Rights Reserved

ABSTRACT

As dimensions in state-of-the-art CMOS devices shrink to less than 0.1 μm, even low levels of impurities on wafer surfaces can cause device degradation. Conventionally, metal contamination on wafer surfaces is measured using Total Reflection X-Ray Fluorescence Spectroscopy (TXRF). However, commercially available TXRF systems do not have the necessary sensitivity for measuring the lower levels of contamination required to develop new CMOS technologies.

In an attempt to improve the sensitivity of TXRF, this research investigates Synchrotron Radiation TXRF (SR TXRF). The advantages of SR TXRF over conventional TXRF are higher incident photon flux, energy tunability, and linear polarization. We made use of these advantages to develop an optimized SR TXRF system at the Stanford Synchrotron Radiation Laboratory (SSRL). The results of measurements show that the Minimum Detection Limits (MDLs) of SR TXRF for 3-d transition metals are typically at a level of $3x10^8$ atoms/cm^2, which is better than conventional TXRF by about a factor of 20.

However, to use our SR TXRF system for practical applications, it was necessary to modify a commercially available Si (Li) detector which generates parasitic fluorescence signals. With the modified detector, we could achieve true MDLs of $3x10^8$ atoms/cm^2 for 3-d transition metals.

In addition, the analysis of Al on Si wafers is described. Al analysis is difficult because strong Si signals overlap the Al signals. In this work, the Si signals are greatly

reduced by tuning the incident beam energy below the Si K edge. The results of our measurements show that the sensitivity for Al is limited by x-ray Raman scattering.

Furthermore, we show the results of theoretical modeling of SR TXRF backgrounds consisting of the bremsstrahlung generated by photoelectrons, Compton scattering, and Raman scattering. To model these backgrounds, we extended conventional theoretical models by taking into account several aspects particular to SR TXRF. The results of the calculated backgrounds will be compared with experimental data.

Based on these calculations, we estimate the improvement of the MDLs as a function of incident beam energy and photon flux density. We will also discuss further improvements in the MDLs through the use of third generation synchrotron radiation sources.

To my parents,

for their love.

ACKNOWLEDGMENTS

I would like to express my sincere gratitude to many people. First of all, I would like to thank my advisor Piero Pianetta for giving me the opportunity to do this research. His support has encouraged me through my years at Stanford.

I would like to thank Dr. Stephen Laderman of Hewlett-Packard Co. for his continued support. I could not have achieved this work without his help and advice. He also deserves thanks for serving on my defense committee.

I would like to thank Dr. Alice Fisher-Colbrie of Hewlett-Packard Co. for providing experimental results used in this thesis. I learned a great deal about semiconductor analytical methods from her profound knowledge.

I would like to thank Dr. Sean Brennan. He kindly instructed me in the theories and experimental techniques of synchrotron radiation.

I would like to thank Dr. Dennis Werho of Motorola, Inc., for providing the experimental results on the GaAs wafers.

I would like to thank Srinka Ghosh for helping me analyze experimental data. I also would like to thank Dr. Ann Waldhauer for useful discussions.

I would also like to express deep appreciation to the HP/SSRL TXRF team for making these data possible.

I would like to thank Professor Bravman and Clemens for serving on my defense committee. I would like to thank Professor Wiedemann for serving as the chair in my defense.

I also thank the SSRL staff for experimental and administrative support. As an HP/Toshiba collaboration, Miyazaki-san and Shimazaki-san from Toshiba supplied us with some standard wafers for calibration. I would also thank Dave Wherry from Kevex who was instrumental in helping us design the detector modifications.

TABLE OF CONTENTS

Title Page		i
Copyright Notice Page		ii
Signature Page		iii
Abstract		iv
Acknowledgments		vii
Table of Contents		ix
List of Tables		xiv
List of Figures		xvi
1.	**INTRODUCTION**	**1**
	1.1 ULSI Problems	**1**
	1.2 Trends in Process Capability	**3**
	1.3 Total Reflection X-Ray Fluorescence Spectroscopy (TXRF)	**3**
	1.4 Minimum Detection Limit (MDL)	**4**
	1.5 Our Research Approach	**6**
	1.6 References	**8**
2.	**PRINCIPLES**	**9**
	2.1 Introduction	**9**
	2.2 Total Reflection	**9**
	2.2.1 Angle Scan	12
	2.2.2 Penetration Depth	13
	2.2.3 Refracted and Reflected Waves	14
	2.2.4 Refracted Field Intensity	18
	2.3 X-Ray Fluorescence	**19**

2.4 **Total Reflection X-Ray Fluorescence Spectroscopy (TXRF)** 21

2.5 **Synchrotron Radiation** 22

2.5.1 Photon Flux 22

2.5.2 Spectrum 24

2.5.3 Radiation Pattern 26

2.5.4 Linear Polarization 27

2.6 **Conclusions** 29

2.7 **References** 29

3. **EXPERIMENTAL SETUP** 32

3.1 **Introduction** 32

3.2 **SR Optics** 32

3.2.1 Optical Configuration for 3-d Transition Metal Analysis 32

3.2.2 Multilayer Monochromators 34

3.2.3 Photon Flux 36

3.2.4 Sample Chamber 38

3.2.5 Vacuum Condition 41

3.2.6 Detector Configuration with Respect to Polarization Vector 48

3.2.7 Optical Configurations of Al Analysis 49

3.3 **Si (Li) Detector** 51

3.3.1 Backgrounds from Si (Li) Detector 52

3.4 **Alignment of Incident Angle** 54

3.5 **Standard Wafers** 55

3.6 **Conclusions** 57

3.7 **References** 59

4. **EXPERIMENTAL RESULTS** 61

4.1 **Introduction** 61

4.2 3-d Transition Metal Analysis on Si Wafer Surfaces 61
4.2.1 Standard Spectrum 61
4.2.2 Comparison with Other Analytical Methods 65
4.2.3 Diffraction Peaks 69
4.2.4 Diffraction Conditions 71
4.2.5 Scattered X-Rays 76
4.2.6 Spurious Fluorescence Signals from the Si (Li) Detector 78
4.2.7 Practical Applications 86

4.3 3-d Transition Metal Analysis on GaAs Wafer Surfaces 92

4.4 Al Analysis on Si Wafer Surfaces 98
4.4.1 MDL with Standard Optical Configuration 98
4.4.2 Energy Tunability 100
4.4.3 MDLs of Al on Si Wafer Surfaces 105
4.4.4 Standard Wafers 107

4.5 Conclusions 110

4.6 References 111

5. THEORETICAL MODELING OF SR TXRF SIGNALS 114

5.1 Introduction 114

5.2 Photoelectron Bremsstrahlung 115
5.2.1 Photoemission in SR TXRF 117
5.2.2 Angular Distribution of Bremsstrahlung 119
5.2.3 Modeling Equation 120
5.2.4 The Bremsstrahlung Emission Probability 122
5.2.5 Surface Correction Factor 124
5.2.6 Normalization with Si Fluorescence Signals 129
5.2.7 Comparison of the Theoretical Model with Experimental Data 130

5.3 Surface Oxide Effect 135
5.3.1 Conventional Theoretical Models 135
5.3.2 Theoretical Models Including Surface Oxide Effects 138
5.3.3. Comparison of the Theoretical Model with Experimental Data 142

5.4 Detector Incomplete Charge Collection Background **150**

5.4.1 Detector Incomplete Charge Collection Background in Fe^{55} Spectrum 150

5.4.2 Detector Incomplete Charge Collection Background in SR TXRF Spectrum 156

5.5 X-Ray Raman Scattering **159**

5.5.1. Comparison of the Theoretical Model With Experimental Data 165

5.6 Conclusions **170**

5.7 References **171**

6. EXTRAPOLATION OF THE MINIMUM DETECTION LIMITS FOR DIFFERENT EXPERIMENTAL CONDITIONS **174**

6.1 Introduction **174**

6.2 The Minimum Detection Limits (MDLs) **174**

6.3 The MDLs of Elements in the Periodic Table **175**

6.4 Energy Tunability **180**

6.5 Incident Photon Flux **183**

6.6 Beam Divergence **185**

6.7 Third Generation Synchrotron Radiation Sources **187**

6.7.1 Low Emittance Beams 187

6.7.2 The MDLs for Ni with SPEAR3 191

6.8 The Calculation of SR Properties **195**

6.8.1 The Parameters Used for the SHADOW Calculation for BL 6-2 Wiggler on SPEAR 195

6.8.2 The Outputs of the SHADOW Calculation for BL 6-2 Wiggler on SPEAR 198

6.8.3 Flux from Insertion Devices 199

6.8.4 Mathematica NoteBook for Flux Calculation 203

6.9 Conclusions 204

6.10 References 204

7. CONCLUSIONS 206

7.1 Summary of Experimental Findings 206

7.2 Summary of Theoretical Findings 208

7.3 Direction of Future Work 209

LIST OF TABLES

Ch. 1 **INTRODUCTION**

Table 1.1 Effects of metal contamination on device properties. 2

Ch. 2 **PRINCIPLES**

Ch. 3 **EXPERIMENTAL SETUP**

Table 3.1 Parameters of wigglers at SSRL. 37

Table 3.2 Interaction volumes of air and silicon in TXRF. 43

Table 3.3 Si (Li) detectors used for SR TXRF measurements at SSRL. 53

Table 3.4 Metals in SC1 solution. 56

Ch. 4 **EXPERIMENTAL RESULTS**

Table 4.1 Fluorescence x -ray energies. 62

Table 4.2 The Ni MDLs with the SR TXRF techniques at SSRL. 65

Table 4.3 Comparison of various methods. 68

Table 4.4 Results of the filtering study with Teflon filters. 82

Table 4.5 Conversion of spurious signals to the contamination on the Si wafer surface. 85

Table 4.6 Signals and concentrations of the impurities on a Si wafer cleaned in CIS. 90

Table 4.7 Wafer cleaning processes in CIS and HP/Toshiba. 90

Table 4.8 Fluorescence x-ray energies of Ga and As. 93

Table 4.9 Comparison of signals and backgrounds from Si and GaAs wafers. 97

Table 4.10 Fluorescence signals of Al and Si signals of Al and Si. 99

Table 4.11 The minimum detection limits of TXRF (atoms/cm^2). 111

Ch. 5	**THEORETICAL MODELING OF SR TXRF BACKGROUND**	
Table 5.1	Properties of Si crystals and oxides.	138
Table 5.2	Surface oxide thickness measured by TXRF.	149
Ch. 6	**EXTRAPOLATION OF THE MINIMUM DETECTION LIMITS FOR DIFFERENT EXPERIMENTAL CONDITIONS**	
Table 6.1	Parameters of storage rings and particle beams.	190
Table 6.2	Insertion device parameters.	190
Table 6.3	Photon flux with SPEAR3.	192
Table 6.4	Projected MDLs for Ni with SPEAR3.	193

LIST OF FIGURES

Ch. 1	**INTRODUCTION**	
Fig. 1.1	Schematic diagram of a MOS device. A precipitate resulting from metal contamination is shown as a closed circle at the gate oxide interface.	2
Fig. 1.2	Elements that have given negative impacts on device properties [1].	3
Fig. 1.3	Trend in process capability for the cleanliness of 3-d transition metal contamination projected by the SIA in 1993 [1], [4]. The sensitivities for Ni with conventional and SR TXRF in 1995 are shown as well, which will be described in Ch. 4 [4]. In addition, the projected sensitivity of SR TXRF with an undulator on SPEAR3 is plotted, which will be described in Ch. 6.	4
Fig. 1.4	Schematic diagram of a signal peak and background component.	6
Ch. 2	**PRINCIPLES**	
Fig. 2.1	Total reflection from a silicon wafer surface. The electric field vectors and wave vector of the incident x-ray wave are represented by E and k, respectively. Those of the evanescent and reflected waves are represented by E' and k', and E" and k", respectively.	10
Fig. 2.2	Angle scan of the penetration depth of 10.6 keV x-rays incident on a silicon wafer.	13
Fig. 2.3	The phase diagram of the amplitude of the electric field of the	

	reflected and refracted waves. The curves for the reflected and refracted waves are shown using dashed and solid lines, respectively, as a function of incident angle, x, where x is the incident angle normalized to the critical angle.	15
Fig. 2.4	The angle scans of the amplitude of the refracted and reflected waves at the surface. The horizontal axis is the incident angle normalized to the critical angle. The vertical axis is the amplitude of the electric field normalized to incident wave. The curves for the reflected and refracted waves are shown in dashed and solid lines, respectively.	17
Fig. 2.5	Angle scan of the refracted field intensity for 10.6 keV x-rays incident on a silicon wafer.	18
Fig. 2.6	Energy diagram of atomic states with a core hole. The bold lines present atomic shells. The dashed lines indicate the electron transfer from the outer-shells to a core hole.	20
Fig. 2.7	Photon flux of the synchrotron radiation at SSRL.	25
Fig. 2.8	Radiation patterns of a) non-relativistic radiation and b) synchrotron radiation [21].	26
Fig. 2.9	Linear polarization of synchrotron radiation.	27
Fig. 2.10	Angular distribution of the Thomson scattering. The solid and dashed lines are the wave vector and electric field vector of the incident x-rays, respectively.	28
Ch. 3	**EXPERIMENTAL SETUP**	
Fig. 3.1	Layout of SR TXRF Optics of BL 6-2 at SSRL.	33
Fig. 3.2	Reflectivity curves of multilayer monochromators at the Bragg angle of 0.12 deg. The results of the theoretical	

calculations are shown in the solid and dashed lines. Experimental data are shown in dots. 35

Fig. 3.3 Photon flux from different monochromators. Data were taken using BL 4-2, BL 6-2, and BL 10-2 using a regular ion chamber at SSRL [4]. 37

Fig. 3.4 A top view of SR TXRF basic sample chamber. 39

Fig. 3.5 The detected area on a Si wafer. 40

Fig. 3.6 Transmission factor of a 25 μm Teflon filter as a function of x-ray energy. 41

Fig. 3.7 The x-ray beam incident on a Si wafer. For the clarity in the drawing, the incident angle of the x-ray beam is drawn larger than the actual incident angle, which is typically 0.1 deg. 42

Fig. 3.8 The x-ray beam incident at a glancing angle on a silicon wafer and air. 45

Fig. 3.9 The volume of air interacting with the x-ray beam. 46

Fig. 3.10 Detector configurations with respect to polarization vector, a) parallel mode and b) normal mode. The wave vector and polarization vector of the incident beam are shown in the solid and dashed lines, respectively. 48

Fig. 3.11 Optical configuration on BL 3-4 for low Z measurements. 50

Fig. 3.12 Optical configuration on BL 6-2 for low Z measurements. 50

Fig. 3.13 An example of fitting the angle scan of the Si fluorescence signal. The critical angle was used as a fitting parameter. 55

Ch. 4 EXPERIMENTAL RESULTS

Fig. 4.1 SR TXRF spectrum taken from a silicon standard wafer with $1x10^{11}$ atoms/cm^2 of Fe, Ni, and Zn. Data was taken using BL 6-2 at SSRL. The energy of the incident x-ray beam was 10.6 keV and the angle of incidence was 0.08 deg. A 25 mm Teflon filter was placed in front of the Si (Li) detector. 62

Fig. 4.2 TXRF data taken with conventional rotating anode (top) and the synchrotron radiation at SSRL (bottom). The conventional TXRF data was taken by S. Laderman et. al at Hewlett Packard [4]. 66

Fig. 4.3 202 and 404 diffraction peaks in a SR TXRF spectrum. Data were taken from a silicon standard wafer with $1x10^{11}$ atoms/cm^2 of Fe, Ni, and Zn at BL 4-2 at SSRL by use of a single multilayer monochromator. The energy of the incident x-ray beam was 10.6 keV with an angle of incidence of 0.08 deg. The x-ray beam was incident on the (001) silicon wafer from the [010] direction. 70

Fig. 4.4 The geometry of the diffraction condition generated from a Si (001) wafer by the incident x-ray beam at glancingly incidence. 71

Fig. 4.5 The diffraction conditions in the case of a Si (001) wafer when the detector acceptance angles are 30 deg. (top) and when it is 20 deg. (bottom) 73

Fig. 4.6 SR TXRF spectra taken with detector parallel and normal to the polarization vector of the incident x-ray beam. Data was taken from a nominally clean wafer. These spectra were

	normalized using the Si fluorescence signals.	77
Fig. 4.7	SR TXRF spectrum of a clean wafer taken with our commercially available Kevex Si (Li) detector (version 1). The spurious fluorescence signals of Fe, Ni, and Cu appeared.	79
Fig. 4.8	A result of the filtering study with 25 μm and 400 μm Teflon filters. The top spectrum is in log scale with the energy axis ranging from 0 to 12 keV. The bottom spectrum is in linear scale with the energy axis ranging from 5 to 10 keV.	81
Fig. 4.9	The Ag x-ray spectrum taken with the version 3 Si (Li) detector. A 0.5 mm Si absorption filter was placed between the Cd source and detector.	83
Fig. 4.10	Spurious fluorescence signal peaks from various Kevex Si (Li) detectors. The detectors used for the measurements were the standard Kevex Model # 3600-0018-0146 (version 1), the Ni modified detector (version 2), and the Cu modified detector (version 3). These spectra were normalized using the intensity of the continuous background at 7 keV. A 10.6 keV x-ray beam was used for the version 1 and 2 detectors, while a 11 keV beam was used for the version 3 detector.	85
Fig. 4.11	Comparison of Si wafers before and after 30 Å gate oxidation.	86
Fig. 4.12	Study of a cleaning equipment at HP.	88
Fig. 4.13	Comparison of the spectra taken from the Si wafers cleaned	

in CIS and HP/Toshiba. Data were taken with the version 2 Si (Li) detector. 89

Fig. 4.14 Difference spectrum between the CIS data and HP/Toshiba data. 89

Fig. 4.15 SR TXRF spectra of a GaAs wafer taken using the incident x-rays with the energies of 9.4 keV (bottom) and 10 keV (top). 93

Fig. 4.16 A SR TXRF spectrum taken from a standard GaAs wafer with $5x10^{12}$ atoms/cm^2 of Ti and $3.5x10^{12}$ atoms/cm^2 of Ni. 96

Fig. 4.17 The Si fluorescence signals generated by the standard 10.6 keV x-ray beam. 99

Fig. 4.18 Al K shell photoionization cross-section as a function of x-ray energy. 100

Fig. 4.19 SR spectrum taken from a Mylar film on BL 3-4. 102

Fig. 4.20 The modeling of the tailored SR spectrum on BL 3-4. 102

Fig. 4.21 SR TXRF spectra taken from 4Å of Al on a Si wafer. Data taken using BL 3-4 and BL 6-2. The spectra were scaled using the Al fluorescence signal counts. 104

Fig. 4.22 A spectrum taken on BL 3-4 from a Si wafer with $7x10^{11}$ atoms/cm^2 of Al. 106

Fig. 4.23 A spectrum taken on BL 6-2 from a Si standard wafer with $8x10^{12}$ atoms/cm^2 of Al. The incident x-ray energy was 1740 eV. 106

Fig. 4.24 (a) The elements on a Si wafer surface.
(b) The elements near a wafer surface. 108

Fig. 4.25 SR TXRF spectra taken on BL 3-4 from a Si standard wafer with $7x10^{11}$ atoms/cm^2 of Al prepared by the dipping method

(top) and a Si standard wafer with $1x10^{12}$ atoms/cm^2 of Al prepared by the droplet method (bottom). 109

Ch. 5 **THEORETICAL MODELING OF SR TXRF BACKGROUND**

Fig. 5.1 Profiles of photoelectron bremsstrahlung radiation generated by Si K shell photoelectrons ionized by 10.6 keV x-rays. The maximum bremsstrahlung energy is the initial photoelectron energy of 8.76 keV. The reduction of the kinetic energy in each thin target is assumed to be 1 keV for simplicity. 116

Fig. 5.2 The SR TXRF geometry in which the polarization vector is perpendicular to a Si wafer surface. The angular distribution of Si K-shell photoelectrons is shown as well. 118

Fig. 5.3 The angular distribution of 5.5 keV bremsstrahlung from 8.8 keV electrons in a silicon atomic field [11], [12]. The arrow indicates the direction of electron motion. 119

Fig. 5.4 The spectra of the continuous background normalized to the silicon fluorescence counts. Data were taken at 0.11 deg. and 0.5 deg. For details of our experimental configuration, see Chs. 2 and 3. 130

Fig. 5.5 The angle scan of the continuous background intensity at 5.6 keV normalized to the silicon fluorescence intensity with the data (•) and calculation (solid line). The continuous background intensity was integrated from 5.5 keV to 5.7 keV. 132

Fig. 5.6 The modeling of the photoelectron bremsstrahlung spectrum taken from a standard silicon wafer intentionally contaminated with 10^{11} atoms/cm^2 of Fe, Ni, and Zn. The incident angle was 0.08 deg. 134

Fig. 5.7 TXRF spectra taken from silicon wafers with native and 80 Å thermal oxides. Data were taken with a conventional RIGAKU TXRF system at 0.12 deg. (a) Si fluorescence peaks. (b) Scattered x-ray peaks. 143

Fig. 5.8 Angle scan of TXRF signals taken from the wafers with native oxide and 55 Å thermal oxide. The vertical axis is the scattered x-ray intensity normalized to silicon fluorescence intensity, which is represented by (Scatter / Si). The theoretical modeling curves for the native oxide and 55 Å thermal oxide wafers are shown in the solid and dashed lines, respectively. 145

Fig. 5.9 The theoretical modeling curves of scattering x-rays which takes into account the surface oxide effect . 147

Fig. 5.10 The surface oxide thickness as a function of the scattered x-ray intensity divided by the silicon fluorescence intensity at 0.03 deg. normalized to that at 0.48 deg. 149

Fig. 5.11 An experimental data from a Fe^{55} radio-active source (dots). The theoretical modeling curves of the Mn fluorescence and Auger bremsstrahlung are shown in solid and dashed lines, respectively. 151

Fig. 5.12 Filtering study of Fe^{55} spectra. Data were taken with and without a 25 μm Teflon filter. The data taken with the filter

was scaled to the data without the filter. 155

Fig. 5.13 Transmission factors of 25 μm and 400 μm Teflon filters. 155

Fig. 5.14 The results of filtering study for the SR TXRF spectra. Data were taken with 25 μm and 400 μm Teflon filters, respectively. 157

Fig. 5.15 The energy diagram of x-ray Raman scattering. a) an initial state. b) intermediate state(s) and c) final state(s). The incident x-ray ($h\upsilon_0$), and scattered x-ray ($h\upsilon'$), are shown as an arrow. The K-level and L-level are shown by a solid line. Continuum states are represented using shaded area. Electrons and vacancies are shown as the black and white circles, respectively. 159

Fig. 5.16 The observation angle, θ, with respect to polarization vector. 162

Fig. 5.17 The x-ray Raman double scattering cross-sections from a Si atom. The cross-sections were calculated for incident x-ray energies of 0.8 x Si K-edge (1472 eV), 0.9 x Si K-edge (1656 eV), and Si K-edge (1840 eV). 162

Fig. 5.18 The profiles of the x-ray Raman scattering of 1740 eV x-rays from silicon atoms passing through a 5 μm Be filter with and without the broadening by the detector resolution (FWHM of 100 eV). Fig. 5.18 (a) shows the energy range between 200 eV and 1800 eV. Fig. 5.18 (b) shows the range between 1450 eV to 1750 eV. 164

Fig. 5.19 SR TXRF spectra taken from a silicon wafer using incident

x-ray energies of 1500 eV (bottom), 1600 eV (middle), and 1700 eV (top). Data were taken using BL 6-2 at SSRL with 1000 sec. measurement times. 166

Fig. 5.20 SR TXRF spectra normalized to the oxygen fluorescence x-ray intensity. 167

Fig. 5.21 Comparison of the theoretical modeling curve and the experimental data for the x-ray Raman profile at a 1740 eV incident x-ray energy. The data were taken from a silicon wafer with 8×10^{12} atoms/cm^2 of Al. 168

Ch. 6 EXTRAPOLATION OF THE MINIMUM DETECTION LIMITS FOR DIFFERENT EXPERIMENTAL CONDITIONS

Fig. 6.1 The background spectrum taken from a Si wafer using an 11.2 keV incident beam. Experimental data are shown by the solid line, while the result of the theoretical calculation of the photoelectron bremsstrahlung is shown by the dashed line. In addition to the continuous background, this spectrum consists of the Si fluorescence signal (at 1.74 keV), the scattered x-ray peak (at 11.2 keV), its escape peak (at 9 keV), and the fluorescence signal peaks of S (at 2.31 keV) and Cl (at 2.62 keV). The fluorescence signals of S and Cl were generated from unintentional contamination on the Si wafer surface. 176

Fig. 6.2 The MDLs of various elements in periodic table. (a) The MDLs from P (Z=15) to Ge (Z=32), and from Zr (Z=40) to Os (Z=76) measured using an incident beam with an energy

	of 11.2 keV. For reference, the experimental MDLs of Na (Z=11) and Al (Z=13) obtained with an 1.74 keV incident beam are plotted as well. (b) The MDLs from P (Z=15) to At (Z=85) using incident beams with an energy equal to the fluorescence energy of the element of interest plus 3.5 keV.	179
Fig. 6.3	Ni photo-ionization cross-section as a function of incident beam energy.	181
Fig. 6.4	The MDLs of Ni at BL 6-2 as a function of incident beam energy. The calculated MDL at 11.2 keV is normalized to $4x10^8$ atoms/cm^2.	181
Fig. 6.5	The MDLs of Ni as a function of incident photon flux density. The horizontal axis is the photon flux density normalized to that of BL 6-2.	184
Fig. 6.6	The MDLs of Ni as a function of beam divergence.	187
Fig. 6.7	A schematic diagram of the SR TXRF geometry in which a photon beam strikes a Si wafer surface at a glancing angle of incidence. The figure is not drawn in scale.	188
Fig. 6.8	Schematic of the SR TXRF geometry in which a photon beam is incident on a Si wafer surface with an angle of incidence of 2 mrad (about 0.11 deg.). These figures are not drawn in scale.	189
Fig. 6.9	The estimated MDLs of Ni obtained by use of third generation synchrotron radiation sources.	194
Fig. 6.10	Radiation geometry represented by polar coordinates.	201

1. INTRODUCTION

Contamination analysis on silicon wafer surfaces is essential for the development of competitive silicon circuit technologies [1]. Conventionally, the metal contamination on the wafer surfaces is analyzed using Total Reflection X-Ray Fluorescence Spectroscopy (TXRF) [2]. However, the semiconductor industry anticipates that current TXRF systems with conventional x-ray sources do not have the sensitivity necessary to characterize the advanced processes needed for future device generations.

A natural way to improve the sensitivity of TXRF is to use synchrotron radiation as an excitation source instead of conventional x-ray sources. This thesis studies Synchrotron Radiation Total Reflection X-Ray Fluorescence Spectroscopy (SR TXRF) at Stanford Synchrotron Radiation Laboratory (SSRL).

Ch. 1 discusses the motivation of this research. Ch. 2 presents the principles of SR TXRF. Ch. 3 describes experimental methods. Ch. 4 shows experimental results. Ch. 6 deals with the methods for theoretical modeling of SR TXRF spectra. Ch. 6 projects possible further improvements in the sensitivity. Finally, Ch. 7 gives the summary and conclusions of this study.

1.1 ULSI Problems

Since the dimensions in state-of-the-art devices are small, even a small amount of the contamination can have negative impacts on the device properties [1], [3]. For example, the contamination which could nucleate and precipitate at the gate oxide interface in a MOS device is schematically shown in Fig. 1.1. Because the gate oxide thickness in state-of-the-art MOS devices is very thin (~ 50 Å), even a small amount of precipitation can decrease

decrease the effective gate oxide thickness. This results in, for instance, the decrease in a breakdown voltage of the device.

For reference, other typical negative impacts of contamination on device properties are shown in Table 1.1 and elements that have given negative impacts on device properties are shown in Fig. 1.2.

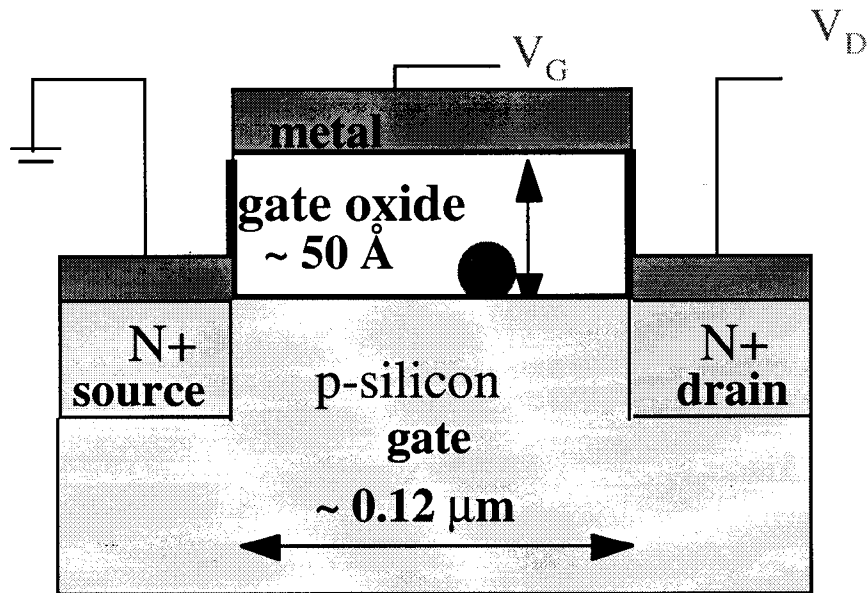

Fig. 1.1 Schematic diagram of a MOS device. A precipitate resulting from metal contamination is shown as a closed circle at the gate oxide interface.

Table. 1.1 Effects of metal contamination on device properties.

reduction of breakdown voltage
change in oxide growth rates
modification of oxide composition
formation of mobile ions
creation of trap levels into the band gap
poor control of FET threshold voltage

H																	He
Li	Be											**B**	C	N	O	F	Ne
Na	Mg											**Al**	Si	P	S	Cl	Ar
K	**Ca**	Sc	**Ti**	V	**Cr**	Mn	**Fe**	**Co**	**Ni**	**Cu**	**Zn**	Ga	Ge	As	Se	Br	Kr
Rb	Sr	Y	Zr	**Nb**	**Mo**	Tc	Ru	Rh	Pd	**Ag**	Cd	In	Sn	Sb	Te	I	Xe
Cs	Ba	La	Hf	**Ta**	**W**	Re	Os	Ir	**Pt**	**Au**	Hg	Tl	Pb	Bi	**Po**	At	Rn
Fr	Ra	Ac															

Fig. 1.2 Elements that have given negative impacts on device properties [1].

1.2 Trends in Process Capability

As device dimensions decrease, analytical methods with better sensitivities are indispensable in developing processes to eliminate even small amounts of metal contamination on wafer surfaces. As an aid in projecting the required sensitivity for metal contamination analysis, the SIA (Semiconductor Industry Association) made a roadmap of the expected trend in wafer cleaning capability as a function of time from 1992 to 2002 (Fig. 1.3) [1], [4]. As shown in Fig. 1.3, it is expected that cleanliness levels below 1×10^8 atoms/cm^2 will be achieved by 1998, and that levels of 1×10^7 atoms/cm^2 will be achieved in the first years of the 21st century.

1.3 Total Reflection X-Ray Fluorescence Spectroscopy (TXRF)

Total Reflection X-Ray Fluorescence Spectroscopy (TXRF) is one of industry-standard methods for analyzing metal contamination on wafer surfaces [5]. TXRF makes use of total external reflection of x-rays from a Si wafer to excite fluorescence x-rays from contamination on the surface.

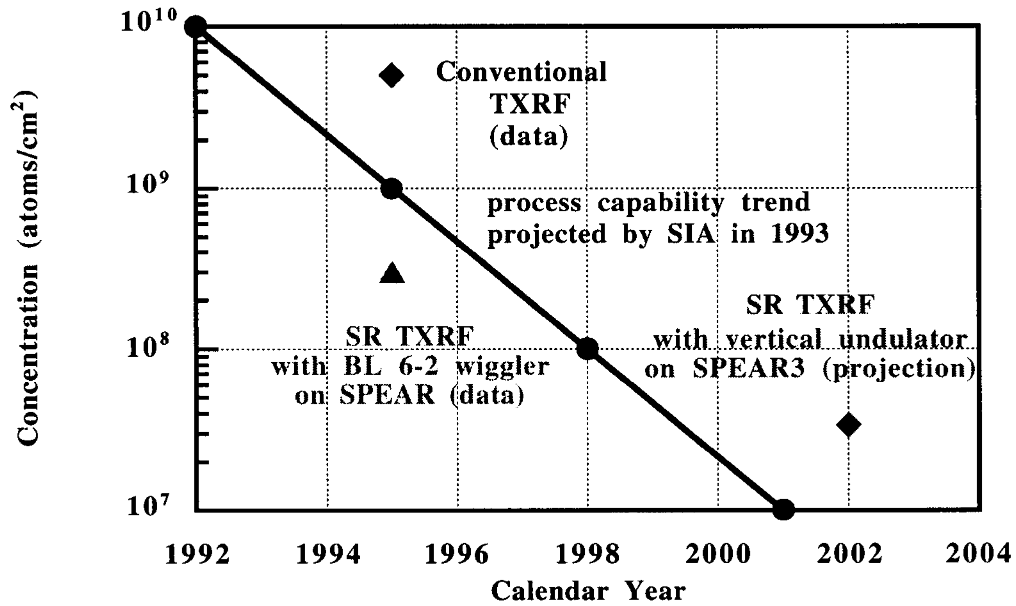

Fig. 1.3 Trend in process capability for the cleanliness of 3-d transition metal contamination projected by the SIA in 1993 [1], [4]. The sensitivities for Ni with conventional and SR TXRF in 1995 are shown as well, which will be described in Ch. 4 [4]. In addition, the projected sensitivity of SR TXRF with an undulator on SPEAR3 is plotted, which will be described in Ch. 6.

Since the penetration of x-rays in the total reflection condition is only approximately 40 Å, the x-ray background generated in a substrate wafer are greatly reduced. As a result, TXRF has an excellent sensitivity for contamination on Si wafer surfaces.

1.4 Minimum Detection Limit (MDL)

The sensitivity of TXRF is defined using the Minimum Detection Limit (MDL), which is given by Eq. (1.1) [7],

$$(\text{MDL}) = X \cdot \frac{3 \cdot \sqrt{(\text{Background})}}{(\text{Signal})} \qquad (1.1),$$

where

X = the concentration of a standard element,

(Background) = background counts, and

(Signal) = signal counts.

Typically, the MDLs are determined by measuring a standard with a known level of contamination for a measurement time of 1,000 sec. In TXRF, the signal is the fluorescence x-ray from the contamination on the wafer surface. The background is due to a number of physical phenomena which will be discussed in subsequent chapters.

Consider the schematic diagram of a signal peak superimposed on a continuous background component (Fig. 1.4). The horizontal axis is photon energy. The vertical axis is in counts per 1000 sec. In Fig. 1.4, the signal peak is separated from the background component using a linear function, which is determined using the background counts on the left and right sides of the signal peak.

Eq. (1.1) indicates that the signal must be larger than 3 times the square-root of the background counts in order for it to be statistically significant, that is, the signal becomes larger than the statistical deviation of the background.

Using Eq. (1.1), the MDL of Ni on a Si wafer surface with a conventional TXRF system at HP was found to be 5×10^9 atoms/cm^2 (See Ch. 4) [6]. Since the surface density of silicon atoms is about 10^{15} atoms/cm^2, the conventional TXRF system is capable of measuring only 10^{-5} of a monolayer of the metal contamination.

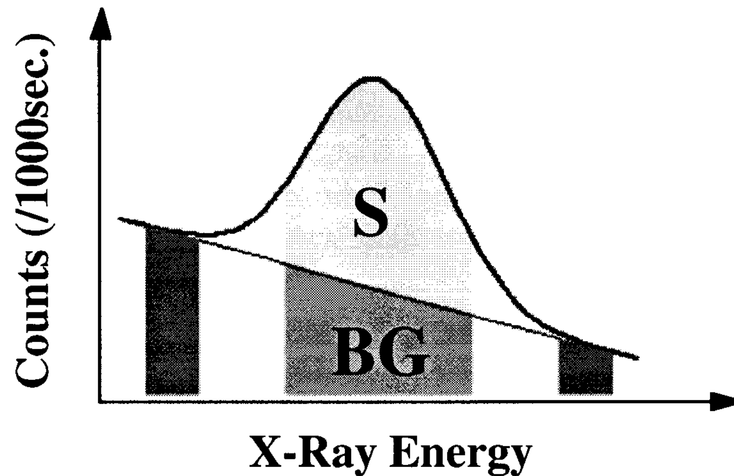

Fig. 1.4 Schematic diagram of a signal peak and background component.

However, as shown in Fig. 1.3, with this level of the MDL, it is difficult to catch up with the trend in process capability in the latter part of the 1990's.

1.5 Our Research Approach

Eq. (1.1) suggests two approaches for improving the MDLs. The first approach is to increase the overall number of counts in the signal peak. Since the overall number of counts increases with the incident photon flux, the MDLs will be improved as a function of the square-root of the incident photon flux. The second approach is to decrease the number of background counts. Note that the MDL is proportional to the square-root of the background counts.

The purpose of this work is to improve the MDLs of TXRF by the use of synchrotron radiation. We will show that synchrotron radiation is better than conventional x-ray excitation sources because of its excellent properties such as higher incident flux, linear polarization, and energy tunability [8].

1.6 References

1. S. Laderman, P. Pianetta-Chairmen, *proceedings of the workshop on applications of synchrotron radiation to trace impurity analysis for advanced silicon processing*, SLAC-415, SLAC/SSRL-0009, 1992.
2. L. Fabry, S. Pahlke, L. Kotz, G. Tolg, Fresenius J. Anal. Chem. **349**, 260 (1994).
3. K. Graff, *Metal Impurities in Silicon-Device Fabrication* , Heidelberg: Springer, 1993.
4. SEMATECH, Technology Transfer #94102578A-TR, 15.
5. Y. Yoneda and T. Horiuchi, Rev. Sci. Instrum. **42**, (1971).
6. A. Fischer-Colbrie, S.S. Laderman, S. Brennan, N. Takaura, P. Pianetta, A. Shimazaki, K. Miyazaki, J. Kortright, D.C. Wherry, Processing of the Second International Symposium on Ultra-Clean Processing of Silicon Surfaces, Edited by M. Heyns, 57, Acco, Leuven / Amerstoort, 1995.
7. P. Bertin, *Principles and Practice of X-ray Spectrometric Analysis*, New York : Plenum, 1975.
8. A. Iida, A. Yoshinaga, K. Sakurai, and Y. Gohshi, Analytical Chemistry, **58**, 394 (1986).

2. PRINCIPLES

2.1 Introduction

This chapter describes the principles of Synchrotron Radiation Total Reflection X-Ray Fluorescence Spectroscopy (SR TXRF). Sec. 2.2 shows the principles of total reflection. Sec. 2.3 presents the principles of Total Reflection X-Ray Fluorescence Spectroscopy (TXRF). Sec. 2.4 describes the principles of synchrotron radiation. Finally, Sec. 2.5 concludes this chapter with a summary.

2.2 Total Reflection

Total reflection is a phenomenon in which incident x-rays are totally reflected from the surface of a material. A schematic diagram of the total reflection geometry is shown in Fig. 2.1. As with visible light, this phenomenon can be described by Snell's law,

$$n \cdot \cos\alpha = n' \cdot \cos\alpha' \qquad (2.1),$$

where

n = index of refraction in vacuum,

n' = index of refraction in a solid,

α = incident angle, and

α' = refracted angle.

The definition of the index of refraction is the velocity of photon in vacuum, c, relative to that in the solid, v, [1]

$$n = \frac{c}{v} \tag{2.2}$$

Eq. (2.2) allows us to relate the magnitudes of the wave vectors in the vacuum and solid to the indices of refraction,

$$\frac{n'}{n} = \frac{k'}{k} \tag{2.3}$$

where

k = magnitude of wave vector in a solid, and

k' = magnitude of wave vector in vacuum.

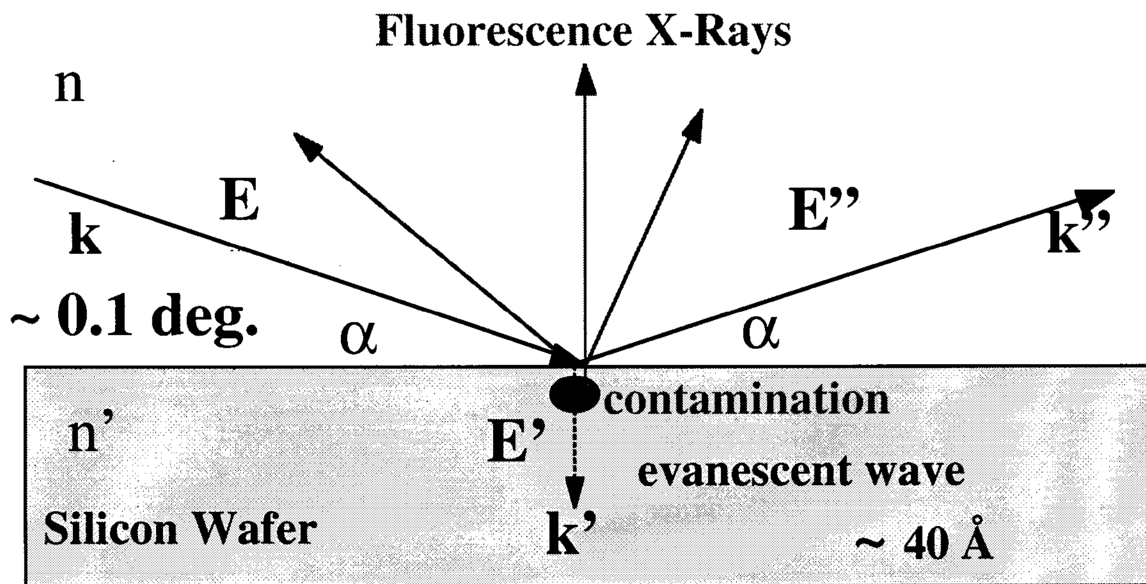

Fig. 2.1 Total reflection from a silicon wafer surface. The electric field vectors and wave vector of the incident x-ray wave are represented by E and k, respectively. Those of the evanescent and reflected waves are represented by E' and k', and E'' and k'', respectively.

Total reflection occurs when the angle of incidence, α, is small and the angle of refraction, α', becomes complex (Eq. (2.1)). The incident angle below which total reflection occurs is referred to as the critical angle, which is given by,

$$\alpha_c = \cos^{-1} \frac{n'}{n} \quad (2.4).$$

It should be pointed out that, since $n' < n$ for x-rays, the reflection occurs when x-rays go from the vacuum to a solid. The reflection of x-rays below the critical angle is referred to as total external reflection instead of total internal reflection as with visible light. By using Eq. (2.4), the critical angle for 10.6 keV x-rays incident on silicon wafers is calculated to be approximately 0.17 deg. [2]

When total reflection occurs, x-rays are totally reflected and cannot penetrate deeply into a material. However, the x-rays can still exist in the solid. The x-ray waves that can exist near the surface are referred to as evanescent waves. The evanescent waves damp exponentially into the material,

$$\exp\left(-\frac{z}{\xi}\right) \quad (2.5),$$

where

z = depth from the surface, and

ξ = penetration depth.

The penetration depth is defined as the distance at which the intensity of the evanescent wave damps to 1/e, which is calculated to as the inverse of the imaginary part of the wave vector of the evanescent wave normal to the surface, k'_z [2],

$$\xi \equiv \frac{1}{2 \cdot |\mathrm{Im} k'z|} \quad (2.6).$$

Note that the factor of 2 in the denominator of Eq. (2.6) is associated with the fact that the intensity of a wave is proportional to the square of its amplitude [3]. In this work, we will refer to the intensity of the refracted (evanescent) wave as the refracted field intensity.

From Eqs. (2.3), (2.4), and (2.6), analytical solutions of the penetration depth can be found as follows,

$$\xi = \frac{1}{2k\left(\cos^2\alpha - \frac{n'^2}{n^2}\right)^{\frac{1}{2}}} \quad (2.7),$$

$$\xi \cong \frac{1}{2k\left(\alpha_c^2 - \alpha^2\right)^{\frac{1}{2}}} \quad (2.8).$$

From Eq. (2.8), the penetration depth of 10.6 keV x-rays incident on a Si wafer is calculated to be about 40 Å at an angle of incidence of 0.1 deg.

2.2.1 Angle Scan

In TXRF, several physical variables change as a function of incident angle. In this work, we will refer to the graphs of these variables as a function of incident angle as angle scans of the particular variable. The latter part of this section describes the angle scans of : a) penetration depth, b) the amplitudes of the electric field of the refracted (evanescent) and reflected waves, and c) the refracted field intensity.

2.2.2 Penetration Depth

First, the angle scan of the penetration depth of 10.6 keV x-rays incident on a silicon wafer is shown in Fig. 2.2. The penetration depth was calculated using Eq. (2.7). As can be seen in Fig. 2.2, the penetration depth increases significantly in the region near the critical angle.

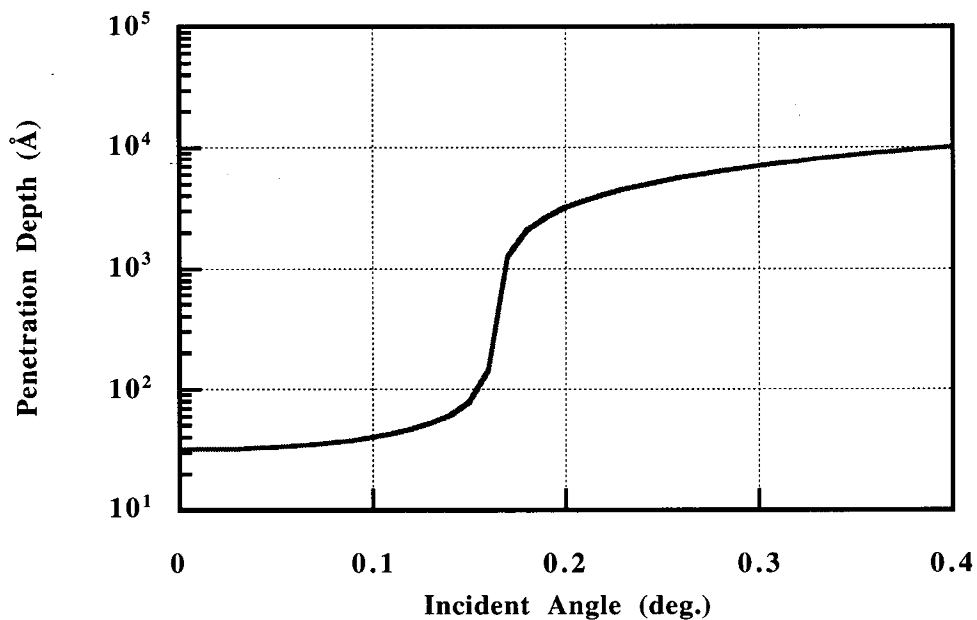

Fig. 2.2 Angle scan of the penetration depth of 10.6 keV x-rays incident on a silicon wafer.

For incident angles appreciably larger than the critical angle, Eq. (2.7) is simplified to Eq. (2.9),

$$\xi = \frac{\sin\alpha}{\mu} \qquad (2.9).$$

where μ is the linear attenuation coefficient of a solid [4]. From Eq. (2.9), the penetration depth at an incident angle of 0.4 deg. for 10.6 keV x-rays incident on a silicon wafer is calculated to be approximately 10,000 Å.

The phenomenon of total external reflection greatly reduces the penetration depth. This results in the reduction of the background x-ray signals from a Si wafer and offers the capability of analyzing small amounts of contaminants near the surface.

2.2.3 Refracted and Reflected Waves

The electric fields of the refracted (evanescent) and reflected waves also vary with incident angle. The amplitude of the electric field of the refracted wave, E' and the reflected wave, E", can be represented by using the Fresnel equations, [2],

$$\frac{E'}{E} = 2x - i \cdot 2x\sqrt{1 - x^2} \qquad (2.10),$$

$$\frac{E''}{E} = 2x - 1 - i \cdot 2x\sqrt{1 - x^2} \qquad (2.11),$$

where

E = the amplitude of the electric field of the incident wave, and,

x = the incident angle normalized to the critical angle.

Note that Eqs. (2.10) and (2.11) are normalized to the amplitude of the electric field of the incident x-ray, E. As shown in Eqs. (2.10) and (2.11), the amplitude of the refracted and reflected waves is complex.

When the incident angle is below the critical angle, the refracted and reflected waves interact with each other. Consider the phase diagram of the amplitude of the refracted and reflected waves shown in Fig. 2.3. The horizontal axis of the phase diagram is the magnitude of the real part of complex number. The vertical axis is the magnitude of the imaginary part of complex number.

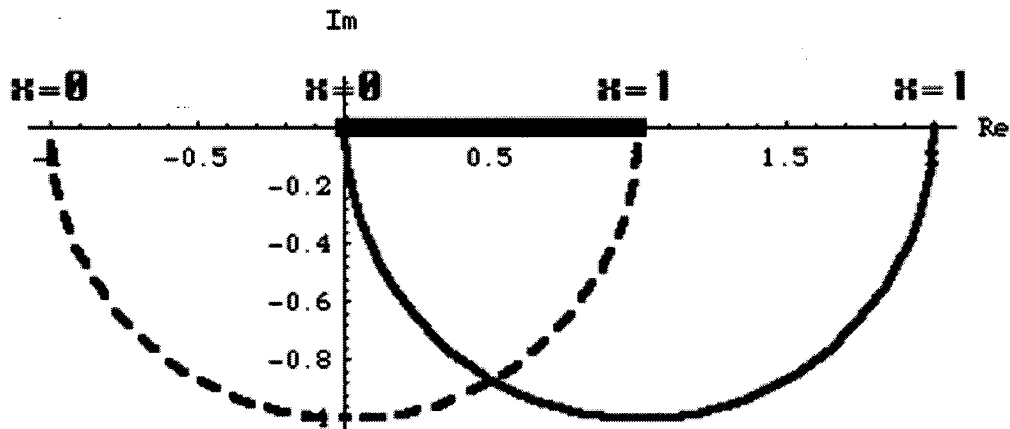

Fig. 2.3 The phase diagram of the amplitude of the electric field of the reflected and refracted waves. The curves for the reflected and refracted waves are shown using dashed and solid lines, respectively, as a function of incident angle, x, where x is the incident angle normalized to the critical angle.

This phase diagram shows the phase shifts of Eqs. (2.10) and (2.11) as a function of the incident angle normalized to the critical angle [5]. The refracted and reflected waves are shown in dashed and solid lines, respectively.

In Fig. 2.3, the incident x-ray is found to lie on the horizontal axis, (Re[1], Im[0]), which is independent of the incident angle. This is because of the conservation of the electric field between the incident, refracted and reflected waves, which is represented by

$$E' = E + E'' \qquad (2.12).$$

However, the refracted wave changes from (Re[0], Im[0]) to (Re[2], Im[0]) and its magnitude changes from zero to two as x increases from zero to one. On the other hand, the reflected wave changes from (Re[-1], Im[0]) to (Re[1], Im[0]) but its magnitude is constant.

Next, the angle scan of the amplitudes of the electric fields of the refracted and reflected waves are shown in Fig. 2.4. The horizontal axis of Fig. 2.4 is the incident angle normalized to the critical angle. The vertical axis is the amplitude of the electric field normalized to that of the incident wave. The refracted wave is shown as a dashed line and the reflected wave is shown as a solid line.

The refracted wave increases linearly from x=0 to x=1. The variation in the refracted wave is due to the interference between the incident and reflected waves. At an incident angle equal to zero (x=0), destructive interference occurs and the amplitude of the refracted wave becomes zero. At an incident angle equal to the critical angle (x=1), constructive interference occurs and the amplitude becomes two.

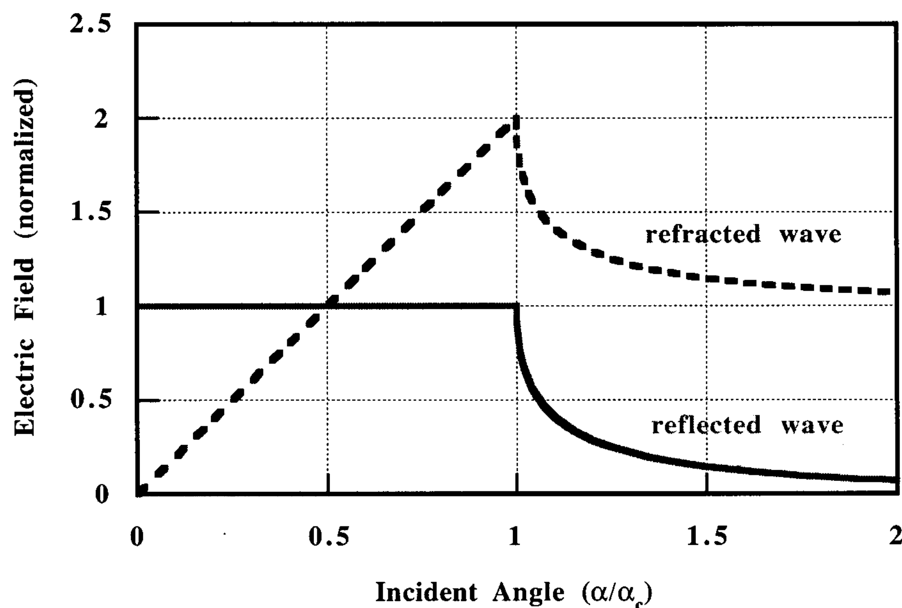

Fig. 2.4 The angle scans of the amplitude of the refracted and reflected waves at the surface. The horizontal axis is the incident angle normalized to the critical angle. The vertical axis is the amplitude of the electric field normalized to incident wave. The curves for the reflected and refracted waves are shown in dashed and solid lines, respectively.

In the region near the critical angle, the amplitude of the refracted wave becomes larger than that of the incident wave.

The reflected wave is constant at incident angles below the critical angle. In the region above the critical angle (x>1), however, the reflected wave decreases significantly and the amplitude of the refracted wave approaches to the amplitude of the incident wave.

2.2.4 Refracted Field Intensity

Since it is the x-ray intensity, i.e. the square of the amplitude of the electric field, which interacts with matter, this section will describe the square of the amplitude of the electric field of the refracted wave, which is referred to as the refracted field intensity.

The angle scan of the refracted field intensity at a Si wafer surface (z=0) for 10.6 keV x-rays is shown in Fig. 2.5. The refracted field intensity was calculated using an equation that included the absorption of the refracted field intensity in a Si wafer. For that equation, see reference [4]. Because of absorption in the wafer, the refracted field intensity is smaller than the square of the refracted wave. For example, the refracted field intensity at the critical angle (0.17 deg.) is about 3.5 rather than 4.

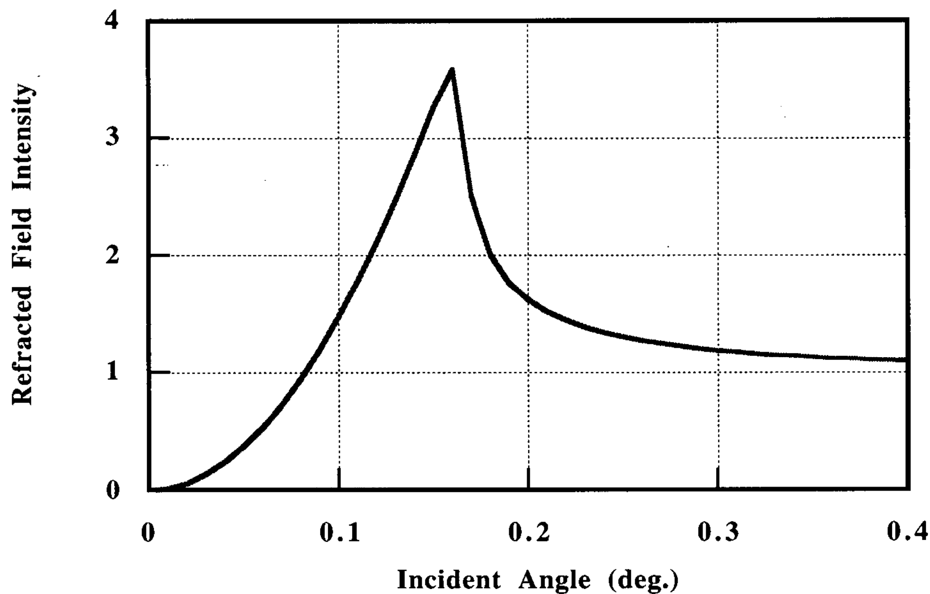

Fig. 2.5 Angle scan of the refracted field intensity for 10.6 keV x-rays incident on a silicon wafer.

The refracted field intensity at a distance z from the surface in a solid, is given by the product of the refracted field intensity at z=0 and penetration depth

$$R(\alpha) \cdot \exp\left(-\frac{z}{\xi(\alpha)}\right) \qquad (2.13).$$

where

α : angle of incidence,

$R(\alpha)$: the refracted filed intensity at z=0, and,

$\xi(\alpha)$: penetration depth.

The intensity of the fluorescence x-rays from contaminants embedded in a Si wafer at a distance z from the surface is proportional to Eq. (2.13).

2.3 X-Ray Fluorescence

When an x-ray is absorbed by an atom, it will ionize the atom creating a core hole. If such a core hole is created, an outer-shell electron can fall into it and, a fluorescence x-ray may be emitted [6]. A energy diagram of the atomic states with a core hole is shown in Fig. 2.6. The processes in this diagram are characterized by the photoionization cross-section, the fluorescence yield, and the relative transition probability.

The photoionization cross-section, σ, represents the probability of the photoionization of an atom as a function of incident x-ray energy. The photoionization can

occur when the energy of the incident x-rays is larger than the absorption edge of the inner-shell of interest [6].

The fluorescence yield, ω_x, represents the probability that the deexcitation process will result in the emission of a fluorescence x-ray which is in competition with the emission of an Auger electron [6]. The fluorescence yield is related to the Auger yield, ω_A, as shown in Eq. (2.8),

$$\omega_x + \omega_A = 1 \quad (2.8).$$

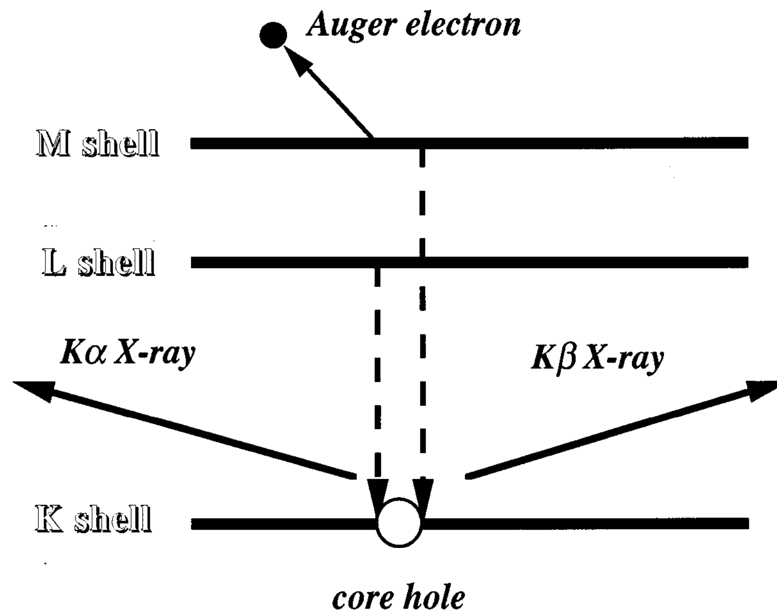

Fig. 2.6 Energy diagram of atomic states with a core hole. The bold lines present atomic shells. The dashed lines indicate the electron transfer from the outer-shells to a core hole.

The relative transition probability, κ, presents a probability of the emission of a Kα x-ray versus a Kβ x-ray. The Kα x-ray is emitted when a K shell hole is filled by an L shell electron, and the Kβ x-ray is emitted when a K shell vacancy is filled by an M shell electron.

The fluorescence x-ray intensity is proportional to the photoionization cross-section, the fluorescence yield, and the relative transition probability,

$$\sigma \, \omega_x \, \kappa \tag{2.15}$$

The fluorescence x-rays can be used for elemental identification because their energy are characteristic to a particular element. They can also be used for quantification of contamination because the intensity of the fluorescence x-rays is proportional to the number of atoms being excited.

2.4 Total Reflection X-Ray Fluorescence Spectroscopy (TXRF)

Total Reflection X-Ray Fluorescence Spectroscopy (TXRF) combines the x-ray fluorescence technique with the concept of total reflection. TXRF offers high surface sensitivity for the non-destructive analysis of multiple elements on wafer surfaces [7], [8], [9], [10].

TXRF is widely used by semiconductor industries for trace metal contamination analysis on Si wafer surfaces [11], [12], [24]. Conventional TXRF instruments typically have MDLs of 5×10^9 atoms/cm^2 for Fe and Ni [13]. This level of sensitivity was adequate

into half of the 1990's. However, advanced wafer surface preparation methods require better MDLs for TXRF, as discussed in Ch. 1 [4].

A natural way to improve the MDLs is to use synchrotron radiation (SR) as the excitation source [15]. Synchrotron radiation is emitted from relativistic electrons and has properties that lead to significant improvements in the MDLs of TXRF [16], [17], [18], [19]. In the next section, we will describe these characteristics.

2.5 Synchrotron Radiation

Synchrotron radiation is an excellent excitation source of TXRF. The advantages of synchrotron radiation over conventional x-ray sources are its higher photon flux, broad band nature, high degree of collimation, and linear polarization [16], [17], [18]. This section will describe how these properties improve the MDLs of TXRF.

2.5.1 Photon Flux

The photon flux of the synchrotron radiation from an electron whose trajectory is bent in a radius, R, by a magnetic field, B, is given by Eq. (2.15), [19],[20],

$$\left[\text{flux}\right] = 1.26 \times 10^{7} \gamma \frac{\varepsilon}{\varepsilon_c} \int_{\frac{\varepsilon}{\varepsilon_c}}^{\infty} K_{\frac{5}{3}}(\eta) d\eta \qquad (2.15),$$

where

γ = the ratio of electron kinetic energy to the electron rest energy,

ε = photon energy (keV),

ε_c = the critical photon energy (keV) is defined as,

$$\varepsilon_c(\text{keV}) = \frac{2.22E^3(\text{GeV})}{R(\text{m})} = \frac{B(\text{Tesla})E^2(\text{GeV})}{1.86} \qquad (2.16),$$

E = electron energy (GeV), (E = 3 GeV for SPEAR),

R = the radius of curvature of the electron (m), (R = 4.5 m for SPEAR),

B = the field strength of magnet (Tesla), (B= 0.8 Tesla for SPEAR),

K = modified Bessel function of the second kind,

$$\eta = \frac{\varepsilon}{2\varepsilon_c}\left\{1+(\gamma\psi)^2\right\}^{\frac{3}{2}} \qquad (2.17),$$

ψ = observation angle with respect to the orbit plane of the accelerated electrons.

In this work, we used the photon flux generated from 54-pole, 1 Tesla permanent magnet wiggler on Beam Line 6-2 (BL 6-2) at SSRL. A wiggler is a insertion device that consists of a periodic array of strong magnets installed along the electron beam path.

The wiggler enhances the photon flux by repeatedly deflecting the electron beam. When the electron beam passes through the wiggler, the electron beam is deflected periodically by the array of strong magnets, resulting in the emission of radiation at each deflection.

The wiggler on BL 6-2 with 54 poles acts like a string of 54 bending magnets aligned in a straight line along the photon beam direction. The effective photon source is

therefore 54 times more intense than the radiation from a single bending magnet with the same field strength [19].

The spectrum of synchrotron radiation can be characterized by the critical energy that is defined in Eq. (2.16). The spectral power contained by photons with energy less than the critical photon energy is equal to the half of the total spectral power, and the spectral intensity falls off rapidly for energies above the critical photon energy.

2.5.2 Spectrum

The spectra of the synchrotron radiation versus photon energy (keV) from a bending magnet and the BL 6-2 wiggler on SPEAR calculated using Eqs. (2.15), (2.16), (2.17), and (2.18) are shown in Fig. 2.7 [20], [26]. The vertical axis is photon flux in log scale in units of photons per sec., per stored electron beam current (mA), per solid angle in the horizontal direction (mrad), and per 100% band width.

The spectra were calculated for ψ in Eq. (2.18) equal to zero in order to simplify the calculation. The strength of the bending magnet and the 54-pole wiggler are 0.8 T and 1T, respectively. The critical energies were calculated to be 4.72 keV for the bending magnet and 5.09 keV for the wiggler.

As can be seen in Fig. 2.7, the photon flux of the synchrotron radiation has a broad spectrum of photon energies. The broad band nature of synchrotron radiation allows us to easily tune the energy of incident x-ray beam with the aid of monochromators. In contrast, conventional x-ray sources have high intensity only near the characteristic energy of the anode material. Furthermore, when wide band pass monochromators are used with the broad band SR source, the maximum possible increase in flux is obtained.

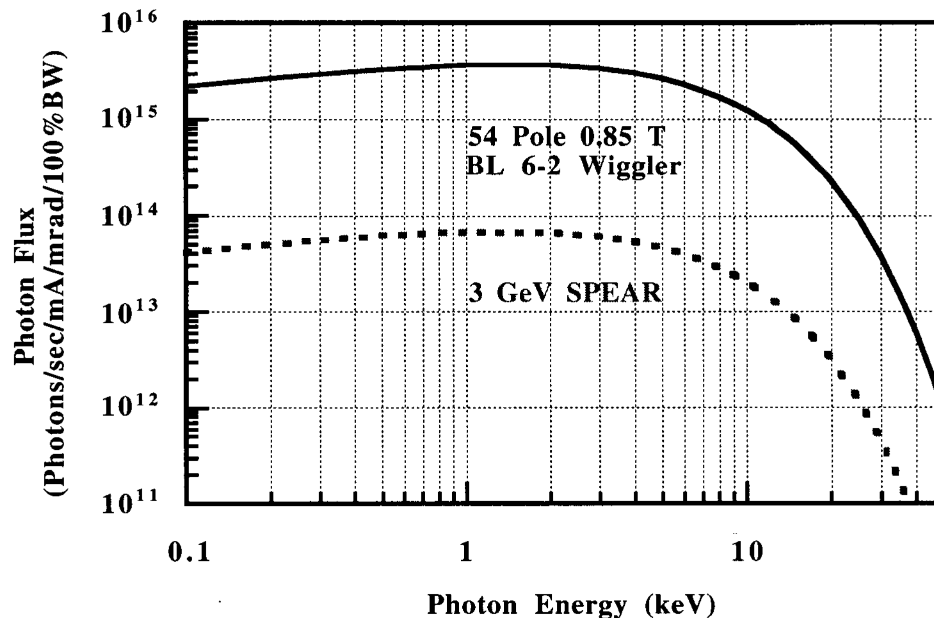

Fig. 2.7 Photon flux of the synchrotron radiation at SSRL.

The energy tunability is indispensable in the analysis of the fluorescence lines which are close to the anode fluorescent lines. For example, a tungsten anode can create high intensity x-rays relevant to TXRF of transition metals only near the energy of W Lβ x-rays, 9.67 keV. This conventional x-ray source cannot prevent the overlap of the lower energy tail of the scattered x-ray peak with the fluorescent x-ray signal peak of Zn at 8.64 keV.

However, by using the tunability of synchrotron radiation, it is possible to reduce the background signals under the Zn fluorescent signal peak. The energy tunability of synchrotron radiation permits high sensitivity over a wide range of elements.

2.5.3 Radiation Pattern

The radiation pattern of synchrotron radiation can be understood as that of dipole radiation (a classical antenna) subject to the Lorentz transformation [21]. The distribution of the radiation pattern is characterized by the ratio of electron kinetic energy to the electron energy at rest, γ.

The angular distribution of the radiation patterns from electrons moving in circular orbits are shown in Fig. 2.8. Fig. 2.8.a is the radiation pattern from a non-relativistic electron, while Fig. 2.8.b is the radiation pattern from a relativistic electron. The non-relativistic electron emits a Larmor radiation pattern (dipole radiation), which is broadly distributed. On the other hand, the highly relativistic electron emits a radiation pattern in a narrow cone along the instantaneous velocity vector of the electron.

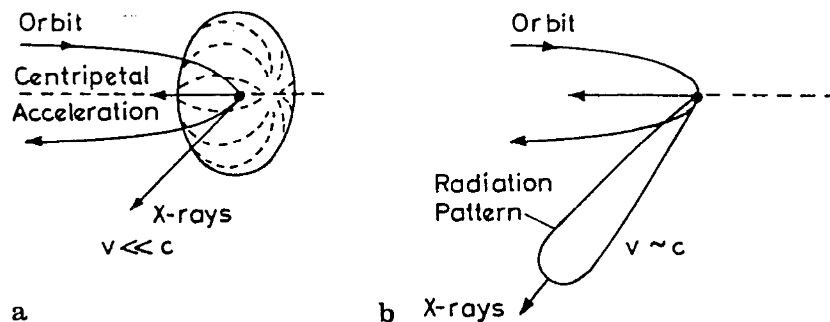

Fig. 2.8 Radiation patterns of a) non-relativistic radiation and b) synchrotron radiation [21].

In the vertical direction, the majority of the synchrotron radiation is emitted within an angle of $1/\gamma$. For SPEAR at 3 GeV, γ is $(3x10^9)/(511x10^3) \sim 6000$, and the width of the radiation pattern becomes $1/6000 \sim 0.17$ (mrad).

It should be pointed out that, in the horizontal plane, the synchrotron radiation from a wiggler has an emission angle larger than $1/\gamma$ because the electron beam is strongly deflected by the wiggler magnets. The angular divergence of the x-rays from a wiggler will be discussed in Ch. 6.

2.5.4 Linear Polarization

Synchrotron radiation has a strong degree of linear polarization in the plane of the electron beam orbit (σ-mode) as shown in Fig. 2.9 [21]. This linear polarization can be used to advantage to reduce the scattered x-ray intensity. Consider the angular distribution of the Thomson scattering of linearly polarized x-rays (Fig. 2.10). Thomson scattering is the scattering of photon from an electron at rest [23].

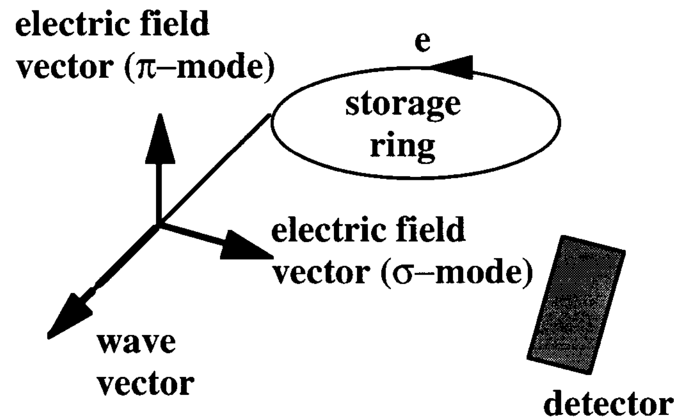

Fig. 2.9 Linear polarization of synchrotron radiation.

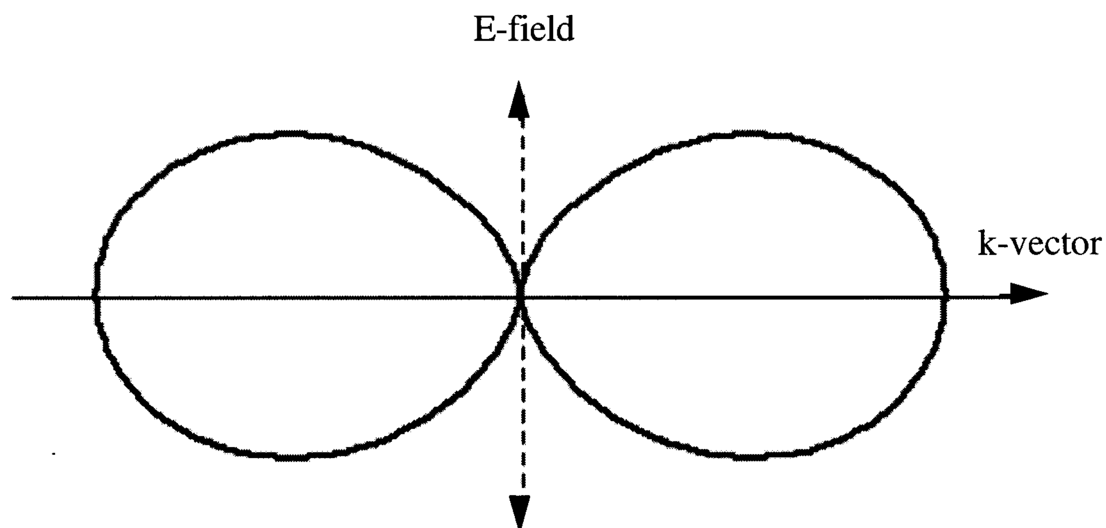

Fig. 2.10 Angular distribution of the Thomson scattering. The solid and dashed lines are the wave vector and electric field vector of the incident x-rays, respectively.

The angular distribution of the Thomson scattering is given by $\sin^2\theta$, where θ is the scattering angle with respect to the electric field vector of the incident x-rays. In Fig. 2.10, the Thomson scattering becomes zero along the electric field vector of incident x-ray. This implies that, if the observation is made in the direction of the linear polarization direction, the scattered x-ray intensity becomes zero.

The linearly polarized x-rays can, therefore, greatly reduce the scattered x-ray intensity compared to conventional unpolarized x-rays [15]. In TXRF, the scattered x-rays from a Si wafer are the dominant x-ray signals which may saturate the detector. However, the high degree of polarization makes it possible to effectively use the high flux available from synchrotron radiation.

It should be pointed out that synchrotron radiation is not perfectly polarized. A component perpendicular to the plane of the orbit (π-mode) is present at observation angles out of the orbital plane [18]. In practice, the degree of polarization is found to be 90 ~ 95% [22].

2.6 Conclusions.

This chapter described the principles of Synchrotron Radiation Total Reflection X-Ray Fluorescence Spectroscopy (SR TXRF). SR TXRF makes it possible to analyze small amounts of contamination on silicon wafer surfaces by using the phenomenon of total external reflection, the fluorescence x-ray technique, and synchrotron radiation. The phenomenon of total external reflection reduces the excitation from the wafer substrate. The fluorescence x-rays can be used for identification and quantification of elements. Synchrotron radiation improves the detection limits of TXRF because of its high flux, broad band nature, and polarization. The combination of these properties allows us to analyze smaller amount of impurities on Si wafer surfaces.

2.7 References

1. B.K. Agawal, *X-ray Spectroscopy*, Chapter 3, Heidelberg: Springer-Verlag, 1991.
2. G.H. Vineyard, Phys. Rev. **B26**, 4146 (1982).
3. H.E. Hecht, *OPTICS*, Chapter 4, Massachusetts : Addison-Wesely, 1987 .
4. B.L. Henke, E.M. Gullikson, and J.C. Davis, Atomic Data and Nuclear Data Tables, **54**, No. 2, 226 (1993).
5. H.E. Hecht, *OPTICS*, Chapter 3, Massachusetts : Addison-Wesely, 1987.

6. B.K. Agawal, *X-ray Spectroscopy*, Chapter 4, Heidelberg: Springer-Verlag, 1991.
7. Y. Yoneda and T. Horiuchi, Rev. Sci. Instrum. **42**, (1971).
8. J.M. Jaklevic, R.D. Giauque and A.C. Thompson, Nucl. Instr. Meth. B10/11, 303 (1985).
9. K.W. Jones, B.M. Gordon, A.L. Hanson, J.B. Hastings, M.R. Howells, H.W. Kraner and J.R. Chen Nuclear Instruments and Methods in Physics Research **B3**, 225 (1984).
10. A. Knockel, W. Petersen and G. Tolkiehn, Nuclear Instruments and Methods **208**, 659 (1983).
11. L.T. Canham, M.R. Dyball, and K.G. Barraclough, Journal of Applied Physics, **66**, No. 2, 15, 920 (1989).
12. A. Bensaid, G. Patrat, M. Brunel, F. de Bergevin, Solid State Communications, **79**, No. 11 923 (1991).
13. S. S. Laderman, Bull. Am. Phys. Soc. **39**, 514 (1994).
14. SEMATECH, Technology Transfer #94102578A-TR, 15.
15. A. Iida, *Advances in X-Ray Analysis*, edited by C. S. Barrett, Vol. 35, p. 795, New York : Plenum , 1992.
16. Japan Physical society ed, *Synchrotron Radiation* (in Japanese), Tokyo : Baifuukan, 1986.
17. E.E. Koch ed., *Handbook on Synchrotron Radiation, Vol.1 a* , North-Holland, 1983.
18. S. Kikuta, *X-Ray Diffraction and Scattering, Vol. 1* (Experimental Techniques in Applied Physics 15), Tokyo : University of Tokyo Press, 1992.
19. A. G. Michette and C. J. Buckley ed., *X-ray Science and Technology*, p. 64, London : Institute of Physics Publishing, 1993.
20. R.A. Mack, CEAL-1027 (1966).

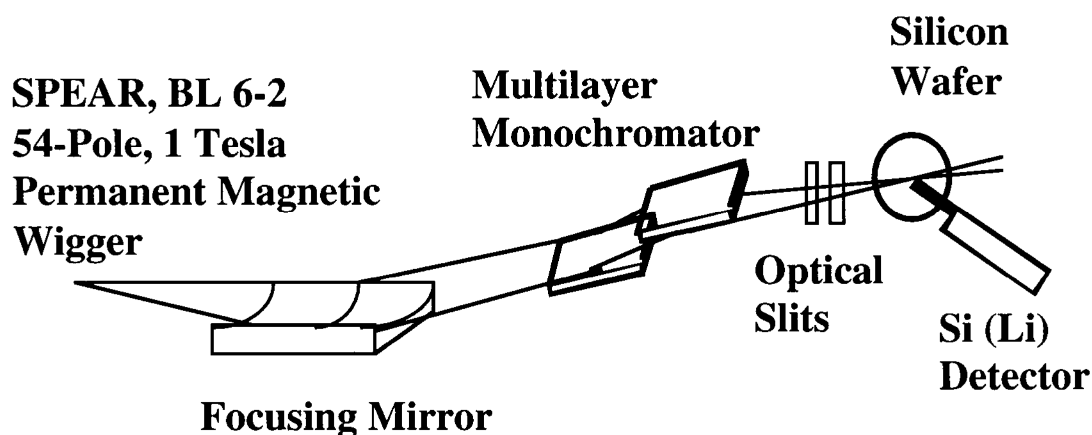

Fig. 3.1 Layout of SR TXRF Optics of BL 6-2 at SSRL.

After being focused by the mirror, the x-ray beam was monochromated by a double multilayer monochromator mounted in a parallel geometry [3]. The multilayer monochromators typically used for this study consisted of 100 periods of Mo and C layers deposited on silicon substrates. The thickness of each period was roughly 29.7 Å and the thickness of the Mo was roughly 0.4 of the total period of the multilayer [4].

The monochromated x-ray beam was collimated by optical slits, which allowed only the central and bright part of the x-ray beam (typically 500 μm width x 2 mm height) to enter a sample chamber. Between the two optical slits, an ion chamber was installed to monitor the intensity of the x-ray beam [4].

The collimated x-ray beam was incident on a vertically mounted silicon wafer in the sample chamber. The x-ray signals generated from the wafer were measured by a Si (Li) solid-state detector. The detector was mounted horizontally along the polarization vector of the incident beam to reduce the scattered x-rays (see Ch. 2).

The beam reflected from the wafer and the portion of the incident beam that did not hit the wafer were incident on a fluorescence screen placed behind the chamber. The separation of the incident and reflected beam on the screen allowed us to roughly align the angle of incidence. The precise alignment of the angle of incidence was done using a computational method that will be described in Sec. 3.4.

3.2.2 Multilayer Monochromators

The multilayer monochromator can deliver a higher incident photon flux because of its wide band pass, where the band pass (dE/E) refers to the FWHM of the primary reflection peak (dE) divided by the primary beam energy (E). According to dynamical scattering theory, the band pass of a monochromator increases as the d-spacing increases [5]. Since the period of multilayer monochromator is much larger than a d-spacing of crystal monochromator, the multilayer monochromator generates higher incident flux than the crystal monochromator [6].

The reflectivity curves for two different multilayer monochromator configurations are shown in Fig. 3.2. The horizontal axis is the x-ray energy and the vertical axis represents reflectivity. In the single multilayer configuration, as its names suggests, a single multilayer optical element was used to diffract the incident x-ray beam. The reflectivity curves were obtained experimentally and theoretically at a Bragg angle of 1.2 deg. On the other hand, in the double multilayer configuration, two multilayer optical element were used and the reflectivity curve was theoretically calculated at the same Bragg angle of 1.2 deg.

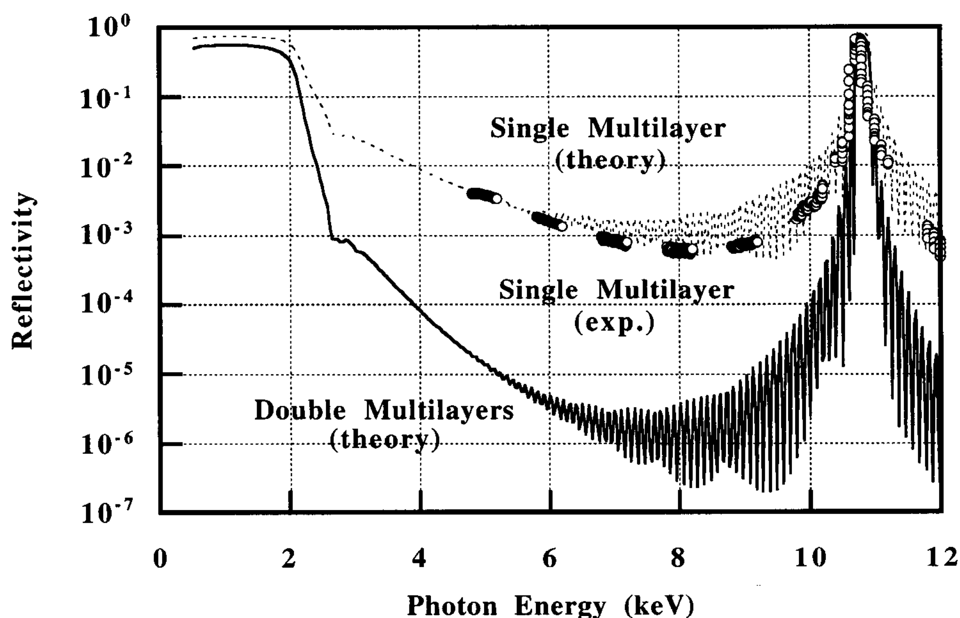

Fig. 3.2 Reflectivity curves of multilayer monochromators at the Bragg angle of 0.12 deg. The results of the theoretical calculations are shown in the solid and dashed lines. Experimental data are shown in dots.

The Bragg angle of 1.2 deg. with the 29.7 Å period multilayer monochromators resulted in a strong Bragg reflection at 10.8 keV. The width of the Bragg reflection was found to be about 200 eV corresponding to a band pass of about 0.02.

In addition to the Bragg reflection at 10.8 keV, a non-zero reflectivity below 10 keV was observed in Fig. 3.2. The non-zero-reflectivity between 2 keV and 10 keV was due to the this low energy tail of the Bragg reflection [4]. The high reflectivity below 2 keV was due to total reflection from the surface.

The reflectivity below 10 keV posed a significant problem. The presence of radiation in this energy region could contribute to backgrounds in the fluorescence signals

in either of two ways. First, there was a continuous background and, second, there was the diffraction generated from the wafer itself. Well defined energies in this spectral range could be diffracted directly into the detector resulting in one or more spurious peaks. Since these backgrounds could directly interfere with fluorescence x-ray peaks, they reduce the detection limits of SR TXRF.

The reflectivity below 10 keV could be eliminated by the following two ways. First, the reflectivity up to 4 keV were eliminated by a 1 mm thick graphite filter placed in the incident beam. Because of the difference in the degree of attenuation, the low energy x-rays in the incident beam were effectively attenuated without significantly reducing the primary Bragg reflection [9]. For example, the transmission factor for 4 keV x-ray is 0.0003, while that for 10.8 keV x-ray is 0.66.

Second, the reflectivity between 4 and 10 keV was mostly eliminated by using two multilayers. This had the effect of squaring the reflectivity over the whole range of energy. At the primary Bragg energy, the reflectivity of the double multilayer is still high (~50%). However, the reflectivity between 4 and 10 keV dropped to below 10^{-5}. The double multilayer configuration effectively eliminated the backgrounds due to the low energy tail of the Bragg reflection.

3.2.3 Photon Flux

Photon flux versus energy for several optical configurations are shown in Fig. 3.3. The horizontal axis is photon energy in keV and the vertical axis is the photon flux per sec. per 100 mA storage ring current. The photon fluxes were measured by the use of a 15-cm-long ion chamber filled with N_2 gas. The photon flux was obtained by converting the

current generated in the ion chamber to the number of the photons incident onto the ion chamber [7].

Fig. 3.3 compares a number of different configurations. First, we compared the photon flux generated on BL 4-2 (with the single multilayer monochromator), BL 6-2 (with the double multilayer monochromator), and BL 10-2 (with the double multilayer monochromator). These photon fluxes were different primarily because of the different wigglers (Table 3.1).

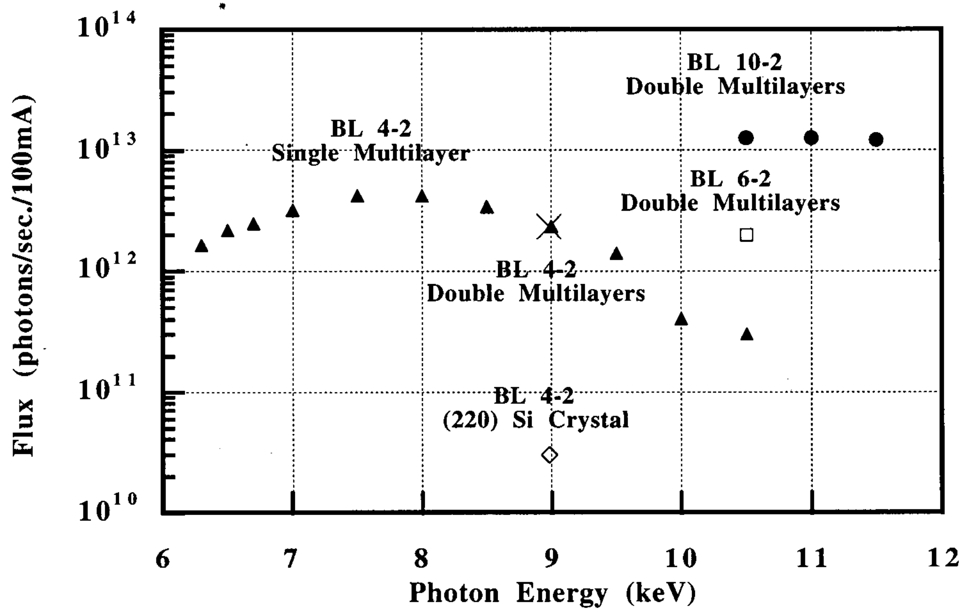

Fig. 3.3 Photon flux from different monochromators. Data were taken using BL 4-2, BL 6-2, and BL 10-2 using a regular ion chamber at SSRL [4].

Table 3.1 Parameters of wigglers at SSRL .

Beam Line	strength of magnet (Tesla)	poles	cut off energy (keV)
4-2	1.8	8	10.2
6-2	1	54	22
10-2	1.45	30	22

The 10.6 keV photon flux from BL 6-2 was found to be $2x10^{12}$ photons/sec. Note that BL 6-2 was typically used for our practical TXRF measurements. The highest flux obtained at BL 10-2 ($1.3x10^{13}$ photons/sec.) was due to the higher raw flux from this source at 10.6 keV. On the other hand, the flux from BL 4-2 was the lowest ($3x10^{11}$ photons/sec.). This was partly due to the 10.2 keV high energy cutoff of the focusing mirror on BL 4-2.

Second, we compared the 9 keV photon flux from BL 4-2 monochromated using a Si (220) crystal, a Mo-C single multilayer, and the double multilayers. From Fig. 3.3, the photon flux on BL 4-2 from the single multilayer was found to be $2x10^{12}$ photons/sec., which was much higher than that from the Si (220) crystal ($3x10^{11}$ photons/sec.). This was due to the wide band pass of the multilayer monochromator.

In Fig. 3.3, the flux from the double multilayer monochromators was found to be almost the same as that from the single multilayer. Because the peak reflectivity of the multilayer was about 0.7, the flux from the double multilayer was expected to be lower than the flux from the single multilayer by a factor of 0.7. However, different conditions during the two measurements were responsible for the higher than expected flux from the double multilayer case.

3.2.4 Sample Chamber

A top view of a sample chamber used for this work is shown in Fig. 3.4. The sample chamber consisted of a vacuum chamber with a wafer mount and a Si (Li) solid state detector. The wafer mount could hold a wafer with a diameter of 150 mm. The chamber was mounted on a Huber goniometer to permit precise adjustment of the angle of

incidence of the x-ray beam. The x-ray beam entered the vacuum chamber through a Be window.

A tungsten collimator was mounted on the end of the detector. The distance between the wafer and collimator was about 2 mm, while the distance between the wafer and detector was about 10 mm. In this work, we typically used two types of collimators with an aperture diameter of 1/8" and 1/16". The area of the Si (Li) detector was 10 mm^2.

The detected area on the silicon wafer surface along the beam direction was determined by the geometry between the collimator and detector as shown in Fig. 3.5. Perpendicular to the beam direction, the detected area on the Si wafer was entirely due to the beam height as set by the entrance slits. With the 1/16" collimator and 500 μm entrance slits, the detected area was found to be about 15 mm^2.

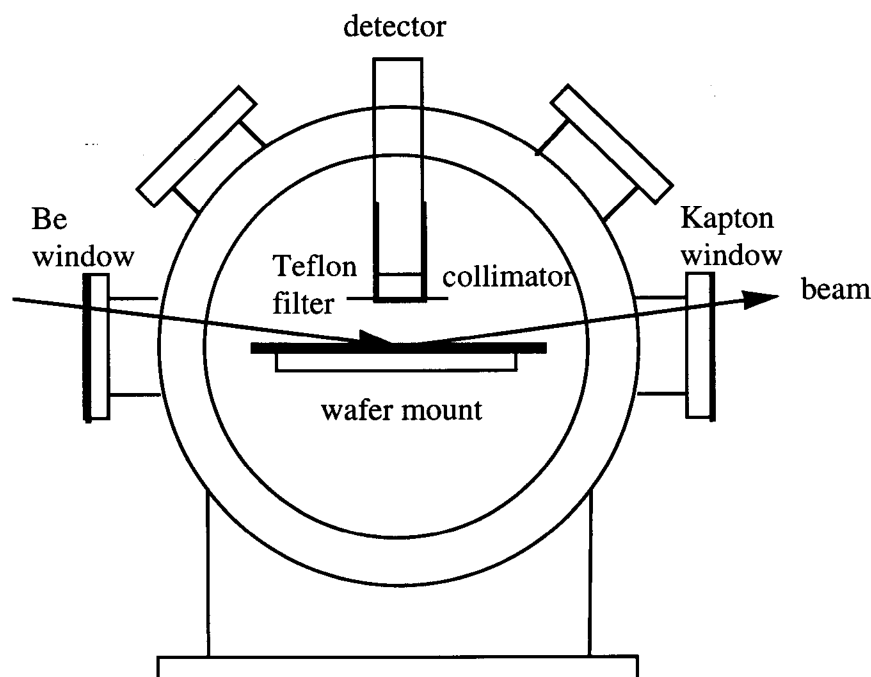

Fig. 3.4 A top view of SR TXRF basic sample chamber.

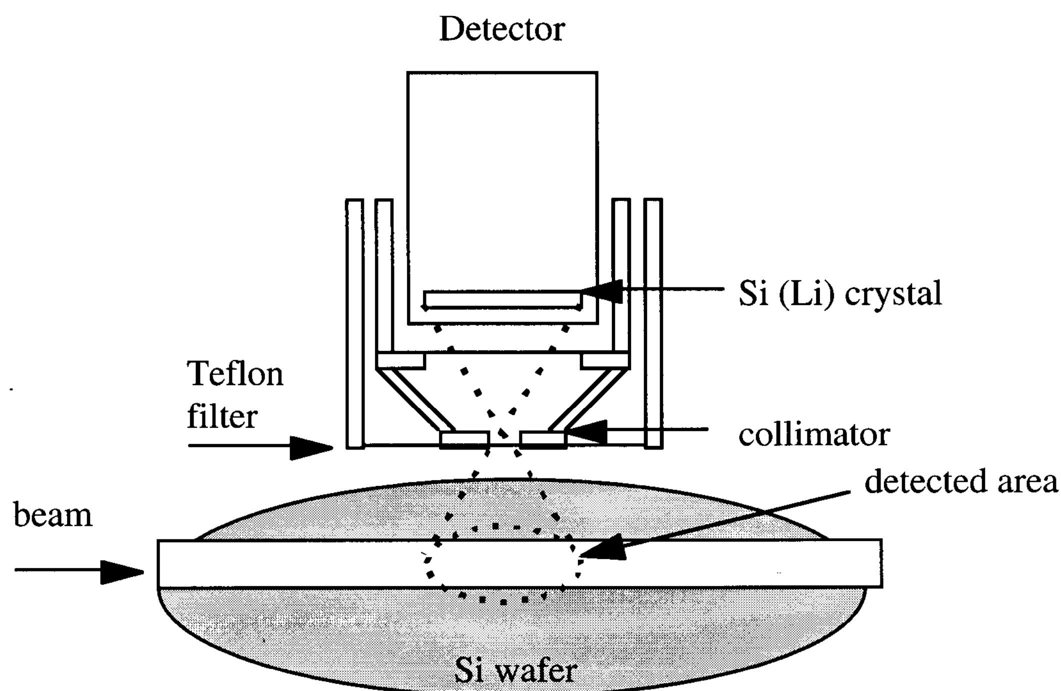

Fig. 3.5 The detected area on a Si wafer.

A 25 μm thick Teflon filter was placed on the tungsten collimator to suppress Si fluorescence x-rays and unwanted low energy photons coming from the wafer [8], [9]. For example, the Teflon filter reduced the Si K fluorescence signal intensity by a factor of about 500. This resulted in the reduction of the overall count-rate, with a typical incident angle of 0.1 deg., to a level of 10,000 cps, at which saturation of the detector did not occur.

It should be pointed out that, although the Si fluorescence signals were greatly attenuated, the attenuation decreases quickly with increasing energy (Fig. 3.6). For example, in case of Fe Kα (at 6.4 keV), the attenuation is only 0.866.

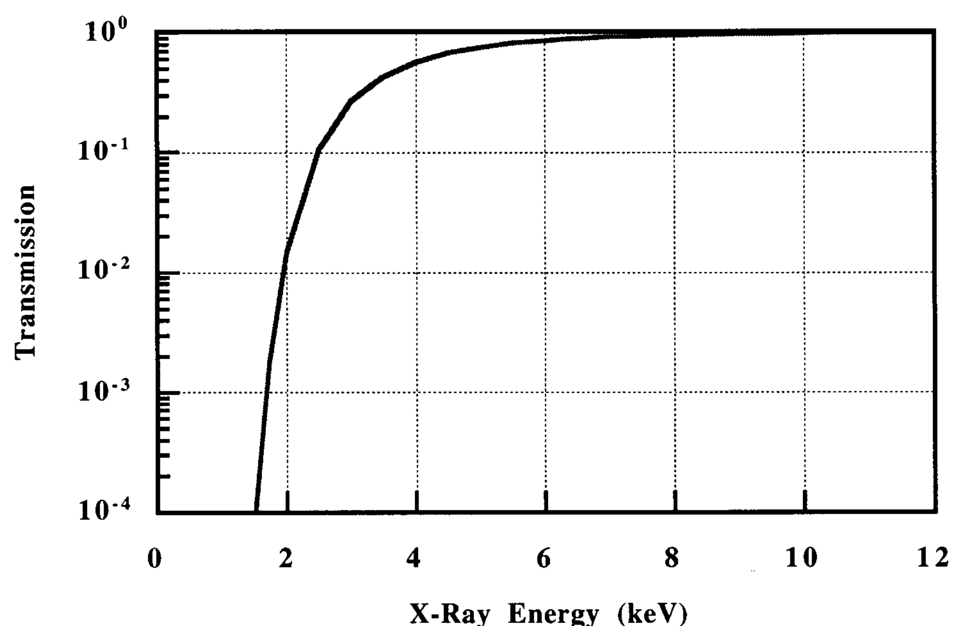

Fig. 3.6 Transmission factor of a 25 μm Teflon filter as a function of x-ray energy.

3.2.5 Vacuum Condition

It is necessary to perform TXRF measurements in vacuum because the interaction of the primary x-ray beam with ambient air would result in unacceptably high backgrounds from x-rays scattered from N_2 and O_2, and fluorescence x-rays from Ar. In order to find the level of vacuum required for TXRF measurements, this section calculates the intensities of the scattered and fluorescence x-rays generated from the air.

Since it is difficult to obtain absolute intensities of scattered x-rays, which properly take into account the geometrical factor, we found it convenient to scale the scattered x-ray intensity from the air (80% N_2 and 20% O_2 at 1 atm.) to the scattered x-ray intensity from the Si wafer.

First, we calculated the scattered x-ray intensities generated from the Si wafer and air. The parameters used for the calculations were scattering cross-sections, areal densities and the numbers of the photons effectively hitting the Si wafer and air (Table. 3.2). The scattering cross-sections are found in the literature [10]. However, the areal densities and the numbers of photons depend on the particular experimental geometry.

Consider a geometry of the x-ray beam incident at a glancing angle on a Si wafer (Fig. 3.7). In Fig. 3.7, the x-ray beam has a photon flux, F, and a beam cross-section of S_b. The x-ray beam is incident on a Si wafer at an angle of incidence, α.

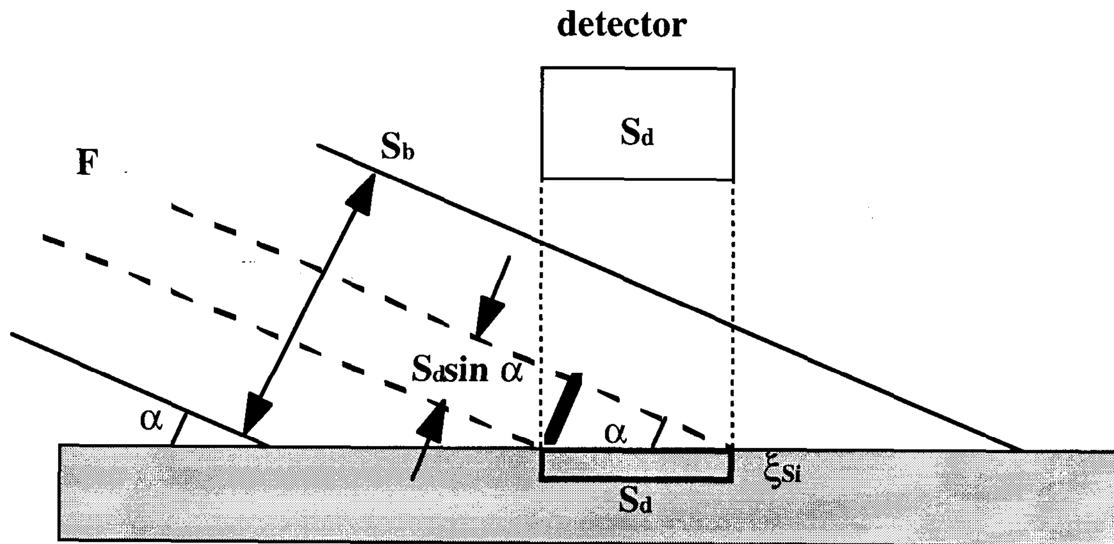

Fig. 3.7 The x-ray beam incident on a Si wafer. For the clarity in the drawing, the incident angle of the x-ray beam is drawn larger than the actual incident angle, which is typically 0.1 deg.

Table 3.2 Interaction volumes of air and silicon in TXRF.

	air (1 atm)	Si
penetration depth (cm)	0.025	4.00E-07
volume density ($atoms/cm^3$)	5.00E+19 (80 % N_2+ 20 %O_2) 4.69E+17(Ar)	5.00E+22
areal density ($atoms/cm^2$)	1.25E+18 (80%N_2+ 20%O_2) 1.17E+16(Ar)	2.00E+16
scattering cross-section (barns)	16 (80% N_2+ 20 %O_2)	32
fluorescence cross-section (barns)	483.345 (Ar)	73.79
transmission factor	0.25 (Ar)	0.002
scattered x-ray intensity (scaled)	32.25	1
fluorescence x-ray intensity (scaled)	479	1

Note : the cross-sections are for 10 keV incident x-rays.

For simplicity, we assume that the detected area on the wafer surface is equal to the detector area, S_d. As a result, the effective interaction volume of the Si wafer is given by the detected area, S_d, times the incident x-ray penetration depth, ξ_{Si} ,

$$S_d\xi_{Si} \quad (3.1),$$

and the number of Si atoms in the effective interaction volume is obtained by multiplying Eq. (3.1) by the volume density of Si, V_{si} ,

$$S_d\xi_{Si}V_{si} \quad (3.2).$$

The areal density of Si is found to be the number of Si atoms in this volume divided by the effective beam cross-section, $S_d\sin\alpha$,

$$\frac{\xi_{Si} \cdot V_{Si}}{\sin\alpha} \quad (3.3).$$

On the other hand, the number of photons in the effective beam cross-section, $S_d \sin\alpha$, is given by,

$$\frac{S_d \sin\alpha}{S_b} \cdot F \quad (3.4).$$

Using Eqs. (3.3) and (3.4) and the scattering cross-section of Si, σ_{Si}, the scattered x-ray intensity generated from the Si wafer is calculated to be

$$\frac{S_d \cdot F}{S_b} \xi_{Si} \cdot V_{Si} \cdot \sigma_{Si} \quad (3.5).$$

Note that, for simplicity, the refracted field intensity at the wafer surface is assumed to be one in Eq. (3.5).

Next, to calculate the scattered x-ray intensity from the air, consider the same geometry, but with the x-ray beam drawn as parallel to the wafer surface (Fig 3.8). Since the actual incident angle of the x-ray beam is very small, which is about 0.1 deg., the incident beam can be assumed to be parallel to the wafer surface. This geometry makes it easier to consider the scattered x-rays from the air, as will be seen in Fig. 3.9. It is also assumed that half of the incident beam with a full width of 500 μm hit the edge of the Si

wafer. Note that the beam width in our measurements was typically set to either 250 μm or 500 μm.

As shown, the effective interaction volume for the air is given by the detected area, S_d, times the beam width, ξ_{air}, (Fig. 3.9).

$$S_d \, \xi_{air} \qquad (3.6).$$

The number of the air molecules in this volume is given by the effective interaction volume times the volume density of the air, V_{air},

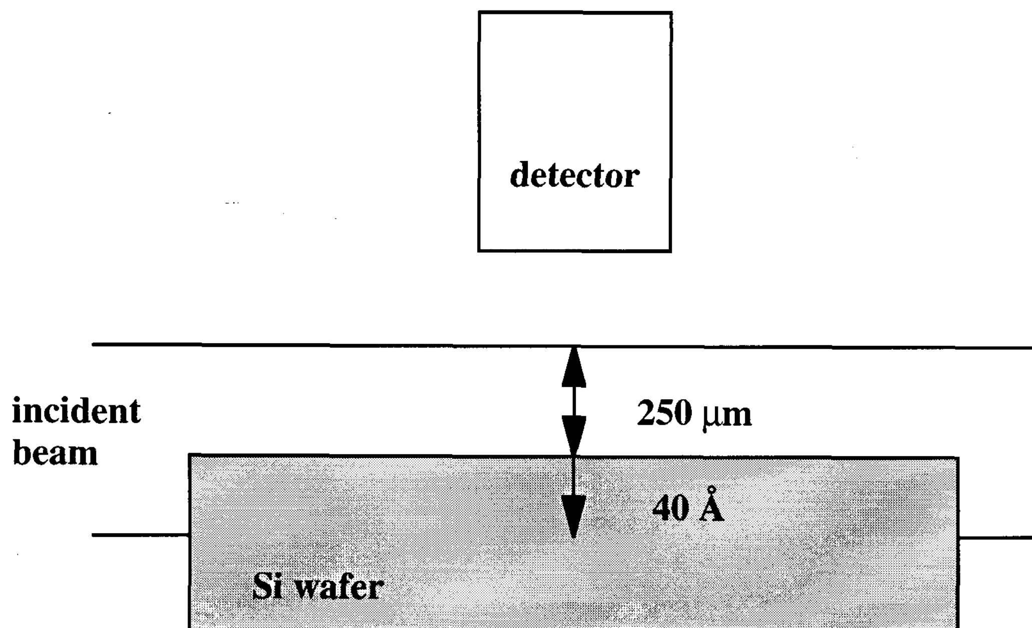

Fig. 3.8 The x-ray beam incident at a glancing angle on a silicon wafer and air.

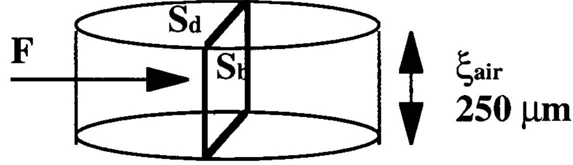

Fig. 3.9 The volume of air interacting with the x-ray beam.

$$S_d \, \xi_{air} \, V_{air} \qquad (3.7),$$

and, therefore, the areal density of the air is given by the number of the air molecules in the volume divided by the total beam cross-section, S_b,

$$\frac{S_d . \xi_{air} \cdot V_{air}}{S_b} \qquad (3.8).$$

Using Eq. (3.4), the scattered x-ray intensity from the air is found to be,

$$\frac{S_d \cdot F}{S_b} \xi_{air} \cdot V_{air} \cdot \sigma_{air} \qquad (3.9).$$

where σ_{air} is the scattering cross-section from the air (80% N_2 and 20% O_2).

Finally, using Eqs. from (3.5) to Eq. (3.9), the scattered x-ray intensity from the air scaled to that from the Si wafer is given by Eq. (3.10),

$$\frac{\xi_{air} \cdot V_{air} \cdot \sigma_{air}}{\xi_{Si} \cdot V_{Si} \cdot \sigma_{Si}} \qquad (3.10).$$

By substituting the penetration depths, volume densities, and scattering cross-sections from Table. 3.2 into Eq. (3.10), the scaled scattered x-ray intensity from air at 760 mm Hg is calculated to be 32.25.

When calculating the fluorescence x-ray intensity from Ar, we scaled it to the Si fluorescence x-ray intensity as shown in Eq. (3.11).

$$\frac{\xi_{air} \cdot V_{Ar} \cdot \sigma^F_{Ar} \cdot T(E_{Ar})}{\xi_{Si} \cdot V_{Si} \cdot \sigma^F_{Si} \cdot T(E_{Si})} \qquad (3.11),$$

where

σ^F_{Ar} = Ar fluorescence production cross-section (barns),

σ^F_{Si} = Si fluorescence production cross-section (barns),

E_{Ar} = Ar K fluorescence energy (2.96 keV),

E_{Si} = Si K fluorescence energy (1.74 keV), and

T = transmission factor of 25 μm Teflon filter.

In Eq. (3.11), the transmission factors of the 25 μm Teflon filter was taken into account because the fluorescence energy of Ar (2.96 keV) is different from that of Si (1.74 keV). Using Eq. (3.11), the scaled Ar fluorescence x-ray intensity from the air at 760 mm Hg is calculated to be 475.

The background x-rays generated from the air at 760 mm Hg are large for TXRF measurements. The scattered x-ray intensity is 32.25 times larger than that from a Si wafer and the Ar fluorescence intensity is 475 times larger than the Si fluorescence intensity from a Si wafer. In order to eliminate the backgrounds from the air, it is recommended that data

be taken under the pressures less than 10^{-4} of 760 mm Hg. In this study, the TXRF measurements were performed at a pressure less than 10 μm Hg resulting in the complete elimination of the scattered and fluorescence x-rays from the air.

3.2.6 Detector Configuration with Respect to Polarization Vector

As mentioned in Ch. 2, the scattered x-ray intensity is at its minimum along the polarization vector of the synchrotron radiation. We experimentally studied this effect through measurements using two different detector configuration as shown in Fig. 3.10. In Fig. 3.10.a, the detector was installed parallel to the polarization vector. We referred to this configuration as the parallel mode. Note that the parallel mode was the standard detector configuration.

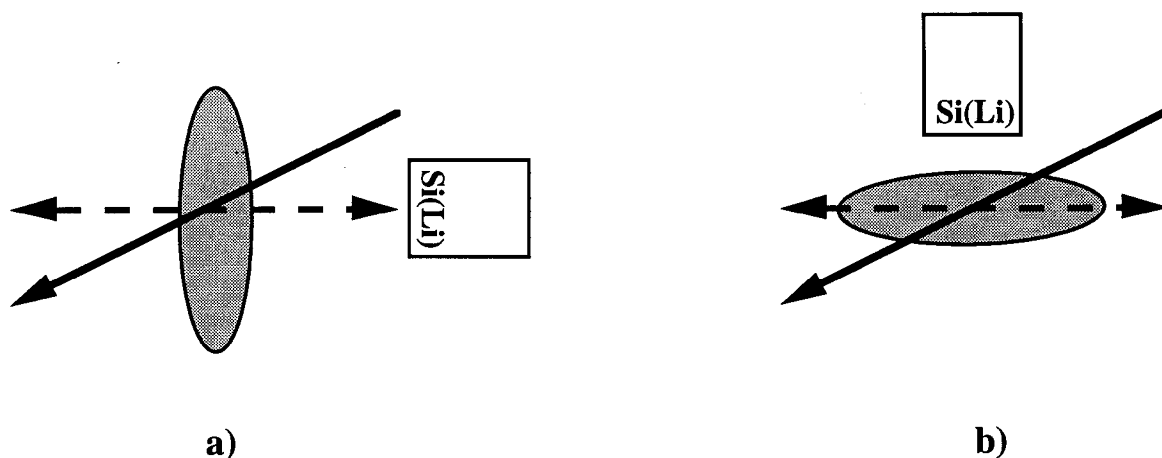

Fig. 3.10 Detector configurations with respect to polarization vector, a) parallel mode and b) normal mode. The wave vector and polarization vector of the incident beam are shown in the solid and dashed lines, respectively.

In Fig. 3.10.b, the detector was installed normal to the polarization vector. We referred to as normal mode. The normal mode was achieved by rotating the sample, chamber, detector and goniometer assembly along the beam axis by 90 deg. This resulted in a configuration in which the wafer was in the horizontal plane with its surface along the polarization vector of the synchrotron radiation with the detector axis now being in a vertical orientation but still along the wafer surface normal. Data taken with these configurations will be discussed in Ch. 4.

3.2.7 Optical Configurations for Al Analysis

The detection of Al on a Si wafer is difficult because of the small energy difference between Al fluorescence (1.49 keV) and Si fluorescence (1.74 keV) lines. Usually, a large Si substrate peak overlaps the small Al peak generated from contaminants in spectra taken with Si (Li) detector.

It should be pointed out that even the higher flux of the synchrotron radiation will not simply improve the detection limit of Al in the normal configuration. This is because the Teflon filter which is necessary to make the count-rates manageable by attenuating the Si signals would equally attenuate the Al signals.

To analyze small amounts of the Al contamination on a Si wafer, it is necessary to reduce the Si signals without loosing the Al signals. This can be done by using an incident beam with an energy below the Si K absorption edge (1.84 keV) and higher than that of the Al K edge (1.56 keV), which generates the Al K fluorescence signals without generating the Si fluorescence signals.

In this study, we exploited the tunable nature of synchrotron radiation for the Al analysis. Two configurations used for our measurements are shown in Fig. 3.11 and 3.12. Fig. 3.11 is the optical configuration used on BL 3-4, where BL 3-4 is a windowless beam line at SSRL which uses a bending magnet radiation source and an Au-coated mirror with a 1.5 deg. angle of incidence resulting in a 3 keV high-energy cut off. The photon flux generated on BL 3-4 is white radiation ranging from visible to 3 keV, which is collimated by optical slits installed in the beam line.

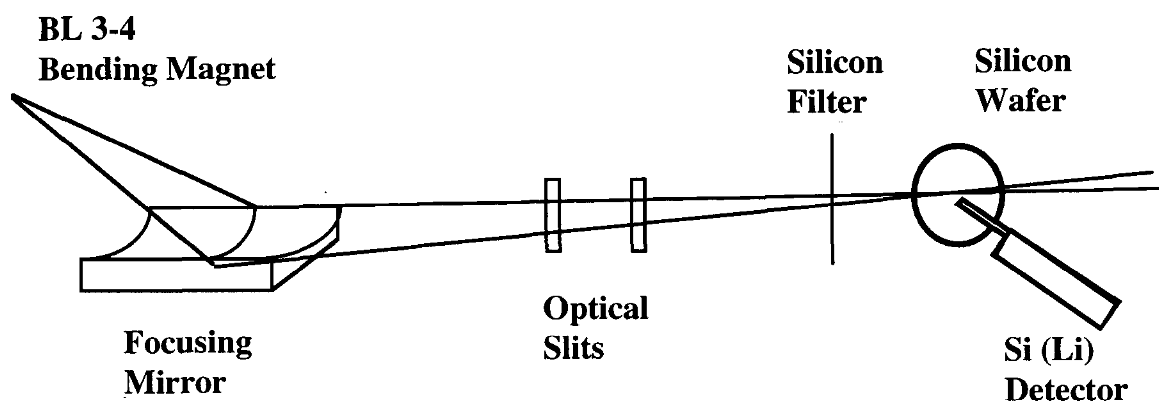

Fig. 3.11 Optical configuration on BL 3-4 for low Z measurements.

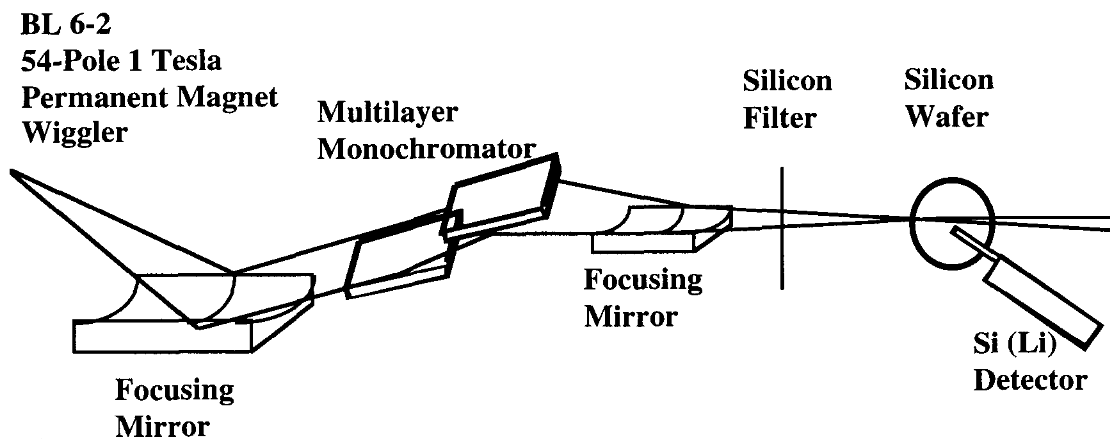

Fig. 3.12 Optical configuration on BL 6-2 for low Z measurements.

In this work, the white radiation on BL 3-4 was tailored by the use of 8 μm of Si filters which absorbed the photons at energies both above the Si K edge and below 1 keV. The resulting spectrum on BL 3-4 will be discussed in Ch. 4.

Fig. 3.12 is the optical configuration used on BL 6-2. This configuration was designed to further eliminate the higher energy photon flux which could not be eliminated on BL 3-4. On BL 6-2, the same multilayer monochromators as for the high Z work was used with a larger Bragg angle. Since BL 6-2 uses a wiggler source, the raw photon flux is more than 50 times higher than BL 3-4. Therefore, it was possible to use a multilayer monochromator and still have high flux.

Furthermore, we used a post monochromator mirror to eliminate the higher order harmonics from the photons monochromated by the multilayers. Finally, in order to insure that the multilayer gives a sharp enough high energy cut off, the same Si filter used on BL 3-4 was installed in the incident beam. The results of the Al measurements with these configurations will be shown in Ch. 4.

3.3 Si (Li) Detector

A Si (Li) detector is basically a large, reverse biased n^+-i-p^+ diode [11], [12]. Lithium is doped in the intrinsic region to compensate p-type impurities. When a photon is incident in the intrinsic region, a number of electron-hole pairs are generated. In the presence of the electric field, the electron-hole pair current is collected and converted to the incident photon energy. To reduce the thermal leakage current, the Si (Li) detector is cooled to liquid nitrogen temperature (77K).

The detectors used for our measurements had an active area of 10 mm^2. The maximum allowable count-rate was 10,000 ~ 15,000 cps. The maximum count-rate is defined to the count-rate which gives rise to a dead time of about 40 %. Note that, with the 40 % dead time, an elapsed time of 1,400 sec. is required to take data with a live time of 1,000 sec. The detector vendor Kevex recommends that the dead times below 40 % be used [13].

The adjustment of the maximum count-rate is possible by changing the shaping time of the main amplifier in the detector electronics. It is known that a smaller shaping time increases the maximum count-rate by deteriorating the energy resolution. For our SR TXRF measurements, the higher maximum count-rate is preferable in order to use the high incident photon flux from synchrotron radiation.

In this work, we selected the minimum shaping time (4 μ sec. in the Kevex electronics) to obtain the maximum count-rate of about 15,000 cps. With this count-rate, the energy resolution (FWHM) at Mn Kα (6 keV) was found to be 220 eV. For reference, with the maximum shaping time (64 μ sec. in the Kevex electronics), the intrinsic energy resolution of 150 eV was obtained with the maximum count-rate of 10,000 cps.

3.3.1 Backgrounds from Si (Li) Detector

The fluorescence signal peak measured by the Si (Li) detector becomes a distorted Gaussian distribution with the tail at the low energy side. This low energy tail is an intrinsic background generated in the Si (Li) detector, which is referred to as the detector incomplete charge collection background because it is generated by the incomplete collection of the

electron-hole pairs created when an x-ray is detected. The low energy tail observed in the SR TXRF data will be discussed in Ch. 4 and Ch. 5.

The Si (Li) detector also generates a background that is related to an energy loss of the detected x-rays caused by the photoionization of Si K-shell electrons. This background is referred to as the escape peak, which appears at an energy equal to the primary measured x-ray energy minus the Si K fluorescence energy (1.74 keV). The problem with the escape peak is that it may overlap with the characteristic fluorescence lines. The effects of the escape peaks observed in SR TXRF will be discussed in Ch. 4 and Ch. 6.

In addition to these well-known detector backgrounds, our results for high sensitivity TXRF measurements found spurious fluorescent signals of Fe, Ni, and Cu. They were generated inside the detector. In order to eliminate these spurious fluorescence signals, we worked with the detector vendor to modify our detector by using detector parts which did not contain these materials. The modified detectors used in this work are listed in Table. 3.3. For example, the spurious Ni signals were eliminated in the version 2 detector by replacing a Ni ohmic contact with that made of Pd.

The Cu spurious signals were partially reduced in the version 2 detector by replacing Cu-Be washer to one made of Pd and completely eliminated in the version 3 detector by replacing an Al alloy containing Cu with a pure Al component. Data taken with these modified detectors will be shown in Ch. 4.

Table 3.3 Si (Li) detectors used for SR TXRF measurements at SSRL.

version	year used	detector area (mm^2)	description
1	till 1993	10	commercially available detector (model no. 3600-0018-0146)
2	1994~1995	10	Ni ohmic contact and Cu-Be washer replaced to Pd
3	1996	50	Al alloy with Cu replaced to 99.999 % Al

3.4 Alignment of Incident Angle

One of the primary experimental parameters in TXRF is the angle of incidence between the primary x-ray beam and the sample surface. An accurate knowledge of this angle is essential in order to make wafer to wafer comparisons meaningful. Such comparisons with standards of known levels make quantitative measurements possible.

At first, the angle of incidence was roughly determined by measuring the distance between the spots of the incident and reflected beams on the fluorescence screen placed behind the sample chamber. For example, when the distance between the two spots on the screen is 5 mm, since the distance from the wafer center to the fluorescence screen is about 2 m in our configuration, the angle of incidence is determined to be about 2.5 mrad (0.15 deg.).

We then performed a more precise alignment by using a computational method. We compared the Si fluorescence x-ray counts as a function of incident angle to the theoretical calculation using the critical angle as a fitting parameter.

It should be pointed out that, in TXRF, the angular divergence of the incident beam may not be negligible because it can be comparable to the angle of incidence. As a result, the components with the angles of incidence near or above the critical angle generate a large background of x-rays from the Si wafer. In our calculation, the angular divergence of the incident beam was set as 0.025 deg.

An example of our fitting method is shown in Fig. 3.13. The horizontal axis is the angle of incidence. The vertical axis plots counts in the Si peak per 20 sec.

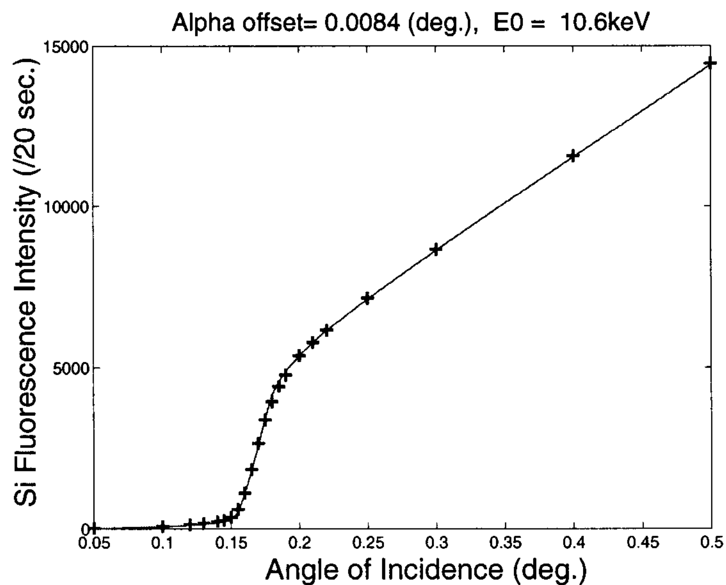

Fig. 3.13 An example of fitting the angle scan of the Si fluorescence signal. The critical angle was used as a fitting parameter.

As can be seen in Fig. 3.13, the Si fluorescence x-ray intensity increases greatly near the critical angle of 0.17 deg. Therefore, a large number of data points were taken in the region near the critical angle to improve the precision of the fitting.

The fitting was done using the least square method with the incident angle as the fitting parameter. Using this computational method, the incident angle was aligned accurately within an error of 0.001 deg.

3.5 Standard Wafers

Quantification in TXRF can only be done by the use of wafers containing known amounts of contaminants on the surface. Therefore, it is relevant to briefly discuss preparation of standards.

There are several ways of preparing standards. Standard wafers with metallic elements can be prepared using an SC1 solution method [14]. The SC1 solution is a alkaline solution with a typical composition (NH_4Cl : H_2O_2 : H_2O = 1 : 1 : 5) [15], [16],[17]. The SC1 solution is one of the most important chemical solutions used in Si processing due to its ability to remove particles on the wafer surfaces [20], [21].

The SC1 solution can also be used for standard preparation due to its low solubility for metals. The chemistry of the deposition is based on Langmuir theory [14]. Standard wafers are created by dipping silicon wafers into a SC1 solution oversaturated with metals. By controlling the temperature, dipping time, and concentration of the metals, it is possible to deposit the desired amount of metal atoms on the wafer surface.

We made standard wafers with 1×10^{12} atoms/cm^2 of Fe, Ni, and Zn at Center for Integrated Systems (CIS) at Stanford University. The temperature of the SC1 solution was room temperature and the dipping time was 10 min. The solution of standard elements were created by diluting 1000 ppm standard metal solutions. For example, the 1000 ppm Fe solution in the form of $FeCl_3\cdot 6H_2O$ in hydrochloric acid was diluted to 25 ppb in the SC1 solution. For Ni and Zn, see Table. 3.4. The concentration of these elements was finally checked by the use of conventional TXRF equipment at HP.

Our standard wafers used for quantification of SR TXRF data were prepared by Shimazaki et. al. at Toshiba using their own method [17].

Table 3.4 Metals in SC1 solution.

element	original solution	concentration in SC-1 solution
Fe	1000 ppm $FeCl_3\cdot 6H_2O$ in hydrochloric acid	25 ppb
Ni	1000 ppm $Ni(NO_3)_2\cdot 6H_2O$ in wafer	250 ppb
Zn	1000 ppm Zn in dilute nitric acid	100 ppb

These standard wafers were intentionally contaminated with 1×10^{11} atoms/cm^2 of Fe, Ni, and Zn. The standard elemental concentrations were cross-checked using both of conventional TXRF at HP and WAS at Toshiba. Note that WAS (Wafer Surface Analysis) is a wet chemical analytical method developed by Shimazaki et. al at Toshiba [18].

Because the levels of 10^{11} atoms/cm^2 were within the detection limits of the conventional TXRF, these standard wafers were used for comparison of conventional TXRF with SR TXRF. A comparison between conventional TXRF and SR TXRF will be discussed in Ch. 4.

3.6 Conclusions

SR TXRF optical configurations were developed at SSRL. We focused on increasing the incident photon flux and decreasing the background x-rays. The high incident flux was obtained by the use of wiggler radiation sources, focusing mirrors, and double-multilayer monochromators. The incident flux available with our optical configuration was about 10^{13} photons/sec.

The high flux of the synchrotron radiation could effectively be used by reducing the background x-rays generated from the Si wafers. The scattered x-rays were greatly reduced by installing the detector along the polarization vector of the incident beam. Furthermore, low energy x-ray backgrounds, such as Si fluorescence lines, were significantly absorbed by a Teflon filter placed in front of the detector. This detector configuration prevented the saturation of the detector and allowed us to use the high photon flux of the synchrotron radiation. The double-multilayer monochromator also helped reduce the low energy tail of the primary Bragg reflection of the incident beam. This also resulted in the elimination of peaks between 4 and 10 keV for an 11 keV incident beam.

The true sensitivity of the SR TXRF measurements was achieved by eliminating the spurious fluorescence signals generated from metallic assemblies inside the Si (Li) detectors. The spurious signals overlapped the fluorescence signals generated from contamination on the wafer surface. We eliminated the spurious signals by replacing the metallic parts containing these metals to those without 3-d transition metals. The modified Si (Li) detector made it possible to perform true high sensitivity SR TXRF measurements.

Quantification of TXRF can only be done by use of standards. In this work, we used standard wafers with 10^{11} atoms/cm^2 of Fe, Ni, and Zn prepared by Toshiba. The angle of incidence of the x-ray beam on the wafer surface was precisely determined by a fitting method in which the Si fluorescence signals was fitted to the theoretical calculation as a function of angle of incidence.

In addition to 3-d transition metals, two optical configurations for measuring elements with lower Z than Si were also developed at SSRL. The low Z element analysis only becomes possible by the use of an incident beam with an energy less than Si K absorption edge resulting in the reduction of the Si fluorescence signals. To achieve this goal, we tuned the energy of the synchrotron radiation by the use of Si filters on BL 3-4 and the additional use of a multilayer monochromators and x-ray mirrors on BL 6-2.

Data taken with the optical configurations developed here will be discussed in the next chapter.

3.7 References

1. S. Brennan, W. Tompkins, N. Takaura, P. Pianetta, S.S. Laderman, A. Fischer-Colbrie, J.B. Kortright, M.C. Madden, D.C. Wherry, Nucl. Instrum. Meth., **A347**, 417 (1994).
2. E. Hoyer, representing the Beam Line VI Design Group, Nucl. Instrum. Meth., **208**, 117 (1983).
3. P. Pianetta, N. Takaura, S. Brennan, W. Tompkins, S.S. Laderman, A. Fisher-Colbrie, A. Shimazaki, K. Miyazaki, M. Madden, D.C. Wherry, J.B. Kortright, SLAC-PUB-6612, SLAC/SSRL-0086, LBL-36011, July (1994).
4. U. Bonse and M. Hart, Appl. Phys. Letters **7** (1965) 238.
5. B.K. Agawal, *X-ray Spectroscopy*, Berlin Heidelberg : Springer-Verlag, 1991.
6. T.Hom, W.Kiszenick, B.Post, J. Appl. Cryst. **8**, 457 (1975).
7. S. Brennan, Flux Calculations for SPEAR, SSRL.
8. S. S. Laderman, Bull. Am. Phys. Soc. **39**, 514 (1994).
9. E.C. Montenegro, G.B. Baptista, and P.W.E.P. Duarte, Atomic Data and Nuclear Data Tables, **22**, 2, 131 (1978).
10. UCRL-50400,V.6.REV.3.
11. J.L. Campbell, J.-X. Wang, W.J. Teesdale, Nucl. Instr. Meth. **B43** 490 (1989).
12. *X-RAY DATA BOOKLET*, Section 6, LBL, 1986.
13. D.C. Wherry (personal communication).
14. J. Ruyta, T. Yoshimi, H. kondo, h. Okuda, and Y. Shimanuki, Jpn. J. Appl. Phys. **31**, 2338 (1992).
15. Proceedings of 20th Symposium on ULSI Ultra Clean Technology (by Ultra Clean Society in Japan).
16. C.R. Helms and H. Park, Mat. res. Soc. Symp. Proc., **315**, 287 (1993).

17. C.R. Helms, H.-S. Park, S. Dhanda, P. Gupta, M. Tan, Processing of the Second International Symposium on Ultra-Clean Processing of Silicon Surfaces, Edited by M. Heyns, 205, Acco, Leuven / Amerstoort, (1994).

18. A. Shimazaki, Proc. ECS, Defects in Silicon II (1991) 47.

19. G.J. Norga, K.A. Black, H. M'saad, J. Michel, and L. C. Kimerling, Processing of the Second International Symposium on Ultra-Clean Processing of Silicon Surfaces, Edited by M. Heyns, 221, Acco, Leuven / Amerstoort, (1994).

20. U. Keller, W. Anderhold, and E.P. Burte, Processing of the Second International Symposium on Ultra-Clean Processing of Silicon Surfaces, Edited by M. Heyns, 111, Acco, Leuven / Amerstoort, (1994).

21. M. Meuris, P.W. Mertens, A. Opdebeeck, H.F. Schmidt, M. Depas, G. Vereecke, M.M. Heyns, and A. Phillipossian, Solid State technology July, 109, (1995).

4. EXPERIMENTAL RESULTS

4.1 Introduction

This chapter discusses the experimental results of the SR TXRF program at SSRL [1],[2],[3]. Sec. 4.2 shows the experimental results for the 3-d transition metal analysis on Si wafer surfaces. This section also compares the sensitivity of SR TXRF with conventional analytical methods. The results of actual applications are shown as well. Sec. 4.3 shows the experimental results for the 3-d transition metal analysis on GaAs wafer surfaces, with an emphasis on the difference between Si and GaAs spectra. Sec. 4.4 presents the analysis of Al on Si wafers. We describe the important effects of background in the analysis of Al and other elements with energies close to and below the Si fluorescence energy. Sec. 4.5 concludes this chapter with summary.

4.2 3-d Transition Metal Analysis on Si Wafer Surfaces

4.2.1 Standard Spectrum

A SR TXRF spectrum taken from a standard wafer with 1×10^{11} atoms/cm^2 of Fe, Ni, and Zn is shown in Fig. 4.1 [3], [4]. The horizontal axis of Fig. 4.1 is x-ray energy. The vertical axis is counts per 1000 sec. Fig. 4.1 primarily consists of three signals : characteristic fluorescence lines, the scattered x-ray signal, and continuous background.

First, let us describe the characteristic fluorescence lines. In Fig. 4.1, the fluorescence signal peaks of Si, S, Cl, Ca, Fe, Ni, Cu, and Zn are labeled. For reference, the energies of these fluorescence signals are shown in Tab. 4.1. The Si fluorescence signals were generated from the Si wafer itself and those of Fe, Ni and Zn were from

intentional contamination at a level of $1x10^{11}$ atoms/cm^2 placed on the wafer using the techniques described in the previous chapter.

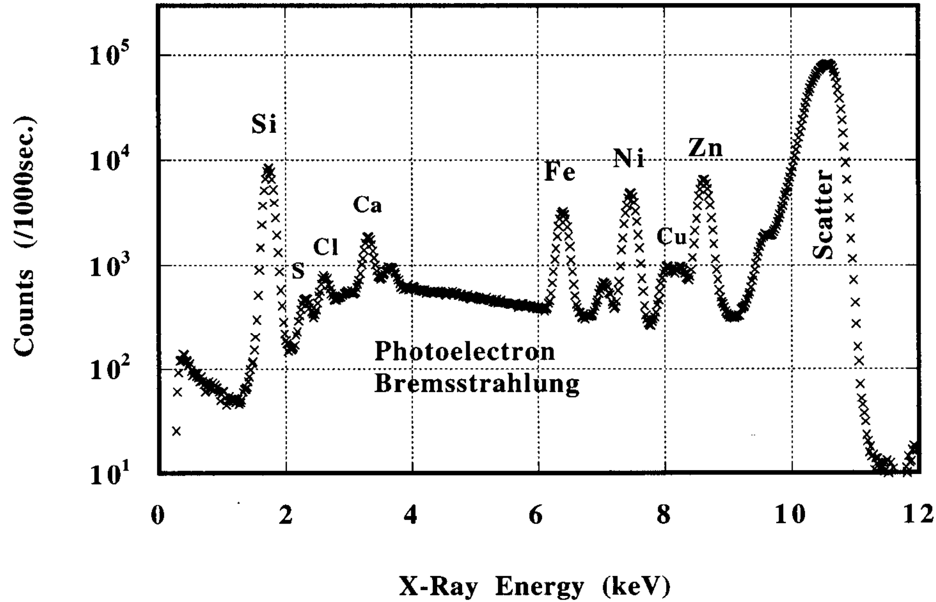

Fig. 4.1 SR TXRF spectrum taken from a silicon standard wafer with $1x10^{11}$ atoms/cm^2 of Fe, Ni, and Zn. Data was taken using BL 6-2 at SSRL. The energy of the incident x-ray beam was 10.6 keV and the angle of incidence was 0.08 deg. A 25 mm Teflon filter was placed in front of the Si (Li) detector.

Table 4.1 Fluorescence x -ray energies.

element	Kα (keV)	Kβ (keV)
Si	1.74	1.84
S	2.31	2.46
Cl	2.62	2.82
Ca	3.69	4.01
Fe	6.39	7.06
Ni	7.46	8.26
Cu	8.03	8.91
Zn	8.62	9.57

On the other hand, the S, Cl, and Ca fluorescence signals were from unintentional contamination possibly from residues created during the wafer cleaning processes. The Cu fluorescence peak in Fig. 4.1 came from the spurious fluorescence signals created inside the detector [1]. The detector used to take this data was the version 1 detector, in which the source of spurious Cu signals had not yet been eliminated.

It is also possible to see the overlaps of the Kα and Kβ X-ray signals of Si, S, and Cl. In addition, the Ni Kβ peak overlaps with the Cu Kα peak and the Cu Kβ peak overlaps with the Zn Kα peak. The Si (Li) detector with an energy resolution of 220 eV could not separate the fluorescence peaks because the energy difference between these peaks was smaller than the energy resolution of the detector.

Secondly, a significant scattered x-ray peak appeared near the incident x-ray energy (10.6 keV). The scattered x-ray peak was made up of Rayleigh and Compton scattered x-ray signals. Rayleigh scattering is elastic scattering of x-rays observed at the incident x-ray energy [6]. On the other hand, Compton scattering is inelastic scattering of x-rays whose profile is mainly observed below the incident x-ray energy [7].

These scattered x-ray peaks also overlap with each other in Fig. 4.1. The Si (Li) detector with an energy resolution of 220 eV could not separate the scattered x-ray peaks because the energy difference between these peaks was only about 220 eV and the width of these peaks were broadened by the incident x-ray beam with band pass of about 200 eV.

The scattered x-rays also generate an escape peak that is an inherent detector background peak generated when x-rays lose their energies by photo-ionizing Si atoms in the Si (Li) detector (see Ch. 3) [8]. In Fig. 4.1, the escape peak appeared at 8.77 keV,

which is equal to the energy of the incident x-ray beam (10.6 keV) minus the Si K absorption edge (1.83 keV).

The problem of the escape peak in Fig. 4.1 was that it overlapped with the Zn Kα peak (8.63 keV). The energy tunability of synchrotron radiation, however, allows us to prevent the overlap of the escape peak with a fluorescence line of interest, which will be discussed later.

Third, a continuous background component appeared between 2 and 9 keV. This continuous background component was primarily made up of bremsstrahlung which was generated when the photoelectrons created by the absorption of x-rays in the silicon wafer travel through and slowed down in the silicon wafer itself [9]. The photoelectron bremsstrahlung is the dominant continuous background component of SR TXRF [5]. Details of the photoelectron bremsstrahlung will be discussed in Ch. 6.

The TXRF data was taken using a 25 μm Teflon filter placed in front of the detector, which absorbed the low energy fluorescence x-rays [10]. Specifically, it reduced the Si fluorescence signal counts by a factor of 500. Without the filter, the Si fluorescence signals would have dominated the spectrum and would have resulted in the saturation of the detector electronics.

In addition to the Si fluorescence signals, the Teflon filter significantly absorbed the lower energy part of the photoelectron bremsstrahlung. The roll-off in the spectrum below 3 keV was due to the presence of the Teflon filter [3]. Since the Teflon filter did not absorb significant amount of other higher energy x-rays (> 90% transmission above 5 keV), the Si

fluorescence signal peak was made comparable to the peaks of the signals from the standard elements in Fig. 4.1.

The data of Fig. 4.1 was used for extrapolating the detection limits of the SR TXRF system at BL 6-2. Using Eq. (1.1), the MDL for Ni, for example, was determined to be $4x10^8$ atoms/cm^2.

In addition to BL 6-2, the MDLs at BL 10-2 and BL 4-2 were also extrapolated by measuring the same standard wafer with $1x10^{11}$ atoms/cm^2 of Fe, Ni, and Zn (Table. 4.2). The MDLs for Ni at BL 10-2 and BL 4-2 were found to be $3x10^8$ atoms/cm^2 and $1x10^9$ atoms/cm^2, respectively.

4.2.2 Comparison with Other Analytical Methods

The comparison between SR TXRF and conventional TXRF was made by measuring the same Si standard wafer with $1x10^{11}$ atoms/cm^2 of Fe, Ni, and Zn (Fig. 4.2). Both standard data were taken for a measurement time of 1000 sec. The conventional TXRF data (top) were taken at Hewlett-Packard Co. using a RIGAKU TXRF system with a W anode that emits W Lβ x-rays (9.67 keV) [4].

Table 4.2 The Ni MDLs with the SR TXRF techniques at SSRL.

Beam Line	flux at 10.6 keV (photons/sec.)	MDL for Ni (atoms/cm^2)
10-2 (double multilayers)	1E+13	3E+08
6-2 (double multilayers)	2E+12	4E+08
4-2 (single multilayer)	3E+11	1E+09

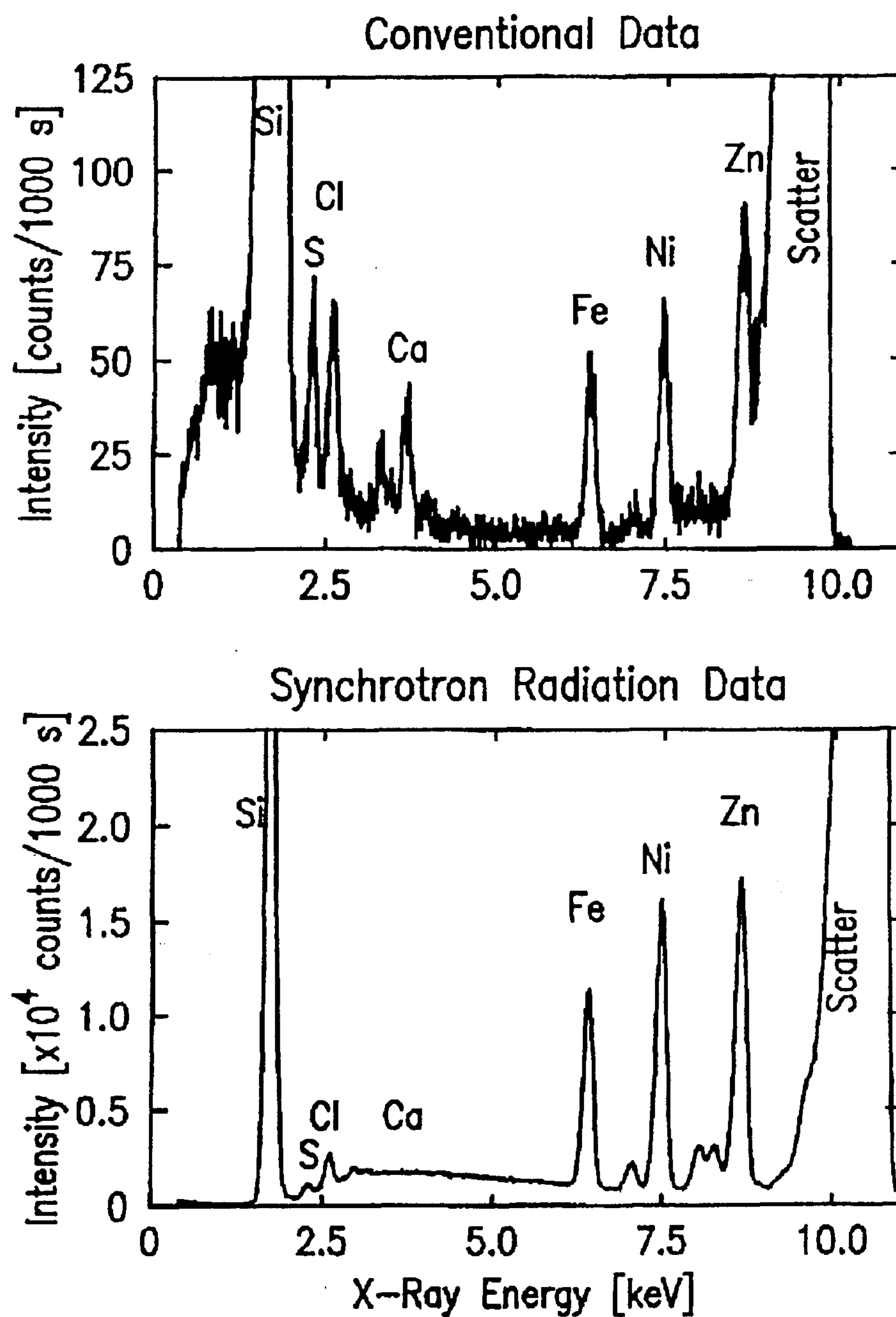

Fig. 4.2 TXRF data taken with conventional rotating anode (top) and the synchrotron radiation at SSRL (bottom). The conventional TXRF data was taken by S. Laderman et. al at Hewlett Packard [4].

The SR TXRF data (bottom) were taken using BL 10-2 at SSRL. The energy of the SR beam was 10.6 keV and the data were taken using a 25 μm Teflon filter, placed in front of a Si (Li) detector, in order to absorb the Si fluorescence signals.

These spectra commonly showed fluorescence signals of Si, S, Cl, Ca, Fe, Ni, Cu, Zn, and primary scattered x-ray signal peaks. As described before, the signals of Fe, Ni, and Zn were created from the standard elements. On the other hand, the signals of S, Cl and, Ca, were created from unintentional contamination and the Cu was a spurious detector signal.

These spectra showed two significant differences. The first difference was the counts in the vertical scale. The counts of the SR TXRF were more than 200 times higher than the counts of the conventional TXRF. This was because of the higher incident flux of the synchrotron radiation.

The second difference was the position of the scattered x-ray peak. The scattered x-ray peak of the conventional TXRF appeared at 9.7 keV, while that of SR TXRF appeared at 10.6 keV. As a result, the SR TXRF spectrum nicely separated the Zn fluorescence peak from the primary scattered x-ray signal peak, while they overlapped with each other in the conventional TXRF spectrum. We could tune the incident x-ray energy of the synchrotron radiation in order to prevent the overlap of the primary scattered x-ray peak with the fluorescence signal peaks.

From Figs 4.2, the MDL for Ni with the conventional TXRF was found to be $5x10^9$ atoms/cm^2, while the Ni MDL with the SR TXRF on BL 10-2 was $3x10^8$ atoms/cm^2. The higher incident flux of synchrotron radiation improves the MDL by about 20 times over the rotating anode.

It should be pointed out that the polarization of the synchrotron radiation gives smaller scattered x-ray peak, which makes it possible to use the more than 200 times higher incident flux of the synchrotron radiation without saturating the detector. However, even if the photon flux from the rotating anode is increased as high as the synchrotron radiation, the MDL would not effectively be improved because the scattered x-ray intensity of the unpolarized photons generated from the rotating anode is about 10 times higher than the scattered x-ray intensity of the synchrotron radiation, which would result in the saturation of the detector and higher detector background, which will be discussed in Ch. 5. Because of the high incident flux and the linear polarization effect, synchrotron radiation can offer higher sensitivity beyond the limits of rotating anode x-ray sources.

Next, we compare the Ni MDL, sampled area, and mass of detected atoms among the methods of SR TXRF, rotating anode TXRF and WSA / ICPMS (Table. 4.3). WSA / ICPMS (Wafer Surface Analysis / Inductively Coupled Plasma Mass Spectroscopy) is a analytical method used by Toshiba to check the concentration of the standard elements [14], [15].

As shown before, the Ni MDL using SR TXRF was $3x10^8$ atoms/cm^2 and that using the rotating anode TXRF was $5x10^9$ atoms/cm^2. Note that the MDL by WSA / ICPMS was the same as the MDL of SR TXRF ($3x10^8$ atoms/cm^2). However, the MDL of WSA/ICPMS was obtained only by integrating over a 6-inch wafer surface.

Table 4.3 Comparison of various methods.

method	MDL (atoms/cm^2)	Sample Area (mm^2)	Mass of Detected Atom (fg)
SR TXRF	3E+08	15	5
Rotating Anode TXRF	5E+09	100	500
WSA / ICPMS	3E+08	18000	5000

An important advantage of SR TXRF over WSA / ICPMS is the spatial resolution. The MDL of SR TXRF was obtained by measuring a sample area of 15 mm^2 (Ch. 3). On the other hand, WSA / ICPMS required the whole surface area of a 6-inch wafer, which was 18000 mm^2. As a result, the absolute mass of atoms detected by SR TXRF was only 5 fg, while it was 5000 fg for WSA / ICPMS. SR TXRF is capable of measuring a smaller number of atoms in a smaller area than WSA / ICPMS.

4.2.3 Diffraction Peaks

In this section, we discuss the diffraction peaks observed in SR TXRF. The purpose of this section is to reveal how the diffraction signals which affected the SR TXRF spectra are eliminated by optimizing the experimental configuration [16], [30].

A SR TXRF spectrum with diffraction peaks is shown in Fig. 4.3. The horizontal and vertical axes of Fig. 4.3 are x-ray energy and counts, respectively. The energy of the incident x-ray beam was 10.6 keV with an angle of incidence of 0.08 deg. Data was taken from the same standard wafer used for Fig. 4.1. Therefore, the characteristic fluorescence lines of Fe, Ni, and Zn were observed as well.

However, Figs. 4.1 and 4.3 were taken using different optical configurations. Fig. 4.1 was taken at BL 6-2 with the double multilayers, while Fig. 4.3 was taken at BL 4-2 with the single multilayer. As a result, Fig. 4.3 clearly showed two diffraction peaks at 4.57 keV (202 peak) and 9.14 keV (404 peak), which were not observed in Fig. 4.1 taken with the double multilayers [3].

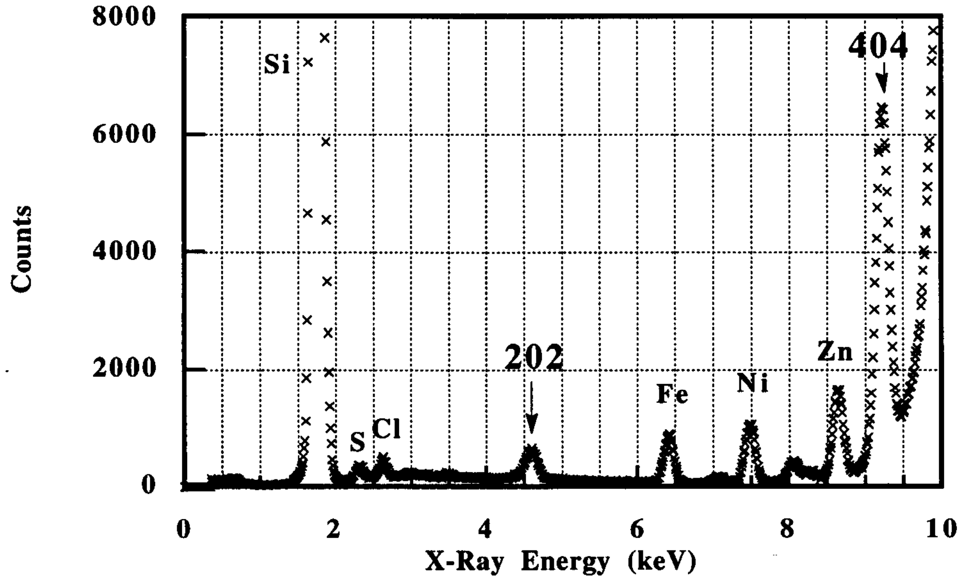

Fig. 4.3 202 and 404 diffraction peaks in a SR TXRF spectrum. Data were taken from a silicon standard wafer with 1×10^{11} atoms/cm^2 of Fe, Ni, and Zn at BL 4-2 at SSRL by use of a single multilayer monochromator. The energy of the incident x-ray beam was 10.6 keV with an angle of incidence of 0.08 deg. The x-ray beam was incident on the (001) silicon wafer from the [010] direction.

The diffraction signals were created by the incident x-ray beam having energies between 2 keV and 10.6 keV that were not eliminated with the single multilayer monochromator configuration (Ch. 3). Even though the flux is low in this region, the reflectivity of the Si wafer is essentially equal to 1 so that a large number of photons can be generated by diffraction.

4.2.4 Diffraction Conditions

The diffraction geometry of this measurement is shown in Fig. 4.4. The x-ray beam is incident on the (001) silicon wafer from the [010] direction. The direction of the diffracted beam can be obtained using the Laue condition [17],

$$H_{hkl} = \frac{s - s_0}{\lambda} \qquad (4.1),$$

where

H_{hkl} = reciprocal lattice vector,

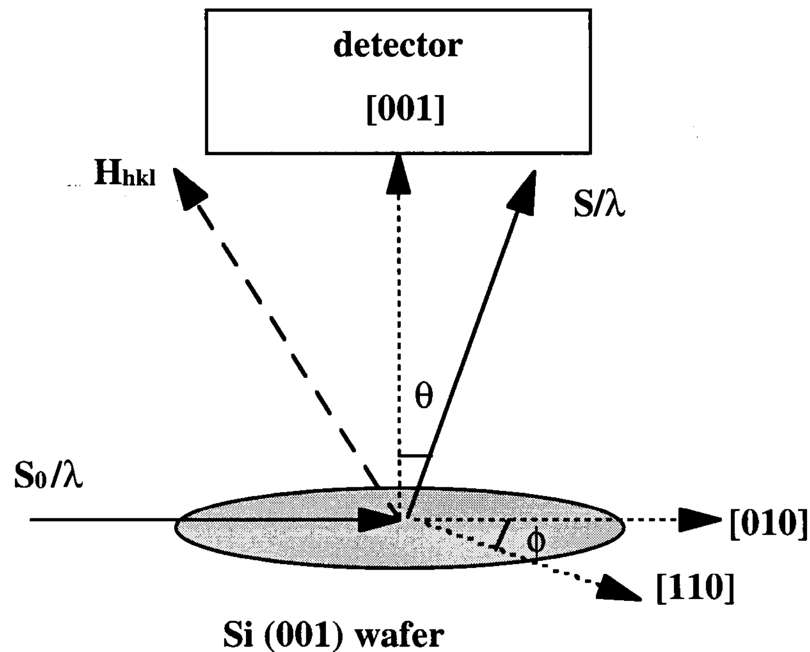

Fig. 4.4 The geometry of the diffraction condition generated from a Si (001) wafer by the incident x-ray beam at glancingly incidence.

λ = wavelength of incident x-ray beam,

s_0/ λ = incident beam vector, and

s/ λ = diffracted beam vector.

With a given H_{hkl} and s_0/ λ, the diffracted beam vector, s/ λ, is determined from Eq. (4.1).

Although a number of diffraction lines are generated, only some of them are measured by the Si (Li) detector. Mathematically, the condition for the observation of the diffraction lines is formulated using the inner product of the diffracted beam vector, s/λ, and the [001] vector, in the direction in which the Si (Li) detector is installed,

$$s/ \lambda \cdot [001] < 1/ \lambda \cos\theta \qquad (4.2),$$

where θ is the acceptance angle of detector that defines the solid angle of the detector (Fig. 4.4). Eq. (4.2) compares the angle of the diffracted beam to the acceptance angle of the detector.

Using Eq. (4.2), we calculated the diffraction conditions as shown in Fig. 4.5. The horizontal axis shown in Fig. 4.5 (bottom) is the azimuthal rotation angle of the Si (001) wafer where zero deg. is chosen so that the [110] direction on the 6-inch wafer (the flat) is along the incident beam direction. The horizontal axis shown in Fig. 4.5 (top) is the corresponding direction of the incident beam vector with respect to [110] crystallographic direction on the Si (0$\bar{1}$0) wafer, which is represented by ϕ in Fig. 4.4. The vertical axis is the photon energy in keV.

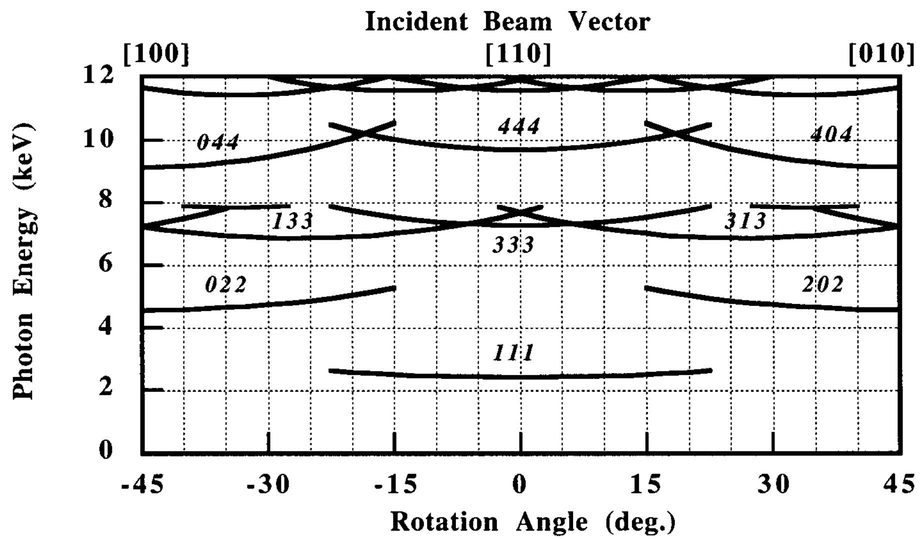

(top) 30 deg. of detector acceptance angle.

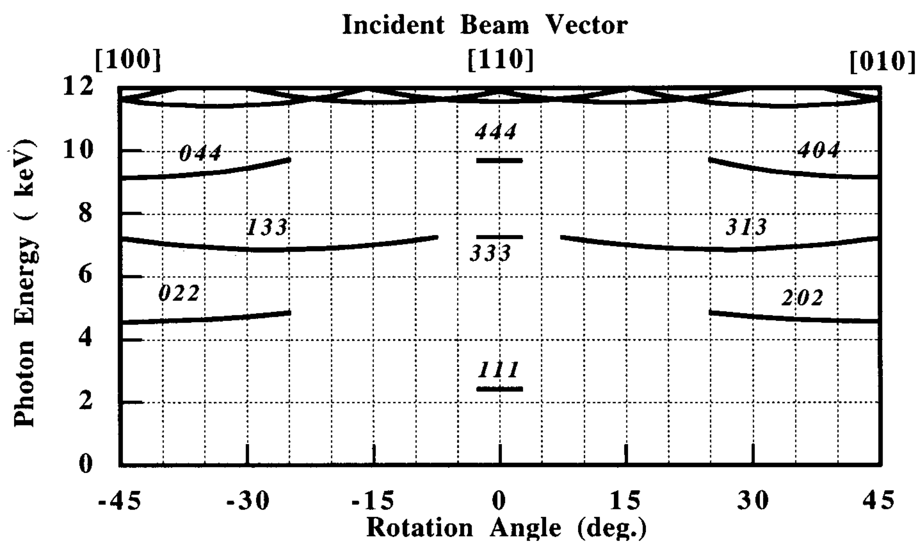

(bottom) 20 deg. of detector acceptance angle.

Fig. 4.5 The diffraction conditions in the case of a Si (001) wafer when the detector acceptance angles are 30 deg. (top) and when it is 20 deg. (bottom)

Figs. 4.5 (top) was calculated with a detector acceptance angle set at 30 deg., while Fig. 4.5 (bottom) was calculated with a detector acceptance angle set at 20 deg. These acceptance angles were achieved by the use of collimators with aperture diameters of 1/8" and 1/16", respectively (Ch. 3).

The data in Fig. 4.3 were measured with the 1/8" collimator with the x-ray beam incident on the (001) silicon wafer on the [010] direction. Note the existence of the 202 (at 4.57 keV) and 404 (at 9.14 keV) diffraction peaks were accurately predicted in Fig. 4.5 (top). However, it should be noted that a 333 diffraction peak, which is predicted in Fig. 4.5, was not observed in Fig. 4.3. This was because the 333 diffraction peak (at 7.23 keV) had low intensity and overlapped with the Ni fluorescence peak at 7.47 keV.

Although the diffraction peaks are serious problems because they may overlap with the characteristic fluorescence lines of interest, there are several ways to avoid them. For example, some diffraction lines can be avoided by narrowing the collimators placed in front of the detector. The collimator effect on the diffraction lines can be seen by comparing the result of the calculations with the 1/8" collimator (Fig. 4.5 (top)) and the 1/16" collimator (Fig. 4.5 (bottom)). Because the detector acceptance angle with the smaller collimator (about 20 deg.) is smaller than that with the larger collimator (about 30 deg.), every diffraction condition with the smaller collimator has a more limited angular extent compared to the corresponding one with the larger collimator.

Therefore, it is possible to avoid some diffraction peaks by using the smaller collimators and properly selecting the incident beam direction with respect to the Si wafer orientation. This method is useful for eliminating a particular diffraction line, however, it cannot eliminate all the diffraction lines from the SR TXRF spectra.

Essentially, we eliminated the diffraction peaks by using a combination of the double multilayer monochromators, a carbon absorption filter, and the wafer orientation. The double multilayer optical configuration significantly reduces the scattered x-rays between 5 keV and 10 keV and the about 1 mm thick carbon filter absorbed the incident x-rays below 5 keV as shown in Ch. 3. As a result, the diffraction peaks in the energy region below 10 keV were adequately eliminated from the SR TXRF spectra.

The diffraction peaks we have discussed up to now are of low intensity and can interfere with the fluorescence signal peaks. As discussed, these can be eliminated by eliminating the radiation in the particular photon energy region. However, an equally serious situation exists when the diffraction condition is met at the primary incident beam energy. It is clear that these photons cannot be eliminated from the incident beam. The diffraction peaks at the primary incident beam energy can generate many more photons from the wafer surface than even the primary scattered beam resulting in the saturation of the detector. This is a difficult problem not only for our SR TXRF system but also for conventional TXRF systems [16].

However, the diffraction peaks of the primary incident beam in SR TXRF measurements are more serious problems than conventional TXRF because a variety of incident x-ray energy are selected for the SR TXRF measurements. For example, a number of diffraction lines can appear above 11.5 keV as shown in Figs. 4.5. We experimentally found that these diffraction lines may be generated even by the tails of the primary incident beam which is monochromated by the wide band pass multilayers in order to obtain higher flux. For the SR TXRF measurements using a primary incident x-ray energy of more than 11.5 keV, the incident x-ray energy and rotation angle of the Si wafer must be chosen carefully in order to avoid the diffraction peaks.

4.2.5 Scattered X-Rays

Now let us consider the effect of the detector orientation with respect to the polarization vector of synchrotron radiation on the intensity of the scattered x-ray peak. As mentioned in Ch. 2 and Ch. 3, the scattered radiation is at a minimum when the detector is placed along the polarization vector of synchrotron radiation [18].

This effect was studied through measurements using two different detector configurations. As described in Ch. 3, we refer to the two detector configurations as parallel mode and normal mode, respectively. In the parallel mode, the detector was installed parallel to the polarization vector of the synchrotron radiation, while, in the normal mode, the detector was installed normal to the polarization vector.

Originally, the overall count-rates in these two modes were very different on BL 6-2 using an incident beam with an energy of 10.6 keV at an incident angle of 0.13 deg. The count-rate in the parallel mode was about 10 K cps, whereas it was much larger in the normal mode. In order to reduce the count-rate in the normal mode, we reduced the incident beam intensity by a factor of 10 using Al filters. This prevented saturation of the detector.

To compare these data meaningfully, we normalized the spectra using the Si K fluorescence signals. The Si K fluorescence signals are useful as a normalization factor because they are emitted isotropically and independent of the detector configuration with respect to the polarization vector [19]. This normalization made it possible to determine the dependence of the scattered x-rays on the detector configuration.

The normalized spectra using the Si fluorescence signals are shown in Fig. 4.6. The data were taken from two different Si wafers but prepared using the same cleaning

method (HF-SC2 method) [20]. The S, Cl, Ca, Ni and, Zn signals observed in the spectra were generated from unintentional contamination and the Fe and Cu signals were primarily the spurious signals generated inside the version 2 detector used at that time.

From Fig. 4.6, it was found that the primary scattered x-ray signal counts at 10.6 keV in the normal mode were about 10 times larger than the counts in the parallel mode. This experimental result was roughly consistent with the results of the theoretical calculation done by assuming 90% linear polarization of the incident beam with the detector solid angle defined by 1/8" collimator (Ch. 3). Details of the theoretical calculation will be discussed in Ch. 5.

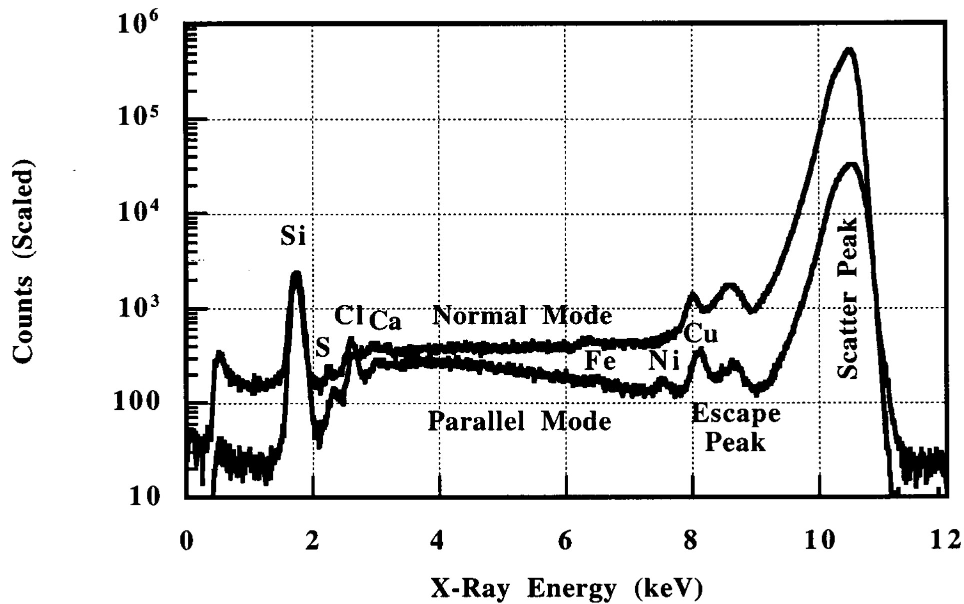

Fig. 4.6 SR TXRF spectra taken with detector parallel and normal to the polarization vector of the incident x-ray beam. Data was taken from a nominally clean wafer. These spectra were normalized using the Si fluorescence signals.

From Fig. 4.6, we found that the continuous background signals between 3 keV and 9 keV also increased in the normal mode. For example, the continuous background signal counts near the Ni K fluorescence line (7.48 keV) increased about 3 times compared to those in the parallel mode. As a result, the Ni fluorescence x-ray peak could not be seen in the normal mode although it was seen in the parallel mode.

The increase in the continuous background in the normal mode was due to the increase in the low energy tail of the primary scattered x-ray peak. As described in Ch. 3, the low energy tail is generated by incomplete charge collection in the detector and its intensity is proportional to the intensity of the x-rays incident on the detector. Although it was small compared to the bremsstrahlung generated by photoelectrons in the parallel mode, the low energy tail became dominant in the normal mode. Details of the low energy tail and bremsstrahlung backgrounds will be discussed in Ch. 6.

The detector configuration normal to the polarization vector resulted in an increase in the magnitude of the scattered x-ray peak and its low energy tail. However, these backgrounds were significantly reduced by installing the detector parallel to the polarization vector, which is the standard detector configuration we have used for SR TXRF.

4.2.6 Spurious Fluorescence Signals from the Si (Li) Detector

This section discusses the spurious fluorescence signal backgrounds generated inside the Si (Li) detector [5]. As mentioned in Ch. 3, the spurious fluorescent signals of Fe, Ni, and Cu were consistently observed in the high sensitivity SR TXRF measurements. An example of spurious signals generated from a clean wafer is shown in Fig. 4.7. The energy of the primary incident beam was 10.6 keV and the Teflon filter used

for this measurement was 25 μm thick. The vertical axis is the counts per 1000 sec. in linear scale and the horizontal axis is x-ray energy ranging from 5 to 10 keV.

It is helpful to quantify the spurious signals by relating their intensity to what one would obtain from a given concentration of contamination if it were present on the Si wafer surface. The results of the quantification then gives a measure of the effective detection limits based on the spurious signals. Using the standard spectrum shown in Fig. 4.1, the spurious signals of Fe, Ni, and Cu in Fig. 4.6 were related to a surface concentration of $1x10^9$ atoms/cm^2, $3x10^9$ atoms/cm^2, and $2x10^{10}$ atoms/cm^2, respectively.

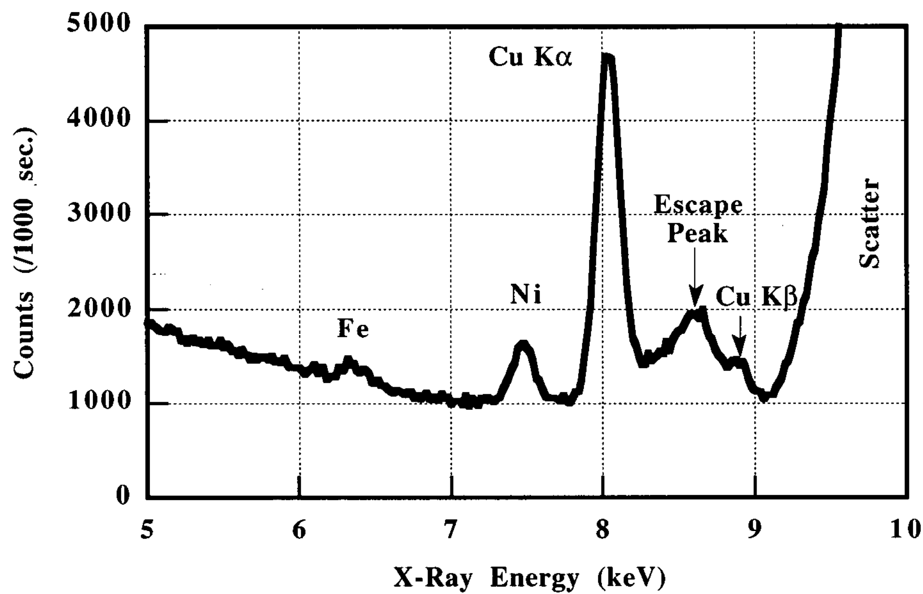

Fig. 4.7 SR TXRF spectrum of a clean wafer taken with our commercially available Kevex Si (Li) detector (version 1). The spurious fluorescence signals of Fe, Ni, and Cu appeared.

It was found that the spurious fluorescence signals were generated when the radiation scattered at the primary energy by the sample entered the detector and was incident on the metallic parts inside the detector which contained these elements. This hypothesis was tested by measuring a series of spectra with different thickness filters placed in front of the detector. We refer to this measurement as the filtering study. In the filtering study, the intensity of the signals originating from the sample would change with the filter thickness proportionally to the difference in attenuation of their respective energies [10]. However, if the signals originated within the detector, the intensity of the signals scaled to the scattered x-ray intensity would remain constant. The filtering study allowed us to find the origin of the spurious signals.

The result of the filtering study is shown in Fig. 4.8. Teflon filters used for this study had the thickness of 25 μm and 400 μm. The spectrum taken with the 400 μm Teflon filter was scaled to the spectrum with the 25 μm Teflon filter by use of the scattered x-ray intensity. Fig. 4.8 (top) shows the whole spectrum in the energy region from 0 to 12 keV. Fig. 4.8 (bottom) shows the spectra in the energy region from 5 to 10 keV on a linear scale.

Significant differences between the spectra were the intensities of Si fluorescence signals and lower energy continuous backgrounds. These low energy backgrounds were greatly absorbed by the thicker 400 μm Teflon filter, indicating that they were generated from the Si wafer. Note that the ratios of the Fe, Ni, and Cu signals between the 400 μm and 25 μm cases are of order one as shown in the entry in Table 4.4 labeled 400 μm / 25 μm (data).

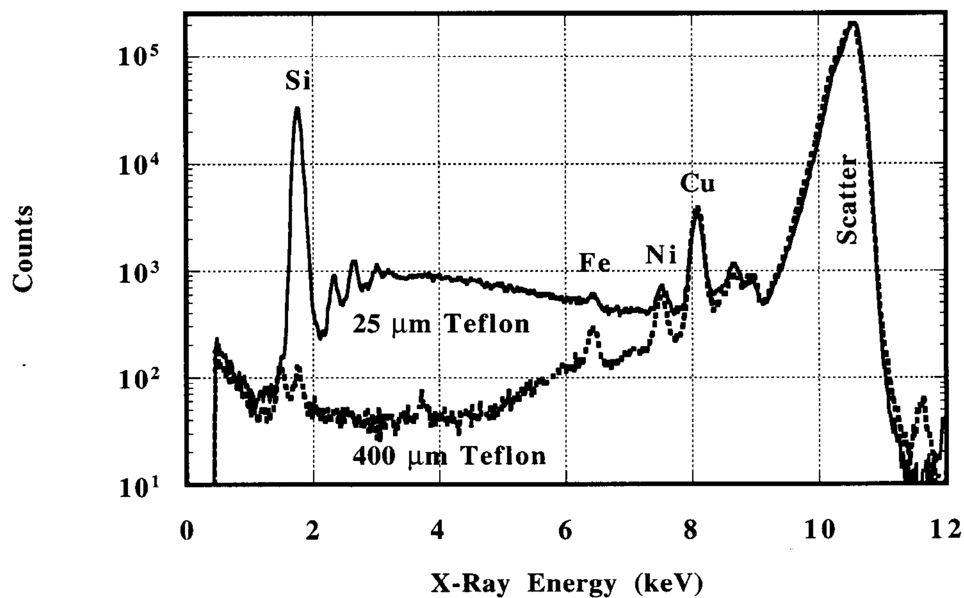

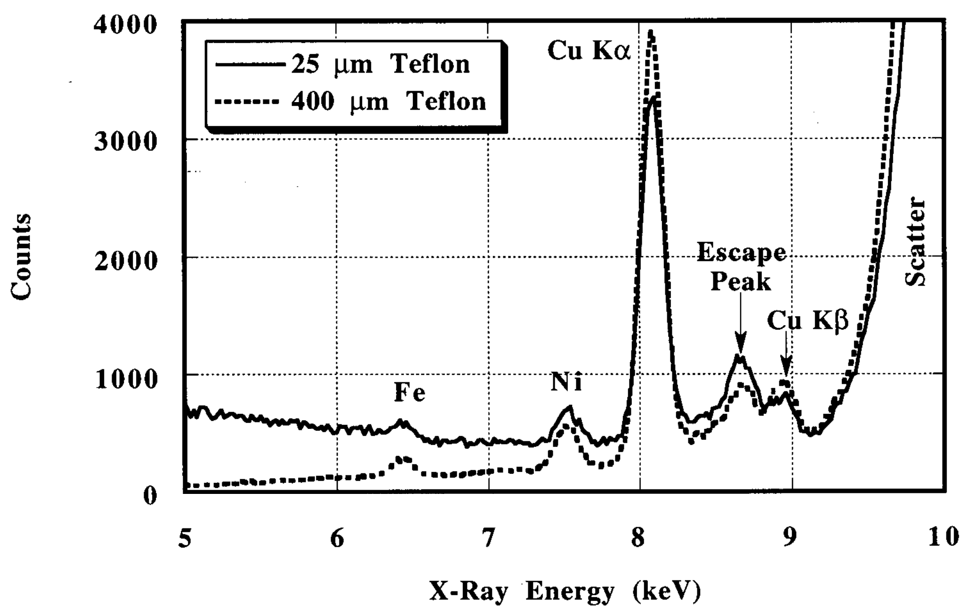

Fig. 4.8 A result of the filtering study with 25 μm and 400 μm Teflon filters. The top spectrum is in log scale with the energy axis ranging from 0 to 12 keV. The bottom spectrum is in linear scale with the energy axis ranging from 5 to 10 keV.

Table 4.4 Results of the filtering study with Teflon filters.

Teflon thickness (mm)	Fe signal (counts)	Ni signals (counts)	Cu signal (counts)
400 μm	981	2135	23435
25 μm	637	1815	18731
400 μm /25 μm (data)	1.54	1.18	1.25
400 μm /25 μm (calculation)	0.18	0.43	0.55

Since these ratios are expected to be less than one if the signals had originated on the wafer surface as shown in the entry in Table 4.4 labeled 400 μm /25 μm (calculation), we concluded that the spurious signals were generated inside the Si (Li) detector.

In order to eliminate these parasitic fluorescence signals, we worked with Kevex to modify the Si (Li) detector by replacing the metallic parts inside the detector. At first, a Ni contact on the Si (Li) crystal and a Cu-Be washer were replaced with their Pd counterparts. Palladium was used because the Pd L fluorescence x-ray peaks ($L\beta$ = 3 keV) did not overlap with the 3-d transition metal peaks.

We refer to this detector as the version 2 detector, while the standard Kevex detector is referred to as the version 1 detector. Furthermore, we replaced the detector crystal housing which was made of an Al alloy containing 0.15-0.4 % of Cu (AA#6061) with a part made from 99.999% Al. This detector is referred to as the version 3 detector.

The spurious fluorescence peaks generated from the version 3 detector were checked with Ag x-rays ($K\alpha_2$ = 22 keV) emitted from a Cd radiation source. The Ag x-ray spectrum taken with the version III Si (Li) detector is shown in Fig. 4.9. The horizontal axis is x-ray energy in keV and the vertical axis is counts on a log scale.

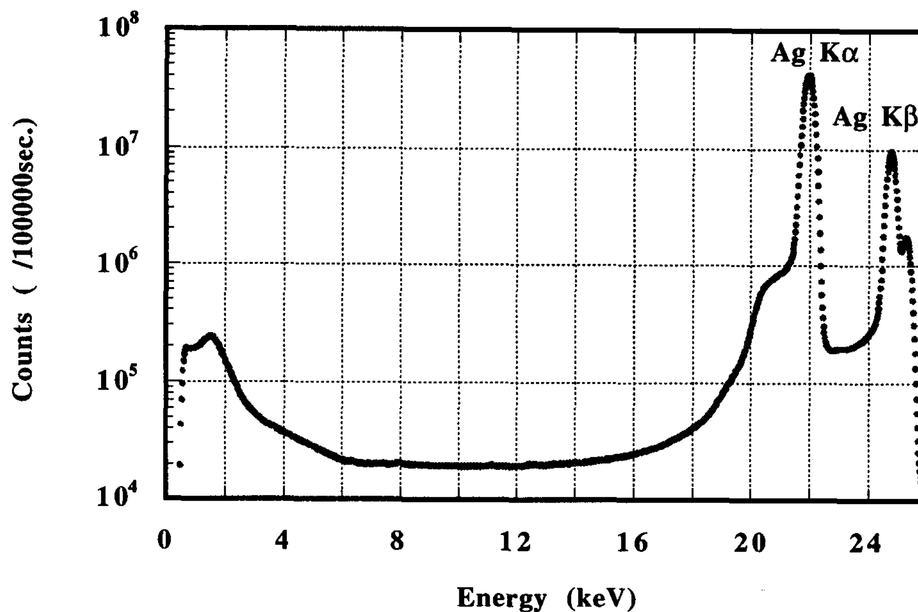

Fig. 4.9 The Ag x-ray spectrum taken with the version 3 Si (Li) detector. A 0.5 mm Si absorption filter was placed between the Cd source and detector.

To acquire this spectrum, a measurement time of 100,000 sec. was required because of the low count-rate of the Ag fluorescence x-rays from the Cd source (~ 200 cps). For reference, the typical SR TXRF measurement time is 1000 sec. with a count-rate of 10,000 cps.

It should be pointed out that a 0.5 mm Si filter was placed between the Cd source and the detector to absorb any fluorescence signals from the 3-d transition metals produced by the Cd source. Because the transmission factor of Cu K fluorescence (8.04 keV) through the 0.5 mm Si filter is 0.00064, while that of the Ag K fluorescence is 0.68, the thick Si filter assured that no spurious fluorescence signals from the Cd source would appear in the spectrum.

In Fig. 4.9, no spurious Fe, Ni, or Cu signals were observed and, therefore, we can conclude that the equivalent signal from contaminant atoms on a Si wafer would be less than our observed MDLs.

Note that an increase of the continuous background below 4 keV was observed in Fig. 4.9. This originated from the low energy tail of the Compton scattering of the Ag x-rays inside the detector. The Compton scattering inside the detector can clearly be observed only when the x-ray energy is high. Therefore, in the SR TXRF spectra taken with an incident beam energy near 11 keV, this background is small. For details of this detector background, see reference [21].

The SR TXRF spectra taken from the modified detectors are shown in Fig. 4.10. The Si (Li) detectors used for the measurements were the standard Kevex Si (Li) detector model No. 3600-0018-0146 (version 1), the Ni modified detector (version 2), and Cu modified detector (version 3). The incident beam energy used with the version 1 and 2 detectors was 10.6 keV, while the incident beam energy used with the version 3 detector was 11 keV. The spectra in Fig. 4.9 were normalized using the continuous background intensity at 7 keV, where no fluorescence signals existed.

In the data taken with the version 2 detector, the Ni and Cu parasitic fluorescence signals were greatly reduced. The levels of the Fe, Ni and Cu spurious signals related to equivalent surface concentrations were found to be $5x10^8$ atoms/cm^2, $4x10^8$ atoms/cm^2, and $7x10^9$ atoms/cm^2, respectively, as shown in Table. 4.5.

In the data taken with the version 3 detector, the residual spurious fluorescence signals were reduced below the detection limit of our measurements. With the version 3 detector, it is now possible to get true minimum detection limits of $3x10^8$ atoms/cm^2 for

these elements without the necessity of subtracting out any background peaks. We estimated that the equivalent surface concentration of the Fe, Ni, and Cu would be below 1×10^8 atoms/cm^2 as extrapolated from the data of Fig. 4.9.

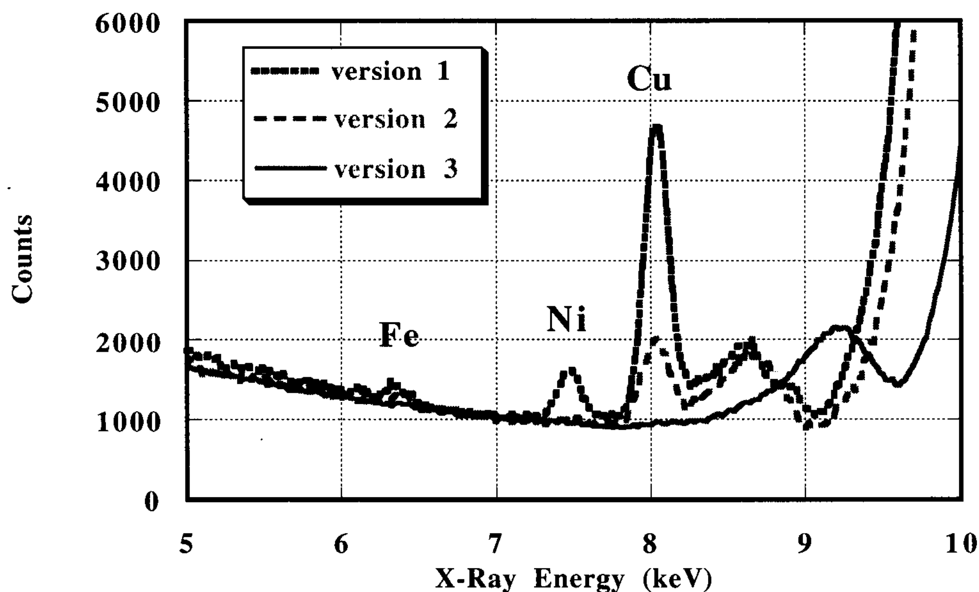

Fig. 4.10 Spurious fluorescence signal peaks from various Kevex Si (Li) detectors. The detectors used for the measurements were the standard Kevex Model # 3600-0018-0146 (version 1), the Ni modified detector (version 2), and the Cu modified detector (version 3). These spectra were normalized using the intensity of the continuous background at 7 keV. A 10.6 keV x-ray beam was used for the version 1 and 2 detectors, while a 11 keV beam was used for the version 3 detector.

Table 4.5 Conversion of spurious signals to the contamination on the Si wafer surface.

detector version	Fe (atoms/cm^2)	Ni (atoms/cm^2)	Cu (atoms/cm^2)
1	1E+09	3E+09	3E+10
2	5E+08	4E+08	7E+09
3	<1E+08	<1E+08	<1E+08

4.2.7 Practical Applications

This section shows three results of our high sensitivity SR TXRF measurements for practical applications [22]. First, the results of the study of a gate oxidation process at HP are shown in Fig. 4.11. Samples used for the measurements were an as-received clean Si wafer and Si wafers before and after 30 Å gate oxidation.

Data were taken with the version 3 Si (Li) detector using an incident beam with an energy of 11 keV and an angle of incidence of 0.07 deg. Three spectra from these wafers were scaled using the continuous background intensity at 7.2 keV, where no fluorescence line existed. From Fig. 4.11, it was found that the levels of the 3-d transition metals on the as-received wafer were below the detection limit of SR TXRF (<$3x10^8$ atoms/cm^2).

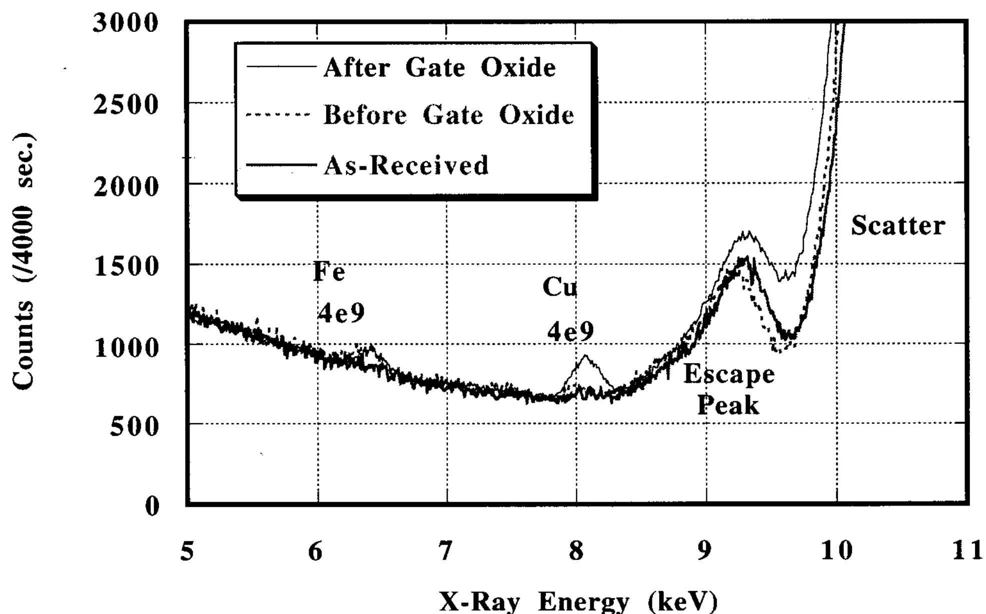

Fig. 4. 11 Comparison of Si wafers before and after 30 Å gate oxidation.

However, on the wafer surface before gate oxidation, a small amount of Fe at a level of $4x10^9$ atoms/cm^2 was measured. The Fe contamination was added during the pre-gate oxidation process. Furthermore, after the gate oxidation, additional Cu signals were detected, which corresponded to the surface concentration of $2x10^9$ atoms/cm^2. The Cu contamination was considered to be generated in the furnace used for the high temperature gate oxidation process.

As shown in Ch. 1, metal contamination at the gate oxide interface has negative impacts on MOS properties [15]. The results of Fig. 4.11 revealed that our SR TXRF system is capable of measuring metal contamination generated during the gate oxidation with high sensitivity.

In a second example, spectra taken as part of a study of a cleaning equipment is shown in Fig. 4.12 [22]. The horizontal axis of Fig. 4.12 is x-ray energy and the vertical axis is counts per 4000 sec. on a linear scale. Data were taken with the version 3 Si (Li) detector using an incident beam with the energy of 11 keV and an angle of incidence of 0.07 deg. Data were taken from wafers before and after a cleaning process performed at HP. The two spectra were scaled using the continuous background intensity at 7.2 keV, where no fluorescence line exists.

Before the cleaning, small amounts of Fe, Ni, Cu, and Zn signals were detected, the concentrations of which were found to be $4x10^9$ atoms/cm^2, $4x10^8$ atoms/cm^2, $4x10^9$ atoms/cm^2, and $8x10^9$ atoms/cm^2, respectively.

The signals from these elements were changed after the wafer cleaning process. After cleaning, the Cu and Zn were removed at least below the detection limit of our system ($<3x10^8$ atoms/cm^2).

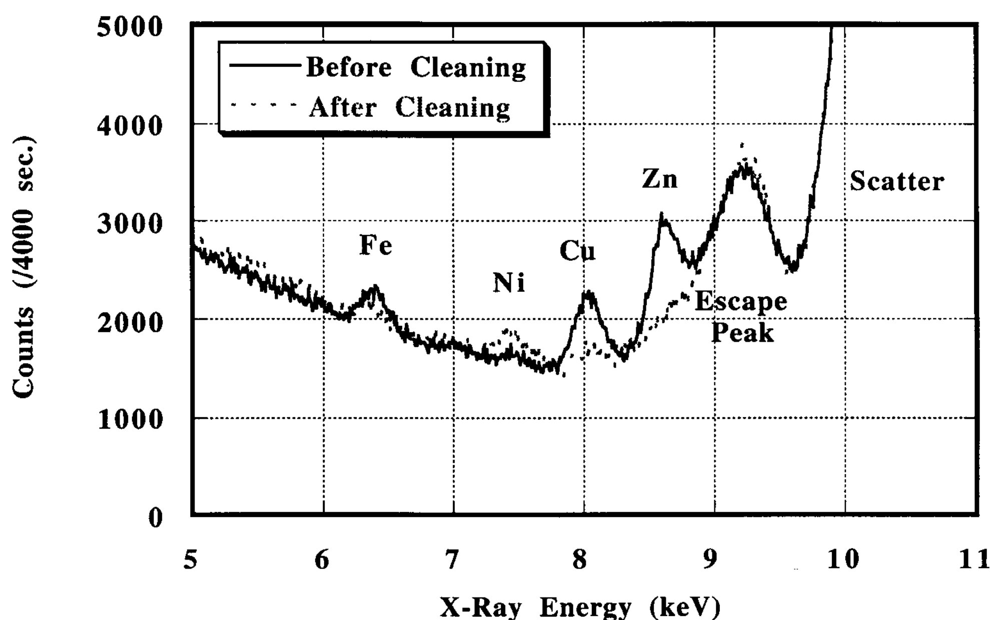

Fig. 4.12 Study of a cleaning equipment at HP.

However, the Ni signals were increased to $2x10^9$ atoms/cm^2 and the Fe was reduced only to $1x10^9$ atoms/cm^2. The high sensitivity of our SR TXRF system made it possible to measure these small signals, which cannot be measured using conventional TXRF.

The final example is a study of the standard Stanford CIS Si wafer cleaning process (Fig. 4.13). Data was taken using an incident beam with the energy of 10.6 keV and an angle of incidence of 0.13 deg. In addition to the CIS wafer, we also took data from a Si wafer cleaned by the HP/Toshiba collaboration. Because of its state-of-the-art cleaning process shown in Table. 4.7, the HP/Toshiba wafer was assumed to be very clean. The two spectra were scaled using the continuous background intensity at 7.2 keV, where no fluorescence line exists. It should be pointed out that the version 2 Si (Li) was used for this measurement. Therefore, small levels of spurious signals of Fe, Ni, and Cu were generated in the detector.

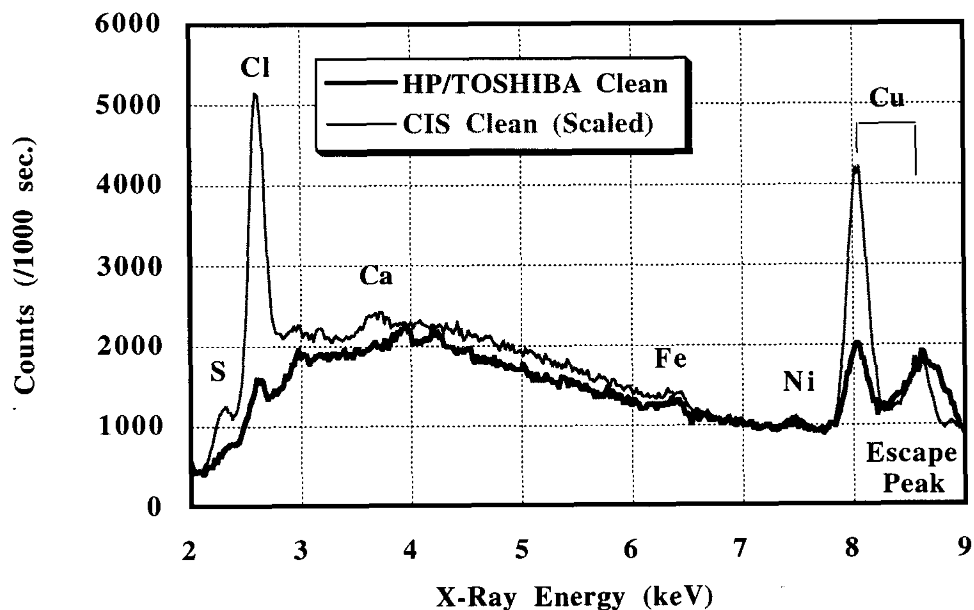

Fig. 4.13 Comparison of the spectra taken from the Si wafers cleaned in CIS and HP/Toshiba. Data were taken with the version 2 Si (Li) detector.

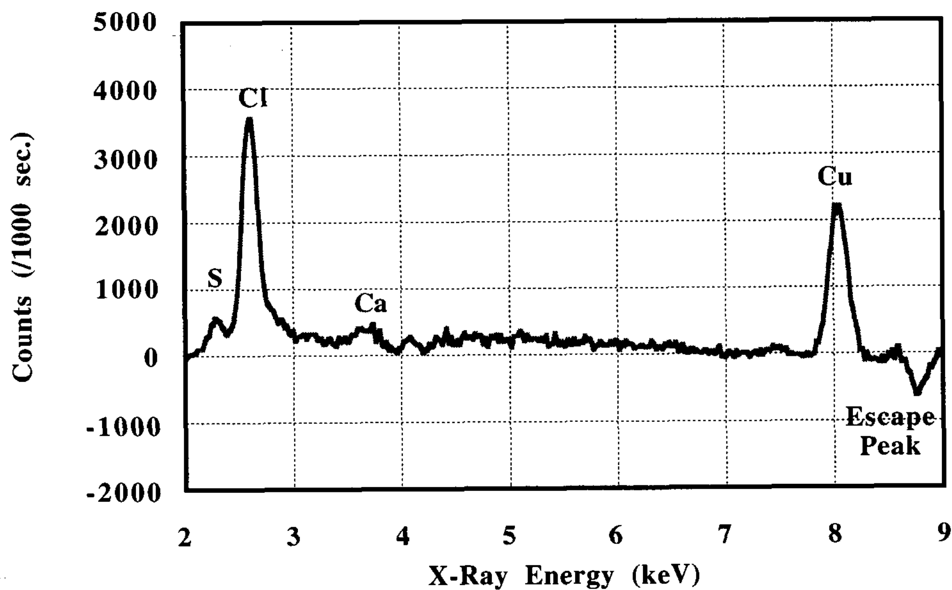

Fig. 4.14 Difference spectrum between the CIS data and HP/Toshiba data.

Table 4.6 Signals and concentrations of the impurities on a Si wafer cleaned in CIS.

element	signal	σ	ω	filter transmission	concentration (atoms/cm^2)
S	4034	2581	0.0761	0.05	1E+12
Cl	27830	3419	0.0942	0.15	2E+12
Ca	3855	6147	0.163	0.5	3E+10
Cu	18231	22970	0.445	0.91	6E+09

Table 4.7 Wafer cleaning processes in CIS and HP/Toshiba.

wafer	process 1	process 2	process 3
CIS	SPM(H_2SO_4/H_2O_2)	SC1($NH_4Cl/H_2O_2/H_2O$)	DHF(HF/H_2O)
HP/Toshiba	DHF(HF/H_2O)	SC2 ($HCl/H_2O_2/H_2O$)	FPM($HF/H_2O_2/H_2O$)

In order to subtract the spurious signals from the CIS data, we subtracted the signals from the HP/Toshiba clean wafer from the signals of the CIS clean wafer (Fig. 4.14). From Fig. 4.14, it was found that trace impurities of S, Cl, Ca, and Cu were present on the surface cleaned using the CIS process.

Using the parameters shown in Table. 4.6 and the results taken from the standard wafer, the concentration of the S, Cl, Ca, and Cu on the CIS wafer were found to be 1×10^{12} atoms/cm^2, 2×10^{12} atoms/cm^2, 3×10^{10} atoms/cm^2, and 7×10^{9} atoms/cm^2, respectively. Although the signal intensity of S was much smaller than that of Cl, the concentration of S was similar to that of Cl. This was due to the difference in the transmission factor of the 25 μm Teflon filter at the S and Cl fluorescence energies as shown in Table 4.6.

Note that the intensity of the escape peak in the CIS data was lower than that in the HP/Toshiba data because of the lower intensity of the scattered primary x-ray peak. The lower scattered x-ray intensity was due to the narrower band pass of the multilayers used for the measurement of the CIS wafer.

These contamination levels originated from the standard wafer cleaning process in CIS (Table 4.7). The CIS standard wafer cleaning was performed using a "diffusion wet bench" with SPM, SC2 and DHF solutions. Note that the SPM is used for removing organic materials, while the SC2 is used for removing particles on the wafer surfaces and DHF is used for etching the surface oxide [20], [23].

We concluded that the S and Cl were deposited on the wafer surface during the SPM (CIS process 1) and SC1 (CIS process 2), respectively. The Ca was deposited in the DHF solution (CIS process 3), in which the Ca impurity exists in the form of CaF_2[23]. Furthermore, the Cu was not removed completely by the DHF process, in which Cu is easily deposited on the bare Si wafer surface [20].

However, these contamination were removed by the HP/Toshiba process using DHF, SC2, and FPM in the wafer cleaning process. Note that SC2 is a standard solution used for removing metal contamination. An important process in the HP/Toshiba cleaning was the use of FPM solution in the final process. The Cu in the HP/Toshiba wafer was effectively removed by use of the FPM solution, in which the Cu on the Si wafer surface is easily ionized due to H_2O_2 . We should note that the HP/Toshiba cleaning process is used in the laboratory and not a manufacturing process.

From the CIS clean wafer, a Cu contamination with the concentration of $7x10^9$ atoms/cm^2 were clearly detected. In order to develop smaller dimension devices would require ultra clean wafer surfaces, the residual Cu contamination in CIS must be removed by the use of advanced wafer cleaning processes. Our SR TXRF system made it possible to study the wafer cleaning process in CIS with high sensitivities beyond the limit of conventional TXRF.

4.3 3-d Transition Metal Analysis on GaAs Wafer Surfaces

This section shows the results of preliminary experiments for GaAs SR TXRF with a focus on describing the differences between the GaAs and Si analysis.

SR TXRF spectra taken from a clean GaAs wafer are shown in Fig. 4.15. The experimental configuration used was the same as the one used for the 3-d transition metal analysis on Si wafers (Fig. 3.1). We took data using incident x-ray energies of 9.4 keV and 10 keV with 300 sec. measurement times at an incidence angle of 0.08 deg. A 25 μm Teflon filter was placed in front of the detector, which significantly absorbed lower energy x-rays such as the Ga and As L fluorescence signals.

We selected incident x-ray energies below the K absorption-edges of Ga (at 10.37 keV) and As (at 11.87 keV) in order to suppress the Ga and As K fluorescence signals. Otherwise, the K fluorescence signals of GaAs would dominate the spectra resulting in the saturation of the detector. The energy of the incident beam was tuned by use of the double multilayer monochromator.

The common features in the two spectra in Fig. 4.15 were the fluorescence lines of Ga As, Si (at 1.74 keV), S (at 2.31 keV), Cl (at 2.62 keV), and Ca (at 3.69 keV). The fluorescence x-ray energies of Ga and As are shown in Tab. 4.8. Note that the scattered x-ray peak created by the 9.4 keV incident x-ray beam overlapped with the Ga Kα peak (9.25 keV). In addition, the Ga L and As L peaks, and the Ga Kβ and As Kα peaks overlapped with each other, respectively.

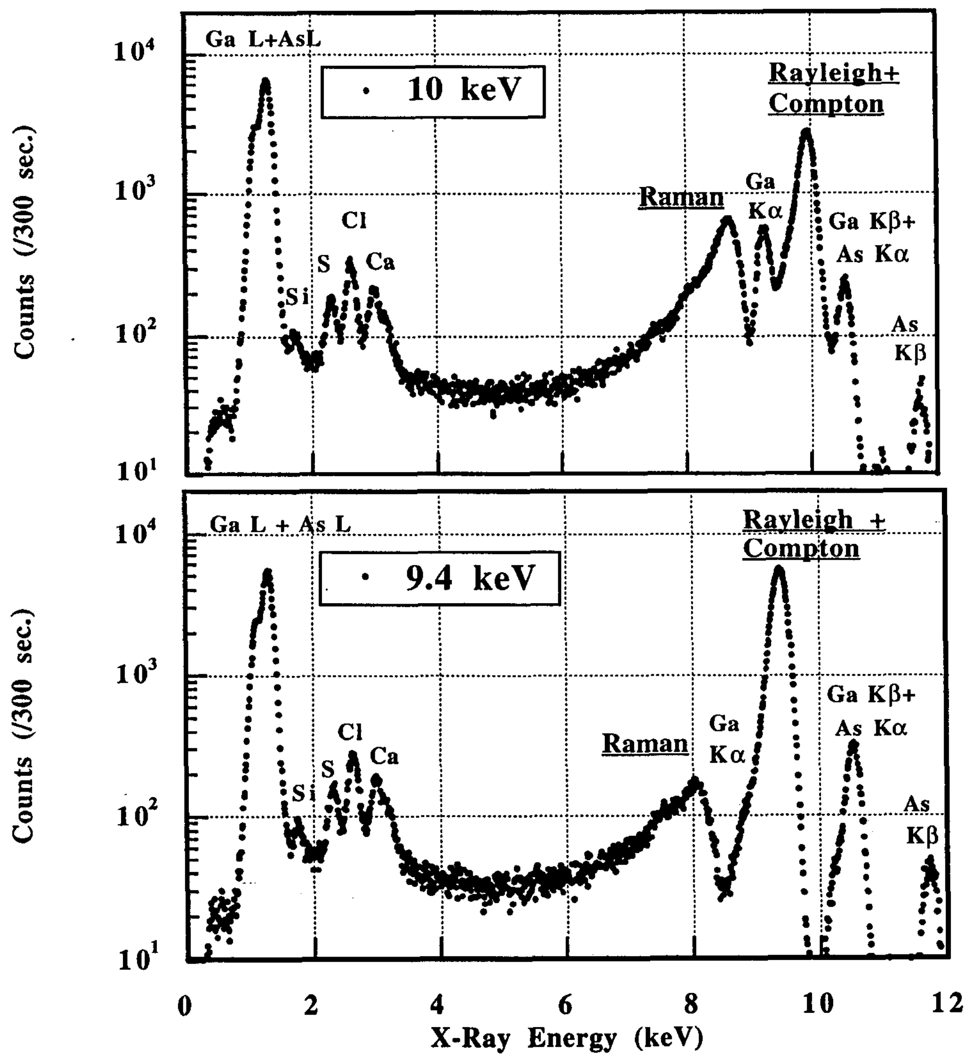

Fig. 4.15 SR TXRF spectra of a GaAs wafer taken using the incident x-rays with the energies of 9.4 keV (bottom) and 10 keV (top).

Table 4.8 Fluorescence x-ray energies of Ga and As.

element	L β (keV)	L edge (keV)	Kα (keV)	Kβ (keV)	K edge (keV)
Ga	1.12	1.14	9.25	10.26	10.37
As	1.32	1.36	10.54	11.73	11.87

The Ga and As K fluorescence signals were created by the high energy components in the incident beam such as the higher harmonic peaks from the multilayer. On the other hand, the Si, S, Cl, and Ca signals were created from unintentional contaminants on the wafer surface. The intensities of the fluorescence signals were almost same in these two spectra because the fluorescence cross-sections with the 9.4 keV and 10 keV x-rays are similar [24].

However, we did observe significant differences in the backgrounds of the two spectra. First, the continuous background between 8 keV and 9 keV increased in the 10 keV spectrum. This was due to the increase in the x-ray Raman scattering. The x-ray Raman scattering is an inelastic scattering process created when the incident x-ray energy is close to but less than an inner-shell absorption edge of material [25], [26].

The x-ray Raman scattering creates a characteristic profile up to an energy equal to the incident x-ray energy minus an outer-shell absorption-edge (1.14 keV for Ga L_{II} edge). In Figs 4.15, the x-ray Raman continuous backgrounds were generated up to 8.46 keV (= 9.6 keV-1.14 keV) in the 9.4 keV spectrum and up to 8.86 keV (= 10 keV -1.14 keV) in the 10 keV spectrum. The intensity of the x-ray Raman scattering increases as the incident X-ray energy approaches the inner-shell absorption edge.

The second difference in the backgrounds was a reduction in the intensity of the scattered x-rays between 9.4 keV and 10 keV, which were made up of the Rayleigh scattering and Compton scattering of the x-rays in the primary incident beam. The scattered x-ray peak generated by the 10 keV incident beam was lower than the scattering peak by the 9.4 keV incident beam by about a factor of 2.

The decrease in the scattered x-ray intensity was due to anomalous dispersion. Anomalous dispersion is a phenomenon in which the atomic form factor varies as a function of the incident x-ray energy. Quantum mechanically, anomalous dispersion is described as a phenomenon related to the first order matrix element, while the x-ray Raman scattering is related to the second-order matrix element. The anomalous dispersion reduces the intensity of elastically scattered x-rays when the incident x-ray energy is close to but less than an absorption edge, while the intensity of the x-ray Raman scattering is increased. We will not discuss the anomalous dispersion further because it does not affect the sensitivity of GaAs SR TXRF. For anomalous dispersion, see reference [27].

In order to determine the sensitivity of GaAs SR TXRF, a standard GaAs wafer with $5x10^{12}$ atoms/cm^2 of Ti and $3.5x10^{12}$ atoms/cm^2 of Ni was measured (Fig. 4.16). The data were taken at BL 6-2 at an angle incidence of 0.08 deg using a 9.5 keV incident x-ray beam. A 25 μm Teflon filter was placed in front of the Si (Li) detector to reduce the low energy x-rays including the Ga and As L x-rays, which were generated from the GaAs substrate.

In addition to the fluorescence lines of Ti, Ni, Ga, and As, the fluorescence lines of Si, S, Cl, K, Ca, and Fe were present in Fig. 4.16. They were generated from unintentional impurities. The Rayleigh and Compton scattered x-rays from the primary incident beam (9.5 keV) were overlapped with the Ga Kα peak (9.25 keV). The x-ray Raman scattering x-rays created the continuous background under the Ni fluorescence signals.

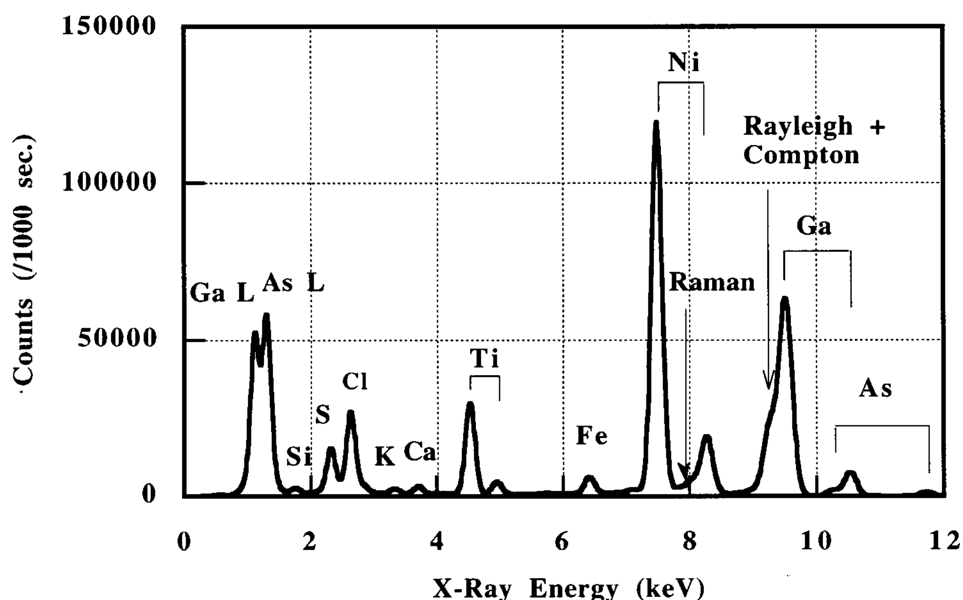

Fig. 4.16 A SR TXRF spectrum taken from a standard GaAs wafer with $5x10^{12}$ atoms/cm^2 of Ti and $3.5x10^{12}$ atoms/cm^2 of Ni.

From Fig. 4.16, the MDLs for Ti and Ni on the GaAs wafer were found to be $5x10^9$ atoms/cm^2 and $1x10^9$ atoms/cm^2, respectively. The MDL of Ti and Ni on the GaAs wafer with SR TXRF were better than the MDLs measured by Motorola with conventional TXRF, which were $5x10^{10}$ atoms/cm^2 and $2x10^{10}$ atoms/cm^2, respectively. The improvement of the MDLs by a factor of about 10 was achieved due to the high incident flux of the synchrotron radiation.

However, the MDL of the Ni on the GaAs wafer with SR TXRF was worse than the MDL of Ni on the Si wafer ($3x10^8$ atoms/cm^2) by a factor of about 3.6 [4]. This was because the MDL of Ni on the GaAs wafer was limited by the high x-ray Raman scattering backgrounds. The negative impact of the x-ray Raman scattering on the MDLs were easily

seen by comparing the signal-to-background ratio between the GaAs data and the Si data shown in Tab. 4.9.

From Tab. 4.9, it was found that the background intensity under the Ni signal peak in the GaAs data was larger than that in the Si data by a factor of about 13, while the Ni signals normalized to the Ni concentration were almost same in these data. The continuous background in the GaAs spectrum was increased by the x-ray Raman scattering, which was small in the Si spectrum because the energy of the incident beam (10.6 keV) was much larger than the Si L absorption edge (1.84 keV).

The x-ray Raman scattering appeared in the GaAs SR TXRF spectra when the incident x-ray beam energy was close to but less than the absorption edge of constituent elements of the substrate. The x-ray Raman scattering becomes the dominant background in the 3-d transition metal analysis on GaAs wafers. In the next section, we will show the results of the Al analysis on Si wafers as another example of SR TXRF measurements in which the x-ray Raman scattering becomes the dominant background.

Table 4.9 Comparison of signals and backgrounds from Si and GaAs wafers.

wafer	Ni (atoms/cm^2)	signal	signal (scaled)	background	MDL(atoms/cm^2)
Si	1.00E+11	58890	5.89E-07	5144	4E+08
GaAs	3.50E+12	2099493	6.00E-07	70651	1E+09

Note : The Ni signals are scaled by the Ni concentration.

4.4 Al Analysis on Si Wafer Surfaces

This section shows the experimental results of the analysis of Al on Si wafers. The analysis of Al on Si wafers is difficult because of the small energy difference between the Al (1.49 keV) and Si (1.74 keV) fluorescence signals and the fact that the Si substrate signal is much stronger than the signal from the Al contamination.

4.4.1 MDL with Standard Optical Configuration.

First, we estimated the MDL of Al on Si wafers with the standard optical configuration for the 3-d transition metal analysis [2]. The incident beam energy used for the standard optical configuration on BL 6-2 was 10.6 keV and the data was taken with a 25 μm Teflon filter placed in front of the Si (Li) detector to reduce the Si fluorescence signal intensity.

The spectrum of the Si fluorescence taken from a clean wafer is shown in Fig. 4.17. The vertical axis shows counts per 1000 sec. and the horizontal axis is energy between 0 and 2.5 keV. From this spectrum, it was found that the Al fluorescence signal peak (at 1.49 keV) would be overlapped with the low energy tail of the Si fluorescence signal peak (at 1.74 keV). The background intensity under the Al signal peak would be about 1/100 of the Si fluorescence signal intensity.

With this background intensity and the Al fluorescence signal intensity calculated by use of the parameters in Table 4.10, the MDL of Al in the standard optical configuration was estimated to be 1×10^{14} atoms/cm^2, which is only 1/10 of the areal density of Si (about 1×10^{15} atoms/cm^2).

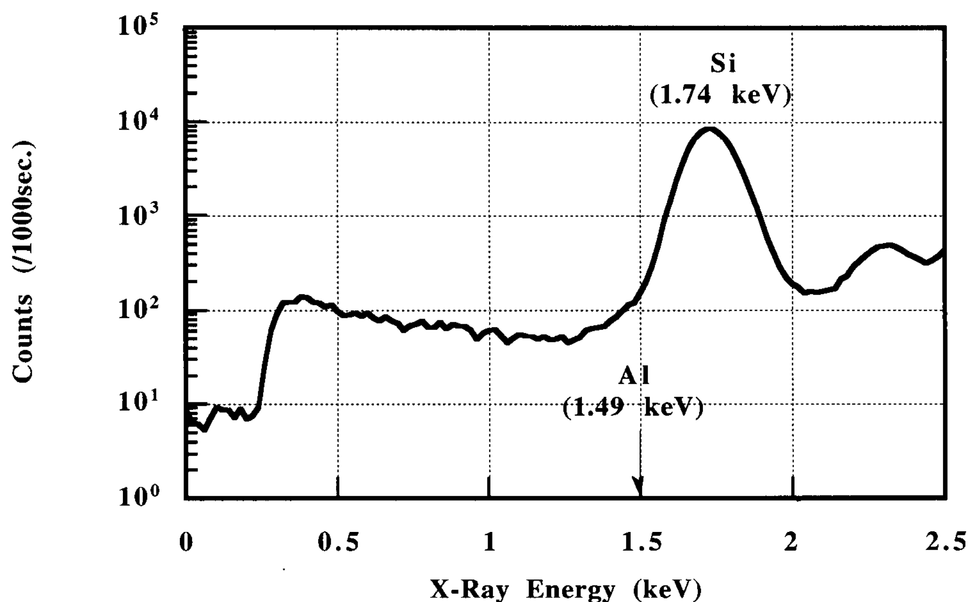

Fig. 4.17 The Si fluorescence signals generated by the standard 10.6 keV x-ray beam.

Table 4.10 Fluorescence signals of Al and Si signals of Al and Si.

element	Kα (keV)	K–edge(keV)	σ (barns)	ω	transmission
Al	1.49	1.56	1151	0.0357	7.50E-05
Si	1.74	1.84	1570	0.047	1.95E-03

Note that, although a 25 μm Teflon filter makes the count-rates manageable, the filter does not help to improve the MDL of Al because the Teflon filters would equally attenuate the Al fluorescence signals. Even if the Teflon filter could no longer be used and the detector could handle the signals with higher count-rate, the MDL would be improved only to 4×10^{12} atoms/cm^2 with the optical configuration on BL 6-2.

4.4.2 Energy Tunability

Because the higher incident flux did not improve the MDL of Al on Si wafers, the tunable nature of synchrotron radiation was exploited to obtain an incident beam with an energy below that of the Si K absorption edge (at 1.84 keV) and higher than that of the Al K edge (at 1.56 keV). The well tuned incident beam would greatly reduce the Si fluorescence signals and increase the Al fluorescence signals.

The Al K shell photoionization cross-section as a function of x-ray energy is shown in Fig. 4.18 [14]. The horizontal axis of Fig. 4.18 is x-ray energy and the vertical axis is the photoionization cross-section in unit of barns (10^{-24} cm^2). By the use of x-ray beam with an energy closer but higher than that of the Al K edge, the cross-section could be increased about 200 times over the cross-section that obtained with the standard 10.6 keV x-ray beam.

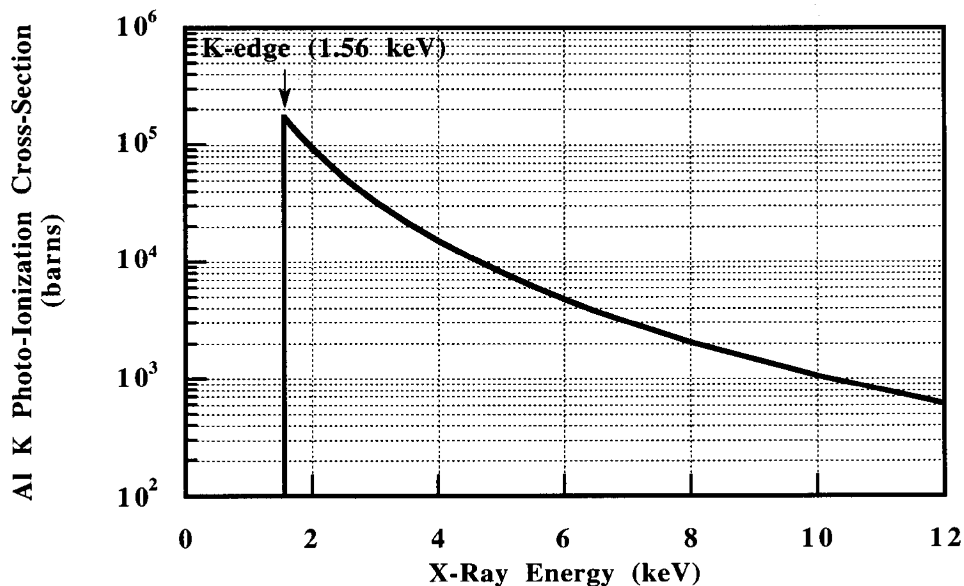

Fig. 4.18 Al K shell photoionization cross-section as a function of x-ray energy.

In this study, two optical configurations were used to measure the Al on Si wafer surfaces. As shown in Ch. 3, one configuration was the BL 3-4 bending magnet beam line with a Si absorption filter while the other configuration was the BL 6-2 wiggler beam line with the double multilayer monochromator and x-ray mirrors in addition to the Si filter.

In order to check the incident photon flux obtained from the BL 3-4 optical configuration, a spectrum was taken from a Mylar film (Fig. 4.19) [1]. The Mylar™ is a thin film made of poly ethylene terephthalate ($(-OCH_2CH_2OCOC_6H_4CO-)_N$). In Fig. 4.19, an oxygen K fluorescence signal peak generated from the Mylar film was present at 0.5 keV. In addition, two scattered x-ray peaks were present at 1.84 keV and at 2.6 keV.

The scattered x-ray peaks were generated by the incident photon flux defined by the x-ray mirror reflectivity and the transmission of the Si filter as shown in Fig. 4.20. At first, the continuous spectrum of the synchrotron radiation on BL 3-4 was defined by the x-ray mirror on BL 3-4 with a high energy cut-off of 3 keV. Because of imperfections and absorption by the mirror, the high energy cutoff at 3 keV was rounded as schematically shown in Fig. 4.20.

The flux defined by the mirror then was absorbed by a Si filter. The degree of absorption is represented by the transmission factor in Fig. 4.20. The transmission factor changes significantly around the Si K absorption edge (1.84 keV) because of the significant change in the photoionization cross-section around the absorption edge. The resulting incident photon flux is determined by the product of the mirror reflectivity and the transmission factor of the Si filter, which generated the two scattered x-ray peaks in Fig. 4.19.

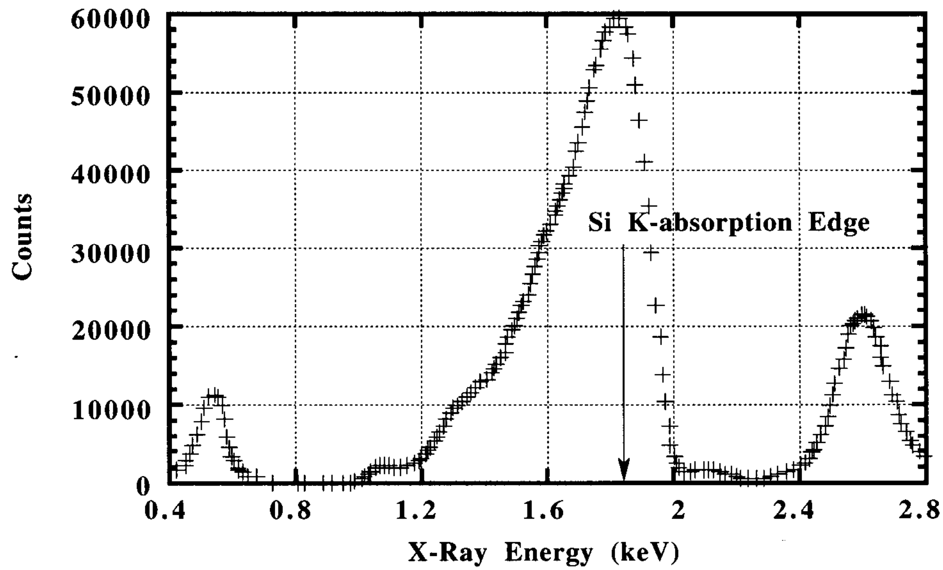

Fig. 4.19 SR spectrum taken from a Mylar film on BL 3-4.

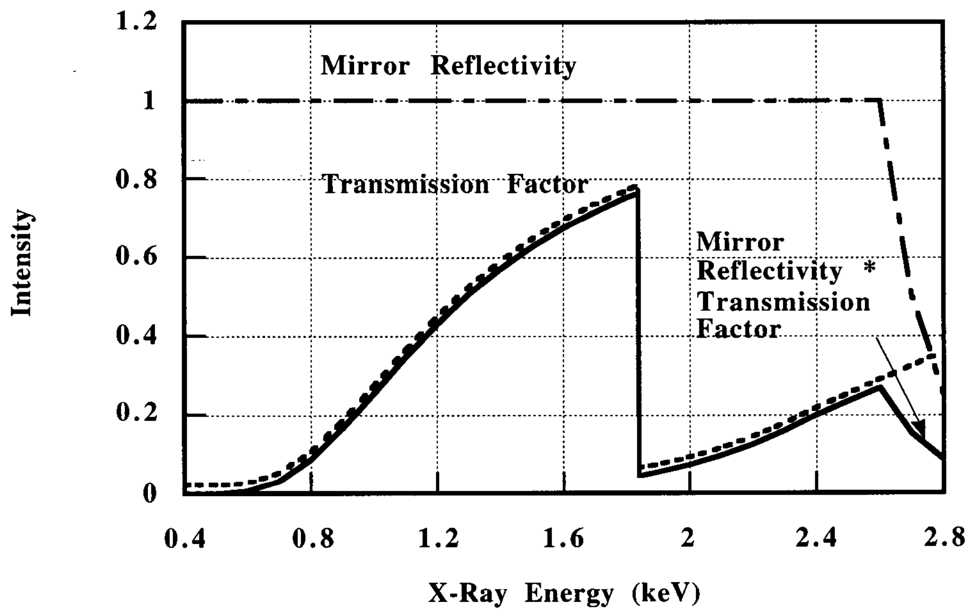

Fig. 4.20 The modeling of the tailored SR spectrum on BL 3-4.

The scattered x-ray peak below the Si K absorption edge in Fig. 4.19 was generated by the incident flux defined by the transmission factor of the Si filter. On the other hand, the incident flux which generated the scattered x-ray peak at 2.6 keV was defined by the product of the transmission factor and the mirror reflectivity. The low energy side of the incident photon flux was defined by the transmission factor, while the high energy side was defined by the mirror cutoff.

The incident flux between 1.5 keV and 1.8 keV excites Al without exciting Si. However, the incident flux around 2.6 keV excites both Al and Si. For the measurements on BL 3-4, Si fluorescence backgrounds are expected due to the higher energies in the incident flux.

The optical configuration on BL 6-2 was designed in order to reduce the higher energies in the incident flux which were not eliminated on BL 3-4. By use of the monochromator and post monochromator x-ray mirror, the incident flux above the Si K absorption edge was greatly reduced on BL 6-2. Since BL 6-2 uses a wiggler source, the raw photon flux is more than 50 times higher than BL 3-4, therefore, it is possible to use a multilayer monochromator and still have high flux.

In order to compare the spectra on BL 3-4 and BL 6-2, data were taken from the same sample consisting of 4 Å of Al on Si wafer prepared by Aracor (Fig. 4.21). Data on BL 6-2 was taken at an angle of incidence of 0.5 deg., while data on BL 3-4 was taken at 0.1 deg. For reference the critical angle for 1.8 keV x-ray beam is about 0.86 deg. It should be pointed out that the angle of incidence on BL 3-4 had to be set smaller than that on BL 6-2 to reduce the Si fluorescence signal counts. The smaller incident angle on BL 3-4 reduced the overall count-rate to prevent saturation of the detector.

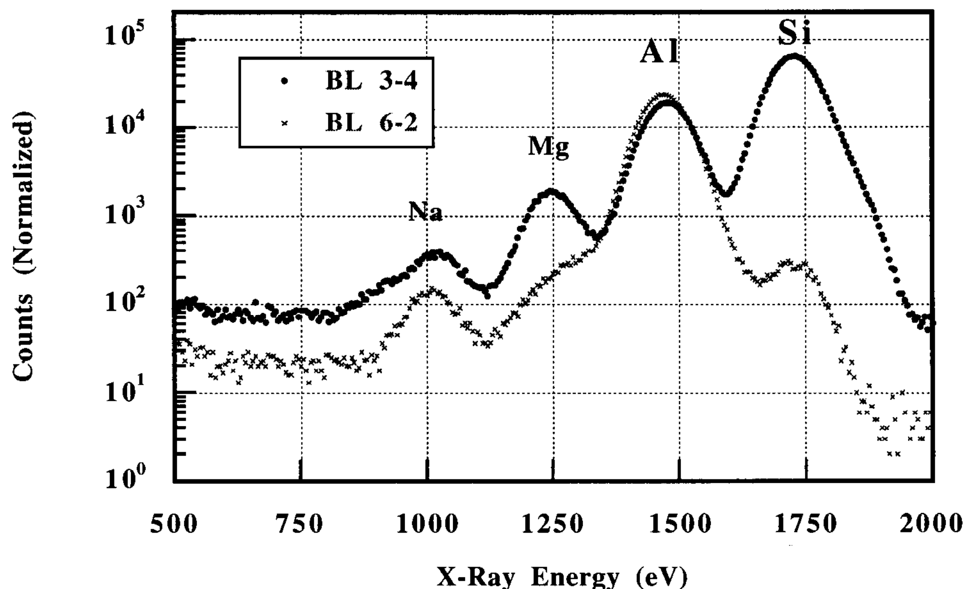

Fig. 4.21 SR TXRF spectra taken from 4Å of Al on a Si wafer. Data taken using BL 3-4 and BL 6-2. The spectra were scaled using the Al fluorescence signal counts.

The Al fluorescence signal counts were used to normalize these spectra. Because the ratio of the Al and Si fluorescence signals does not change very much at incident angles well below the critical angle, this normalization made it possible to compare the Si fluorescence signals generated from the different optical configurations.

In Fig. 4.21, the fluorescence signal peaks of Na, Mg, Al, and Si were present. The Si signals were generated from the Si wafer and the Al was generated from the intentional contamination. On the other hand, Na and Mg were unintentional contaminants generated during the wafer preparation or wafer handing.

From Fig. 4.21, it was found that the intensity of the Si fluorescence signals on BL 6-2 was about 200 times smaller than that on BL 3-4. This result indicated that the optical

configuration on BL 6-2 with the double multilayer monochromator and post monochromator x-ray mirror successfully reduced the incident flux with energies above the Si K absorption edge.

4.4.3 MDLs of Al on Si Wafer Surfaces

The high intensity of the Al signals in Fig. 4.21 allowed us to effectively compare the Si fluorescence signals between data taken on BL 6-2 and BL 3-4. However, in order to find out the MDL of Al, it was necessary to take data from standard wafers with lower levels of Al, which would clearly show the backgrounds under the Al signals.

First, the MDL of Al on BL 3-4 was obtained from the data taken from a standard wafer with 7×10^{11} atoms/cm^2 of Al prepared by Intel using a dipping method (Fig. 4.22). The concentration of the Al on the wafer surface was checked by Intel using ICPMS [28]. In Fig 4.22, the dominant background under the Al signals was made up of the low energy tail of the Si fluorescence signals and the MDL of Al was found to be 1×10^{11} atoms/cm^2.

Next, the MDL of Al on BL 6-4 was obtained from the data taken from a standard Si wafer with 8×10^{12} atoms/cm^2 Al on BL 6-2 (Fig. 4.23). The standard wafer was supplied by an HP / Toshiba collaboration and the concentration of Al was checked with WSA/ICPMS [14]. The energy of the incident x-ray beam used for the measurement was 1740 eV.

There were three peaks present in Fig. 4.23. The left peak at 1490 eV was the Al fluorescence signal peak. The right peak at 1740 eV was the overlap of the Si fluorescence signal peak and elastically scattered x-ray peak.

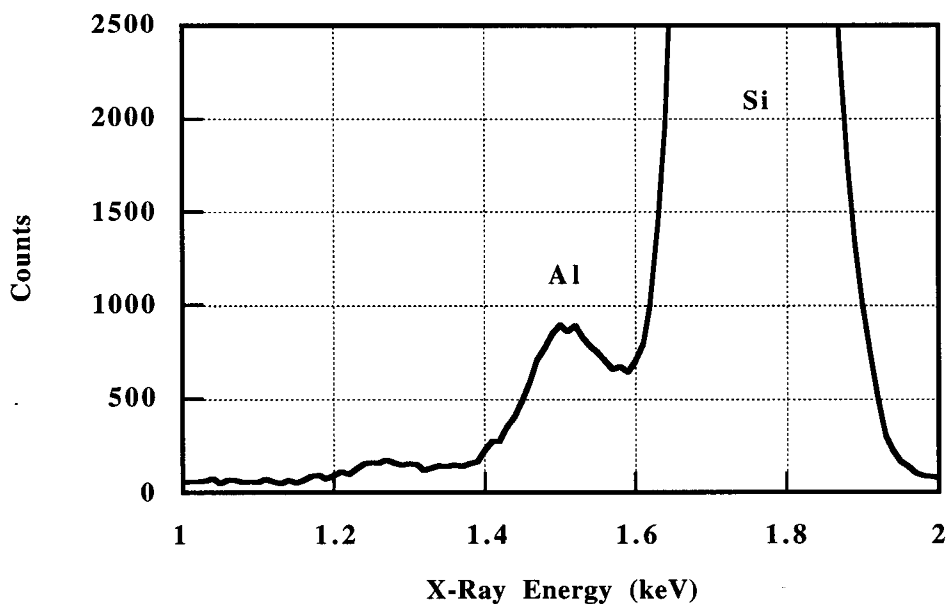

Fig. 4.22 A spectrum taken on BL 3-4 from a Si wafer with 7×10^{11} atoms/cm^2 of Al.

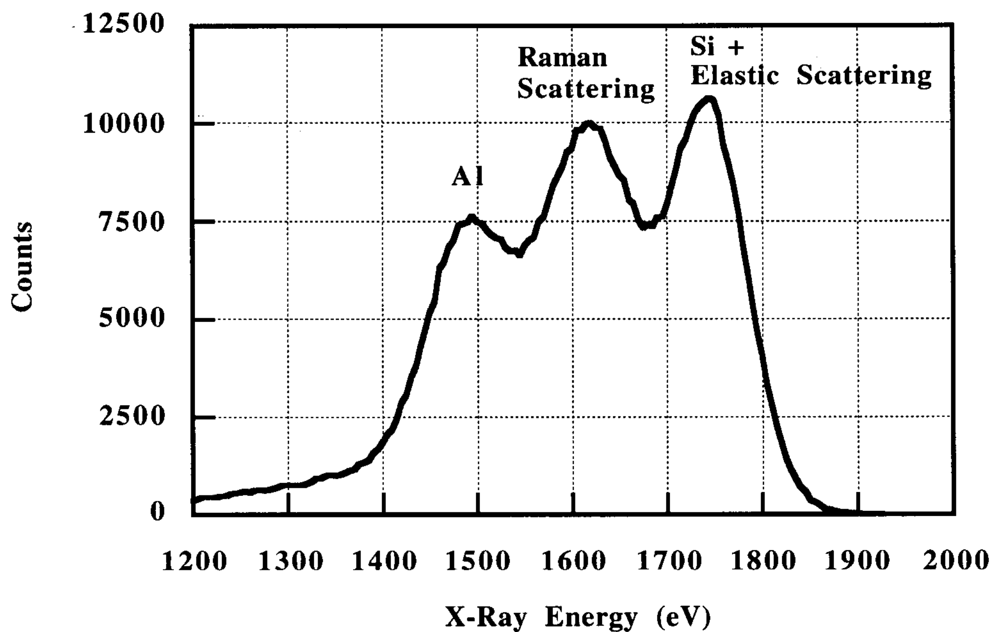

Fig. 4.23 A spectrum taken on BL 6-2 from a Si standard wafer with 8×10^{12} atoms/cm^2 of Al. The incident x-ray energy was 1740 eV.

The peak between the Al and Si fluorescence peaks was attributed to the x-ray Raman effect. The results of Fig. 4.22 showed that, although the Si fluorescence signals were greatly reduced on BL 6-2, the x-ray Raman scattering peaks then appeared as the dominant background x-rays which limited the SR TXRF sensitivity for Al. The identification of the x-ray Raman peak will be discussed in Ch. 6.

From Fig. 4.23, the MDL of SR TXRF for Al on a Si wafer was found to be 5×10^{10} atoms/cm^2, which was better than the MDL on BL 3-4 (1×10^{11} atoms/cm^2). The improvement of the MDL on BL 6-2 was due to the reduction of the Si fluorescence background under the Al signal peak. As a result, although the MDL of Al on BL 3-4 was limited by the Si fluorescence signals, the MDL of Al on BL 6-2 was limited by the high intensity of the x-ray Raman background.

4.4.4 Standard Wafers

This section discusses the difference in the MDLs of Al obtained from standard wafers prepared by the dipping and droplet methods. The dipping method is a standard preparation method in which standard wafers are dipped into the solution containing the standard elements, as shown in Ch. 3. By dipping, the standard elements are atomically dispersed under Si wafer surfaces, as shown in Fig. 4.24 (a) [15], [20], [29].

On the other hand, the droplet method is another standard preparation method in which the standard elements are deposited by dropping a droplet containing the standard elements on the wafer surface. It is known that the standard elements prepared by the droplet method exist as particulates on the wafer surface, as shown in Fig. 4.24 (b) [15], [20], [29].

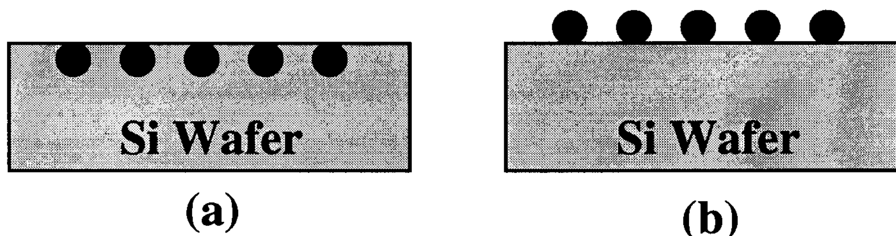

Fig. 4.24 (a) The elements on a Si wafer surface. (b) The elements near a wafer surface.

Spectra taken using BL 3-4 from the standard wafers prepared by these methods are shown in Fig. 4.25. Fig. 4.25 (top) was taken from a standard wafer prepared using the dipping method by Intel (with Dhanda in the Helms group at Stanford), which is same as Fig. 4.21. Fig. 4.25 (bottom) was taken from a standard wafer prepared using the droplet method by Intel (with Madden). The concentrations of Al were 7×10^{11} atoms/cm^2 (dipping) and 1×10^{12} atoms/cm^2 (droplet), which were checked with ICPMS by Intel.

Both data were taken with a 1000 sec. measurement time. However, the data for the dipped wafer was taken at an angle of incidence of 0.1 deg., while data for the droplet wafer was taken at an angle of incidence of 0.5 deg. The difference in the angles of incidence resulted in the difference in the intensity of the data as shown in vertical scale of Fig. 4.25.

Fig. 4.25 showed that, although the Al concentration of the dipped wafer (7×10^{11} atoms/cm^2) was close to that on the droplet wafer (1×10^{12} atoms/cm^2), the signal-to-background (S/B) ratio of the dipped wafer (about 0.9) was much lower than that of the droplet wafer (about 4.6). As a result, the MDL of Al prepared using the dipping method was found to be 1×10^{11} atoms/cm^2, while the MDL prepared using the droplet method was 1×10^{10} atoms/cm^2.

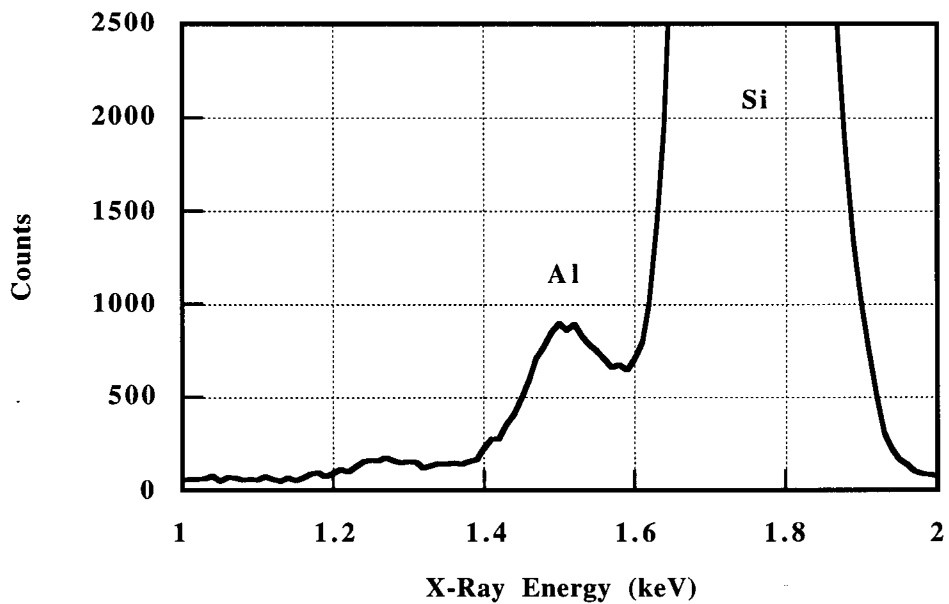

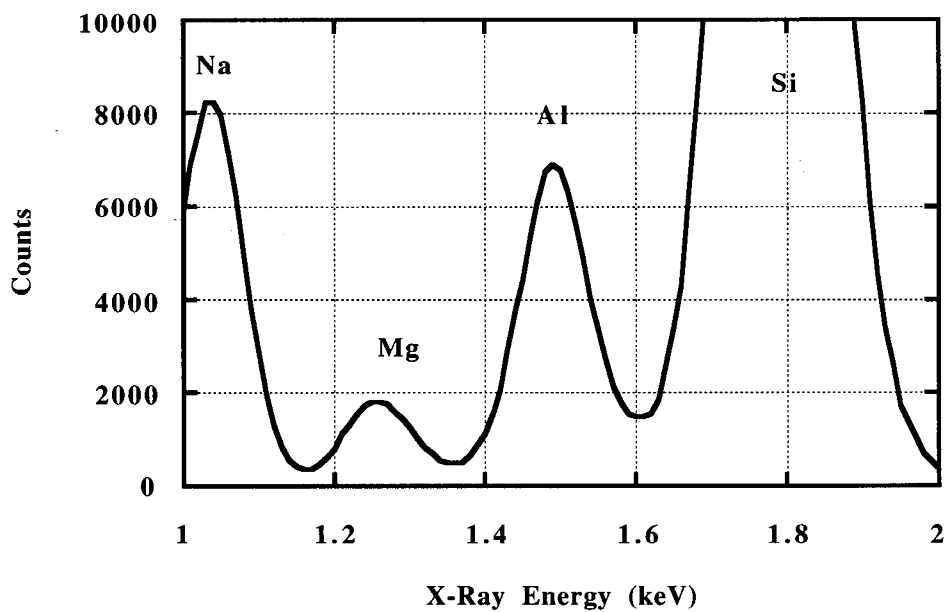

Fig. 4.25 SR TXRF spectra taken on BL 3-4 from a Si standard wafer with 7×10^{11} atoms/cm^2 of Al prepared by the dipping method (top) and a Si standard wafer with 1×10^{12} atoms/cm^2 of Al prepared by the droplet method (bottom).

Note that the MDL for the droplet method on BL 3-4 was found to be even better than the MDL obtained from the wafers prepared by a different dipping method on BL 6-2 ($5x10^{10}$ atoms/cm^2), in which the background due to the Si fluorescence signals was greatly reduced, while the background on BL 3-4 was still made up of the Si fluorescence signals.

4.5 Conclusions

This chapter showed experimental results for SR TXRF. Data were taken with the optimum optical configurations to reduce the background x-ray components. The scattered x-rays of the primary incident beam were reduced by setting a Si (Li) detector along the polarization vector of the incident beam. This also reduced the detector incomplete charge collection backgrounds. Furthermore, the scattered x-rays consisting of the low energy tail of the primary incident beam and their diffraction signals were greatly reduced by the combination of absorption filters and the double multilayer monochromator.

Using the optimum optical configuration and standard wafers, we extrapolated the MDLs of our SR TXRF system (Table. 4.11). First, the MDL for Ni on the Si wafer was found to be $3x10^8$ atoms/cm^2, which was about 20 times better than the MDL of rotating anode TXRF, $5x10^9$ atoms/cm^2. This true detection limit was achieved by use of the spurious-signal-free Si (Li) detectors.

The spurious-signal-free Si (Li) detector made it possible to perform high sensitivity SR TXRF measurements. Our SR TXRF system was capable of measuring smaller amounts of metal contamination, which cannot be measured by conventional TXRF system, with the sensitivity expected for the smaller dimension ULSI to be developed in the first years of 21st century.

Furthermore, we measured Ni on a GaAs wafer and Al on a Si wafer. The analysis of these elements were more difficult than the 3-d transition metal analysis on a Si wafer because the substrate fluorescence lines interfered with the fluorescence signals of interest. We eliminated the substrate fluorescence background x-rays by use of the incident beam with a well-tuned energy. Using a well-tuned incident beam, the MDLs for the Ni on GaAs and Al on Si were found to be 1×10^9 atoms/cm^2 and 5×10^{10} atoms/cm^2, respectively. The MDLs for these measurements were limited by the x-ray Raman scattering backgrounds.

Table 4.11 The minimum detection limits of TXRF (atoms/cm^2).

method	Ni on Si	Ni on GaAs	Al on Si
SR TXRF	3E+08	1E+09	5E+10
conventional TXRF	5E+09	2E+10	1E12~1E13

4.6 References

1. S. Brennan, W. Tompkins, N. Takaura, P. Pianetta, S.S. Laderman, A. Fischer-Colbrie, J.B. Kortright, M.C. Madden, D.C. Wherry, Nucl. Instrum. Meth., **A347**, 417(1994).
2. P. Pianetta, N. Takaura, S. Brennan, W. Tompkins, S.S. Laderman, A. Fisher-Colbrie, A. Shimazaki, K. Miyazaki, M. Madden, D.C. Wherry, J.B. Kortright,, SLAC-PUB-6612, SLAC/SSRL-0086, LBL-36011, July (1994).
3. P. Pianetta, N. Takaura, S. Brennan, W. Tompkins, S.S. Laderman, A. Fisher-Colbrie, A. Shimazaki, K. Miyazaki, M. Madden, D.C. Wherry, J.B. Kortright, Rev. Sci. Instrum. **66** 2, (1995).
4. S.S. Laderman, A. Fisher-Colbrie, A. Shimazaki, K. Miyazaki, S. Brennan, N. Takaura, P. Pianetta, J.B. Kortright, Analytical Sciences, **11**, 515 (1995).

5. N. Takaura, S. Brennan, P. Pianetta, A. Fischer-Colbrie, J.B. Kortright, D.C. Wherry, K. Miyazaki, A. Shimazaki, Advances in X-ray Chemical Analysis Japan, **26s**, 113 (1994).

6. B.E. Warren, *X-RAY DIFFRACTION* , Chapter 1, 1969, Dover.

7. P.P. Kane, Physics Repors 218, **2**, 67 (1992).

8. J.L. Campbell, J.-X. Wang, W.J. Teesdale, Nucl. Instr. Meth. **B43** 490 (1989).

9. F.S. Goulding and J.M. Jacklevic, Nucl. Instrum. Meth. **142**, 323 (1977).

10. E.C. Montenegro, G.B. Baptista, and P.W.E.P. Duarte, Atomic Data and Nuclear Data Tables, **22**, 2, 131 (1978).

11. S. S. Laderman, Bull. Am. Phys. Soc. **39**, 514 (1994).

12. P. Bertin, *Principles and Practice of X-ray Spectrometric Analysis*, 1975, New York : Plenum.

13. SEMATECH, Technology Transfer #94102578A-TR, 15.

14. A. Shimazaki, Proc. ECS, Defects in Silicon II, 47 (1991).

15. S. Laderman, P. Pianetta-Chairmen, SLAC-415, SLAC/SSRL-0009, *proceedings of the workshop on applications of synchrotron radiation to trace impurity analysis for advanced silicon processing* ,1992.

16. K. Yakushiji, S. Ohkawa, A. Yoshinaga, and J. Harada, Jpn. J. Appl. Physc., **32**, 1191 (1993).

17. H.P. Myers, *Introductory Solid State Physics* , Chapter 2, 1990, Taylor & Francis.

18. U. Bose and M. Hart, Appl. Phys. Letters **7**, 238 (1965).

19. B. K. Agarwal, *X-ray Spectroscopy* , Chapter 2, 1991, Berlin Heidelberg : Springer-Verlag.

20. C.R. Helms, H.-S. Park, S. Dhanda, P. Gupta, M. Tan, Processing of the Second International Symposium on Ultra-Clean Processing of Silicon Surfaces, Edited by M. Heyns, 205, 1994, Acco, Leuven / Amerstoort.

21. Y. Inagaki, K. Shima, H. Maezawa, Nucl. Instr. Meth. **B27** 353 (1987).

22. A. Fisher-Colbrie, et. al. to be published in MRS.

23. H. Ohmi et. al. : *Ultra Clean ULSI Technology* , 1995, Baifukan.

24. UCRL-50400,V.6.REV.3.

25. P.P. Kane, Physics Repors 218, **2**, 67 (1992).

26. J. M. Jaklevic, R.D. Giauque, and A.C. Thompson, Anal. Chem. (1988), 60, 482

27. B.K. Agawal, *X-Ray Spectroscopy,* Chapter 3, 1991, Berlin Heidelberg : Springer-Verlag.

28. Klaus Graff, *Metal Impurities in Silicon-Device Fabrication* , 135, 1994, Springer.

29. Advances in X-ray Chemical Analysis Japan (1994).

30. Rigaku Corp. (private communication).

5. THEORETICAL MODELING OF SR TXRF BACKGROUND

5.1 Introduction

It is important to understand the components of the SR TXRF background because they determine the ultimate sensitivity of this technique. Many researchers have investigated backgrounds observed in x-ray fluorescence spectroscopy [1], [2]. However, earlier analysis were not adequate to explain the experimental backgrounds relevant to TXRF. We build on the earlier work, which was focused on explaining bulk fluorescence data [3], [4], [5].

To analyze the backgrounds in SR TXRF, more sophisticated theoretical models are required. In this work, we have extended the earlier work to include effects particular to SR TXRF. An example of such effects is the so called "surface effect". Since the SR TXRF signals are created near the wafer surface, the surface effect can remarkably modify the backgrounds.

Sec. 5.2 will model the photoelectron bremsstrahlung created in SR TXRF. The photoelectron bremsstrahlung is a continuous radiation generated when high energy photoelectrons ionized from Si atoms are decelerated in a material. We will take into account a surface effect which changes the bremsstrahlung intensity.

Sec. 5.3 will consider the backgrounds generated from surface oxides. In TXRF, the surface oxide is not negligible because the penetration depth of incident x-ray is short

and may be comparable to the surface oxide thickness. We will show that the effect of the surface oxides on the Si fluorescence signals and scattered x-rays.

Sec. 5.4 will deal with the detector incomplete charge collection background, which is an inherent detector background whose intensity is proportional to the scattered x-ray intensity of the primary incident beam.

Sec. 5.5 will show the modeling results of the x-ray Raman scattering. We will show that the x-ray Raman scattering is the dominant continuous background when the energy of an incident beam is close to, but less than the absorption edge of substrate materials, which is the case for the Al analysis on Si wafer surfaces.

Finally, Sec. 5.6 will summarize this chapter with conclusions.

5.2 Photoelectron Bremsstrahlung

Photoelectron bremsstrahlung is a continuous radiation created when high energy photoelectrons travel through the Coulomb field of an atomic nucleus [6], [7]. In SR TXRF measurements, the photoelectrons are ionized from a Si K-shell (E_{edge} = 1.84 keV) by incident x-rays (typically with an energy of $h\upsilon$ = 10.6 keV) with the initial kinetic energy of 8.76 keV ($E_{initial} = h\upsilon - E_{edge}$).

The spectrum of photoelectron bremsstrahlung originates from a time variation in the electric field induced by fast moving photoelectrons. For the photoelectrons with the kinetic energy of 8.76 keV, the speed of the photoelectrons is about 15 % of the speed of light in vacuum and, therefore, the time variation of the electric field is close to a delta

function. Since the Fourier transform of a delta function is a continuous spectrum, the bremsstrahlung generated from the photoelectrons results in a continuous spectrum [8].

The maximum bremsstrahlung energy is equal to the initial photoelectron kinetic energy. Therefore, in the first order approximation, the profile of the photoelectron bremsstrahlung generated from a thin target is represented by a step function with the high energy limit equal to the initial photoelectron kinetic energy (Fig. 5.1).

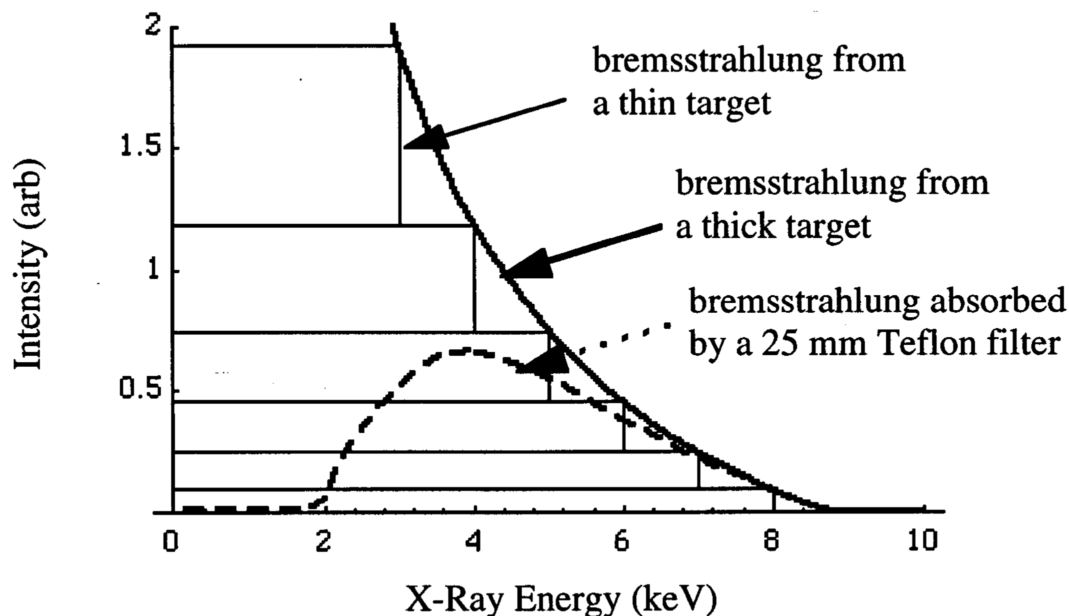

Fig. 5.1 Profiles of photoelectron bremsstrahlung radiation generated by Si K shell photoelectrons ionized by 10.6 keV x-rays. The maximum bremsstrahlung energy is the initial photoelectron energy of 8.76 keV. The reduction of the kinetic energy in each thin target is assumed to be 1 keV for simplicity.

The photoelectron bremsstrahlung generated from a thick target can be modeled by summing the bremsstrahlung generated from a number of virtual thin targets. In this case, however, the change in photoelectron kinetic energy needs to be taken into account since the photoelectrons reduce the kinetic energy in passing through the targets. This results in the corresponding reduction of the maximum bremsstrahlung energy. Therefore, the spectrum of the bremsstrahlung from a thick target becomes continuous, the intensity of which increases as the bremsstrahlung energy decreases, as shown in Fig. 5.1.

In practice, the low energy bremsstrahlung is attenuated by absorption filters. Because of the difference in the degree of absorption, the lower energy bremsstrahlung is attenuated more strongly than the higher energy bremsstrahlung. In Fig. 5.1, the profile of the bremsstrahlung absorbed by a 25 μm Teflon filter is shown by the dashed line, which has a maximum around 4 keV.

Note that the intensity of the bremsstrahlung from a thin target (the height of the step function) changes as a function of the photoelectron kinetic energy in Fig. 5.1. The formalism for calculating the bremsstrahlung intensity will be described in Sec. 5.2.3.

5.2.1 Photoemission in SR TXRF

The photoionization cross-section from the Si K-shell is about 10 times higher than that from Si L-shell (1.18 x 10^3 barns versus 0.12 x 10^3 barns), with a typical incident x-ray energy of 10.6 keV [9]. Therefore, when measuring a Si wafer, the photoelectrons are primary generated from the Si K-shell.

The angular distribution of the Si K-shell photoelectrons is shown in Fig. 5.2. According to the theory of photoemission, the angular distribution of K-shell

photoelectrons is represented by the p-orbital lobe whose axis is defined by the polarization vector [7]. In SR TXRF, the electric field (polarization vector) of the incident beam is set perpendicular to the wafer surface [2]. Therefore, the most of the photoelectrons are emitted perpendicular to the surface.

In addition, the photoelectrons are generated only near the wafer surface because the incident x-ray penetration depth is short (about 40 Å) [10]. This results in the escape of half of the photoelectrons out of the wafer.

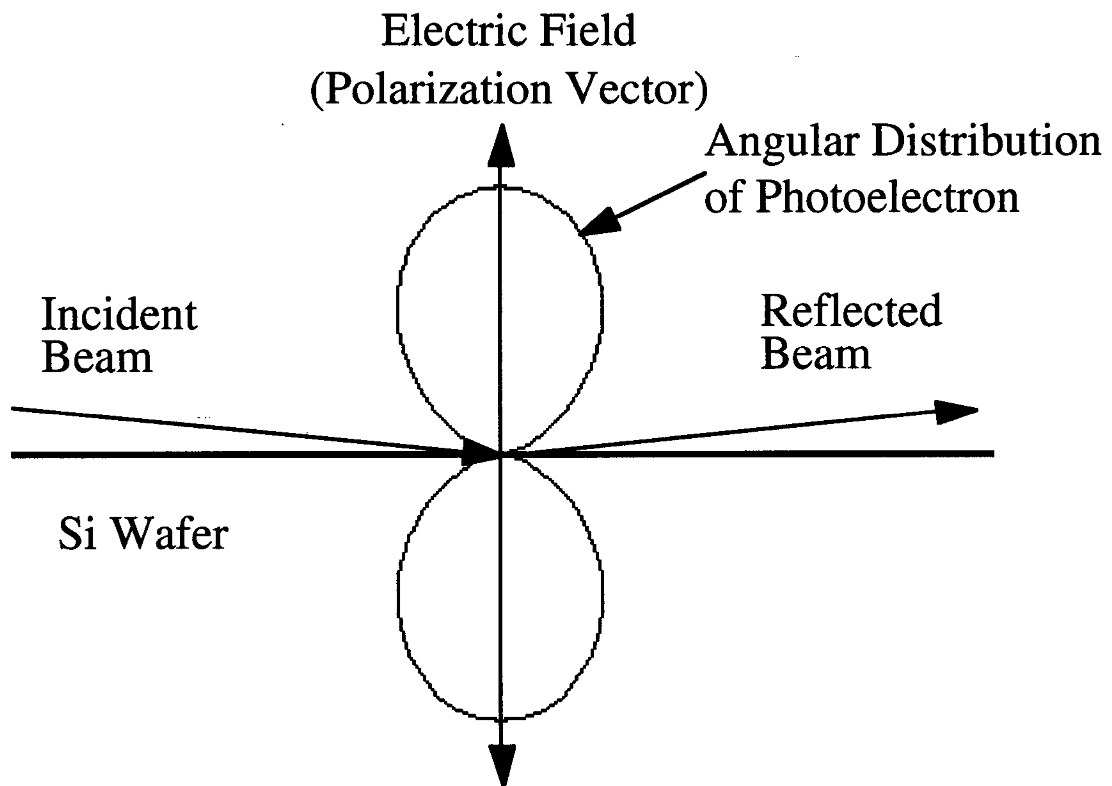

Fig. 5.2 The SR TXRF geometry in which the polarization vector is perpendicular to a Si wafer surface. The angular distribution of Si K-shell photoelectrons is shown as well.

The photoelectrons which have escaped from the sample do not generate bremsstrahlung in the wafer. This is an important characteristic of the bremsstrahlung observed in SR TXRF, the analytical expression of which will be discussed in Sec. 5.2.5.

5.2.2 Angular Distribution of Bremsstrahlung

The angular distribution of the bremsstrahlung generated by the photoelectrons emitted perpendicular to a Si wafer surface is shown in Fig. 5.3. This angular distribution was calculated for the 5.5 keV bremsstrahlung generated from the electrons with the kinetic energy of 8.76 keV in an atomic field of Si using the formalism by Pratt et. al [11],[12].

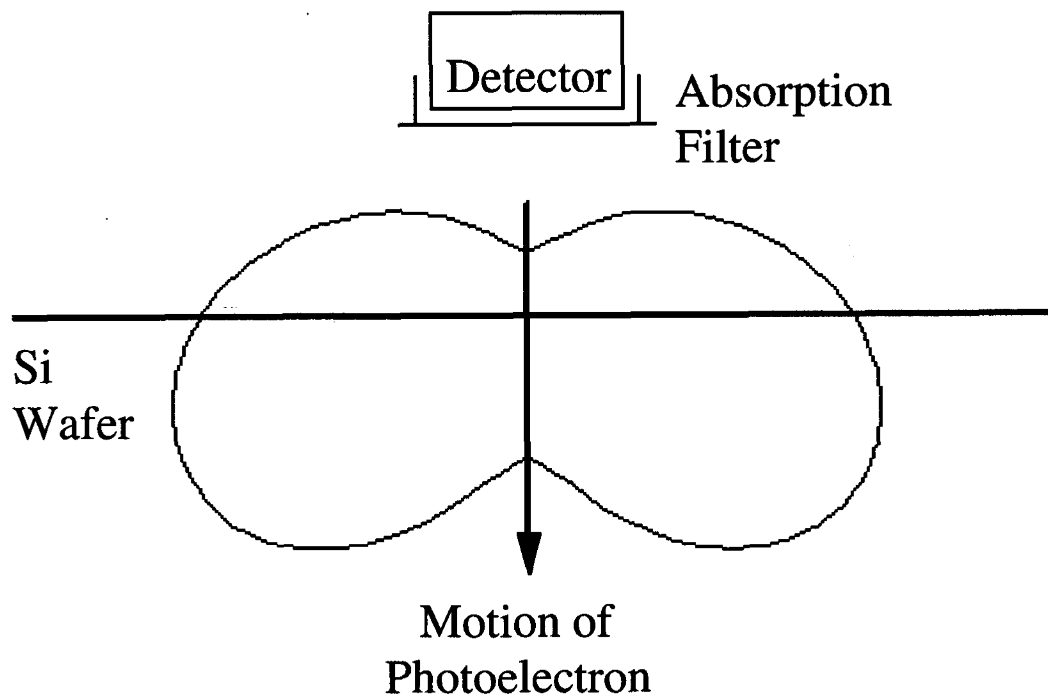

Fig. 5.3 The angular distribution of 5.5 keV bremsstrahlung from 8.8 keV electrons in a silicon atomic field [11], [12]. The arrow indicates the direction of electron motion.

There are two significant differences between the angular distributions of the photoelectron bremsstrahlung (Fig. 5.3) and the Thomson scattering (Fig. 2.13) [13]. First, the angular distribution of the photoelectron bremsstrahlung is asymmetric with respect to the direction of the photoelectron motion. The bremsstrahlung intensity emitted along the photoelectron motion is larger than that emitted away from the photoelectron motion. This is due to the relativistic retardation of the fast moving photoelectrons [6].

Second, the photoelectron bremsstrahlung intensity along the polarization vector is not zero. Since the bremsstrahlung is a dipole radiation, the intensity along the polarization vector is expected to be zero in the first order theory. However, the bremsstrahlung in this direction is generated by the photoelectrons with their motion vector deflected from the polarization vector due to deflection by the atomic Coulomb field [12].

It is known that the finite emission of the bremsstrahlung in this direction makes the angular distribution of the bremsstrahlung almost isotropic. This fact has been confirmed by several experiments [6]. Therefore, in this work, we assume that the emission of photoelectron bremsstrahlung is isotropic in order to simplify the calculation.

5.2.3 Modeling Equation

The modeling equation for the photoelectron bremsstrahlung created from a Si wafer is given by Eq. (5.1),

$$I(E_0, E_x, \alpha) = \frac{F(E_0, E_x, \alpha) \cdot C_1 \cdot \frac{E_{initial} - E_x}{Ex} \cdot dE_x \cdot T(E_x)}{\sigma(E_0) \cdot \omega_{SiK} \cdot T(E_{SiK})} \quad (5.1),$$

where

E_0 = incident beam energy (keV),

E_x = bremsstrahlung energy (keV),

dE_x = energy per channel (keV/Ch),

$E_{initial}$ = initial photoelectron kinetic energy (keV),

E_{SiK} = silicon K fluorescence energy (1.74 keV),

C_1 = constant,

α = angle of incidence (deg.),

σ = the ionization cross-section of the silicon K electron (=1.18 x 10^3 barns for 10.6 keV x-ray) [9],

ω_{SiK} = the fluorescence yield for silicon K shell (= 0.047) [9],

T = the transmission factors of a 25 μm Teflon absorption filter (Ch. 3), and

F = surface correction factor.

Eq. (5.1) is made up of four factors; the bremsstrahlung emission probability, $C_1 \cdot \frac{E_{initial} - E_x}{Ex} \cdot dE_x$, the surface correction factor, $F(E_0, E_x, \alpha)$, the normalization factor using the Si fluorescence signals, $\sigma(E_0) \cdot \omega_{SiK}$, and the transmission factor of a 25 mm Teflon filter, $T(E_x)$ [9], [15]. The effect of the Teflon filter has already been discussed in Sec. 5.2.1. We will describe other three factors in the following sections.

5.2.4 The Bremsstrahlung Emission Probability

This section describes the analytical expression for the emission probability of the bremsstrahlung used in Eq. (5.1) [3]. We start by describing the general expression of the bremsstrahlung emission probability, p, when an electron of an energy E passes through a thin material with thickness, dz :

$$p = \sigma(E, E_x) \cdot dz \qquad (5.2),$$

where $\sigma(E, E_x)$ is the cross-section for the bremsstrahlung of E_x (keV) generated by an electron with a kinetic energy of E (keV). Bremsstrahlung of E_x (keV) can be created by the electrons with $E > E_x$.

Eq. (5.2) can be transformed using the electron stopping power, S(E), into a form which is a function of the electron kinetic energy :

$$p = \frac{\sigma(E, E_x) \cdot dE}{S(E)} \qquad (5.3),$$

$$S(E) = \frac{dE}{dz} \qquad (5.4),$$

where dE represents the lost kinetic energy.

The emission probability of the bremsstrahlung generated when photoelectrons pass though a infinitely thick material is obtained by integrating Eq. (5.4) with respect to the

electron kinetic energy E from the initial electron kinetic energy $E_{initial}$ to the bremsstrahlung energy E_x,

$$p_x = \int_{E_x}^{E_{initial}} \frac{\sigma(E, E_x) \cdot dE}{S(E)} \qquad (5.5).$$

Note that the bremsstrahlung with an energy of E_x can be generated by photoelectrons with the kinetic energy of more than E_x.

An analytical expression for the bremsstrahlung emission probability is given by substituting the expressions of the cross-section and stopping power into Eq. (5.5). In this work, we use the simplified Heitler's relationship for cross-section and the Bethe-Bloch relationship for stopping power derived in an earlier study by Goulding and Jaklevic[3]. These expressions are shown in Eq. (5.6) and Eq. (5.7), respectively,

$$\sigma(E, E_x) = 1.5 \times 10^{-24} \frac{Z^2}{E} \left\{ \frac{dE_x}{E_x} \right\} \quad (\mathrm{cm^2/atom}) \qquad (5.6),$$

$$S(E) = \frac{dE}{dz} = \frac{Z}{1.67 \times 10^8 E} \quad (\mathrm{atoms/cm^2}) \qquad (5.7),$$

where Z is the atomic number (Z = 14 for Si). Noted that Eq. (5.6) assumes isotropic emission of the bremsstrahlung for simplicity.

By substituting Eqs. (5.6) and (5.7) into Eq. (5.3), the analytical expression for the emission probability of the bremsstrahlung generated from a thin target is found to be

$$p = C_1 \frac{dE}{E_x} dE_x \qquad (5.8),$$

$$\text{where} \quad C_1 = 2.5 \times 10^{-6} \cdot Z \qquad (5.9).$$

On the other hand, from Eq. (5.5), the analytical expression of the emission probability of the bremsstrahlung from a thick target is found to be

$$p_x = \frac{C_1}{2} \cdot \frac{E_i(E_0) - E_x}{E_x} \cdot dE_x \qquad (5.10).$$

Note that Eq. (5.10) is the bremsstrahlung emission probability used in the modeling equation, Eq. (5.1).

5.2.5 Surface Correction Factor

The surface correction factor in Eq. (5.1) takes into account the reduction of the bremsstrahlung intensity due to the escape of the photoelectrons out of the wafer surface. In order to obtained the analytical solution for the surface correction factor, we separately consider the photoelectron bremsstrahlung generated from the photoelectrons going toward the wafer surface and going into the wafer.

The bremsstrahlung emission probability for the photoelectrons going into the wafer, $p_{in}(E_0)$, is given by Eq. (5.11),

$$P_{in}(E_0) = \frac{C_1}{2} \cdot \frac{E_i(E_0) - E_x}{E_x} \cdot dE_x \qquad (5.11).$$

In Eq. (5.11), the initial kinetic energy of photoelectron is represented as a function of incident x-ray energy, E_0.

Eq. (5.11) is obtained by dividing Eq. (5.10) by 2, indicating that half of the photoelectrons go into the wafer. Because the wafer thickness (about 500 μm) is much larger than the electron mean free path for the photoelectrons with the kinetic energy of 8.76 keV (about 1.2 μm) [38], the bremsstrahlung generated from the photoelectrons going into the wafer is the same as that generated from a infinitely thick Si target.

On the other hand, the bremsstrahlung emission probability for the photoelectrons going out of the wafer, p_{out} (E_0, E_X) is represented in Eqs. (5.12) and (5.13),

$$P_{out}(E_0, E_x) = \frac{C_1}{2} \cdot \frac{E_i(E_0) - E_f}{E_x} \cdot dE_x \qquad \text{if} \quad E_f \geq E_x \qquad (5.12),$$

$$P_{out}(E_0, E_x) = \frac{C_1}{2} \cdot \frac{E_i(E_0) - E_x}{E_x} \cdot dE_x \qquad \text{if} \quad E_f < E_x \qquad (5.13).$$

Eqs. (5.12) and (5.13) take into account the final kinetic energy of the photoelectrons at the surface because bremsstrahlung with the energy of E_x can only be created by photoelectrons with the kinetic energy more than E_x.

The final kinetic energy of the photoelectrons, E_f, is calculated using the Bethe-Bloch relationship for electron stopping power in Eq. (5.7) :

$$E_f(E_0,z) = E_i(E_0)\cdot\sqrt{1-\frac{z}{\zeta_e(E_0)}} \qquad (5.14),$$

where ξ_e is the mean free path of the electron with an initial kinetic energy which is a function of incident x-ray energy :

$$\zeta_e(E_o) = \frac{C_2 \cdot E_i^2(E_o)}{2} \qquad (5.15).$$

Eq. (5.14) is a function of the depth from the surface, z.

The effect of the escaped photoelectrons, $f(E_0, E_x)$, can be factored out from Eqs. (5.12) and (5.13),

$$p_{out}(E_0,E_x) = f(E_0,E_x)\cdot p_x \qquad (5.16.1),$$

$$f(E_0,E_x) = \frac{1}{2} - \frac{E_f - E_x}{2(E_i(E_0) - E_x)} \qquad \text{if} \quad E_f \geq E_x \qquad (5.16.2),$$

$$f(E_0,E_x) = \frac{1}{2} \qquad \text{if} \quad E_f < E_x \qquad (5.16.3).$$

Furthermore, to account for the actual photoelectron bremsstrahlung generated in SR TXRF, Eqs. (5.16) are averaged over all the photoelectrons going toward the wafer surface,

$$\int_0^{z_x(E_0,E_x)} \left(\frac{1}{2} - \frac{E_f(E_0,E_x,z) - E_x}{2(E_i(E_0) - E_x)} \right) \frac{\exp\left(-\frac{z}{\zeta(E_0,\alpha)} \right)}{\zeta(E_0,\alpha)} dz + \int_{z_x(E_0,E_x)}^{\infty} \frac{1}{2} \frac{\exp\left(-\frac{z}{\zeta(E_0,\alpha)} \right)}{\zeta(E_0,\alpha)} dz \quad (5.17),$$

where $\zeta(E_0, \alpha)$ is the incident x-ray penetration depth as a function of incident x-ray energy, E_0, and incident angle, α and Z_x is the distance traveled in the Si in order for the photoelectrons to reduce their kinetic energies to E_X (keV) :

$$Z_x(E_0,E_x) = \zeta_e(E_0) \cdot \left(1 - \frac{E_x^2}{E_i^2(E_0)} \right) \quad (5.18).$$

Eq (5.18) is calculated by substituting the Bethe-Bloch relationship for electron stopping power in Eq. (5.10).

Eq. (5.17) is normalized by an exponential factor,

$$\frac{\exp\left(-\frac{z}{\zeta(E_0,\alpha)} \right)}{\zeta(E_0,\alpha)} \quad (5.19),$$

which represents the density of the final kinetic energy of the photoelectrons at the wafer surface. Note that the photoelectron kinetic energy at the surface is a function of the distance, z, where the photoelectron generated from the surface. Eq. (5.17) integrates Eqs (5.16) multiplied by Eq. (5.19) over the distance from the wafer surface to z.

The first term in the right side of Eq. (5.17) gives the emission probability generated from the photoelectrons with their final kinetic energy at the surface, E_f, being more than the energy of the bremsstrahlung of interest, E_x. On the other hand, the second term gives the emission probability from the photoelectrons with their final kinetic energy being less than the energy of the bremsstrahlung of interest.

Finally, using Eqs. (5.10) and (5.15), the analytical solution of the total emission probability of the bremsstrahlung is found to be,

$$P_{in}(E_0) + P_{out}(E_0, E_x, \alpha) = F(E_0, E_x, \alpha) P_x \tag{5.20}$$

where

$$F(E_0, E_x, \alpha) = 1 - \frac{E_i(E_0) \int_0^{z_x(E_0, E_x)} \sqrt{1 - \frac{z}{\zeta_e(E_0)}} \frac{\exp\left(-\frac{z}{\zeta(E_0, \alpha)}\right)}{\zeta(E_0, \alpha)} dz - E_x \cdot \left(1 - \exp\left(-\frac{Z_x(E_0, E_x)}{\zeta(E_0, \alpha)}\right)\right)}{2\left(E_i(E_0) - E_x\right)} \tag{5.21}$$

We refer to the factor F in Eq. (5.21) as surface correction factor that represents the reduction of the TXRF photoelectron bremsstrahlung intensity due to the photoelectrons which escaped from the wafer surface.

5.2.6 Normalization with Si Fluorescence Signals

The modeling equation Eq. (5.1) normalizes the photoelectron bremsstrahlung intensity to the Si fluorescence signal intensity. The primary purpose of the normalization is to eliminate the incident photon flux when modeling the bremsstrahlung intensity. Note that the photon flux incident on the measured area is difficult to measure accurately in experiments.

In addition, normalization with the Si fluorescence signal intensity is physically equivalent to normalization with the photoelectron intensity because the Si fluorescence signal intensity is proportional to the photoelectron intensity. According to the fluorescence yield for the silicon K-shell, which is about 0.05, about 20 photoelectrons are generated per one silicon K photon [9].

Because of its physical origin, the Si fluorescence signal intensity is a better normalization factor of the photoelectron bremsstrahlung than the scattered x-ray intensity, which is not directly related to the photoemission.

The normalization with the Si fluorescence signal intensity clearly shows the "surface effect" of the photoelectrons on the bremsstrahlung intensity because this normalization gives the bremsstrahlung intensity per photoelectron. The comparison of the theoretical modeling of the surface correction factor and experimental data will be discussed in the next section.

5.2.7 Comparison of the Theoretical Model with Experimental Data

This section compares the results of calculations and experimental data for the photoelectron bremsstrahlung. Before the comparison, however, let us present data which verifies our conclusion that the photoelectron bremsstrahlung is reduced as a result of the photoelectrons escaping out of the wafer surface.

SR TXRF spectra taken from a clean Si wafer at incident angles of 0.11 deg. and 0.5 deg. are shown in Fig. 5.4. We normalized these spectra to the Si fluorescence intensity. The main features of these spectra were the silicon fluorescence peak at 1.74 keV, the incident x-ray scattered peak at 10.6 keV, and the continuous background component between the two peaks.

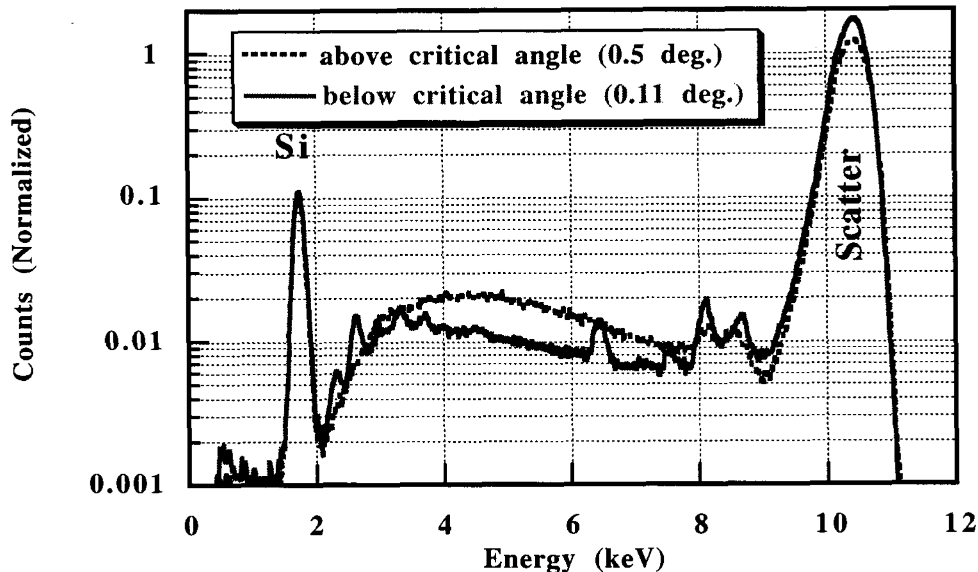

Fig. 5.4 The spectra of the continuous background normalized to the silicon fluorescence counts. Data were taken at 0.11 deg. and 0.5 deg. For details of our experimental configuration, see Chs. 2 and 3.

In addition, there are several fluorescence peaks in the spectra which originated from unintentional contamination.

A significant difference between the two spectra was the continuous background intensity. The background intensity at 0.11 deg. was less than the intensity at 0.5 deg. This was due to the photoelectrons escaping out of the wafer for the case when the x-rays were incident below the critical angle.

When the incident angle was 0.11 deg., which was below the critical angle of 0.17 deg., the penetration depth normal to the surface was 45 Å for 10.6 keV incident x-rays and, therefore, most of the photoelectrons were created near the surface. Because the penetration depth was much shorter than the mean free path of the 8.77 keV photoelectrons, which was about 12,000 Å [14],[15], the photoelectrons emitted toward the surface could escape out of the silicon wafer almost without losing their energy and, therefore, without creating photoelectron bremsstrahlung in the Si wafer.

On the other hand, when the incident angle was 0.5 deg., which was significantly above the critical angle, the penetration depth of the incident x-ray beam was about 12,000 Å, which became comparable to the electron mean free path. Therefore, the photoelectrons emitted toward the surface could create the bremsstrahlung in the Si wafer, which results in the photoelectron bremsstrahlung intensity being larger than the intensity at 0.11 deg.

We calculated the surface correction factors using Eq. (5.20) with the values for the initial photoelectron kinetic energy of 8.76 keV and bremsstrahlung energy of 5.6 keV. The surface correction factor at 0.11 deg. was calculated to be about 0.5, whereas the surface correction factor at 0.5 deg. was about 0.8. The ratio of the factors at these angles was about 1.6, indicating that the bremsstrahlung intensity normalized to the Si fluorescence

intensity at 0.5 deg. was about 1.6 times higher than that at 0.11 deg. The calculations agreed with the experimental data for the continuous background intensity at 5.6 keV.

The points in Fig. 5.5 show the continuous background intensity normalized to the Si fluorescence between 0.07 deg. and 0.33 deg. We used the background at 5.6 keV where no fluorescence signals existed. In Fig. 5.5, the background intensity normalized to the Si fluorescence signal intensity greatly increased above the critical angle. This was due to the increase in the incident x-ray penetration depth resulting in the generation of most of the photoelectrons inside the Si wafer.

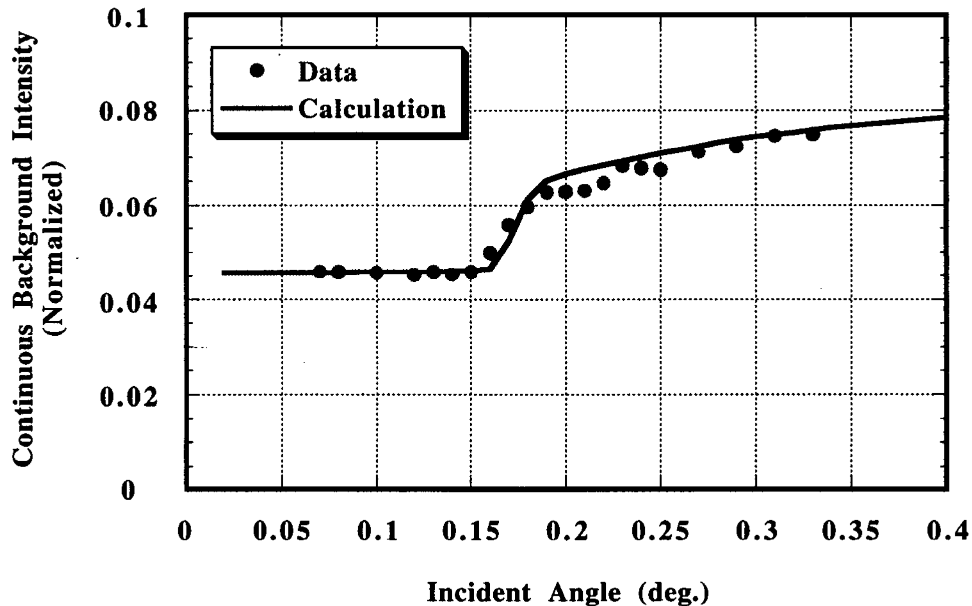

Fig. 5.5. The angle scan of the continuous background intensity at 5.6 keV normalized to the silicon fluorescence intensity with the data (•) and calculation (solid line). The continuous background intensity was integrated from 5.5 keV to 5.7 keV.

In addition, using the surface correction factor shown in Eq. (5.20), we modeled the angle scan of the SR TXRF continuous background intensity using the parameters for the initial photoelectron energy of 8.76 keV and bremsstrahlung energy of 5.6 keV.

The modeling curve is shown in the solid line. We normalized the modeling curve to the experimental data at 0.1 deg. The modeling curve agreed fairly well with experimental data below and above the critical angle. The success of the theoretical modeling indicates that the continuous background at 5.6 keV was primarily consisted of photoelectron bremsstrahlung.

Finally, we modeled the photoelectron bremsstrahlung in a SR TXRF spectrum in the energy region between 0 and 10 keV (Fig. 5.6). The actual data were taken using an incident beam with an energy of 10.6 keV from a standard Si wafer intentionally contaminated with 10^{11} atoms/cm^2 of Fe, Ni, and Zn (Ch. 4).

In addition to the bremsstrahlung curve, the calculated curves for the fluorescence signals and a part of the calculated curve for scattered x-rays are shown. The fluorescence signal peaks were convoluted with the Gaussian distribution with the standard deviation equal to the energy resolution of Si (Li) detector (~200 eV). The calculation of the scattered x-ray peak is discussed in more detail in Sec. 5.3.

The modeling curve of the low energy bremsstrahlung is decreased below 3 keV due to the absorption by the 25 μm Teflon filter. The maximum bremsstrahlung energy in the modeling curve is equal to the initial photoelectron kinetic energy (at 8.76 keV).

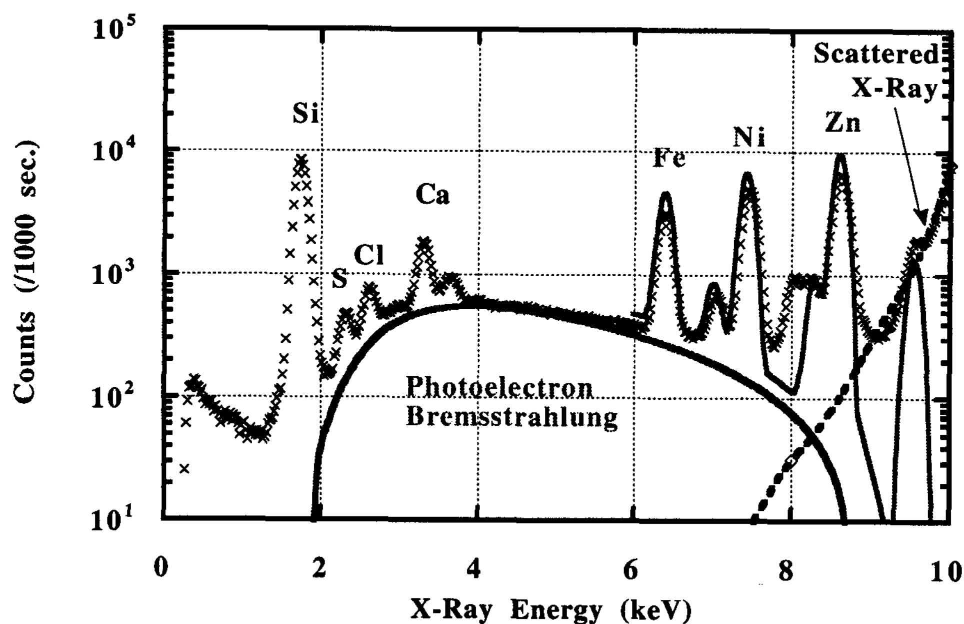

Fig. 5.6 The modeling of the photoelectron bremsstrahlung spectrum taken from a standard silicon wafer intentionally contaminated with 10^{11} atoms/cm^2 of Fe, Ni, and Zn. The incident angle was 0.08 deg.

The modeling curve of the photoelectron bremsstrahlung gave good agreement with the experimental data for the continuous background, specifically in the energy region between 4 and 7 keV. Therefore, we conclude that the continuous background in the SR TXRF measurements primarily consists of photoelectron bremsstrahlung.

5.3 Surface Oxide Effect

The effect of surface oxides on Si wafer surfaces is not negligible in TXRF because the incident x-ray penetration depth may be comparable to the surface oxide thickness. For example, the penetration depth of 10 keV x-rays below the critical angle is typically 40 Å, while the Si native oxide thickness is about 15 Å. This section shows theoretical models that take into account the surface oxides.

5.3.1 Conventional Theoretical Models

We start by considering the analytical expression of the Si fluorescence signals when no surface oxide is present,

$$
\begin{aligned}
I_{Si}^{F} &= A_{Si} \cdot \sigma_{pi} \cdot \omega \cdot R(\theta) \int_0^{\infty} \exp\left(-\frac{z}{\zeta(\theta)}\right) dz \\
&= A_{Si} \cdot \sigma_{pi} \cdot \omega \cdot R(\theta) \cdot \zeta(\theta)
\end{aligned}
\qquad (5.22),
$$

where

A_{si} = Si atomic density in the Si crystal (atoms/cm^2),

σ_{pi} = photoionization cross-section of the Si K-shell (barns) [9],

ω = fluorescence yield for the Si K-shell [9],

$R(\theta)$ = refracted field intensity at the surface as a function of incidence angle,

θ = angle of incidence (deg.),

$\zeta(\theta)$ = incident x-ray penetration depth (Å), and

z = the depth from the wafer surface.

The exponential factor, $\exp\left(-\frac{z}{\zeta(\theta)}\right)$, is proportional to the x-ray intensity at a distance, z, from the wafer surface, and the Si fluorescence signal intensity generated from the Si wafer is proportional to the integration of the exponential factor with respect to the distance, z, which results in $\zeta(\theta)$. For the fundamental aspects of Eq. (5.22), see Ch. 2.

In the same way, the scattered x-ray intensity generated from the Si wafer when no surface oxide is present is,

$$I_{Si}^{S} = A_{Si} \cdot \sigma_{Si} \cdot R(\theta) \cdot \zeta(\theta) \quad (5.23),$$

where

σ : the scattering x-ray cross-section (barns).

The subscript in Eq. (5.23) indicates that the material of interest is Si.

The formalism for the scattering x-ray cross-section is given by,

$$\sigma = \iint \frac{d^2\sigma}{d\Omega dE_x} d\Omega dE_x \quad (5.24),$$

which is integrated with respect to solid angle, Ω. and x-ray energy, E_x.

We assume that the scattered x-rays from the primary incident photon beam consist of thermal diffuse scattering (TDF) and Compton scattering. TDF is inelastic scattering that occurs due to the interaction between an incident x-ray and a phonon [16]. The TDF peak appears at the energy equal to that of the incident x-rays because the energy transfer between the x-ray and phonon is small (about 0.01 eV) [17].

On the other hand, the Compton scattering is inelastic scattering that occurs due to the interaction between an incident x-ray and an electron in a solid [16]. Because electrons in solids have a momentum distribution, the Compton scattered x-rays also have momentum and energy distributions [36], [38], [39], [40].

The scattering x-ray cross-section, $\frac{d^2\sigma}{d\Omega dE_x}$, is obtained by use of the Compton and Rayleigh scattering formalisms,

$$\frac{d^2\sigma}{d\Omega dE_x} = \frac{d^2\sigma_{Compton}}{d\Omega dE_x} + \left(1 - e^{-2M}\right)\frac{d\sigma_{Rayleigh}}{d\Omega} \qquad (5.25),$$

where

$\frac{d^2\sigma_{Compton}}{d\Omega dE_x}$ = Compton scattering cross-section (barns/sr/keV),

Ω = solid angle subtended by the detector (sr),

E_x = Compton scattering x-ray energy (keV),

$\frac{d\sigma_{Rayleigh}}{d\Omega}$ = Rayleigh scattering cross-section (barns/sr), and

M = Debye-Waller factor.

The first term of the right side of Eq. (5.25) represents the Compton scattering cross-section with respect to the solid angle and scattering x-ray energy. The second term of the right side of Eq. (5.25) represents the TDF scattering x-ray cross-section, which consists of the Rayleigh scattering cross-section and a factor, $(1- e^{-2M})$, where M is the Debye-Waller factor. The Raleigh scattering cross-section can be calculated using an atomic form factor [9], [16].

In Eq. (5.25), it is assumed that the incident x-ray beam is coherent and, therefore, the Rayleigh (elastically) scattered x-ray intensity itself is zero if the Brag condition is not satisfied in the first order approximation. However, this assumption is too simple to quantify the surface oxide effect on the scattered x-ray intensity.

5.3.2 Theoretical Models Including Surface Oxide Effects

First, let us list several properties of Si crystal and oxide in Table 5.1 [19], [20]. The critical angles and the penetration depths at an angle of incidence of 0.1 deg. were calculated for 9.67 keV (W Lβ_2) x-rays. Note that, for simplicity, we assume the chemical composition of the surface Si oxides is SiO_2.

The critical angles and penetration depths for the Si crystal and the oxide were almost the same because the electron densities for these materials are almost the same.

Table 5.1 Properties of Si crystals and oxides.

material	Si crystal	Si oxide (SiO_2)
critical angle (deg.)	0.185	0.179
penetration depth (Å)	37.6	39.2
electron density (cm^{-3})	6.60E+23	7.00E+23
Si atomic density (cm^{-3})	5.00E+22	2.20E+22
atomic structure	diamond structure	amorphous

Therefore, it can be assumed that the surface oxide does not effect the total reflection condition itself. This also allows us to take the critical angle and penetration depth for these materials to be the same in the calculations that follow.

However, the Si atomic density is about 2.3 times greater in the Si crystal than that in the oxide. Because the Si fluorescence signal is proportional to the Si atomic density, the Si fluorescence signal created in the Si oxide will be less by a factor of approximately 2.3 than the Si signals created in the Si crystal. This will be shown quantitatively in our model.

Second, since the atomic structure of the oxide and crystal differ, i.e., amorphous vs. crystalline, we know from the theory of x-ray scattering that the elastic scattering x-ray signals will differ significantly [21]. However, calculating the elastically scattered x-ray intensity from a thin amorphous layer is beyond the scope of this work. Therefore, the ratio of the scattered x-ray intensity between the oxide and crystal will be obtained experimentally and then factored into the model as will be shown below.

Based on Eq. (5.22), the Si fluorescence signal intensity generated from a wafer with a surface oxide with the thickness, x_{ox}, is given by Eqs. (5.26),

$$I^F = \sigma_{pi} \cdot \omega \cdot R(\theta) \left[A_{ox} \int_0^{x_{ox}} \exp\left(-\frac{z}{\zeta(\theta)} \right) dz + A_{Si} \int_{x_{ox}}^{\infty} \exp\left(-\frac{z}{\zeta(\theta)} \right) dz \right] \quad (5.26.1),$$

$$= A_{Si} \cdot \sigma_{pi} \cdot \omega \cdot R(\theta) \cdot \zeta(\theta) \left[\frac{A_{ox}}{A_{Si}} - \left(\frac{A_{ox}}{A_{Si}} - 1 \right) \exp\left(-\frac{x_{ox}}{\zeta(\theta)} \right) \right] \quad (5.26.2),$$

$$= A_{Si} \cdot \sigma_{pi} \cdot \omega \cdot R(\theta) \cdot \zeta(\theta)\left[A - (A-1)\exp\left(-\frac{x_{ox}}{\zeta(\theta)}\right)\right] \quad (5.26.3),$$

$$= I_{Si}^{F} \cdot C^{F}(x_{ox}, \theta) \quad (5.26.4),$$

where

$$A = \frac{A_{ox}}{A_{Si}} \quad (5.27),$$

A_{ox} : Si atomic density in the oxide (atoms/cm^2), and

$$C^{F}(x_{ox}, \theta) = A - (A-1)\exp\left(-\frac{x_{ox}}{\zeta(\theta)}\right) \quad (5.28).$$

Note that, for simplicity, the surface oxide is represented as a step function with the homogeneous Si atomic density, A_{ox}.

The first term in the parenthesis in Eq. (5.26.1) represents the number of the Si atoms in the oxide struck by the x-ray beam and the second term represents the number of the Si atoms in the Si crystal struck by the x-ray beam. The factor that represents the surface oxide effect on the Si fluorescence intensity is shown in Eq. (5.28) as a function of angle of incidence and surface oxide thickness.

In the same way, the scattered x-ray intensity generated from the wafer with the surface oxide can be calculated as follows;

$$I^S = R(\theta)\left[A_{ox}\sigma_{ox}\int_0^{x_{ox}}\exp\left(-\frac{z}{\zeta(\theta)}\right)dz + A_{Si}\sigma_{Si}\int_{x_{ox}}^{\infty}\exp\left(-\frac{z}{\zeta(\theta)}\right)dz\right] \quad (5.29.1),$$

$$= A_{Si}\cdot\sigma_{Si}\cdot R(\theta)\cdot\zeta(\theta)\left[\frac{A_{ox}}{A_{Si}}\frac{\sigma_{ox}}{\sigma_{Si}} - \left(\frac{A_{ox}}{A_{Si}}\frac{\sigma_{ox}}{\sigma_{Si}} - 1\right)\exp\left(-\frac{x_{ox}}{\zeta(\theta)}\right)\right] \quad (5.29.2),$$

$$= A_{Si}\cdot\sigma_{Si}\cdot R(\theta)\cdot\zeta(\theta)\left[A\cdot\Sigma - (A\cdot\Sigma - 1)\exp\left(-\frac{x_{ox}}{\zeta(\theta)}\right)\right] \quad (5.29.3),$$

$$= I_{Si}^F\cdot C^S(x_{OX},\theta) \quad (5.29.4).$$

where

$$\Sigma = \frac{\sigma_{ox}}{\sigma_{Si}} \quad (5.30),$$

σ_{ox} : the scattering cross-section of the oxide, and,

$$C^S(x_{OX},\theta) = A\cdot\Sigma - (A\cdot\Sigma - 1)\exp\left(-\frac{x_{ox}}{\zeta(\theta)}\right) \quad (5.31).$$

The factor that represents the surface oxide effect on the scattered x-ray intensity is shown in Eq. (5.31) as a function of angle of incidence and surface oxide thickness. Note that the ratio of the scattering cross-sections of the Si crystal to that of the oxide is

represented as Σ. As mentioned above, it is difficult to calculate the scattering cross-section of the thin oxides. Therefore, we will experimentally determine the value of Σ in the next section.

Furthermore, to cancel the refracted field intensity, $R(\theta)$, and the incident x-ray penetration depth, $\zeta(\theta)$, we will normalize Eq. (5.29.4) to Eq. (5.26.4),

$$\frac{I^S}{I^F} = \frac{I^S_{Si} \cdot C^S(x_{OX}, \theta)}{I^F_{Si} \cdot C^F(x_{OX}, \theta)} = \frac{R(\theta) \cdot \zeta(\theta) \cdot \sigma_{Si} \cdot C^S(x_{OX}, \theta)}{R(\theta) \cdot \zeta(\theta) \cdot \sigma_{pi} \cdot \omega \cdot C^F(x_{OX}, \theta)} = \frac{\sigma_{Si} \cdot C^S(x_{OX}, \theta)}{\sigma_{pi} \cdot \omega \cdot C^F(x_{OX}, \theta)} \quad (5.32),$$

Using Eq. (5.32), it is possible to model the surface oxide effect on the scattered x-ray intensity normalized to the Si fluorescence signal intensity (Scatter / Si) as a function of angle of incidence. In the next section, we will model data taken from Si wafers with several surface oxides using Eq. (5.32).

5.3.3. Comparison of the Theoretical Model with Experimental Data

This section compares experimental data with the results of the theoretical model which includes surface oxides. We took the data using a W rotating anode TXRF system, RIGAKU 3700 at Hewlett Packard [22]. For incident angles below the critical angle (0.185 deg.), the W x-ray source was operated at 30.0 keV and 400 mA. For incident angles above the critical angle, the it was operated at 30.0 keV with 40 mA. We measured three 6-inch Si wafers: an as-received wafer (i.e., with a native oxide), a wafer with a 55 Å

thermal oxide, and a wafer with a 80 Å thermal oxide. The thickness of the oxides was measured by ellipsometry at HP.

The spectra of the Si fluorescence peaks from the 80 Å thermal oxide and native oxide wafers taken at an angle of incidence of 0.12 deg. are shown in Fig. 5.7.a. In this figure, the Si fluorescence intensity from the wafer with the 80 Å thermal oxide was smaller than that from the wafer with the native oxide. This was due to the smaller Si atomic density in the oxide than in the Si crystal. From Fig. 5.7.a, it was found that the Si wafer with the 80 Å oxide generated smaller Si fluorescence signal intensity than the wafer with the native oxide by a factor of 0.69.

The spectra of the scattered x-ray peaks are shown in Fig. 5.7.b. In contrast to the Si fluorescence signals, the scattered x-ray intensity from the 80 Å thermal oxide wafer was larger than that from the native oxide wafer by a factor of 1.94.

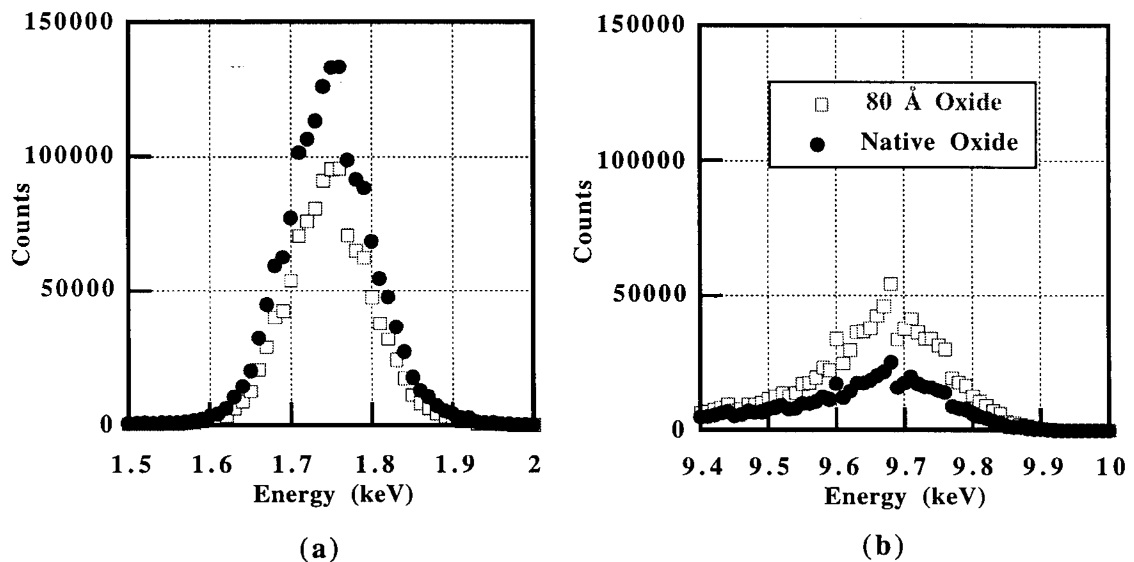

Fig. 5.7 TXRF spectra taken from silicon wafers with native and 80 Å thermal oxides. Data were taken with a conventional RIGAKU TXRF system at 0.12 deg. (a) Si fluorescence peaks. (b) Scattered x-ray peaks.

Using the results in Fig. 5.7 and Eq. (5.31), the vale of Σ was found to be 5.25.

Next, by using the experimentally determined Σ and Eq. (5.32), we modeled the scattered x-ray intensity normalized to the Si fluorescence intensity, (Scatter / Si), as a function of angle of incidence (Fig. 5.8). The results of the theoretical modeling curves are shown in the solid line (for the 55 Å oxide) and dashed line (for the native oxide).

From Fig. 5.8, it was found that, when the angles of incidence were below the critical angle, the (Scatter / Si) from the 55 Å thermal oxide was larger than that from the native oxide wafer. The 55 Å thermal oxide created larger scattered x-rays and smaller Si fluorescence x-rays than the native oxide.

It was also found that the (Scatter / Si) decreased as the angle of incidence increased. This was due to the corresponding increase in the incident x-ray penetration depth, resulting in the generation of more Si fluorescence signals in the Si crystal. Above the critical angle (0.185 deg. for Si crystal), the surface oxides became negligible and the intensity approached the value from the Si crystal.

The modeling curves calculated using Eq. (5.32) agreed well with the experimental data below and above the critical angle. Using Eq. (5.21) and the experimentally determined value of Σ, we could successfully model the surface oxide effect observed in TXRF.

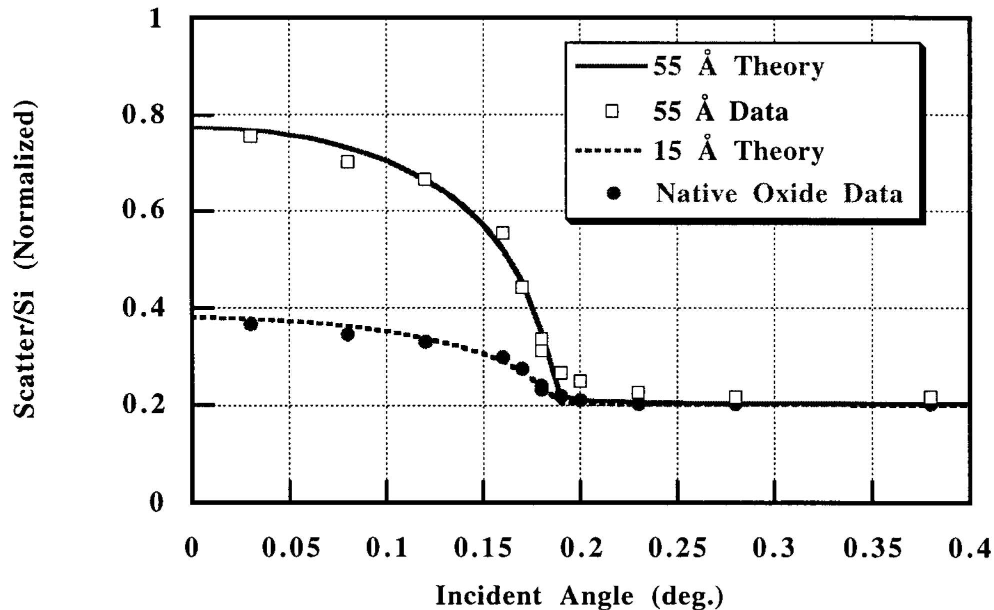

Fig. 5.8 Angle scan of TXRF signals taken from the wafers with native oxide and 55 Å thermal oxide. The vertical axis is the scattered x-ray intensity normalized to silicon fluorescence intensity, which is represented by (Scatter / Si). The theoretical modeling curves for the native oxide and 55 Å thermal oxide wafers are shown in the solid and dashed lines, respectively.

So far, we have discussed the surface oxide effect on the integrated (TDF + Compton) scattered x-ray intensity. However, as mentioned above, the surface oxides modify the elastically scattered x-rays because of their amorphous structure.

Therefore, now, let us derive the formalism representing the profile of the scattered x-ray peaks which satisfies this assumption. We start by defining the integrated scattering cross-section with the surface oxide factor C^S, σ_S,

$$\sigma_S = C^S\left(x_{OX},\theta\right)\left(\int\left(1 - e^{-2M}\right)\frac{d\sigma_{Rayleigh}}{d\Omega}d\Omega + \iint\frac{d^2\sigma_{Compton}}{d\Omega dE_x}d\Omega dE_x\right) \qquad (5.33),$$

In order for the surface oxides to increase the elastically scattered x-ray intensity, we will transform Eq. (5.33) into Eq. (5.34),

$$\sigma_S = K\left(x_{OX},\theta\right)\int\left(1 - e^{-2M}\right)\frac{d\sigma_{Rayleigh}}{d\Omega}d\Omega + \iint\frac{d^2\sigma_{Compton}}{d\Omega dE_x}d\Omega dE_x \qquad (5.34),$$

where

$$K\left(x_{OX},\theta\right) = C^S\left(x_{OX},\theta\right) + \left[C^S\left(x_{OX},\theta\right) - 1\right]\frac{\iint\frac{d^2\sigma_{Compton}}{d\Omega dE_x}d\Omega dE_x}{\int\left(1 - e^{-2M}\right)\frac{d\sigma_{Rayleigh}}{d\Omega}d\Omega} \qquad (5.35).$$

Now, the surface oxide effect is represented by a factor K, which only increases the TDF intensity. Note that, because of the small energy difference (about 0.01 eV), the TDF peak overlaps the elastically scattered x-ray peak. Therefore, the formalism in Eqs. (5.34) and (5.35) also represents the increases in the elastically scattered x-ray intensity.

Using Eq. (5.34), we modeled the profile of the scattered x-ray peak in a SR TXRF spectrum in the energy range between 8 and 12 keV (Fig. 5.9). The data was taken using an incident beam with an energy of 10.6 keV from a standard Si wafer with $1x10^{11}$ atoms/cm^2 of Fe, Ni, and Zn (Ch. 4). Therefore, in addition to the scattered x-ray peak, the fluorescence signal peaks of Ni $K\beta$, Zn $K\alpha$, and Zn $K\beta$ are present in Fig. 5.9.

Furthermore, the modeling curve of the photoelectron bremsstrahlung is shown between 8 keV and 8.8 keV.

We assumed that the wafer had a native oxide with a thickness of 15 Å. The value of the factor K when measuring the native oxide at an angle of incidence of 0.08 deg. is calculated to be 2.13. In addition, the theoretical modeling curves took into account the detector energy resolution and beam divergence, which will be discussed in Ch. 6.

From Fig. 5.6, it was found that the modeling curve for the scattered x-ray peak gave good agreement with experimental data below 11 keV. However, the theoretical intensity of the scattering x-ray peak above 11 keV was larger than the experimental data.

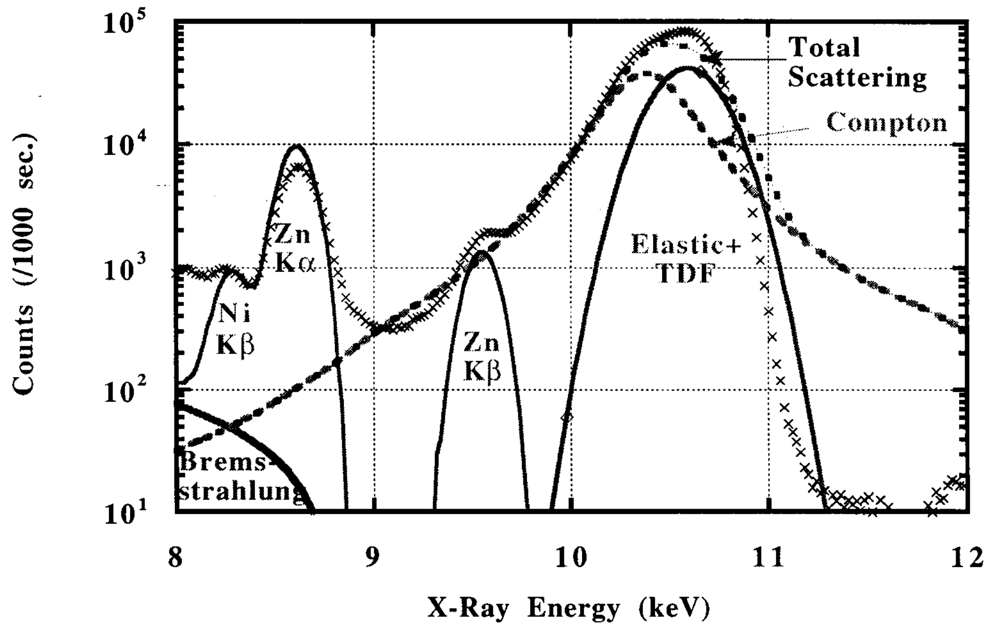

Fig. 5.9 The theoretical modeling curves of scattering x-rays which takes into account the surface oxide effect.

We concluded that the error above 11 keV was due to the inaccuracy in the Compton scattering cross-section (the Compton profile). The Compton scattering cross-sections used for the modeling were calculated based on the impulse approximation that requires a large transfer of energy and momentum to bound electrons from the incident x-rays [18]. However, our experimental conditions were beyond the validity of the impulse approximation. In order to obtain good agreement in this energy region, the exact Compton scattering cross-sections would be required.

In this section, it is found that the surface oxides on Si wafers increase the elastic scattering x-ray intensity. Therefore, the surface oxide also increases the count-rate and escape peak background intensity, both of which are proportional to the scattered x-ray intensity.

Before closing this section, it should be pointed out that Eq (5.32) can be used for measuring the surface oxide thicknesses. The theoretical oxide thickness vs. the (Scatter / Si) is shown in Fig. 5.10. The horizontal axis is the (Scatter / Si) at 0.03 deg. normalized to that at 0.48 deg. The vertical axis is the oxide thickness. The data taken from the wafers with the native oxide, the 55 Å thermal oxide and the 80 Å thermal oxide are plotted in dots.

As can be seen in Fig. 5.10, using the TXRF technique, the thickness of the native oxide was determined to be 15.5 Å ± 0.3 Å. The error of ± 0.3 Å indicates a statistical standard deviation, which corresponds to an error of only 2% of the oxide thickness (Table 5.2). Furthermore, the thickness of the thermal oxides determined with the TXRF technique obtained good agreement with the thickness determined with the ellipsometry at HP.

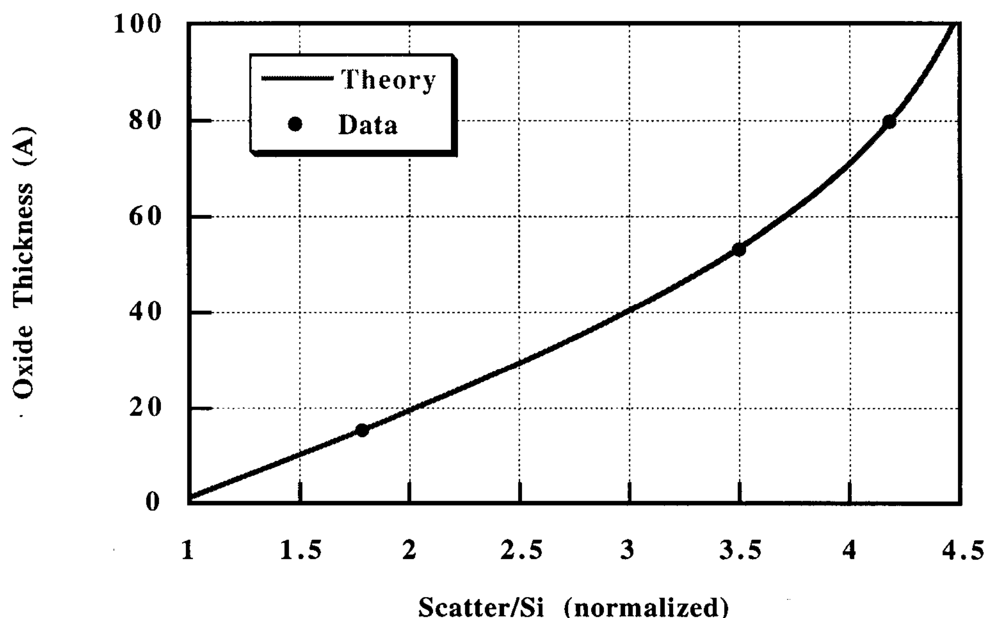

Fig. 5.10 The surface oxide thickness as a function of the scattered x-ray intensity divided by the silicon fluorescence intensity at 0.03 deg. normalized to that at 0.48 deg.

Table 5.2 Surface oxide thickness measured by TXRF.

native oxide	55 Å thermal oxide	80 Å thermal oxide
15.5±0.3 A	53.1±0.7A	79.9±1.6A

The thickness of the thermal oxide was measured by an ellipsometry at HP.

This benchmark study revealed that the surface oxide thickness can be determined by the use of the TXRF technique. This technique is accurate and easy, and requires no special precautions. We believe this technique will become truly useful after examining and extending the validity of the theoretical model by measuring data from oxides with various thickness and compositions.

5.4 Detector Incomplete Charge Collection Background

The detector incomplete charge collection background is a background created inside a Si (Li) detector [23], [24]. When an x-ray is incident on a Si (Li) detector, it is transformed into electron-hole pairs, the number of which is proportional to the x-ray energy. However, when the electron-hole pairs are collected incompletely, the x-ray energy is underestimated. It is known that the incomplete charge collection results in a continuous background.

5.4.1 Detector Incomplete Charge Collection Background in Fe^{55} Spectrum

Before discussing the detector charge collection background in SR TXRF spectra, let us describe the detector incomplete charge collection background in a Fe^{55} spectrum. The spectrum from a Fe^{55} radio active source is widely used to determine the detector incomplete charge collection background because it produces Mn K fluorescence x-rays with little inherent physical background.

Mn K fluorescence x-rays are generated from Fe^{55} source as a result of internal conversion [25], in which an Fe^{55} atom is converted to an Mn^{55} atom with a K shell vacancy decaying either in fluorescence or Auger radiation.

An experimental spectrum taken from a Fe^{55} source (No. F-175 at SSRL) is shown in Fig. 5.11. The count-rate was about 200 cps and the live time for the measurement was 10^5 sec. The Si (Li) detector used for the measurement was a Kevex detector (model no. 3600-0018-0146).

The primary features in Fig. 5.11 are a Mn Kα peak at 5.9 keV and a Mn Kβ signal peak at 6.49 keV. The fluorescence signals of Cr at 5.41 keV were created from a small amount of Cr impurities in the Fe^{55} source. The peak at 4.1 keV is an escape peak. The escape peak is generated when the Si K fluorescence signals generated inside the detector escape out of the detector and are not transformed to electron-hole pairs. The escape peak appears at an energy equal to the primary x-ray energy (6 keV) minus Si K fluorescence energy (1.74 keV).

As can be seen from Fig. 5.11, the continuous background intensity below the Mn K fluorescence signals was larger than that above. The background below the Mn peaks was flat whereas the background above the Mn peaks followed the tail of the Mn K fluorescence peaks.

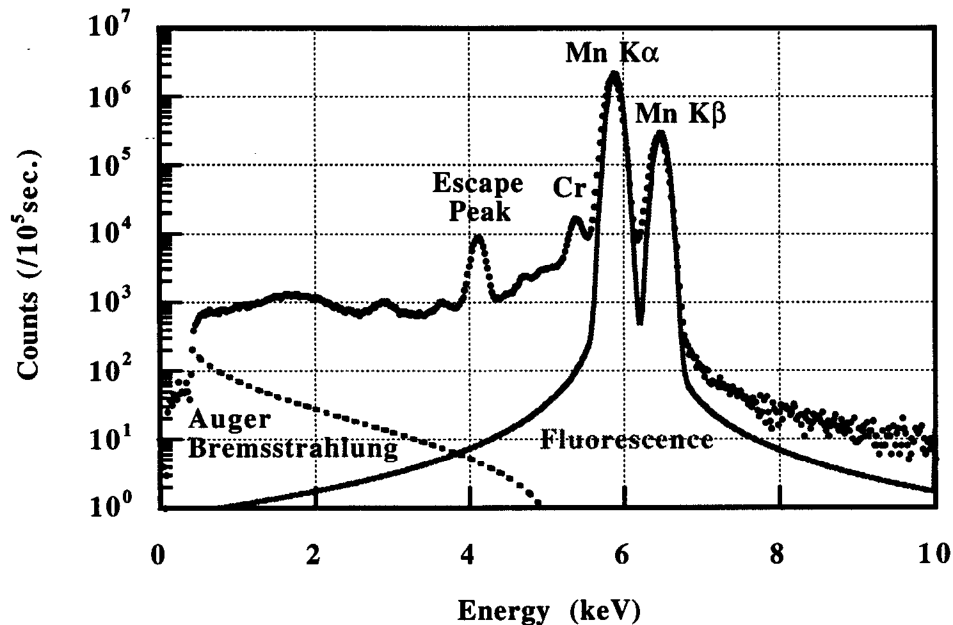

Fig. 5.11 An experimental data from a Fe^{55} radio-active source (dots). The theoretical modeling curves of the Mn fluorescence and Auger bremsstrahlung are shown in solid and dashed lines, respectively.

We investigated the background below the Mn K fluorescence peaks both on theoretical and experimental basis. Theoretically, we modeled x-ray backgrounds generated from the Fe^{55} source, which were Mn K fluorescence and the bremsstrahlung generated by the Auger electrons.

The profile of the Mn K fluorescence signals, $f_{MnK}(E_x)$, is modeled with the Lorenz distribution [26],

$$f_{MnK}(E_x) \propto \frac{\kappa_{MnK}}{\left(E_{MnK\alpha} - E_x\right)^2 + \left(\frac{\Gamma_{MnK}}{2}\right)^2} + \frac{1 - \kappa_{MnK}}{\left(E_{MnK\beta} - E_x\right)^2 + \left(\frac{\Gamma_{MnK}}{2}\right)^2} \quad (5.36),$$

where

E_x = x-ray energy (keV),

$E_{MnK\alpha}$ = Mn Kα fluorescence energy (= 5.89 keV) [9],

$E_{MnK\beta}$ = Mn Kβ fluorescence energy (= 6.49 keV) [9],

Γ_{MnK} = natural line width of Mn K (= 5.6 eV) [27], and

κ_{MnK} = relative transition probability of Mn K fluorescence (= 0.88) [9].

The first term in the right-side of Eq. (5.36) represents the profile of the Mn Kα peak, while the second term represents the profile of the Mn Kβ peak.

To model the experimental data taken by a Si (Li) detector, we convolved Eq. (5.36) by a Gaussian distribution with the standard deviation equal to the FWHM of the Si (Li) detector used for the measurement (150 eV).

The intensity of Mn Auger electron bremsstrahlung, $f_{MNA}(E_x)$, is calculated by Eq. (5.37),

$$f_{MnA}(E_x) = C_{MnA} \cdot C_1 \cdot \frac{E_{MnA} - E_x}{E_{MnA}} \qquad (5.37),$$

where

C_1 = constant (=2.6x10^{-6} Z),

Z = atomic number of Fe^{55} (= 26),

E_{MnA} = Mn Auger electron energy (= 5.8 keV).

C_{MnA} = the number of the Auger electrons that create the bremsstrahlung, which is represented with,

$$C_{MnA} = \frac{(1 - \omega_{MnK})}{\omega_{MnK}} \cdot C_{MnK} \qquad (5.38)$$

ω_{MnK} = the fluorescence yield of Mn K-shell (= 0.5) [8], and

C_{MnK} = Mn K fluorescence x-ray counts.

Eq. (5.37) was obtained using the theory of photoelectron bremsstrahlung derived in Sec. 5.2 by adding the factor (Eq. (5,38)), which accounts for the emission of Auger electrons.

The theoretical modeling curves of the Mn fluorescence and Auger bremsstrahlung are shown in solid and dashed lines, respectively, in Fig. 5.11. The modeling curves were normalized using the integrated intensity of these Mn K fluorescence signals. As can be seen in Fig. 5.11, the experimental data below the Mn K fluorescence signal peaks was much larger than the theoretical modeling curves. This indicates that the continuous background below the Mn peaks was not x-ray background generated from the Fe^{55} source.

Experimentally, we checked the origin of the continuous background by a filtering study [28]. The filtering study measures the change in the continuous background intensity with filter thickness. If the continuous background is generated by x-rays created outside the detector, the background is absorbed by a thicker filter more than by a thinner filter. However, if it is created inside the detector by the primary beam, the ratio of the background intensity to the primary beam intensity is independent of the filter thickness.

The result of the filtering study is shown in Fig. 5.12. Data were taken with and without a 25 μm Teflon filter installed in front of the Si (Li) detector. Data taken with the 25 μm Teflon filter was normalized using the intensity of Mn K fluorescence signals.

If the continuous background below the Mn K fluorescence peak was generated outside the detector, it would have been absorbed by the Teflon filter, the transmission factor of which is shown in Fig. 5.13. However, as can be seen in Fig. 5.12, the continuous background taken with the filter was same as that without the filter. Therefore, we concluded that the continuous background was created inside the detector due to the detector incomplete charge collection background.

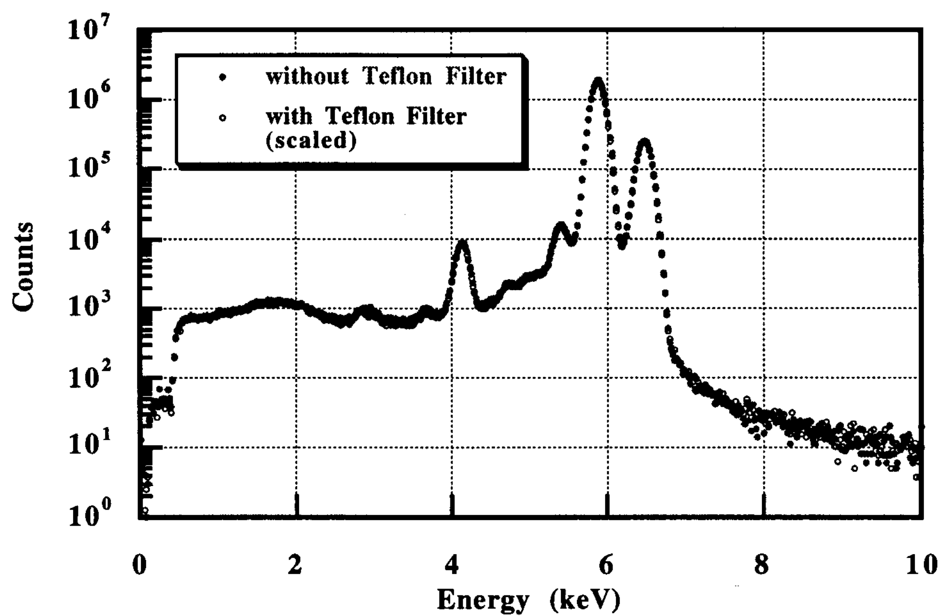

Fig. 5.12 Filtering study of Fe^{55} spectra. Data were taken with and without a 25 μm Teflon filter. The data taken with the filter was scaled to the data without the filter.

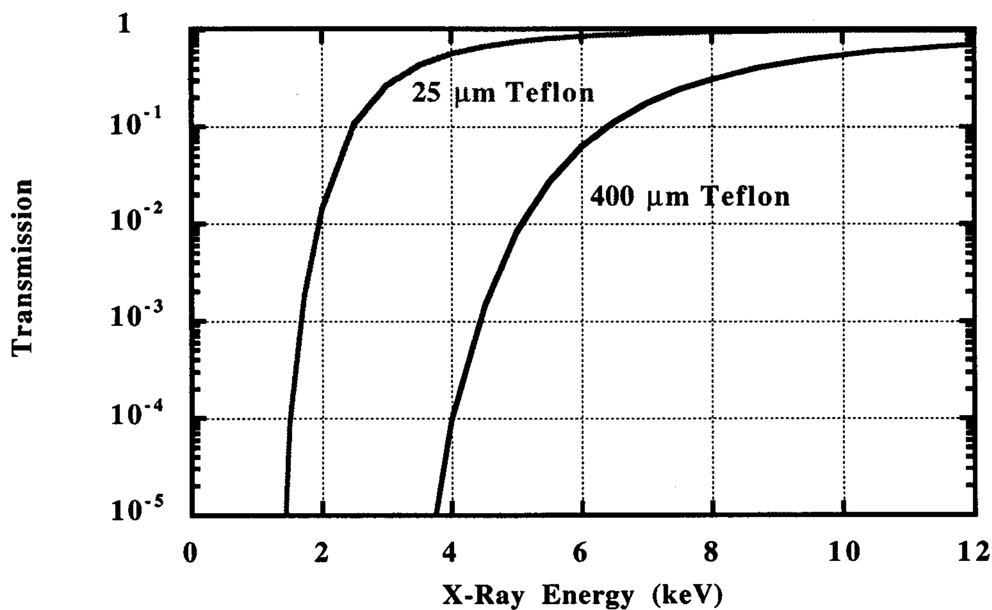

Fig. 5.13 Transmission factors of 25 μm and 400 μm Teflon filters.

From Fig. 5.12, it is found that the intensity of the detector incomplete charge collection background between 0 and 4 keV was about 8×10^{-3} of the Mn K fluorescence signal intensity. At 1 keV, the background intensity per 10 eV was about 2×10^{-5} of the Mn K fluorescence signal intensity.

5.4.2 Detector Incomplete Charge Collection Background in the SR TXRF Spectrum

Next, we determined the contribution of the detector incomplete charge collection background in SR TXRF spectra by performing a filtering study. In this study, we used thin (25 μm) and thick (400 μm) Teflon filters placed in front of a Si (Li) detector, as we did in the previous section, to differentiate between x-rays generated from a sample and those created inside the detector.

The result of the filtering study is shown in Fig. 5.14. Two spectra were taken with an incident beam with the energy of 10.6 keV, which generated scattered x-ray peaks at 10.6 keV. The two spectra were scaled using the scattered x-ray peak intensity. The fluorescence peaks from S, Cl, Fe, Cu, and Zn were created from the impurities on the Si wafer. The fluorescence peaks of Zn overlapped the escape peaks.

The filtering study showed that the 400 μm filter absorbed the spectrum more than the 25 μm filter. The continuous background below 5 keV was also greatly reduced by the 400 μm filter and, especially, the Si fluorescence signals were completely absorbed.

To check the residual background below 5 keV, we modeled the spectrum taken with the 400 μm filter.

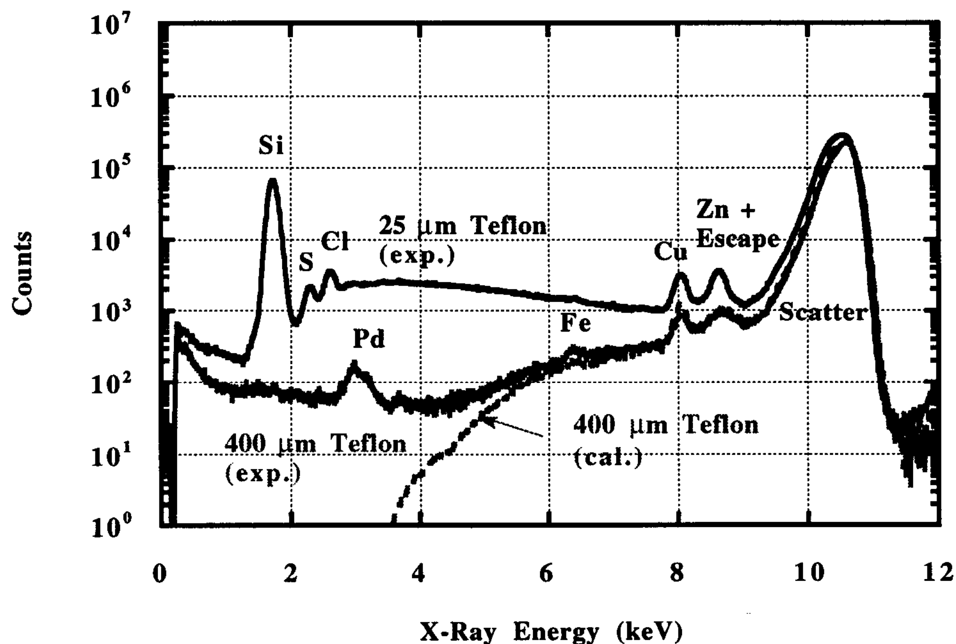

Fig. 5.14 The results of filtering study for the SR TXRF spectra. Data were taken with 25 µm and 400 µm Teflon filters, respectively.

The spectrum was modeled by multiplying the spectrum taken with the 25 µm filter by the Teflon transmission factor with the thickness of 375 (= 400 - 25) µm. For the transmission factors of the Teflon filters, see Fig. 5.13. This modeling assumed that the whole spectrum taken with the 25 µm filter was made up of x-rays generated from a Si wafer.

The result of the modeling is shown in dashed line in Fig. 5.14. From this figure, it was found that the experimental data below 5 keV was much higher than the theoretical modeling curve. From this result, we concluded that the background below 5 keV is generated inside the detector due to the detector incomplete charge collection background.

The intensity of the detector incomplete charge collection background between 0 and 4 keV was about $4x10^{-3}$ of the scattered x-ray intensity. At 1 keV, the background intensity per 10 eV was about $1x10^{-5}$ of the scattered x-ray intensity. The detector incomplete charge collection background component was estimated to be less than 10% of the continuous background in the spectrum taken with the 25 μm Teflon filter.

Note that the detector incomplete charge collection background intensity in Fig. 5.14 was lower than that in Fig. 5.12 by a factor of about 2. This was due to the difference in incident x-ray energy. The x-rays with higher energy generated lower detector incomplete charge collection background because the incident x-ray penetration depth into the Si crystal is longer and less electron-hole pairs are generated near the surface of the crystal, where the electron-hole pairs tend not to be completely collected.

Note that the L fluorescence signal peak of Pd at 3 keV was observed in the data taken with the 400 μm Teflon filter. The Pd signal peak was created inside the type 2 detector from a Pd contact. However, the Pd peak was not observed in Figs. 5.11 and 5.12, which were taken with the detector which did not have the Pd contact. For details of the Pd contact, see Chs. 3 and 4.

This section discussed the contribution of the detector incomplete charge collection background on the SR TXRF continuous background. We conclude that the detector incomplete charge collection background is less than 10 % of the continuous background at 5 keV, which is negligible compared to the photoelectron bremsstrahlung.

5.5 X-Ray Raman Scattering

X-ray Raman scattering is an inelastic scattering of x-rays that occurs resonantly when the energy of incident x-ray is close to but less than an inner-shell absorption edge of a material [18]. In quantum mechanics, x-ray Raman scattering is represented as a second-order process, which can be described using energy diagrams (Fig. 5.15) [29].

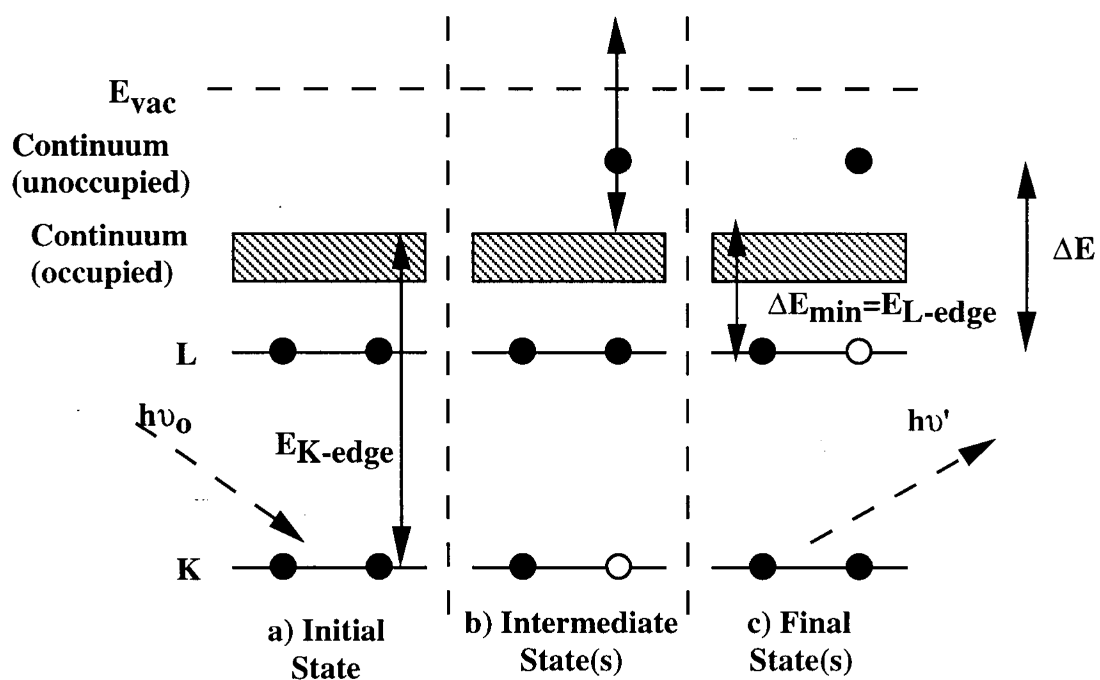

Fig. 5.15 The energy diagram of x-ray Raman scattering. a) an initial state. b) intermediate state(s) and c) final state(s). The incident x-ray ($h\upsilon_0$), and scattered x-ray ($h\upsilon'$), are shown as an arrow. The K-level and L-level are shown by a solid line. Continuum states are represented using shaded area. Electrons and vacancies are shown as the black and white circles, respectively.

In the initial state (Fig. 5.15.a), an x-ray with an energy of $h\upsilon_0$ is incident on an atom. Note that the incident x-ray energy is smaller than the K-shell absorption-edge, $E_{K\text{-}edge}$. Then, a K-shell electron is transferred to an unoccupied state in the continuum or above the vacuum level (Fig. 5.15.b). This state is referred to as a intermediate state.

Although the transition to an intermediate state violates conservation of energy, it is "virtually" allowed in quantum mechanics before the initial state transfers to a final state, in which the conservation of energy is satisfied. The contribution of the intermediate states characterizes the x-ray Raman scattering.

In the final state, an x-ray is emitted with the energy $h\upsilon'$ and an electron is excited from the L-shell to a state with an energy ΔE higher that the L-shell (Fig. 5.15 (c)). The energy of the scattered x-ray emitted in the final state is found to be,

$$h\upsilon' = h\upsilon_o - \Delta E \tag{5.39}$$

Because ΔE can have a spread in energies, the spectrum of the x-ray Raman scattering becomes continuous.

As can be seen in Fig. 5.15 (c), ΔE has the low energy limit, ΔE_{min}, which is equal to the L-shell absorption-edge, $E_{L\text{-}edge}$. Therefore, the x-ray Raman scattering has a high energy limit defined by Eq. (5.40),

$$h\upsilon'_{max} = h\upsilon_o - \Delta E_{min} = h\upsilon_o - E_{L-edge} \tag{5.40}$$

As a result, x-ray Raman scattering creates a characteristic profile up to an energy equal to the incident x-ray energy minus the L-shell absorption-edge. When 1.74 keV x-rays are incident on Si atoms with a L-shell absorption edge at 0.1 keV, x-ray Raman scattering is generated up to an energy of 1.74 keV - 0.1 keV = 1.73 keV.

X-ray Raman scattering cross-section, $\frac{d^2\sigma}{dE_2 d\Omega}$ (mbarns/keV/sr), is given by

$$\frac{d^2\sigma}{dE_2 d\Omega} = \frac{r_o^2}{2E_K}\left[C_1^{pol} + C_2^{pol}\cos^2\theta\right] \qquad (5.41),$$

where

E_2 = scattered x-ray energy (keV),

Ω = solid angle subtended by a detector (sr),

r_o = classical electron radius (= 2.818×10^{-13} cm),

E_K = K-shell absorption-edge (keV),

C_1^{pol} and C_2^{pol} = coefficients, and

θ = observation angle with respect to the linear polarization vector of incident beam.

The coefficients C_1^{pol} and C_2^{pol} were calculated by Gavrila [29], [30], [31], [32]. For the geometry of the observation angle, see Fig. 5.16.

The x-ray Raman scattering cross-sections from a Si atom calculated by Eq. (5.41) is shown in Fig. 5.17. The horizontal axis is the energy of the scattered x-ray in units of eV. The vertical axis is the x-ray Raman scattering cross-section in units of mbarns/keV/sr.

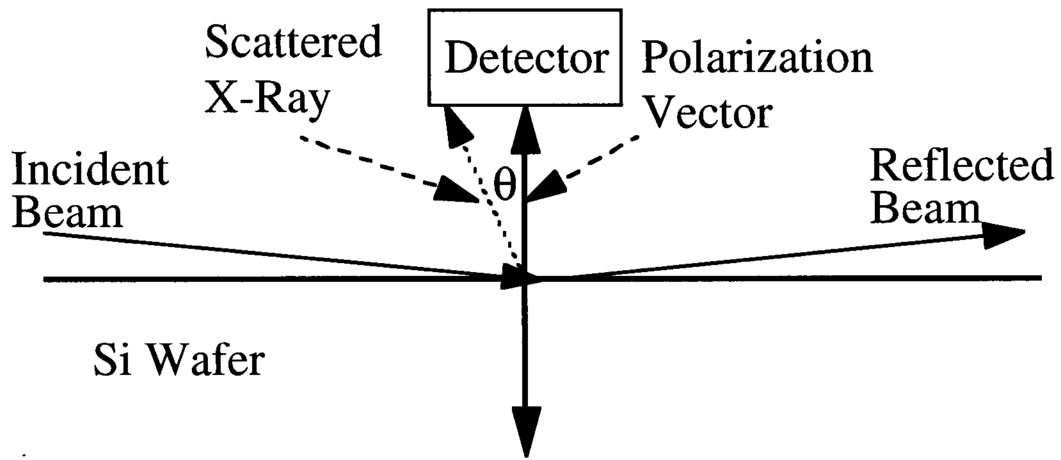

Fig. 5.16 The observation angle, θ, with respect to polarization vector.

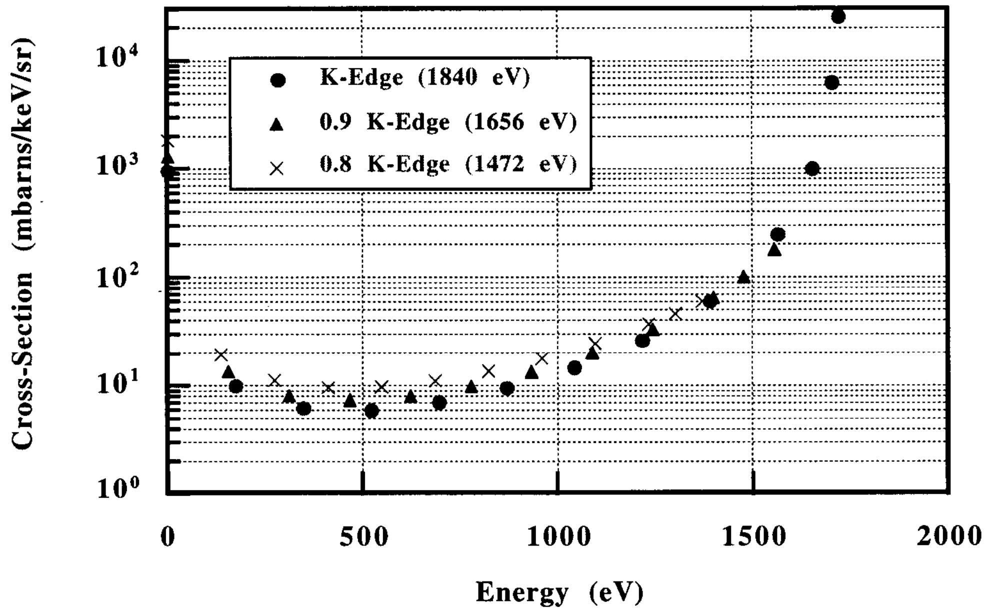

Fig. 5.17 The x-ray Raman double scattering cross-sections from a Si atom. The cross-sections were calculated for incident x-ray energies of 0.8 x Si K-edge (1472 eV), 0.9 x Si K-edge (1656 eV), and Si K-edge (1840 eV).

The cross-sections were calculated at θ =0 for incident x-ray energies of 0.8 E_{abs} (1472 eV), 0.9 E_{abs} (1656 eV), and E_{abs} (1840 eV), where E_{abs} is the Si K-shell absorption-edge. From Fig. 5.17, it is found that the cross-sections increase up to the energy equal to the incident x-ray energy minus Si L-shell absorption-edge ($E_{LIII\ abs}$ = 0.1 keV). Fig. 5.17 corresponds to the profile of the x-ray Raman scattering before being measured by a detector.

Note that the cross-sections blows up as the scattered x-ray energy approaches to zero. This phenomenon is called the infrared divergence [4], [5], [32]. Note that the infrared divergence could not be observed in our SR TXRF measurements because absorption filters in front of the detector significantly attenuate the low energy x-rays.

The actual profile of the x-ray Raman scattering is obtained by convoluting the cross-section with detector broadening, which is represented by a Gaussian distribution with the standard deviation equal to the FWHM of the Si (Li) detector [26]. This is shown in Fig. 5.18. The parameters used in the calculation were : Si atoms for the target material, 1740 eV for the incident x-ray energy, 100 eV for the detector FWHM, a 5 μm Be filter for the absorption filter placed in front of the detector.

The Be filter eliminated the low energy x-rays including the x-rays due to the infrared divergence mentioned above. In Fig. 5.18 (a), the spectra in the energy region between 200 eV and 1800 eV is shown. An expanded region between 1450 eV and 1750 eV is shown in Fig. 5.3.b.

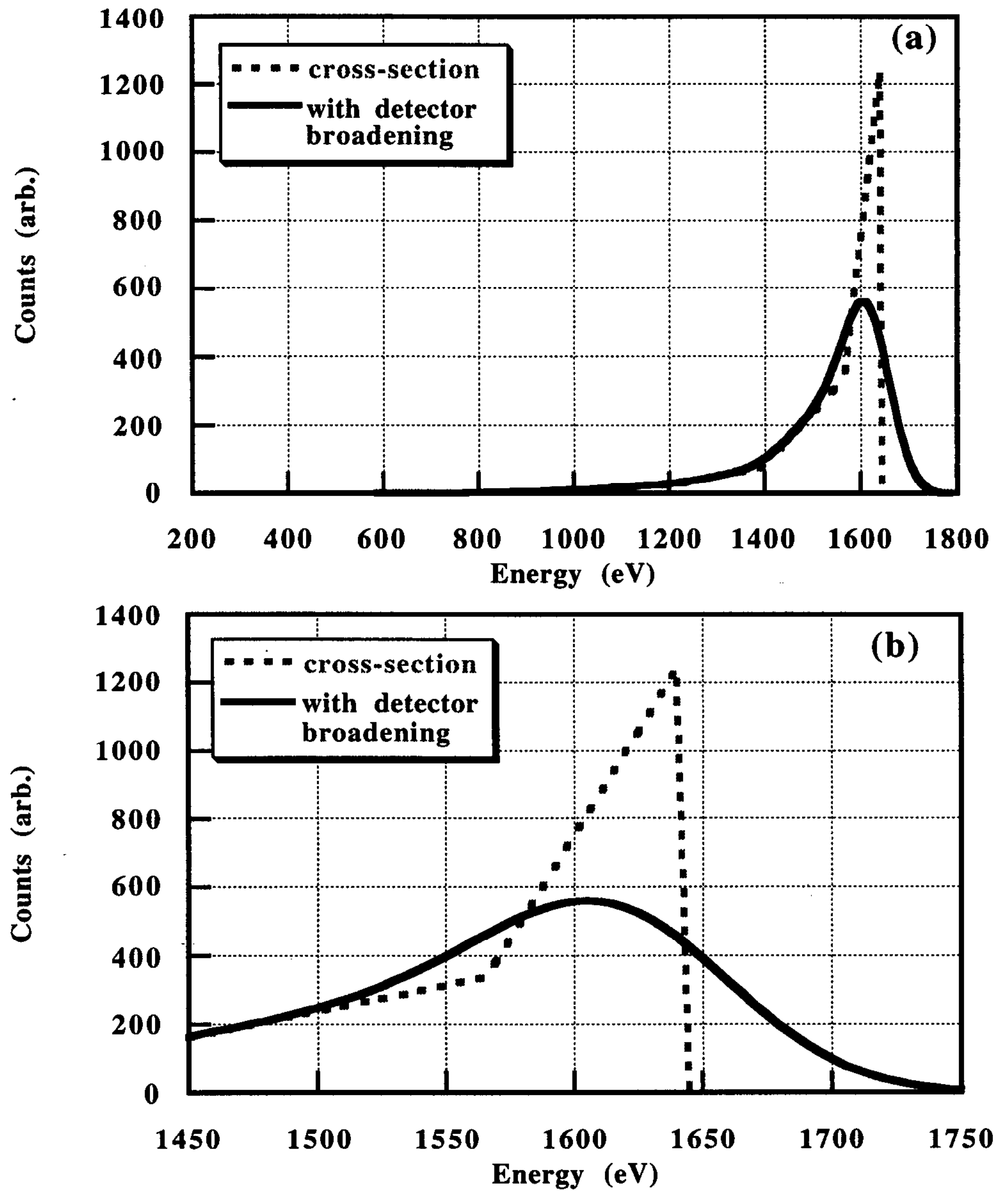

Fig. 5.18 The profiles of the x-ray Raman scattering of 1740 eV x-rays from silicon atoms passing through a 5 μm Be filter with and without the broadening by the detector resolution (FWHM of 100 eV). Fig. 5.18 (a) shows the energy range between 200 eV and 1800 eV. Fig. 5.18 (b) shows the range between 1450 eV to 1750 eV.

We observed two significant differences between the two curves in Fig. 5.18 (a). First, the detector broadening lowered the maximum x-ray Raman intensity to about half of what it could be without the broadening, while the profile in the tail below 1500 eV did not change very much. The x-ray Raman profile was primarily broadened in the energy range between 1500 eV and 1750 eV as shown in Fig 5.18 (b).

The second significant difference is the energy of the maximum. The detector broadening changed the maximum energy of the peak from 1640 eV to 1605 eV. As can be seen in Fig. 5.18 (b), this is simply a result of the convolution of the symmetric Gaussian detector resolution profile with the triangular-like shape of the Raman profile. Note that a change in the center position does not occur in symmetric peaks such as the fluorescence signal peaks.

5.5.1. Comparison of the Theoretical Model With Experimental Data

SR TXRF spectra taken from a silicon wafer are shown in Figs. 5.19. The data were taken by use on BL 6-2 at SSRL (see Ch. 3 and Ch. 4). The energies of the incident x-ray beam used for the measurements were 1500 eV (bottom), 1600 eV (middle), and 1700 eV (top), respectively. In Figs 5.19, three different peaks are observed. The first peak is the Si fluorescence peak at 1740 eV.

The second peak is at incident x-ray energy, which is composed of the Rayleigh and Compton scattering x-rays, which shifts with the incident x-ray energy, as expected. The Rayleigh and Compton scattered signal peaks overlap each other because the difference in energy between these x-rays (about 50 eV) is small compared to the detector energy resolution. The scattered x-ray peak at the incident x-ray energy of 1700 eV also overlaps the silicon fluorescence peak.

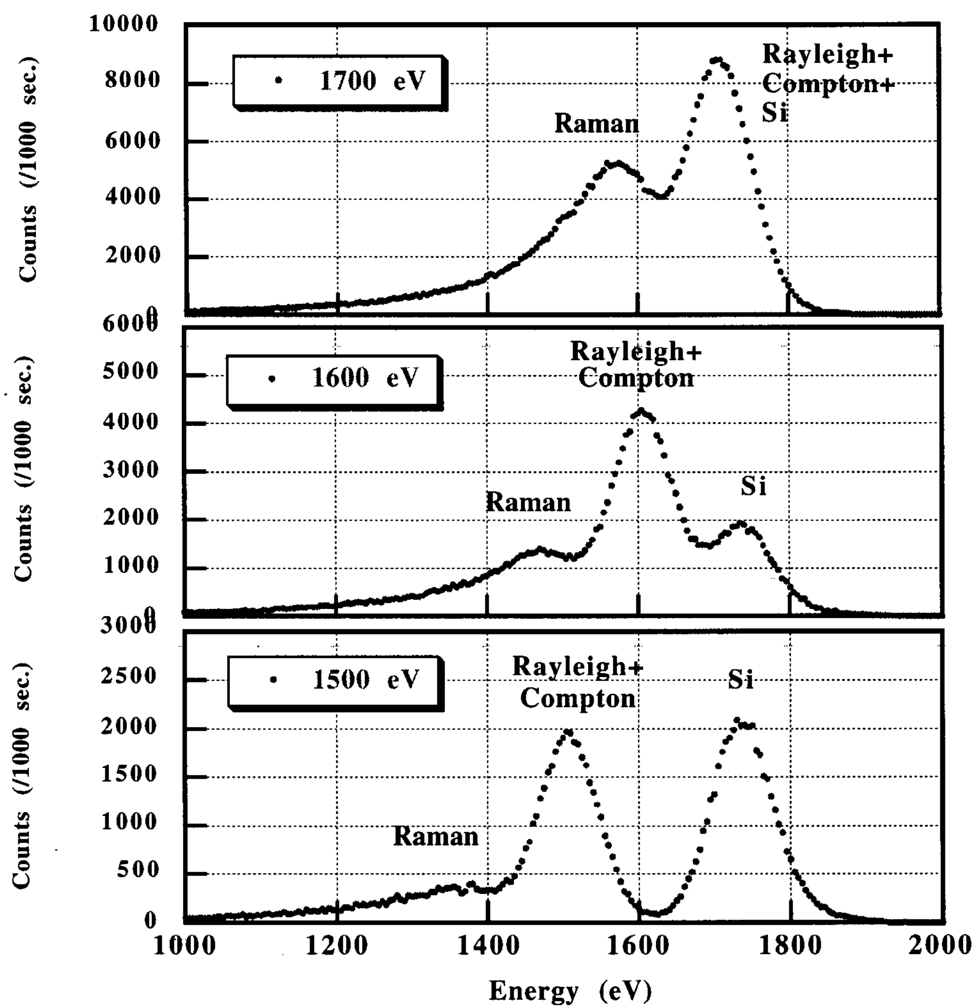

Fig. 5.19 SR TXRF spectra taken from a silicon wafer using incident x-ray energies of 1500 eV (bottom), 1600 eV (middle), and 1700 eV (top). Data were taken using BL 6-2 at SSRL with 1000 sec. measurement times.

The third peak is located below the scattered x-ray peak. It was found that this peak shifted with the incident x-ray energy and its maximum was a constant value (135 eV) below the incident x-ray energy, which was the Si L-shell absorption edge (~100 eV) plus the peak shift due to the detector convolution (35 eV).

In order to check the profile of the third peak, we normalized the three spectra using the oxygen fluorescence signals (at 523 eV) coming from a native oxide (Fig 5.20). The horizontal axis of Fig. 5.20 ranges from 200 eV to 2000 eV and the vertical axis is shown on a log scale. In addition to the O fluorescence peaks, the F fluorescence peaks (at 677 eV) were present. They were created from impurities left on the wafer surface during HF cleaning processes. Significant changes between these spectra were observed in the energy range between 1350 eV and 1800 eV.

From the observations of the peak shift in Fig. 5.19 and peak profile in Fig. 5.20, we concluded that the third peak was generated due to the x-ray Raman scattering.

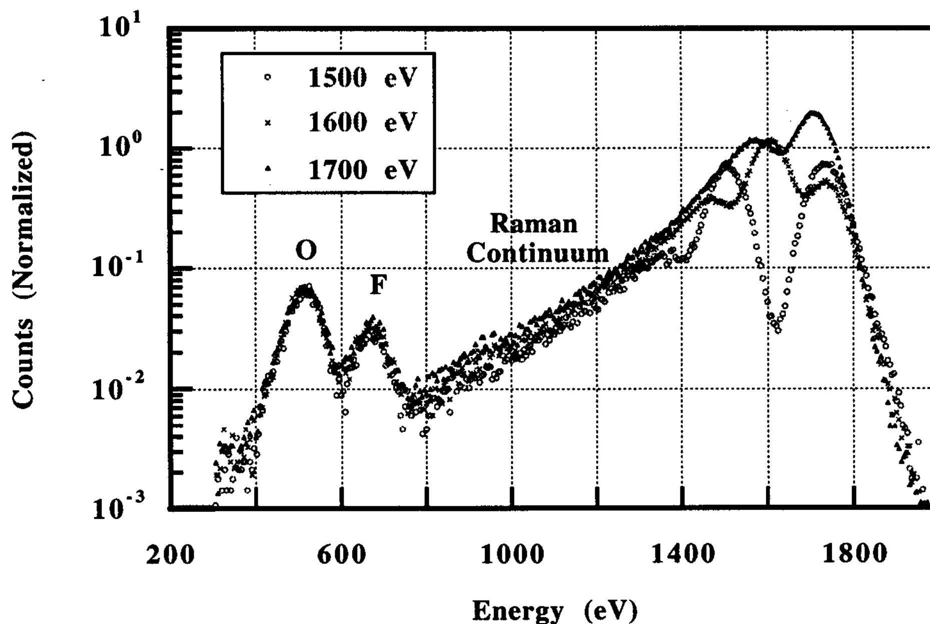

Fig. 5.20 SR TXRF spectra normalized to the oxygen fluorescence x-ray intensity.

Finally, we compare the theoretical modeling curve for the x-ray Raman scattering with experimental data (Fig. 5.21). In order to model the x-ray Raman scattered x-rays, we took data from an Si wafer with intentional Al contamination at a concentration of $8x10^{12}$ atoms/cm^2. The Al fluorescence intensity from the standard wafer was used for normalizing the theoretical modeling profile to the experimental data.

The modeling equation for the x-ray Raman scattering intensity, I_{Raman}, is given by

$$I_{Raman}(E_0, E_x, \alpha) = \frac{N_{Si} \cdot \zeta(\alpha) \frac{d^2\sigma}{dE_x d\Omega} \cdot dE_x \cdot T_{Be}(E_x)}{A_{Al} \cdot \sigma_{AlK}(E_0) \cdot \omega_{AlK} \cdot T_{Be}(E_{AlK})} \quad (5.42),$$

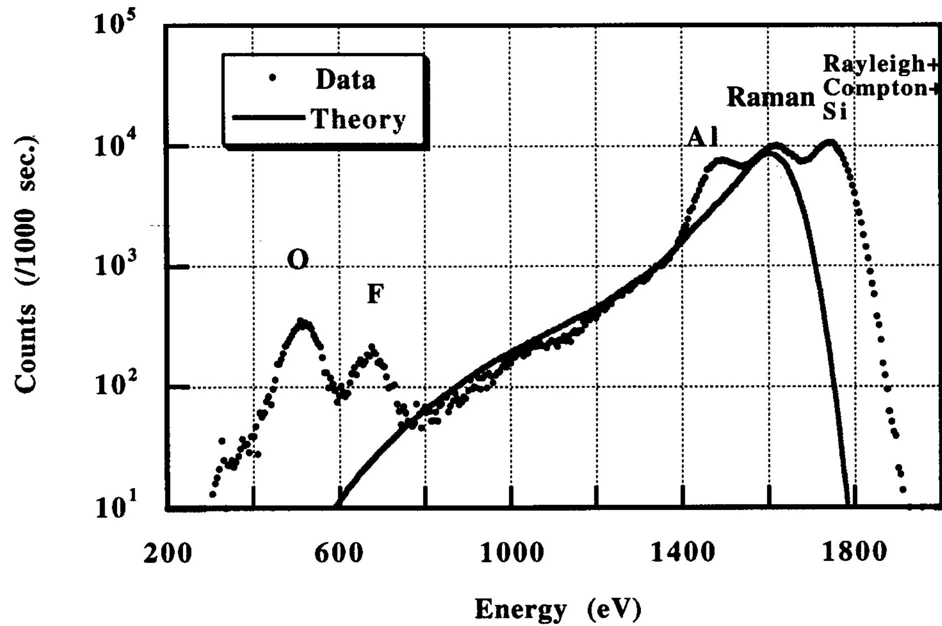

Fig. 5.21 Comparison of the theoretical modeling curve and the experimental data for the x-ray Raman profile at a 1740 eV incident x-ray energy. The data were taken from a silicon wafer with $8x10^{12}$ atoms/cm^2 of Al.

where

$\frac{d^2\sigma}{dE_x d\Omega}$ = x-ray Raman scattering cross-section (mbarns/keV/sr),

E_0 = incident beam energy (1740 eV),

E_x = scattered x-ray energy (keV),

dE_x = energy per channel (5 eV/Ch),

N_{si} = Si volume density ($5x10^{22}$ atoms/cm^3),

ζ = incident x-ray penetration depth (50 Å),

A_{Al} = aluminum areal density ($8x10^{12}$ atoms/cm^2),

E_{AlK} = aluminum K fluorescence energy (1.49 keV),

α = angle of incidence (at 0.5 deg.),

σ_{AlK} = the ionization cross-section of aluminum K-shell ($1.3x10^5$ barns) [9],

ω_{AlK} = the fluorescence yield for aluminum K-shell (0.036) [9], and

T_{Be} = the transmission factors of a 5 μm Be absorption filter.

In Fig. 5.21, the theoretical modeling curve of the x-ray Raman scattering is shown by the solid line. The theoretical modeling curve agreed with the experimental data of the continuous background between 700 eV and 1400 eV.

The maximum intensity of the x-ray Raman peak was estimated to be slightly lower than the experimental data. This was because the experimental x-ray Raman peak at 1605 eV overlapped with the Rayleigh and Compton scattered x-ray peaks, and Si fluorescence peaks at 1740 eV.

From Fig. 5.21, it was found that the x-ray Raman scattering is the dominant background when measuring the Al on Si wafers. The MDL for Al is found to be 5×10^{10} atoms/cm^2, which is much worse than the MDLs of 3-d transition metals on Si wafers measured using 10.6 keV incident x-rays (typically 3×10^8 atoms/cm^2). The x-ray Raman scattering degrades the MDL of Al by a factor of about 170 compared to the MDLs of 3-d transition metals.

5.6 Conclusions

This section investigated the SR TXRF backgrounds, which came from photoelectron bremsstrahlung, Si fluorescence signals, scattered x-rays, and detector incomplete charge collection background. The photoelectron bremsstrahlung was successfully modeled by taking into account the photoelectrons escaping out of a wafer surface. Si fluorescence and scattered x-rays were found to be affected by surface oxides. It was also found that the detector incomplete charge collection background was negligible in SR TXRF.

The dominant continuous background in SR TXRF spectra was characterized by the combination of the filtering study, incident angle scan, and intensity calculation. First, the filtering studies revealed that the continuous background components were primary created outside the detector. This indicated that the detector incomplete charge collection background component was negligible.

Second, the angle scans of the continuous background showed the effect of the photoelectron escape, by which the photoelectron bremsstrahlung is decreased. If the scattered x-rays were dominant, the continuous background should have shown the surface oxide effect, by which the scattered x-ray intensity is increased.

Finally, the intensity of the continuous background could be accurately modeled using photoelectron bremsstrahlung. As a result, we concluded that the photoelectron bremsstrahlung was the dominant continuous background in SR TXRF spectrum for 3-d transition metal analysis on Si wafers.

In addition, we modeled the x-ray Raman scattering. The modeling included a detector broadening. The result of the modeling obtained good agreement with data. It was found that the x-ray Raman scattering greatly deteriorated the MDL for AL.

5.7 References

1. A. Simionovici, J.P. Briand, P. Indelicato, and P. Chevallier, Phys. Rev. A **41**, 7 , 3707 (1990).
2. A. J. J. Bose and M. Hart, Nucl. Instr. Meth., **B3**, 232 (1984).
3. F.S. Goulding and J.M. Jacklevic, Nucl. Instrum. Meth. **142**, 323 (1977).
4. V. Marchetti and C. Franck, Phys. Rev. Lett. **65**, 2, 268 (1990).
5. J.P. Briand, A. Simionovici, P. Chevallier, and P. Indelicato, Phys. Rev. Lett. **65** 2, 269 (1990).
6. B.K. Agawal, *X-ray Spectroscopy*, Chapter 1, Berlin Heidelberg : Springer-Verlag, 1991.
7. B.K. Agawal, *X-ray Spectroscopy*, Chapter 4, Berlin Heidelberg : Springer-Verlag, 1991.
8. H.E. Hecht, *OPTICS*, Chapter 11, Massachusetts : Addison-Wesely, 1987.
9. UCRL-50400,V.6.REV.3.
10. G. H. Vineyard, Phys. Rev. **B26**, 4146 (1982).
11. R.H. Pratt, H.K. Tseng, C.M. Lee, Lynn Kissel, Atomic Data and Nuclear Data Tables, **20**, 175 (1977).

12. Lynn Kissel, C.A. Quarles, R.H. Pratt, Atomic Data and Nuclear Data Table, **28,** No.3, 381 (1983).

13. B.K. Agawal, *X-ray Spectroscopy*, Chapter 5, Berlin Heidelberg : Springer-Verlag, 1991.

14. P. Pianetta, N. Takaura, S. Brennan, W. Tompkins, S.S. Laderman, A. Fisher-Colbrie, A. Shimazaki, K. Miyazaki, M. Madden, D.C. Wherry, J.B. Kortright, Rev. Sci. Instrum. **66** 2, (1995).

15. E.C. Montenegro, G.B. Baptista, and P.W.E.P. Duarte, Atomic Data and Nuclear Data Tables, **22**, 2, 131 (1978).

16. B. E. Warren : *X-RAY DIFFRACTION* , (Dover), 37.

17. H. P. Meyer, *INTRODUCTORY SOLID STATE PHYSICS* (Taylor & Francis), 116.

19. R.S. Muller and T.I. Kamins, *DEVICE ELECTRONICS FOR INTEGRATED CIRCUITS*, second edition, p 54.

20. B.L Henke, E.M. Gullikson, and J.C. Davis, Atomic Data and Nuclear Data Tables **54**, 2, 220 (1993).

21. B.E. Warren, *X-RAY DIFFRACTION*, Chapter 12, New York : Dover, 1969.

22. Rigaku Production Report.

23. Y. Inagaki, K. Shima, H. Maezawa, Nucl. Instr. Meth. **B27**, 353 (1987).

24. J.L. Campbell, J.-X. Wang, W.J. Teesdale, Nucl. Instr. Meth. **B43** 490, (1989).

25. B.K. Agawal, *X-ray Spectroscopy*, p192, Berlin Heidelberg : Springer-Verlag, 1991.

26. B.K. Agawal, *X-ray Spectroscopy*, p177, Berlin Heidelberg : Springer-Verlag, 1991.

27. J.H. Scofield, Phys. Rev. A **9** 1041 (1974).

28. N. Takaura, S. Brennan, P. Pianetta, A. Fischer-Colbrie, J.B. Kortright, D.C. Wherry, K. Miyazaki, A. Shimazaki, Advances in X-ray Chemical Analysis Japan, **26s** 113 (1994).

29. J. M. Jaklevic, R.D. Giauque, and A.C. Thompson, Anal. Chem. (1988), 60, 482

30. M. Gavrila, Roum. Phys. Tome 19, **5**, 473 (1974).

31. M. Gavrila, Roum. Phys. Tome 20, **3**, 209 (1974).

32. V. Marchetti and C. Franck, Phys. Rev., **A39**, 2, 647 (1989).

33. S. Brennan, W. Tompkins, N. Takaura, P. Pianetta, S.S. Laderman, A. Fischer-Colbrie, J.B. Kortright, M.C. Madden, D.C. Wherry, Nucl. Instrum. Meth., **A347**, 417(1994).

34. P. Pianetta, N. Takaura, S. Brennan, W. Tompkins, S.S. Laderman, A. Fisher-Colbrie, A. Shimazaki, K. Miyazaki, M. Madden, D.C. Wherry, J.B. Kortright, SLAC-PUB-6612, SLAC/SSRL-0086, LBL-36011, July (1994).

35. R.E. Kirby, D. Wherry, M. Madden, J. Vac. Sci. Techol. A 11(5) 2687 (1993).

36. P.P. Kane, Physics Repors 218, **2**, 67 (1992).

37. J.C.Ashley, C.J.Tung, R.H.Ritchie, and V.E.Anderson, IEEE Trans.Nucl.Sci. **NS-23**, 1833 (1976).

38. F. Biggs, L.B. Mendelsohn, J.B. Mann, Atomic Data and Nuclear Data Tables, **16**, No.3, 201 (1975).

39. M.J. Cooper, Rep. Prog. Phys., **48**, 415 (1985).

40. N. Sakai, N. Shiotani, F. Itoh, O. Mao, M. Ito, H. Kawata, Y. Amemiya, and M. Ando, Journal of Physical Society of Japan, **58**, No. 9, 3270 (1989).

6. EXTRAPOLATION OF THE MINIMUM DETECTION LIMITS FOR DIFFERENT EXPERIMENTAL CONDITIONS

6.1 Introduction

This chapter estimates the Minimum Detection Limits (MDLs) of SR TXRF with advanced synchrotron radiation sources. Sec. 6.2 shows the definition of the MDLs. Sec. 6.3 presents the MDLs of various elements using an incident beam with a fixed energy. Sec. 6.4 presents the MDLs as a function of incident beam energy. Sec. 6.5 describes the MDLs as a function of incident photon flux density. Sec. 6.6 evaluates the MDLs as a function of beam divergence. Sec. 6.7 projects the improvements of the MDLs by use of third generation synchrotron radiation x-ray sources. Sec. 6.8 shows the results of the calculation of SR properties. Finally, Sec. 6.9 concludes this chapter with a summary.

6.2 The Minimum Detection Limits (MDLs)

The Minimum Detection Limits (MDLs) are defined as the minimum detectable concentrations of elements with a standard measurement time, which for TXRF is typically 1,000 sec. [1]. The MDL for a given element Z can be determined experimentally by measuring a sample of a known concentration and using Eq. (6.1),

$$MDL_Z \equiv X_Z \frac{3 \bullet \sqrt{BG_Z}}{S_Z} \qquad (6.1),$$

where

BG : background counts,

S : integrated signal counts,

X : concentration of elemental standard (atoms/cm^2),

Eq. (6.1) represents a statistical criterion in which the signal peak can be distinguished from the background under the signal peak when the signal intensity is higher than 3 times of the square-root of the background intensity.

In this chapter, we will calculate the MDLs obtained using various experimental configurations and compare them to those obtained using our conventional experimental configuration.

6.3 The MDLs of Elements in the Periodic Table

We start by calculating the MDLs for various elements measured by an incident beam with a fixed energy of 11.2 keV, which is the typical beam energy used our 3-d transition metal analysis.

Elements of interest for this study are those with fluorescence energies higher than the Si K fluorescence energy (1.74 keV) and absorption edges lower than 11.2 keV. With these conditions, the elements detectable with Kα fluorescence signals are from P (Z=15, $E_{K\alpha}$ at 2.01 keV) to Ge (Z=32, E_{Kabs} at 11.10 keV), and the elements detectable with Lβ_1 fluorescence signals are from Zr (Z=40, $E_{L\beta 1}$ at 2.12 keV) to Os (Z=76, E_{LIII} at 10.87 keV) [4].

As mentioned in Sec. 6.2, Eq. (6.1) can be used to determine the MDLs by modeling the signal counts and background counts for each of the elements of interest. Fortunately, for most of the elements, the background counts could be determined from the experimental data shown in Fig. 6.1. The spectrum was taken from a nominally clean wafer with unintentional S + Cl contamination. This approach is possible since the signals of interest will simply appear as a peak superimposed on the spectrum for the clean wafer in Fig. 6.1.

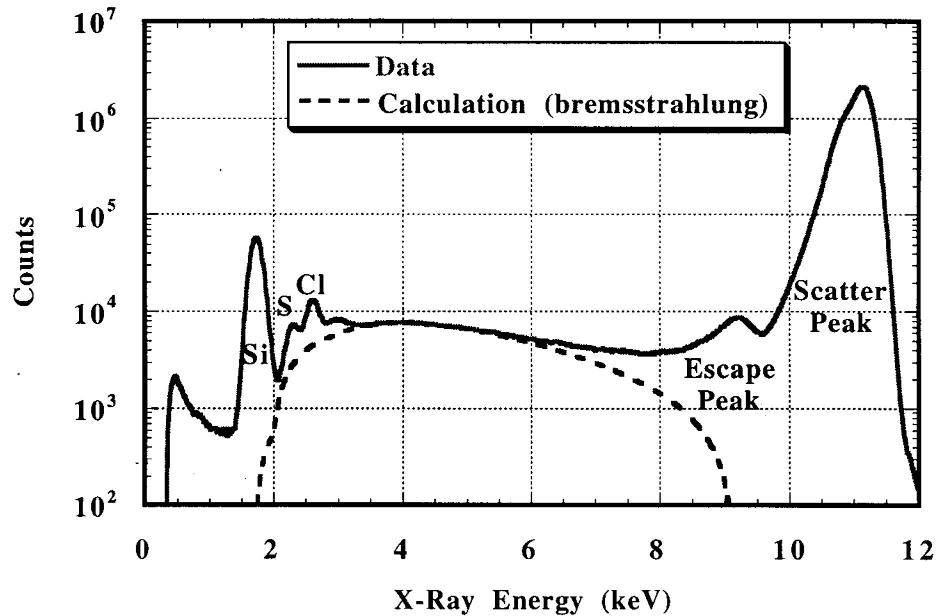

Fig. 6.1 The background spectrum taken from a Si wafer using an 11.2 keV incident beam. Experimental data are shown by the solid line, while the result of the theoretical calculation of the photoelectron bremsstrahlung is shown by the dashed line. In addition to the continuous background, this spectrum consists of the Si fluorescence signal (at 1.74 keV), the scattered x-ray peak (at 11.2 keV), its escape peak (at 9 keV), and the fluorescence signal peaks of S (at 2.31 keV) and Cl (at 2.62 keV). The fluorescence signals of S and Cl were generated from unintentional contamination on the Si wafer surface.

However, for elements whose fluorescence signals overlap with the S and Cl peaks, the background counts were calculated using the formalism in Sec. 5.2. Sec. 5.2 showed that the primary source of the background in the region between 2 and 7 keV was photoelectron bremsstrahlung. As shown in Fig. 6.1, using the formalism in Sec. 5.2, it is possible to accurately calculate the background counts in the region of interest.

Note that the elements whose background counts were calculated using the formalism in Sec. 5.2 were those from P (Z=15, $E_{K\alpha}$ at 2.01 keV) to K (Z=19, $E_{K\alpha}$ at 3.31 keV), and from Zr (Z=40, $E_{L\beta 1}$ at 2.12 keV) to Pd (Z=46, E_{LIII} at 3.33 keV).

The signal counts for all the elements of interest were calculated using Eq. (6.3) (see Ch. 2),

$$S_Z = N_{ph} \cdot X_Z \cdot \sigma_Z(E) \cdot \omega_Z \cdot \kappa_Z \cdot T(E_Z) \cdot d\Omega \qquad (6.3),$$

where

N_{ph} = incident photon flux (photons/sec.),

σ_Z = photo-ionization cross-section (barns)[6],

ω_Z = fluorescence yield [6],

κ_Z = the relative transition probability of $K\alpha$ to $K\beta$ [6],

T = transmission factor due to a filter placed in front of detector [7],

E_Z = fluorescence x-ray energy (keV) [6], and

$d\Omega$ = solid angle subtended by detector (sr).

In Eq. (6.3), the refracted field intensity at a wafer surface is assumed to be one.

By substituting Eq. (6.3) into Eq. (6.2), the MDLs are obtained using,

$$MDL_Z = X_Z \frac{3 \bullet \sqrt{BG_Z}}{N_{ph} \cdot X_Z \cdot \sigma_Z(E) \cdot \omega_Z \cdot \kappa_Z \cdot T(E_Z) \cdot d\Omega} \qquad (6.4).$$

Furthermore, in order to eliminate the incident photon flux and solid angle subtended by detector, which are specific to a particular experiment, it is convenient to use the data from a Ni standard in Eq. (6.4):

$$MDL_Z = \frac{3 \bullet \sqrt{BG_Z}}{\sigma_Z(E) \cdot \omega_Z \cdot \kappa_Z \cdot T(E_Z)} \cdot \frac{X_{Ni} \cdot \sigma_{Ni}(E) \cdot \omega_{Ni} \cdot \kappa_{Ni} \cdot T(E_{Ni})}{S_{Ni}} \qquad (6.5)$$

where

S_{Ni} = the data of Ni signal counts taken from a 1×10^{11} atoms/cm^2 standard (54116 counts), (see Ch. 4)

X_{Ni} = concentration of Ni (1×10^{11} atoms/cm^2).

Eq. (6.5) gives the MDLs as a function of background intensity, photo-ionization cross-section, fluorescence yield, the relative transition probability, and transmission factor [6], [7].

The MDLs calculated by Eq. (6.4) are shown in Fig. 6.2 (a). The horizontal axis of Fig. 6.2 (a) is the atomic number. The vertical axis represents the MDLs in units of

atoms/cm^2. From Fig. 6.2 (a), it is found that the MDLs for these elements range from 2.6×10^8 atoms/cm^2 for (Yb, Z=70) to 3.4×10^{11} atoms/cm^2 for (P, Z=15).

Note that, for reference, Fig. 6.2 (a) also shows the experimental MDLs of Na (Z=11) and Al (Z=13), which were determined using an incident beam with an energy of 1.74 keV. For the measurements of elements with Z lower than Si, we employed a different experimental configuration from that used for 3-d transition metals (see Ch. 4).

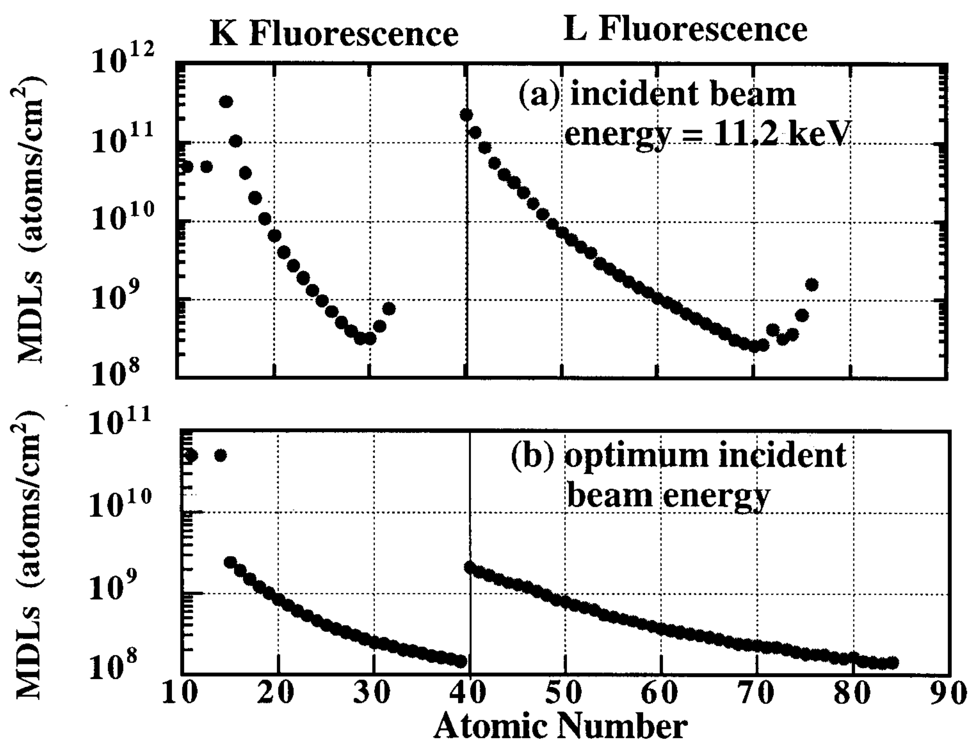

Fig. 6.2 The MDLs of various elements in periodic table. (a) The MDLs from P (Z=15) to Ge (Z=32), and from Zr (Z=40) to Os (Z=76) measured using an incident beam with an energy of 11.2 keV. For reference, the experimental MDLs of Na (Z=11) and Al (Z=13) obtained with an 1.74 keV incident beam are plotted as well. (b) The MDLs from P (Z=15) to At (Z=85) using incident beams with an energy equal to the fluorescence energy of the element of interest plus 3.5 keV.

In this work, the MDLs of the elements from Ga (Z=33) and Y (Z=39), and elements above Ir (Z=77) were not calculated because the absorption edges of interest are greater than 11.2 keV. However, these elements can be measured by tuning the incident beam energy, which will be described in the next section.

6.4 Energy Tunability

It is possible to improve the MDLs for the various elements by tuning the energy of synchrotron radiation and thereby optimizing the photoionization cross-section and minimizing the background counts for each element.

First, consider the photo-ionization cross-section of Ni in Fig. 6.3 [6]. As can be seen in this figure, the photo-ionization cross-section is at its maximum when the incident beam energy is equal to the Ni K absorption edge energy. This results in the maximum core hole creation and, thus, a maximum Ni signal intensity. However, the background intensity is not at its minimum because the primary scattered x-ray peak overlaps the fluorescence peak at this energy. To find the energy for the optimum MDL, we calculated the MDLs of Ni as a function of incident beam energy from 8.5 keV to 12 keV (Fig. 6.4).

The signal intensity was calculated using the cross-section of Fig. 6.3. The background counts under the Ni peak were obtained by assuming that the shape of the background spectrum in Fig. 6.1 was independent of incident beam energy above 8.5 keV and below 12 keV. Therefore, for an arbitrary incident photon energy, E, between 8.5 keV and 12 keV, the horizontal axis of Fig. 6.1 would be, in effect, shifted by dE = E - 11.2 keV, where 11.2 keV is the incident x-ray beam energy in Fig. 6.1. This places the scattered x-ray peak at the new value of incident beam energy.

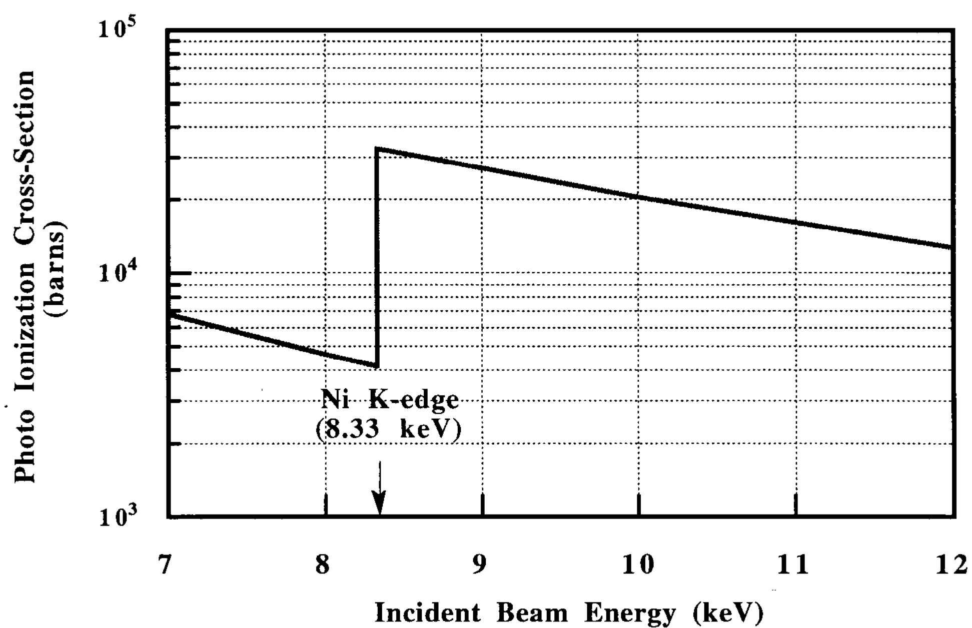

Fig. 6.3 Ni photo-ionization cross-section as a function of incident beam energy.

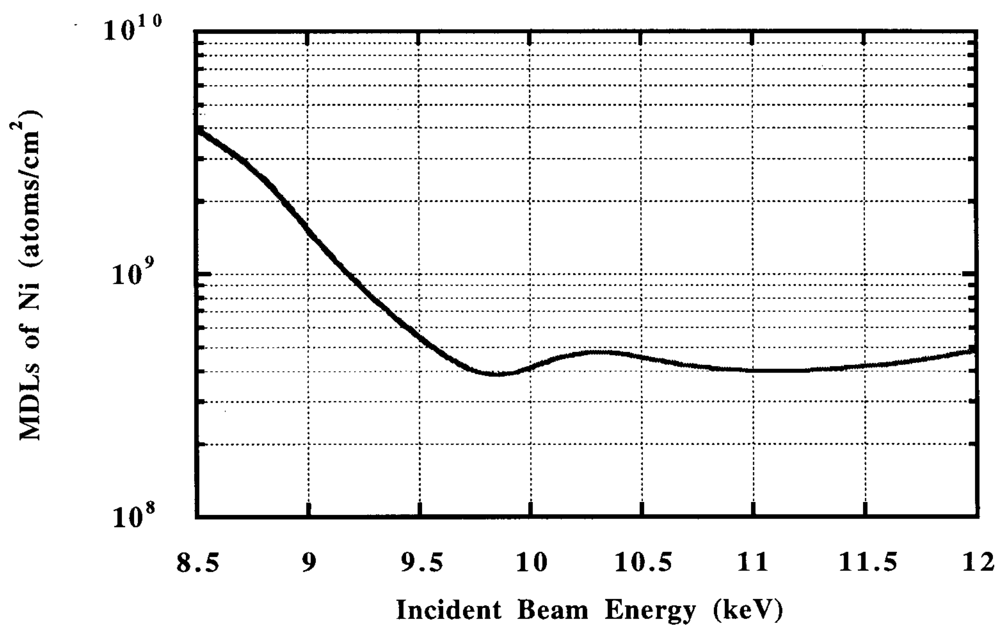

Fig. 6.4 The MDLs of Ni at BL 6-2 as a function of incident beam energy. The calculated MDL at 11.2 keV is normalized to 4×10^8 atoms/cm^2.

The background of interest is then located at 7.47 keV on the shifted axis or 7.47 keV - dE on the original unshifted axis of Fig. 6.1. Therefore, the background counts for 10.2 keV incident beam would be assumed to be equal to the background intensity at 7.47 keV - (10.2 keV -11.2 keV) = 6.47 keV.

In Fig. 6.4, the MDLs are greatly increased around an incident beam energy of 8.5 keV. This is a direct result of the overlap of the scattered x-ray peak with the Ni fluorescence peak. In addition, the MDLs increase slightly around 10.3 keV. This is due to the overlap of the escape peak, which is generated around the energy equal to the incident beam energy minus Si K absorption edge (1.84 keV), with the Ni fluorescence peak [8].

From Fig. 6.4, it was found that the best MDL for Ni is obtained when the incident beam energy is 11 keV, which is 3.5 keV higher than the fluorescence energy (7.48 keV). If we extend this condition to elements other than Ni, we can make an estimate of the MDLs for different elements at an optimum incident beam energy which is 3.5 keV higher than the fluorescence energy of the element of interest.

The MDLs obtained using the optimum incident beam energies are shown in Fig. 6.2 (b). We arbitrarily set the high energy limit of the incident beam energy to be 17 keV. The elements covered in Fig. 6.2 (b) are those with the absorption edges less than 17 keV and fluorescence energies greater than 1.74 keV, i.e., from P (Z=15) to At (Z=85).

The MDLs of these elements ranged from about 1.4×10^8 atoms/cm^2 for Y (Z=39) to 2.4×10^9 atoms/cm^2 for P (Z=15). In comparison to the MDLs in Fig. 6.2 (a) with a fixed incident beam energy (11.2 keV), the MDLs in Fig. 6.2 (b) were greatly improved because of the energy tunability of the incident beam. For example, the MDL of Zr can be improved

by a factor of about 100 by tuning the photon energy to 5.6 keV versus simply using the fixed energy of 11.2 keV.

By tuning the energy up 17 keV, it was possible to include the elements between As (Z=33) and Y(Z=39) and the elements between Ir (Z=77) and At (Z=85). The energy tunability of synchrotron radiation makes it possible to measure most of the elements in periodic table.

6.5 Incident Photon Flux

It is also possible to improve the MDLs by increasing the photon flux density of incident beam. From Eq. (6.2), the MDLs as a function of incident photon flux are given by,

$$MDL_Z(N_{ph1}) = \sqrt{\frac{N_{ph0}}{N_{ph1}}} MDL_Z(N_{ph0}) \qquad (6.5).$$

Because signal and background intensities are simply proportional to the incident photon flux density, the MDLs change with the square-root of incident photon flux.

The Ni MDLs calculated using Eq. (6.5) are shown in Fig. 6.5. The horizontal axis is the photon flux density normalized to that on BL 6-2. The vertical axis plots the MDLs. As shown in Fig. 6.5, by increasing the photon flux density by a factor of 10, the MDL is improved to about 1×10^8 atoms/cm^2 from 4×10^8 atoms/cm^2. Furthermore, by increasing the photon flux density by a factor of 100, the MDL is improved to 4×10^7 atoms/cm^2. An MDL of about 1×10^7 atoms/cm^2 is expected by increasing the photon flux by a factor of 1000.

Theoretically, it is possible to improve the MDLs as much as possible by increasing the photon flux density. As an experimental method of increasing the photon flux density, the use of third generation synchrotron radiation sources will be discussed in Sec. 6.8.

It should be pointed out that, to achieve the MDLs in Fig. 6.5, it is necessary to use a detector system which is capable of handling high count-rate x-ray signals. Our detector system used on BL 6-2 at SPEAR is a Kevex system (model No. 021), which can only handle a count-rate of 10~15 K cps. Detectors which can handle higher count-rates are being developed.

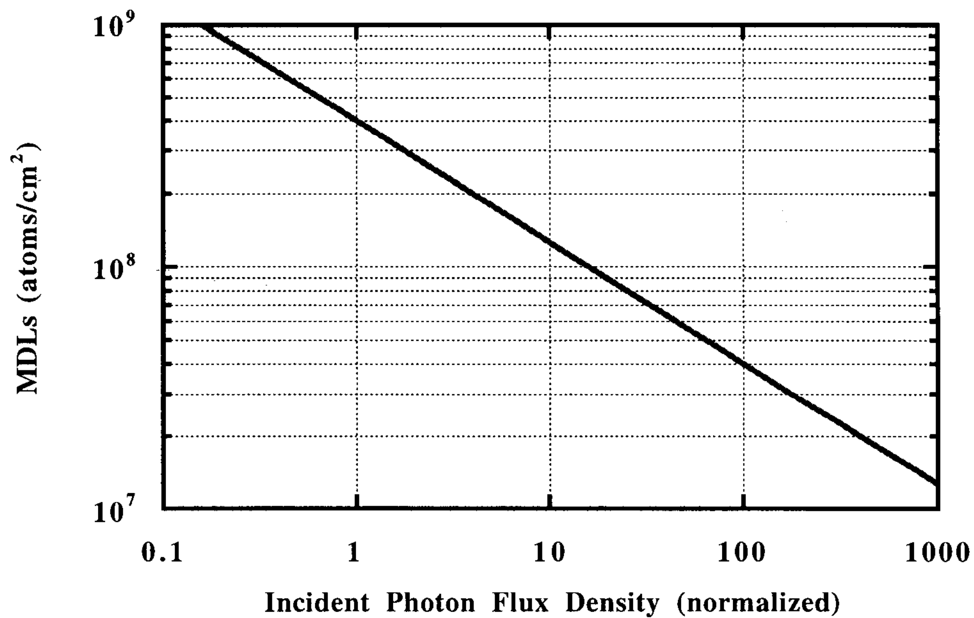

Fig. 6.5 The MDLs of Ni as a function of incident photon flux density. The horizontal axis is the photon flux density normalized to that of BL 6-2.

6.6 Beam Divergence

The beam divergence of synchrotron radiation affects signal and background intensities because the incident x-rays have various angles of incidence resulting in a range of incident x-ray penetration depths. In TXRF, the beam divergence of the synchrotron radiation beam may not be negligible because the beam divergence may be comparable to the angle of incidence.

Theoretically, the beam divergence is taken into account by using a Gaussian distribution function with a standard deviation equal to beam divergence,

$$S\left(E_0,\alpha,N_{ph},\sigma_{x'}\right) \propto \frac{\int_0^\infty R(\alpha)G\left(\alpha,\theta,\sigma_{x'}\right)d\theta}{\int_0^\infty G\left(\alpha,\theta,\sigma_{x'}\right)d\theta} \qquad (6.6),$$

$$BG_Z\left(E,\alpha,N_{ph},\sigma_{x'}\right) \propto \frac{\int_0^\infty R(\alpha)\xi(\alpha)G\left(\alpha,\theta,\sigma_{x'}\right)d\theta}{\int_0^\infty G\left(\alpha,\theta,\sigma_{x'}\right)d\theta} \qquad (6.7),$$

where

α = angle of incidence, and

G = Gaussian distribution function,

$$G(\alpha,\theta,\sigma_{x'}) = \frac{1}{\sqrt{2\pi}\sigma_{x'}} \exp\left(-\frac{(\theta - \alpha)^2}{2\sigma_{x'}^{\ 2}} \right) \qquad (6.8),$$

where

$R(\alpha)$ = refracted field intensity at wafer surface,

$$R(\alpha) = \left(\frac{2\alpha}{\alpha_c} \right)^2 \qquad (6.9),$$

$\zeta(\alpha)$ = incident x-ray penetration depth,

$$\zeta(\alpha) \propto \frac{1}{\sqrt{\alpha_c^2 - \alpha^2}} \qquad (6.10),$$

α_c = critical angle, and

x = distance from a wafer surface.

Note that Eq. (6.6) assumes that an element of interest is present near the surface (Fig. 4.23 (a)). For the expression of the refracted field intensity and incident x-ray penetration depth, see Ch. 2 and references [9].

By substituting Eqs. (6.6) and (6.7) into Eq. (6.2), we calculated the Ni MDLs as a function of beam divergence (Fig. 6.6). Note that, as mentioned in Sec. 6.2, the beam divergence on BL 6-2 is calculated to be 0.046 deg. by the computer code SHADOW [2], [3]. From Fig. 6.6, the MDL of Ni is expected to be improved by a factor of about 2 by decreasing the beam divergence from 0.045 deg. to 0.015 deg. An incident beam with low divergence can be obtained from third generation synchrotron radiation sources, which will be described in the next section.

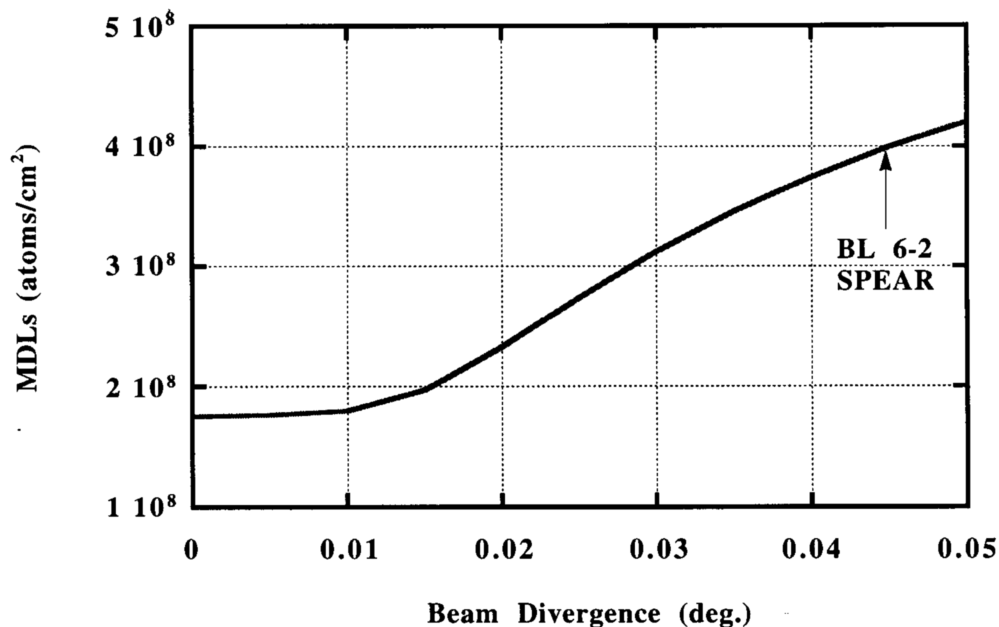

Fig. 6.6 The MDLs of Ni as a function of beam divergence.

6.7 Third Generation Synchrotron Radiation Sources

This section discusses the improvement of the MDLs through the use of third generation synchrotron radiation sources. We start by describing the merits of the low emittance beams of third generation synchrotron radiation sources in Sec. 6.7.1. Second, the radiation from an undulator will be described in Sec. 6.7.2. Third, the MDL for Ni by the use of third generation sources will be estimated in Sec. 6.7.3.

6.7.1 Low Emittance Beams

The third generation synchrotron radiation sources are characterized by low emittance beams, where emittance is an invariant property of the beam defined as the beam divergence times the beam size [11]. An important benefit of low emittance photon beams

for TXRF is the increase in the number of photons hitting the wafer surface. Consider a situation shown in Fig. 6.7 where a photon beam hits the wafer surface in the standard SR TXRF geometry discussed in Ch. 3. Since the angle of incidence is very small, most of the photon beam does not hit the part of the wafer surface in the detector's field of view.

A schematic of the detailed geometry with beam size and detector field of view is shown in Fig. 6.8. Fig. 6.8 (a) shows a cross-sectional view along the direction of the incident beam. Fig. 6.8 assumes the standard 1:1 focusing geometry with the electron beam parameters shown in Tab. 6.1 and the BL 6-2 parameters shown in Table. 6.2 [20].

Fig. 6.8 (b) shows the top view of the geometry, in which the detector is placed normal to the wafer surface with an incident angle of 2 mrad (about 0.11 deg.). Note that these figures are not drawn to scale for clarity of viewing.

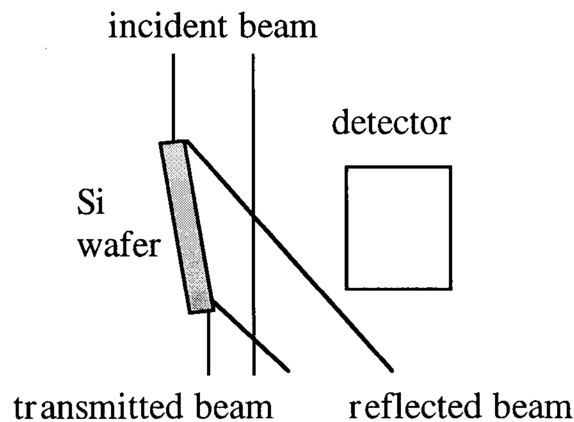

Fig. 6.7 A schematic diagram of the SR TXRF geometry in which a photon beam strikes a Si wafer surface at a glancing angle of incidence. The figure is not drawn in scale.

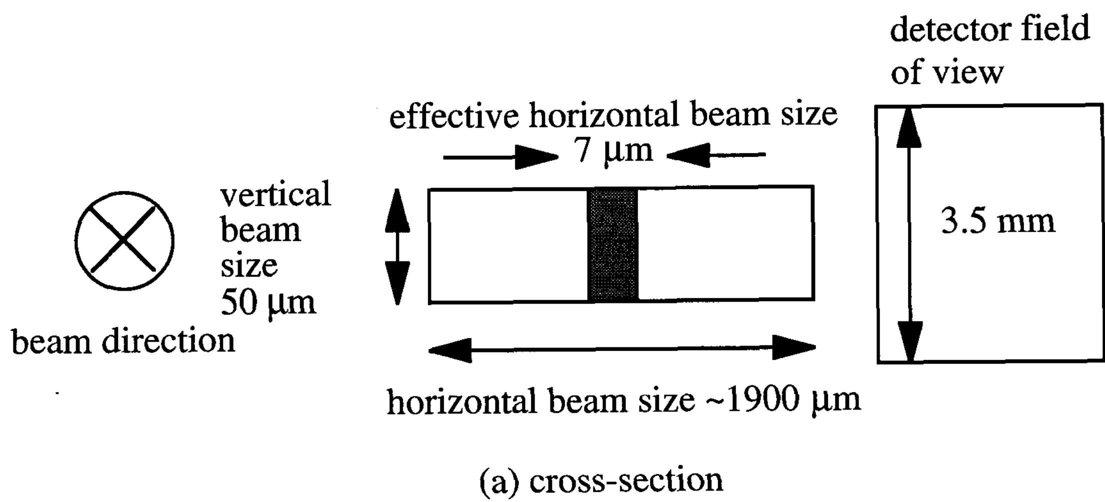

(a) cross-section

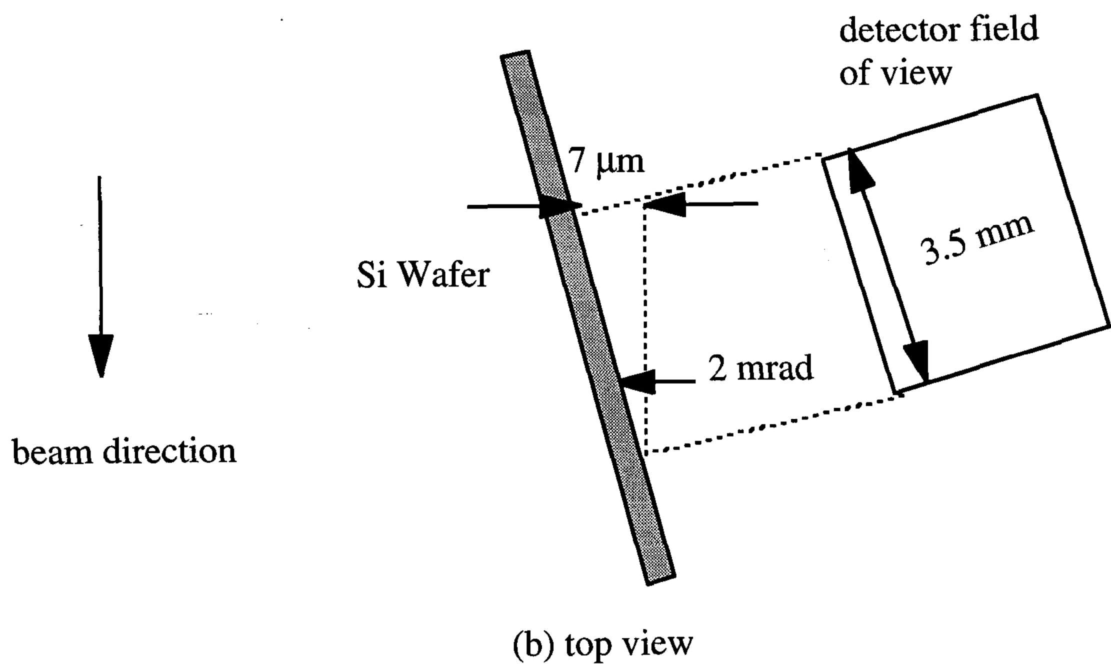

(b) top view

Fig. 6.8 Schematic of the SR TXRF geometry in which a photon beam is incident on a Si-wafer surface with an angle of incidence of 2 mrad (about 0.11 deg.). These figures are not drawn in scale.

Table 6.1 Parameters of storage rings and particle beams.

storage ring	particle energy (GeV)	particle current (A)	horizontal emittance (nm-rad)	vertical emittance (nm-rad)	horizontal beam size (mm)	vertical beam size (mm)
SPEAR	3	0.1	143	1.43	1.9	0.05
SPEAR3	3	0.2	17	0.17	0.3	0.025

Table 6.2 Insertion device parameters.

device	device period (cm)	total periods	insertion device parameter	first harmonic energy (keV)
BL6-2 wiggler	7	27	6.5	0.0576
undulator	2.86	140	1	2

As can be seen in Fig. 6.8, the effective vertical beam size hitting the area on the wafer surface in the detector field of view is simply equal to the original vertical beam size because the detector field view of 3.5 mm is much larger than the vertical beam size (Fig. 6.8 (a)). It should be pointed out that the experimental vertical beam size is about 1 mm. Although the experimental value is larger than the theoretical value shown in Fig. 6.8 (50 μm), it is still smaller than the detector field of view.

On the other hand, in the horizontal direction, only 7 μm of the beam is in the detector's field of view which is determined by the detector size (3.5 mm) times the tangent of angle of incidence (2 mrad). This is much smaller than the actual horizontal beam size of 1900 μm (Fig. 6.8 (b)).

Fig. 6.8 shows that the width of the photon beam, which is in the detector's field of view, is smaller than the actual photon beam size by a factor of about 270. This indicates that most of the incident beam does not hit the analyzed area. Therefore, it should be clear that significant gains in the fluorescence signals would be obtained with smaller horizontal beam sizes. Since low emittance photon beams from third generation sources have small

beam sizes, we will show that the use of the third generation sources will result in the improvement of the MDLs in SR TXRF.

6.7.2 The MDLs for Ni with SPEAR3

This section estimates the improvement of the Ni MDLs through the use of SPEAR3. SPEAR3 is a proposed upgrade of the SPEAR storage ring into a third generation source.

The parameters of SPEAR and SPEAR3 are shown in Table. 6.1 [15], [16]. The SPEAR3 beam current is twice that of SPEAR. The increase in beam current results in a proportional increase in the incident photon flux. Furthermore, SPEAR3 reduces the horizontal beam size by a factor of about 7 and the vertical beam size by a factor of 2.

It should be pointed out that the properties of the photon beam are directly related to those of the electron beam. Therefore, the small electron beam size for SPEAR3 will result in a smaller photon beam size and subsequent increase in the photon flux hitting the wafer surface, as shown in the Sec. 6.7.1.

In this study, we take into account the insertion devices of the BL 6-2 wiggler and horizontal and vertical undulators. For the BL 6-2 wiggler, see Ch. 2 and reference [20]. The horizontal undulator is a standard undulator on SPEAR3, which employs a vertical magnetic field resulting in a horizontal polarization vector for the photon beam as is used in the standard TXRF geometry. The vertical undulator employs a configuration in which the magnetic field is in the horizontal direction and results in a vertical polarization vector. This configuration allows the wafer to be placed horizontally in the beam, which results in a vertical photon beam deflection.

The parameters of the two possible insertion devices for SPEAR3 are shown in Table. 6.2 [17], [18]. These are the existing BL 6-2 wiggler and a new undulator. The first harmonic energy for the undulator radiation is 2 keV for a gap of 1.6 cm for the undulator magnets. For TXRF measurements, the 5th harmonic would be utilized. The equation for calculating the harmonic energy is shown in Eq. (6.14) in Sec. 6.8.3.

Using the parameters in Tables 6.1 and 6.2, the flux densities obtained from SPEAR3 were given by Brennan (Table. 6.3) [19]. The photon flux density (photons/sec./mm^2) was calculated by dividing the total photon flux by electron beam size. The equations for the total photon flux are shown in Sec. 6.8.

The linear flux density (photons/sec./mm), which is proportional to the number of photons hitting a wafer surface, was given by Eq. (6.11),

$$\begin{aligned}&\left[\text{linear flux density}\right](\text{photons/sec./mm}) = \\ &\quad \left[\text{flux density}\right](\text{photons/sec./mm}^2) \times \left[\text{beam size}\right](\text{mm})\end{aligned} \quad (6.11),$$

The beam size on the right-side of Eq. (6.11) is the size of the photon beam perpendicular to the wafer surface, as shown in Sec. 6.7.1. For the flux density of the BL 6-2 wiggler and horizontal undulator, the beam size was assumed to be equal to the vertical electron beam size.

Table 6.3 Photon flux with SPEAR3.

storage ring	insertion device	flux density (photons/sec./mm^2)	linear flux density (photons/sec./mm)
SPEAR	BL 6-2 wiggler	4E+15	2E+14
SPEAR3	BL 6-2 wiggler	4E+16	2E+15
SPEAR3	horizontal undulator	2E+16	5E+14
SPEAR3	vertical undulator	2E+16	7E+15

On the other hand, for the flux density of the vertical undulator, it was assumed to be equal to the horizontal electron beam size. We will calculate the MDL for Ni as a function of the square-root of the photon flux density as shown in Eq. (6.5) in Sec. 6.5.

In addition to the increase in the photon flux density, we calculated the divergence of the photon beams as shown in Table 6.4. The beam divergence with the BL 6-2 wiggler were obtained using SHADOW. The output of the calculation with SHADOW is shown in Sec. 6.8. The divergence with the horizontal and vertical undulators were obtained from reference [20]. With the horizontal and vertical undulators, the divergence of the photon beams would greatly be reduced to 0.0002 deg. and 0.00003 deg., respectively. The reduction of the beam divergence would result in the improvement of the Ni MDL by a factor of about 2, as shown in Sec. 6.6.

The projected MDLs for Ni with SPEAR3 are shown in Table 6.4 and Fig. 6.9. The BL 6-2 wiggler on SPEAR3 would improve the Ni MDL relative to the same wiggler on SPEAR ($1.3x10^8$ atoms/cm^2 versus $4x10^8$ atoms/cm^2). This is due to an increase in the photon flux density. The standard undulator (i.e., horizontal undulator) on SPEAR would improve the MDL relative to the wiggler on SPEAR ($1.3x10^8$ atoms/cm^2 versus $4x10^8$ atoms/cm^2). This is due to both an increase in the photon flux density and an decrease in the beam divergence.

Table 6.4 Projected MDLs for Ni with SPEAR3.

storage ring	insertion device	flux density (scaled)	beam divergence (deg.)	MDLs (atoms/cm^2)
SPEAR	BL 6-2 wiggler	1	0.046	4.0E+08
SPEAR3	BL 6-2 wiggler	1	0.046	1.3E+08
SPEAR3	horizontal undulator	2.5	0.0002	1.3E+08
SPEAR3	vertical undulator	35	0.00003	3.4E+07

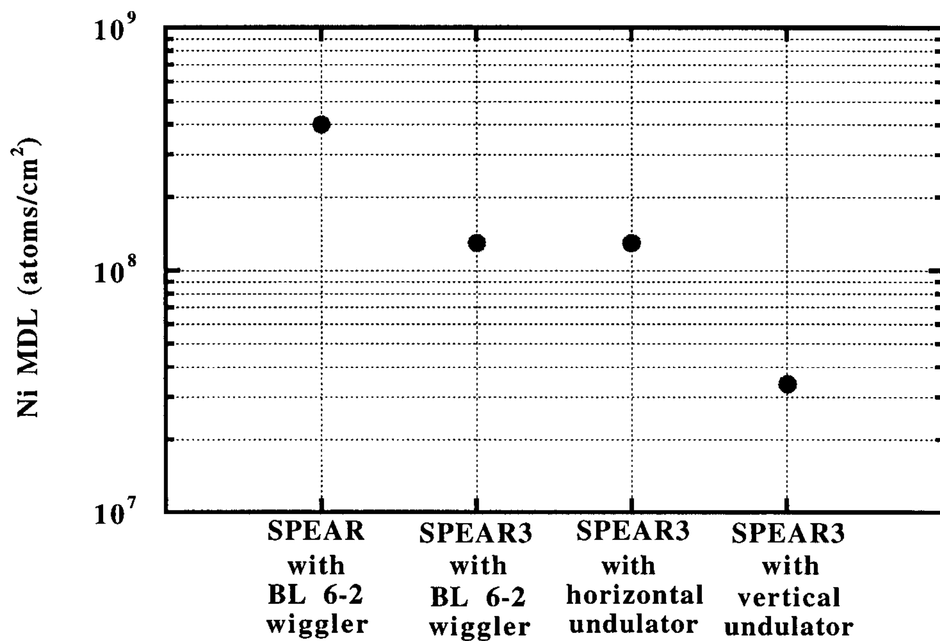

Fig. 6.9 The estimated MDLs of Ni obtained by use of third generation synchrotron radiation sources.

Fig. 6.9 also compares two different undulator configurations. The smaller footprint of the beam on the wafer in the vertical undulator configuration would directly result in an increase in flux density and thus subsequent reduction in the Ni MDL (1.3×10^8 atoms/cm^2 versus 3.4×10^7 atoms/cm^2).

We conclude that the combination of third generation synchrotron radiation sources with the vertical undulator will make it possible to achieve the detection limits less than 5×10^7 atoms/cm^2.

6.8 The Calculation of SR Properties

6.8.1 The Parameters Used for the SHADOW Calculation for BL 6-2 Wiggler on SPEAR

Note: 1) there are some bugs in "SHADOW primer 2" and,

2) you may see the message, "disk quota exceeded", during the calculation.

```
Number of periods          =        27
------ INPUT ---------
Insertion device  Wavel. [ m ] =  7.000000000000001E-002
Beam Energy          [ GeV ] =  3.00000000000000
K                          =  6.50000000000000
Field correction factor    =  1.00000000000000
------ OUTPUT ---------
Gamma                      =  5870.15822410162
Peak Magnetic field  [ Tesla ] =  0.994569181061753
Fundamental          [ Ev ] =  55.1783664801638
Fundamental     [ Angstroms ] =  224.725165523557
Equivalent SR C.W.   [ Angs ] =  2.07795164581753
          C.E.     [ eV ] =  5966.70284650537
```

Source Definition

```
File to store the rays               BEGIN.DAT
Source Type (+)                      RAN/RAN
Number of random rays (+)            1000
Wiggler,undulator,elli_wigg (+)      WIGGLER
Spatial Type (+)                     GAUSSIAN
Depth                                OFF
Angle Distribution (+)               GAUSSIAN
Photon Energy distribution (+)       OFF
Store optical path                   NO
Polarization (+)                     NO
Coherence                            COHERENT
```

Wiggler specification

```
External file                        RADIAT.DAT
Conversion factor                    1.000000000000
```

Electron emit. [rads*user units]

Emittance in X 0.1830000000000E-06
Z 0.1410000000000E-08
Device's center from X wais 0.0000000000000E+00
Z 0.0000000000000E+00

Polarization component TOTAL

Source Spatial Characteristics

Source type GAUSSIAN
Depth OFF
width [X] n/a 0.0000000000000E+00
height [Z] n/a 0.0000000000000E+00
depth [Y] n/a 0.0000000000000E+00
sigma X 0.2017000000000E-02
sigma Z 0.4800000000000E-04
sigma Y n/a 0.0000000000000E+00

Source Angle Distribution

Angle distribution (+) GAUSSIAN

Use RADIANS for angles here.
Use ABSOLUTE values.
Horizontal divergence [X(+)] 0.5000000000000E-04
[X(-)] 0.5000000000000E-04
Vertical divergence [Z(+)] 0.1500000000000E-04
[Z(-)] 0.1500000000000E-04
Cone internal half-aperture n/a 0.0000000000000E+00
external n/a 0.0000000000000E+00
Horizontal Sigma [X] 0.1830000000000E-06
Vertical Sigma [Z] 0.1410000000000E-08

MAIN MENU Optical Element 1

Files to write out ALL
Source plane distance 13.35700000000
Image plane distance 10.00000000000
Incidence angle 0.2000000000000
Reflection angle 0.2000000000000
Mirror Orientation Angle 0.0000000000000E+00
Source file BEGIN.DAT

Type of element (+) REFLECTOR
Figure (+) TOROIDAL

Diffraction (+) MIRROR
Crystal (+) NO
Mirror movement (+) NO
Exit Slit (+) NO
Modified Surface (+) NO
Source Movement (+) NO
Goto OE (+)

OE specifications Optical Element 1

Mirror parameters (+) INTERNAL
Surface curvature CONCAVE
Cylindrical NO
orient. [CCW from X axis] n/a 0.0000000000000E+00
Reflectivity (+) OFF
Limits check (+) YES

Mirror Shape Optical Element 1

Shape selected RECTANGLE

Mirror dimensions along axis:
use ABSOLUTE values.

rectangle / ellipse

X(+) Half Width / Int Maj Ax 0.4160000000000E-01
X(-) / Ext Maj Ax 0.4160000000000E-01
Y(+) / Int Min Ax 3.500000000000
Y(-) / Ext Min Ax 3.500000000000

External parameters Optical Element 1

Type selected TOROIDAL
Spherical radius n/a 0.0000000000000E+00
Ellipse major Axis n/a 0.0000000000000E+00
minor Axis n/a 0.0000000000000E+00
Angle of MajAx and Pole [CCW] n/a 0.0000000000000E+00
Paraboloid param. n/a 0.0000000000000E+00
Hyperbola major Axis n/a 0.0000000000000E+00
minor axis n/a 0.0000000000000E+00
Angle of MajAx and Pole [CCW] n/a 0.0000000000000E+00
Torus major Radius 1500.000000000
minor Radius 0.4000000000000E-01
Cone half-aperture [deg] n/a 0.0000000000000E+00

6.8.2 The Outputs of the SHADOW Calculation for BL 6-2 Wiggler on SPEAR

Col	Par	Minimum:	Maximum:	Center:	St. Dev.:
1	X	-0.44696E-02	0.48854E-02	0.34513E-04	0.15085E-02
2	Y	-0.21479E-15	0.51724E-15	0.12554E-15	0.13893E-15
3	Z	-0.15254E-03	0.13878E-03	0.68944E-06	0.37444E-04
4	X'	-0.21479E-02	0.22954E-02	0.14153E-04	0.80868E-03
5	Y'	1.0000	1.0000	1.0000	0.24414E-03
6	Z'	-0.35631E-04	0.39223E-04	-0.15314E-06	0.14349E-04
11	Photon Energy (eV)	10590.	10620.		
20	Numerical Aperture	0.27200E-05	0.22955E-02		

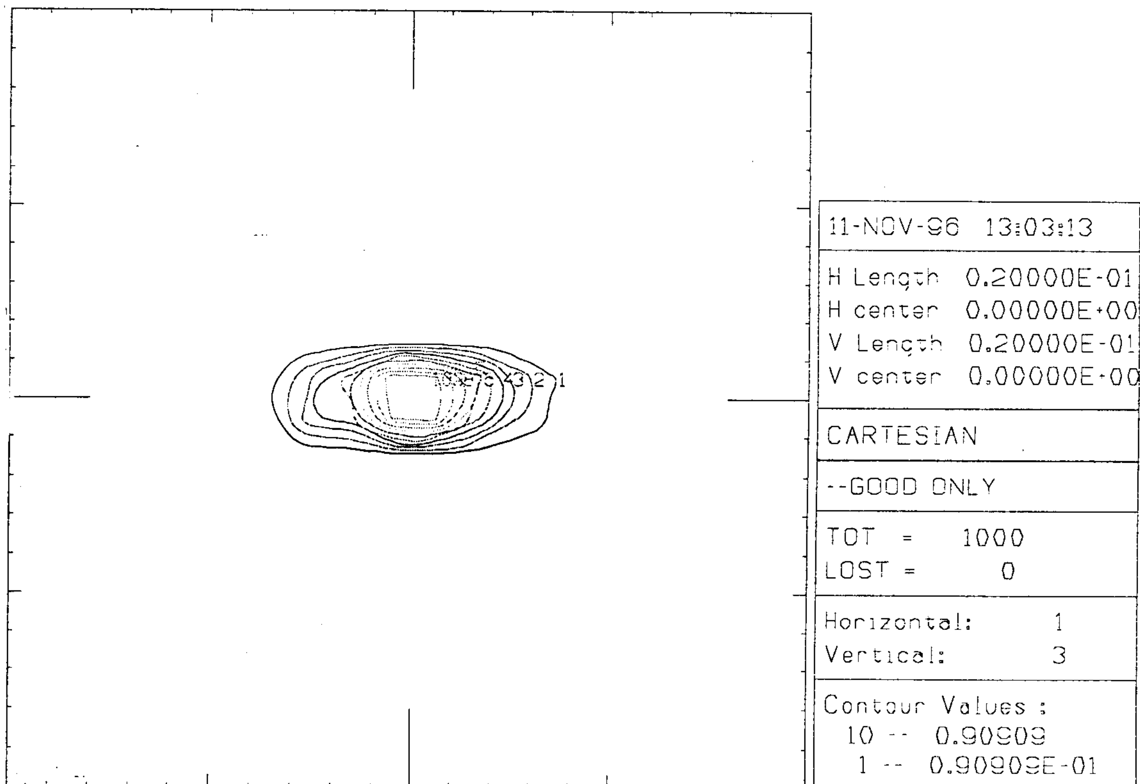

6.8.3 Flux from Insertion Devices

The third generation storage rings are also characterized by the use of undulators. An undulator is an insertion device that increases photon flux by the coherent interaction of the synchrotron radiation. These interactions are maximized by low emittance of electron beams [12].

The equation for calculating the flux from an insertion device, $\frac{dN_{ph}(E_x)}{d\Omega}$, is given by Eq. (6.12) [13],[14],

$$\frac{dN_{ph}(E_x)}{d\Omega} = \alpha \cdot \gamma^2 \cdot N_p^2 \cdot \frac{\Delta E}{E} \cdot \frac{I}{e} \cdot \sum_{i=0}^{\infty} i^2 \cdot \frac{\sin^2\left(\pi N_p\left(E_x - E_i\right)/E_1\right)}{\left(\pi N_p\left(E_x - E_i\right)/E_1\right)^2} \cdot \left(F_\sigma^2 + F_\pi^2\right) \quad (6.12),$$

where

$$E_i(\text{keV}) = \frac{29.6\gamma^2 i}{\lambda_p\left(2 + K^2\right)} \qquad (\lambda_p \text{ in unit of Å}) \quad (6.13)$$

$$F_\sigma = \frac{2\gamma \cdot \theta \cdot \Sigma_1 \cdot \cos\varphi - K \cdot \Sigma_2}{1 + 1/2K^2 + \gamma^2 \cdot \theta^2} \quad (6.14)$$

$$F_\pi = \frac{2\gamma \cdot \theta \cdot \Sigma_1 \cdot \sin\varphi}{1 + 1/2K^2 + \gamma^2 \cdot \theta^2} \quad (6.15)$$

$$\Sigma_1(i) = \sum_{m=-\infty}^{\infty} J_{-m}(u) J_{-i-2m}(v) \quad (6.16)$$

$$\Sigma_2(i) = \sum_{m=-\infty}^{\infty} J_{-m}(u)\left[J_{-i-2m-1}(v) - J_{-i-2m+1}(v)\right] \quad (6.17)$$

$$u = \frac{E_x}{E_1} \frac{\beta \cdot K^2}{4\left(1 + 1/2K^2 + \gamma^2 \cdot \theta^2\right)} \quad (6.18)$$

$$v = \frac{E_x}{E_1} \frac{2\beta \cdot K^2 \cdot \gamma \cdot \theta \cdot \cos\varphi}{1 + 1/2K^2 + \gamma^2 \cdot \theta^2} \quad (6.19)$$

where

E_x = x-ray energy (keV),

α = fine structure constant (= 1/137),

β = the ratio of the velocity of the particle to the velocity of light,

γ = the Lorentz relativistic factor,

i = the order of harmonics,

K = deflection parameter,

N_p = insertion device period,

E_1 = the energy of the first order harmonics (keV),

λ_p = the wavelength of insertion device magnets (Å),

I = beam current (A),

e = electron charge (= 1.602×10^{-19} Coulomb),

$\frac{\Delta E}{E}$ = band pass, and

J = Bessel function.

The angles of θ and φ are those of the polar coordinates representing the radiation geometry shown in Fig. 6.10.

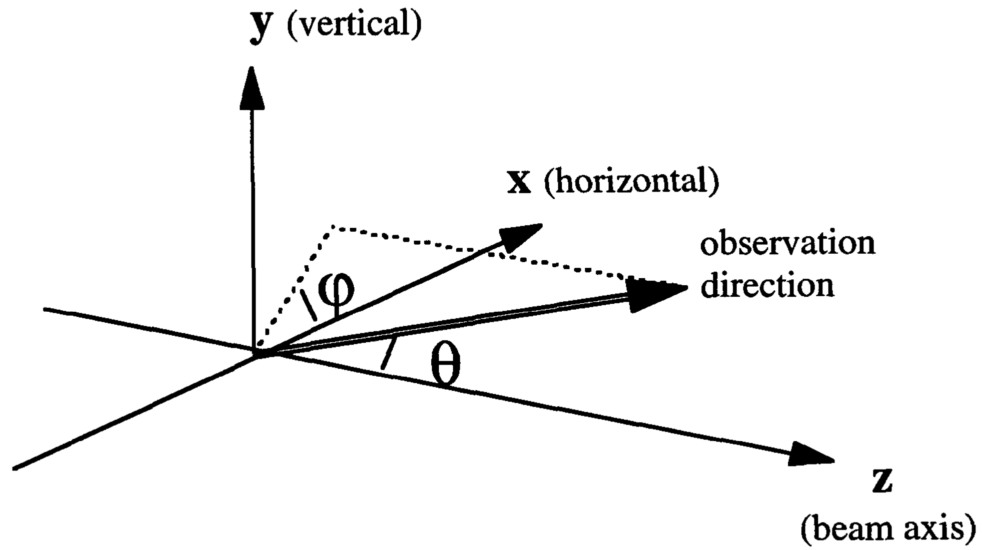

Fig. 6.10 Radiation geometry represented by polar coordinate.

In the forward direction ($\theta = 0$), Eq. (6.12) simplifies to,

$$\frac{dN_{ph}(E_x)}{d\Omega} = \alpha\gamma^2 N_p^2 \frac{\Delta E}{E}\frac{I}{e}\sum_{i=0}^{\infty} i^2 \frac{\sin^2\left(\pi N_p (E_x - E_i)/E_1\right)}{\left(\pi N_p (E_x - E_i)/E_1\right)^2}\left[J_{\frac{i-1}{2}}\left(\frac{i\cdot K^2}{4+2K^2}\right) - J_{\frac{i+1}{2}}\left(\frac{i\cdot K^2}{4+2K^2}\right)\right]^2$$

(6.20).

Using the size of the forward cone (the standard deviation of the emission of the synchrotron radiation),

$$\sigma \approx \frac{1}{\gamma}\sqrt{\frac{2+K^2}{4iN_p}} \tag{6.21}$$

the total photon flux of the i-th harmonic into the forward cone of $\pm\ \sigma$ is given by Eq. (6.22),

$$N_{ph} = \pi \cdot \alpha N_p \frac{\Delta E}{E} \frac{I}{e} \frac{2i \cdot K^2}{2+K^2} \left[J_{\frac{i-1}{2}}\left(\frac{i \cdot K^2}{4+2K^2} \right) - J_{\frac{i+1}{2}}\left(\frac{i \cdot K^2}{4+2K^2} \right) \right]^2 \qquad (6.22).$$

Furthermore, by substituting the width of the spectral line,

$$\frac{\Delta E_x}{E_x} = \frac{1}{i \cdot N_p} \qquad (6.23),$$

in the expression for the band pass in Eq. (6.22), the total flux is calculated using Eq. (6.24),

$$N_{ph} = 1.44 * 10^{17} \cdot I \cdot \frac{2 \cdot K^2}{2+K^2} \left[J_{\frac{i-1}{2}}\left(\frac{i \cdot K^2}{4+2K^2} \right) - J_{\frac{i+1}{2}}\left(\frac{i \cdot K^2}{4+2K^2} \right) \right]^2 \qquad (6.24).$$

6.8.4 *Mathematica* Notebook for Flux Calculation

SPEAR 3 Parameters

$$mc2 = 0.5 * 10^{-3};\ (*\text{electron mass in unit of GeV}*)$$

$$\alpha = \frac{1}{137.036};\ (*\text{fine structure constant}*)$$

$$e = 1.602 * 10^{-19};\ (*\text{electron charge in unit of Coulomb}*)$$

$$E_{SPEAR3} = 3;(*\text{particle energy in unit of GeV}*)\ //;;;;;;;;$$

$$\gamma_{SPEAR3} = \frac{E_{SPEAR3}}{mc2};$$

$$i_{und} = 5;\ (*5\text{ th harmonics}*)$$

$$I_{SPEAR3} = 0.2;\ (*\text{particle beam current in A}*)$$

$$K_{SPEAR3} = 0.991688;\ (*\text{deflection parameter}*)$$

$$\lambda p_{SPEAR3} = 2.8658 * 10^{8};\ (*\text{undulator period length (A)}*)$$

(*fundamental wavelength in unit of Angstrom*)

$$\lambda 1_{SPEAR3} = \frac{\lambda p_{SPEAR3}}{2 * \gamma_{SPEAR3}{}^{2}}\left(1 + \frac{1}{2} K_{SPEAR3}{}^{2}\right);$$

Equations

$$JJ[i_, K_] := \left(\text{BesselJ}\left[\frac{i-1}{2}, \frac{i * K^2}{4 + 2 * K^2}\right] - \text{BesselJ}\left[\frac{i+1}{2}, \frac{i * K^2}{4 + 2 * K^2}\right]\right)\text{^}2$$

$$fi[i_, K_] := \frac{i^2 * K^2 * JJ[i, K]}{\left(1 + \frac{K^2}{2}\right)^2}$$

$$g[i_, K_] := \frac{K^2 * JJ[i, K]}{\left(1 + \frac{K^2}{2}\right)}$$

$$N_{ph}[i_, K_, Ie_] := \frac{\pi \alpha}{e} * Ie * g[i, K]\ (*\text{total photon flux}*)$$

Fundamental Energy

$$e1_{SPEAR3} = \frac{12.4}{\lambda 1_{SPEAR3}}\ (*\text{keV}*)$$

2.08843

Total spectral undulator photon flux of the 5th harmonics into forward cone of angle +-$\sigma_{u'}$

$$N_{ph}[i_{und}, K_{SPEAR3}, I_{SPEAR3}]\ //\ N$$

9.43574×10^{13}

6.9 Conclusions

This chapter discussed the improvement of the MDLs as a function of incident beam energy, photon flux density, beam divergence, and polarization. It is found that the energy tunability of synchrotron radiation makes it possible to measure various elements in the periodic table with the MDLs ranging from about $1x10^8$ atoms/cm^2 to $3x10^9$ atoms/cm^2.

We projected that the MDLs of Ni would be improved to about $1x10^8$ atoms/cm^2 by use of the BL 6-2 wiggler with SPEAR3. It was also found that the further improvement is possible by the use of undulators. With an undulator on SPEAR3, the MDL would be improved to less than $5x10^7$ atoms/cm^2.

6.10 References

1. P. Bertin, *Principles and Practice of X-ray Spectrometric Analysis* , New York : Plenum, 1975.
2. F. Cerrina, C. Welnak, G.J. Chen, M. Sanches del Rio, *Shadow Primer 2.0* , Center for X-ray Lithography, 1990.
3. F. Cerrina, C. Welnak, G.J. Chen, M. Sanches del Rio, *Shadow User's Guide Ver. 1.0 draft* , Center for X-ray Lithography, 1989.
4. *X-RAY DATA BOOKLET*, 1986, LBL.
5. N. Takaura, S. Brennan, P. Pianetta, A. Fischer-Colbrie, J.B. Kortright, D.C. Wherry, K. Miyazaki, A. Shimazaki, Advances in X-ray Chemical Analysis Japan, **26s**,113 (1994).
6. UCRL-50400,V.6.REV.3.
7. E.C. Montenegro, G.B. Baptista, and P.W.E.P. Duarte, Atomic Data and Nuclear Data Tables, **22**, 2, 131 (1978).

8. J.L. Campbell, J.-X. Wang, W.J. Teesdale, Nucl. Instr. Meth. **B43**, 490 (1989).

9. G. H. Vineyard, Phys. Rev. **B26**, 4146 (1982).

10. A. J. J. Bos and M. Hart, Nucl. Instr. Meth., **B3**, 232 (1984).

11. E.E. Koch ed., *Handbook on Synchrotron Radiation, Vol.1 a* , North-Holland, 1983.

12. A. G. Michette and C. J. Buckley ed., *X-ray Science and Technology*, London : Institute of Physics Publishing, 1983.

13. H. Wiedemann (to be published in *Synchrotron Radiation*).

14. H. Wiedemann (to be published in *Synchrotron Radiation Chapter 3.1 in Handbook on Accelerator Physics and Engineering*).

15. H.D. Nuhn, *Optical Function Values for the SPEAR NOQ3 Lattice* (e-mail to M. Rowen), 1996.

16. S. Brennan, Spear3 Upgrade Scientific Case (e-mail to SSRL group), 1997.

17. S. Brennan (private communication).

18. Safranek thesis.

19. S. Brennan, SPEAR3 Workshop at SSRL proceedings, 1997

20. E. Hoyer, representing the Beam Line VI Design Group, Nucl. Instrum. Meth., **208**, 117 (1983).

21. J.H. Hubbell, W. Viewless, E.A. Briggs, R.T. Brown, D.T. Cromer, and R.J. Howerton, J. Phys. Chem. Ref. Data, **4**, No.3, 471 (1975).

7. CONCLUSIONS

This research investigated SR TXRF for microcontamination analysis on wafer surfaces. We focused on developing an optimized optical configuration for SR TXRF, extrapolating the Minimum Detection Limits (MDLs) of SR TXRF, eliminating spurious signals generated from Si (Li) detectors, modeling backgrounds, and projecting opportunities for the improvement of the MDLs. The development of the SR optical configuration allowed us to obtain the MDLs of Ni to be $3x10^8$ atoms/cm^2 in 1993. The improvement of Si (Li) detectors eliminated spurious signals generated from the detectors, which made it possible to achieve a true MDL of $3x10^8$ atoms/cm^2 in 1996. The modeling of SR TXRF backgrounds obtained good agreement with data, which allowed us to project the further improvement of the MDLs by use of third generation synchrotron radiation sources in the early years of 21st century.

7.1 Summary of Experimental Findings

We developed an optimized SR optical configuration for 3-d transition metal analysis on Si wafer surfaces. With wide band pass double multilayers ($\Delta E/E = 0.02$ at 11 keV), the 11 keV incident photon flux available from BL 10-2 wiggler beam on SPEAR was found to be about $1x10^{13}$ photons/sec. The photon flux from the synchrotron radiation resulted in more than 200 times higher x-ray signal count-rates than those from conventional x-ray sources.

Furthermore, our SR configuration greatly reduced the background intensity. The double multilayer monochromator arrangement reduced the non-Bragg reflection continuous background component to a negligible level, which prevented the generation of

diffraction peaks below the primary incident beam energy. Furthermore, a 25 μm Teflon absorption filter placed in front of a Si (Li) detector reduced the Si fluorescence background signal intensity by a factor of about 500. By installing the detector along the polarization vector of the synchrotron radiation, the scattered x-ray background count-rate was also reduced by a factor of about 10 compared to conventional TXRF. The reduction of the Si fluorescence signals and scattered x-rays prevented the saturation of detector electronics due to the higher x-ray count-rates of SR TXRF.

We determined the MDLs for SR TXRF using a standard Si wafer with intentional contamination of Fe, Ni, and Zn with the concentration of $1x10^{11}$ atoms/cm^2. The MDL of Ni on the Si wafer was found to be $3x10^8$ atoms/cm^2. This was about 20 times better than that by conventional TXRF ($5x10^9$ atoms/cm^2). The spatial resolution of SR TXRF (absolute detectable mass of 5 fg on an analyzed area of 15 mm^2) was also found to be much better than destructive wet chemical methods (absolute detectable mass of 5000 fg on the area of 18,000 mm^2).

We improved Si (Li) detectors by replacing detector parts containing 3-d transition metals with those not containing 3-d transition metals. The improved detector eliminated spurious fluorescence signals created inside the detector, which made it possible to achieve the true MDLs of $3x10^8$ atoms/cm^2.

We used our SR TXRF system for practical applications. For example, we analyzed contamination generated during gate oxidation processes. Our SR TXRF system could analyze the contamination of 3-d transition metals below the level of $1x10^9$ atoms/cm^2. The combination of synchrotron radiation and improved detector made it possible to analyze these small amount of contamination on Si wafer surfaces, which were difficult to analyze using conventional TXRF systems.

In addition, we extrapolated the MDLs of Ni on GaAs wafers and Al on Si wafers. The measurements of these elements were done by tuning the energy of the incident beam to prevent the excitation of substrate elements. The MDL of Ni on GaAs wafer surfaces was found to be about $1x10^9$ atoms/cm^2. The MDL of Al on Si wafer surfaces was found to be $5x10^{10}$ atoms/cm^2. Compared to the MDLs of 3-d transition metals on Si wafer surfaces, these MDLs were degraded by x-ray Raman scattering backgrounds.

7.2 Summary of Theoretical Findings

We theoretically modeled SR TXRF backgrounds consisting of photoelectron bremsstrahlung, Si fluorescence, Compton and Rayleigh scattering, x-ray Raman scattering, and detector incomplete charge collection backgrounds. To model these backgrounds accurately, we took into account the effects specific to SR TXRF.

The photoelectron bremsstrahlung generated in SR TXRF measurements could successfully be modeled by taking into account the photoelectrons escaping out of the Si wafer surface, which decreased the bremsstrahlung intensity by a factor of 2 compared to what it could be when incident angle is much higher than the critical angle. The combination of the calculations, measurements as a function of angle of incidence, and the filtering study revealed that the photoelectron bremsstrahlung was the dominant continuous background for the SR TXRF measurements of 3-d transition metals on Si wafer surfaces.

The Si fluorescence signals and Rayleigh scattered x-rays were modeled by taking into account surface oxides. We found that the surface oxides decreased the Si fluorescence intensity due to its lower Si atomic density ($2.2x10^{22}$ atoms/cm^3) compared to that of a Si crystal ($5x10^{22}$ atoms/cm^3). However, the surface oxides increased the intensity of the Rayleigh scattered x-rays. We successfully modeled the change in the intensities of these x-

rays as a function of oxide thickness. It was also found that, using our theoretical method, it was possible to measure the thickness of a surface oxide within an statistical error of 2% for thickness between 0 and 100 Å.

We could also successfully model the x-ray Raman scattering background by convolving the scattering cross-sections of the x-ray Raman scattering with the detector broadening. It was found that the x-ray Raman scattering background degraded the MDL of Al (5×10^{10} atoms/cm^2) by a factor of about 170 compared to the MDL of Ni (3×10^{8} atoms/cm^2).

The detector incomplete charge collection background was found to be less than 10% of the photoelectron bremsstrahlung intensity in the energy range between 2 keV and 6 keV.

7.3 Direction of Future Work

We estimated the further improvement of the MDLs of SR TXRF with respect to energy tunability, incident beam energy, incident photon flux density, and beam divergence.

It was found that, with the optimum incident beam energy (the fluorescence x-ray energy of interest plus 3.5 keV), the MDLs ranged from 1.4×10^{8} atoms/cm^2 for Y (Z=39) to 2.4×10^{9} atoms/cm^2 for P (Z=15). Furthermore, by increasing the incident photon flux by a factor of 10, the MDL of Ni would be improved by a factor of about 3 (4×10^{8} atoms/cm^2 vs. 1.3×10^{8} atoms/cm^2 for Ni).

A lower divergence beam also can improve the MDLs. By use of the computer code "SHADOW", we calculated the beam divergence of the SR beam on BL 6-2 with SPEAR to be 0.046 deg. With an incident beam with no beam divergence, the Ni MDL would be improved by a factor of about 2.

We estimated the Ni MDL obtained using third generation synchrotron radiation sources. With BL 6-2 wiggler on SPEAR3, which is an upgrade of SPEAR, the Ni MDL would be improved to about 1×10^{8} atoms/cm^{2}. Furthermore, with an undulator with SPEAR3, the MDL would be improved to 5×10^{7} atoms/cm^{2}. The undulator on SPEAR3 is expected to achieve a new goal for the MDLs required by semiconductor industries for the first years of 21st century.